ABSTRACT

Title of Dissertation:	A COMPREHENSIVE CHARACTERIZATION OF PYROLYSIS AND COMBUSTION OF INTUMESCENT AND CHARRING POLYMERS USING TWO-DIMENSIONAL MODELING: A RELATIONSHIP BETWEEN THERMAL TRANSPORT AND THE PHYSICAL STRUCTURE OF THE INTUMESCENT CHAR
	Joshua D. Swann, Doctor of Philosophy, 2019
Dissertation directed by:	Associate Professor Stanislav I. Stoliarov, Fire Protection Engineering

A quantitative understanding of an intumescent material's reaction to fire remains largely an unsolved challenge. More specifically, the relationship between thermal transport and the resulting char structure is not well understood. Improved pyrolysis models for intumescent materials are necessary to advance the fields of fire modeling and material development. To aid in this endeavor, a systematic methodology to parameterize comprehensive pyrolysis models for charring and intumescent materials is presented. Rigid poly(vinyl chloride), flexible poly(vinyl chloride), Bisphenol A poly(carbonate), poly(ether ether ketone), and poly(vinylidene fluoride) were analyzed in this work.

First, thermogravimetric analysis and differential scanning calorimetry were employed simultaneously to characterize the kinetics and thermodynamics of thermal decomposition. Microscale combustion calorimetry was utilized to parameterize the heats of complete combustion of gaseous pyrolyzates. ThermaKin, a numerical pyrolysis solver, was employed to inversely analyze all milligram-scale tests. A multi-step reaction mechanism, consisting of sequential steps, was constructed to capture all observed physical changes and chemical reactions.

Gasification tests were conducted on 0.07 m diameter disk-shaped samples using the newly developed Controlled Atmosphere Pyrolysis Apparatus II to parameterize the thermal transport within the undecomposed material and developing char layer. A recently expanded version of ThermaKin, ThermaKin2Ds, was employed to inversely model the gasification experimental results. The model accounted for spatially non-uniform swelling of the sample and the ensuing changes within the thermal boundary conditions. The resulting two-dimensional models were shown to reproduce the experimental sample shape profiles, unexposed surface temperatures, and mass loss rates with excellent accuracy.

An analysis of the char pore structure was also conducted to determine the pore size distribution and char porosity. Further analysis enabled the mean, median, and volume-weighted mean pore diameters to be computed from pore size distributions. Quantitative relationships were subsequently developed between relevant thermal transport quantities and the char's physical structure. It was determined that the thermal insulating potential of the fully developed char was related to the number of pore walls positioned perpendicular to the direction of heat flow. Therefore, designing charring polymers capable of producing

many small pores will aid in the development of intumescent materials with an enhanced thermal insulating potential.

A COMPREHENSIVE CHARACTERIZATION OF PYROLYSIS AND COMBUSTION OF INTUMESCENT AND CHARRING POLYMERS USING TWO-DIMENSIONAL MODELING: A RELATIONSHIP BETWEEN THERMAL TRANSPORT AND THE PHYSICAL STRUCTURE OF THE INTUMESCENT CHAR

by

Joshua D. Swann

Dissertation submitted to the Faculty of the Graduate School of the
University of Maryland, College Park, in partial fulfillment
of the requirements for the degree of
Doctor of Philosophy
2019

Advisory Committee:
Professor Stanislav Stoliarov, Chair
Professor Christopher Cadou, Dean's Representative
Professor Michael Gollner
Professor Peter Sunderland
Professor Bao Yang

Acknowledgements

First, I would like to thank my family for their unwavering support. Specifically, I would like to acknowledge the tireless encouragement and love from my wife, Elizabeth. You have relentlessly cheered for me and have patiently endured me being preoccupied with countless hours of studying, researching, writing, and pursuing my educational and career dreams. I am beyond grateful for your endless love and I look forward to welcoming our son, Rhett, into this world together. I would also like to thank my parents for always striving to demonstrate the importance of hard work, honesty, and integrity by living out those values every day. You have undoubtedly set the bar high as parents and I pray that I can love others as well as each of you have loved me.

Next, I would like to sincerely thank my advisor, Dr. Stanislav Stoliarov. Stas, I am extremely appreciative of you giving me the opportunity to work with you these past five years. Your work ethic and desire for excellence in your research is unrivaled and it has helped me become a better researcher. I greatly appreciate that you set high expectations and required hard work, but also provided an abundance of time to assist with any challenges that arose; your guidance and insight was and will continue to be invaluable. Thank you again for sharing your wisdom and inspiring a great attention to detail. I look forward to applying the skills and principles I have learned from you throughout my career.

I would like to thank those in my research group for embarking on this education journey together. I would like to specially acknowledge Dr. Mark McKinnon for his invaluable support and guidance as I began my graduate research. Mark, I am grateful for

the pivotal role you played in helping me get acclimated with the world of academic research and the numerous hours you spent assisting me with building the CAPA II. Next, Dr. Yan Ding was a great help with many experimental and modeling challenges. Yan, I'm not only thankful for your technical assistance, but for providing the group with endless energy and entertainment. I'm also grateful for everyone else I had the pleasure of working with during the past five years for their constructive conversations and invaluable feedback. I extend a special thank you to Ahmed, Cara, Chad, Chris, Conor, Dushyant, Fernando, Geri, Greg, Isaac, Jacques, Jess, and Xuan. I look forward to seeing how you all continue to impact the field of fire science.

I would like to thank all of the committee members who have generously given their time to provide critical feedback and guidance in varying capacities during this doctoral research. My advisory committee consisted of Dr. Christopher Cadou, Dr. Michael Gollner, Dr. Peter Sunderland, and Dr. Bao Yang. Thank you again for your comments and questions that have strengthened the outcome of this research. I would also like to acknowledge the U.S.A. National Science Foundation (CAREER Award #1347196 under the grant monitor Dr. Song-Charng Kong) for the generous financial support which made this research possible.

Table of Contents

List of Tables

List of Figures

Chapter 1: Introduction

1.1: Motivation

The widespread use of synthetic polymeric materials in the built environment has been increasing rapidly over the past several decades. Several key features, including the availability of raw materials for manufacturing, controllable physical properties, and the ease and flexibility of processing make the use of synthetic polymeric materials a viable substitution for traditional building products [1]. However, as the use of these materials continues to become more prominent in the built environment, there is an urgency to understand their inherent flammability more completely. A thorough understanding of a material's reaction to fire enables well-informed decisions to ensure adequate life safety in all engineering design applications.

In general, polymeric materials used in a wide range of common household as well as very specific engineered applications have well defined fire performance criteria. To satisfy fire safety regulations, conventional flame-retardants are often employed [2]. These flame retardants inhibit the fire growth through several methods: reducing the heat produced by the pyrolyzing material, reducing the rate of production of pyrolyzate gases, reducing the heat flow to the undecomposed material (thermally insulating), and reducing the rate at which the volatile gaseous products are transported to the sample surface [3–5]. Each of these methods have associated advantages and disadvantages; however, they all inhibit one or more of the controlling mechanisms of pyrolysis or flame spread. Although

many different flame-retardant agents and compounds are used in practice, this study will focus on the mechanism of char production and intumescence.

Char production is one mechanism that is known to contribute to making materials more resistant to fire growth and flame spread. Materials can be chemically manipulated in order to increase their propensity to produce a non-combustible carbonaceous layer of residual material [4]. One method to manufacture charring materials is through the engineering design of entirely new molecules. Alternatively, flame-retardant additives can be introduced to existing materials in order to initiate the production of a char layer and intumescent behavior during the pyrolysis process. In both scenarios, it is crucial to understand the mechanisms in which the char layer inhibits a materials reaction to fire in order to adequately design for each specific material application.

Char formation in polymeric materials, whether newly synthesized compounds or existing materials with additives, generally have a chemical and/or a physical aspect to their performance. The chemical aspect of char forming flame-retardants is due to the retention of carbon through dehydration during pyrolysis [6,7]. When the carbon molecules are effectively retained in the residual char, it reduces the amount of pyrolyzate gases released to contribute to the combustion process, which ultimately leads to a reduction in the heat of combustion of the pyrolyzate gases per unit initial mass of the solid sample. The formation of a char layer, on the other hand, has also been shown to provide a thermal barrier to the undecomposed material underneath [5,6]. The formation of a thermal barrier serves to protect the underlying polymer below by preventing increased thermal exposure. Lastly, it has been found that a char layer may serve as a physical barrier to mass transport

[7–9]. If the mass transport is inhibited, the rate at which combustible gases can escape the thermally decomposing material is reduced, which improves the overall fire safety by limiting the delivery of volatile gaseous products to the flame on the sample surface.

Although many flame retarding agents and compounds have been shown to perform very well in reducing a material's flammability, several health and environmental concerns have been identified. Poly-brominated diphenyl ethers were once one of the most commonly used flame-retardants; however, their persistence in the environment, high bioaccumulation potential, and possible toxicity led to their phase-out in much of the world nearly twenty years ago [10]. Several additional studies [11–13] have linked various flame-retardants to possibly contributing to papillary thyroid cancer, liver and kidney malfunction, behavioral modification, and gastrointestinal lesions. It is important to note that the risk of health effects from exposure to chemical compounds is a combination of the intrinsic toxic potential and the actual exposure to the compound itself [14]. Therefore, the flame retardant industry has since turned its attention to alternative methods (including the improvement of charring materials) to meet flammability standards while also promoting positive health and environmental impacts.

Therefore, the design of polymeric materials that satisfies fire safety regulations while also promoting positive health and environmental impacts is largely the focus of the materials engineering and fire safety communities. To design advanced fire resistant charring polymers, it is important to understand which characteristics and properties of the char layer provide the most efficient thermal insulating potential to the undecomposed polymer below. A thorough understanding of the coupling between the char growth

dynamics and the rate of formation of flammable gases is also of great importance. It is vital to have a quantitative understanding of the heat and mass transport of thermally decomposing charring and intumescent solids to guide the design of next generation fire resistant polymeric materials. This quantitative understanding of pyrolysis of charring and intumescent materials significantly depends on the foundation of numerical pyrolysis modeling.

1.2: Background

1.2.1: Review of Pyrolysis Model Development

Over the past several decades, tremendous advancements have been made in the development of numerical fire models. A significant portion of this work is related to the gas phase activity of the fire problem. However, it is generally recognized that the condensed phase pyrolysis plays a critical role in the ignition and early stages of fire development [15]. Kashiwagi [15] presented a thorough review of the critical chemical and physical mechanisms that drive the condensed phase combustion of polymers, specifically, the complexity of the production of pyrolyzate gases. Therefore, many mathematical pyrolysis models have been developed to obtain a more thorough understanding of condensed-phase pyrolysis. Several review studies [16–18] were conducted to identify the state-of-the-art in pyrolysis model development.

In general, pyrolysis models may be classified into two categories based on various simplifying assumptions: either simple thermal models or comprehensive pyrolysis models. One major distinction is that thermal models rely on the assumption of infinite-rate reaction

kinetics while comprehensive models account for finite-rate reaction kinetics. Therefore, the thermal decomposition process in thermal models begins abruptly when the temperature reaches a critical threshold. The application of the critical decomposition temperature, however, greatly reduces the model complexity to a single energy balance equation. This simplification effectively decouples the thermal degradation reaction kinetics from other physical processes. Comprehensive pyrolysis models, on the other hand, incorporate finite rate chemical reactions, which is achieved by solving partial differential equations for heat and mass conservation to account for user prescribed reaction kinetics. The inclusion of finite rate chemistry enables the model to capture thermal transport as well as chemical reaction rates. Although demanding more computational power, their ability to represent all relevant physics has made comprehensive pyrolysis models a desirable option for the vast majority of fire simulations.

As computational power has continually increased, several generalized numerical comprehensive pyrolysis solvers have been developed. These solvers are capable of predicting the gasification rate of pyrolyzing materials accounting for finite-rate chemical reactions. The most prominent and commonly used are the solid-phase model from the National Institute of Standards and Technology (NIST) Fire Dynamics Simulator (FDS) [19], Gpyro [20], and ThermaKin [21]. It should be noted that the term “model”, when used in this study, represents both the modeling tools as well as the specific sets of material properties.

The FDS condensed-phase model [19] was developed at NIST. Conservation equations of species, energy, and mass are solved to predict the mass loss rate of a

pyrolyzing material. Condensed-phase chemical reactions are defined with Arrhenius reaction rate expressions to allow multi-component, nth-order reaction schemes. All gases produced in-depth by thermal decomposition are instantaneously transported to the top surface; therefore, mass transport within the condensed-phase is neglected within FDS. The heat equation takes into account conduction in the solid phase, heats of reaction, radiation absorption, and in-depth emission of radiation. A "two-flux" model is employed to account for the radiation heat transfer both into and out of the pyrolyzing sample. A primary advantage of the FDS solid phase model is its ability to be coupled directly to the FDS gas phase solver and can be applied in a wide range of scenarios.

Gpyro [20] is an open-source fire model developed by Lautenberger and Fernandez-Pello capable of simulating a wide range of scenarios. Temperature, species, and pressure distributions inside the sample are determined by solving the corresponding conservation equations for both the gas-phase and condensed-phase. The chemical reactions are described in Gpyro with Arrhenius reaction parameters, where both heterogeneous and homogeneous reactions can be captured. The heat equation takes into account conduction, heats of reaction, convection from the gas-phase to the condensed-phase materials, and in-depth absorption. The contribution from in-depth radiation emission is neglected by Gpyro. The heat transfer between the gas-phase and condensed-phase can be calculated using either thermal equilibrium or two-temperature (non-equilibrium) formulations. The gas phase momentum is represented using Darcy's law. Gpyro also has the capability to be coupled with the gas-phase solver from FDS, making this numerical tool very versatile.

ThermaKin was developed by Stoliarov and Lyon [21] at the Federal Aviation Administration (FAA). Overall, ThermaKin is formulated similarly to the FDS condensed-phase model and Gpyro; however, the treatment of in-depth absorption is one notable difference. In ThermaKin, the external radiation is absorbed within a single (possibly in-depth) element that is selected at each time step using a random absorption algorithm. The Beer-Lambert distribution of absorbed energy is applied as a probability density function to guide this selection. Radiative heat transfer inside the sample is computed by applying the radiation diffusion approximation [22]. Both first- and second-order (two solid components) Arrhenius reactions can be defined. ThermaKin has the ability to define most of the thermo-physical parameters of a component as a function of temperature using a flexible polynomial formulation. One important feature of ThermaKin, which is also included in the FDS condensed-phase model and Gpyro, is the ability to account for the expansion and contraction of pyrolyzing objects (intumescence). In this work, ThermaKin is employed to develop pyrolysis models for a collection of commonly used charring and intumescent polymers. Details of the ThermaKin framework are provided in Chapter 3.

The FDS condensed-phase model, Gpyro, and ThermaKin all require a complete set of material properties as model input parameters in order to predict the rate of gaseous pyrolyzate production during the pyrolysis of solid materials. These parameters include kinetics and thermodynamics of thermal decomposition as well as thermal transport properties. The dependence upon a complete set of parameters often limits the use of these generalized comprehensive pyrolysis models. As increasingly complex materials are formulated for specific highly-engineered applications, a new set of input parameters must

be determined to enable these sophisticated models to provide adequate estimates of the material's burning rate.

To develop a comprehensive set of model input parameters, a number of experimental techniques have been designed to estimate material properties through independent experiments. These experimental methodologies often rely on small-scale laboratory experiments to reduce cost and complexity; however, they must be designed carefully to ensure adequate representation of the full-scale behavior. Each of these techniques requires well-defined boundary conditions to ensure secondary behavior is avoided in the parameter extraction process. Many of these methodologies employ milligram-scale experiments to determine the kinetics and thermodynamics of thermal decomposition as well as various gram-scale experiments to characterize the associated thermal transport. A review of the studies implementing these methodologies is outlined in the following sections.

1.2.2: Review of Kinetics and Thermodynamics of Thermally Decomposing Charring and Intumescent Materials

Thermogravimetric analysis (TGA) and differential scanning calorimetry (DSC) are employed to measure the mass loss and heat flow to a thermally decomposing sample as a function of sample temperature. These milligram-scale experiments are employed to decouple thermal degradation from transport processes. Conducted in a nitrogen atmosphere, TGA experiments enable the parametrization of a kinetics model to predict the mass loss rate of thermally decomposing materials as a function of sample temperature. DSC enables the parametrization of the thermodynamics of thermal decomposition to

account for the heat flow in and out of the thermally decomposing sample. More details on each of these instruments are provided in section 2.2.1.

The thermal degradation of a solid material is the first step of an unwanted fire event, such as smoldering combustion, ignition, and flame spread. Therefore, it is of utmost importance to understand the mechanisms controlling the interactions between the chemical and physical processes during pyrolysis. Additionally, a global understanding of the resulting volatile gaseous products is crucial for modeling flame spread. Solid fuels, when subjected to sufficient levels of external heating, begin thermal decomposition resulting in the production of volatile gases and, for some materials, a solid carbonaceous char. The combustion process of charring materials, when exposed to sufficient oxygen, results in either smoldering or flaming combustion [16].

Smoldering is a slow, low temperature, flameless form of combustion that occurs when sufficient heat and oxygen are not present to sustain flaming [23]. It is sustained by the heat evolved from oxygen directly attacking the surface of the condensed phase fuel, also known as surface oxidation. During flaming combustion, the flame sheet is believed to consume all the surrounding oxygen [24,25]; therefore, smoldering does not occur. However, surface oxidation can effect on the ignition of certain fuels and continue to consume the residual char layer after the flame is extinguished. Although smoldering combustion may influence the char formation process, it is outside to scope of this study and will not be discussed. Flaming combustion occurs when sufficient heat, pyrolyzate gases, and oxygen are combined at the surface of the condensed phase material [16]. The majority of this study is focused on the thermal decomposition of materials that occurs in

the condensed phase only, largely neglecting a detailed analysis of gas-phase phenomenon; however, the heats of complete combustion are measured and employed to conduct simplified large-scale simulations of the combustion of charring and intumescent polymers.

Di Blasi [26] authored a review paper comprised of a collection to studies addressing the state-of-the-art of the combustion of charring solid fuels. It was found that the thermal degradation of wood presents unique challenges, as the structure of the wood is anisotropic and the burning behavior is dependent upon the grain direction [27]. The products of wood decomposition are often grouped into three categories: char, gas, and tar. Arrhenius reaction rate equations are often employed to compute the thermal degradation by prescribing global kinetic reaction schemes as a function of temperature. Di Blasi [16] outlines three reaction schemes commonly used in the literature. One-step global reaction schemes that employ a single reaction to describe the total mass loss process. One-step, multi-reaction schemes utilizing several parallel reactions, which includes a single reaction step for each virgin material. Lastly, multi-step, semi-global schemes represent the most realistic reaction mechanisms by including primary and secondary reactions that represent further degradation of the intermediate condensed-phase products. Each of these classifications offer a varying level of complexity aiming to capture both the chemical and physical aspects of the charring combustion of wood.

Numerically modeling the combustion of synthetic polymers is fundamentally similar to that of wood because it first requires a detailed understanding of the kinetics and thermodynamics of thermal decomposition. These reaction schemes must then be coupled with the heat and mass transfer physics to accurately predict the entire pyrolysis problem.

Early attempts to capture the kinetics of thermal decomposition were conducted using a simplified application of first-order kinetics to model the in-depth degradation process [28–33]. Wichman and Atreya [34] introduced a simplified method to model char formation with Arrhenius rate equations by defining the density (a function of temperature) proportionally to the thermal conductivity.

Lyon [35] developed a similar approach by analytically solving a mechanistic pyrolysis model for char forming polymers to estimate the mass loss history of burning. The objective of this study was to obtain insight on the fuel generation process of flaming combustion, but it was constructed on the foundation of the kinetics of thermal decomposition. The mechanistic model, using a single first-order rate law (the polymer decomposed into volatile gases and char), was constructed with the following assumptions. The first assumption is that primary bond dissociation is the rate-limiting first step. Mass loss was assumed to proceed through an active intermediate reactant in a steady state. Primary gas and char production were competing processes whose magnitude and rate constants are large compared to successive products and rate processes. The last assumption is that all modeling conditions were performed in an anaerobic environment. A critical finding in this study was that the simple analytical solution for peak mass loss rate during steady heating showed that the maximum fuel generation rate decreased linearly with an increasing char yield. Additionally, the peak mass loss rate was found to be inversely proportional to the square of the peak decomposition temperature. Therefore, it was concluded that the mass loss was physically related to temperature and heating rate dependent product yields.

A mathematical model developed by Watt et al. [36] was utilized to explore the influence of char formation on the ignition of polymeric materials through a theoretical numerical approach. A non-competitive reaction scheme (the polymer was reduced to char and volatiles by parallel reactions) was utilized in this study. It was found that, in general, there was no significant difference between model results when using competitive versus non-competitive reaction schemes [37]. Due to the formation of the char layer, the volume was changing in time, which lead to a moving top boundary in the model development. It was found that as the theoretical char yield increased, the time to ignition also increased. Ignition was defined to occur when a critical mass flux through the top surface was achieved. It was found that if the char yield was too large, for a given applied heat flux, the samples would not ignite. The lack of ignition was due to the presence of the char layer prohibiting thermal degradation, which ultimately prevented the critical mass flux for ignition from being achieved.

Staggs [38] proposed a theoretical model to account for the mass transport of the condensed phase material during thermal decomposition through the introduction of an advection term. The advection term, which was often neglected, assumed that the condensed phase material would instantaneously fill the void left by the volatile gases escaping the condensed phase. Such calculations were only possible when using a finite-rate kinetics model which accounted for the in-depth degradation of the material instead of strictly surface decomposition. It is important to note that this model neglected the specific mechanism of gaseous transport. The aim of this study was to construct a heat transfer

model to represent the kinetics of thermal decomposition. This degradation model could then ultimately scale up to predict bench scale tests, such as the cone calorimetry.

More recently, a study by Li and Stoliarov [39] was conducted to demonstrate a systematic methodology for the measurement of the kinetics and thermodynamics of thermal decomposition of charring polymeric materials. This methodology employed TGA and DSC experiments conducted simultaneously, in the same experiment. A numerical model was subsequently employed to inversely analyze the TGA and DSC data to obtain degradation kinetics and thermodynamics. The resulting parameters obtained through inverse analysis were shown to reproduce the experimental dataset with a high degree of detail. This parameterization methodology was successfully applied to a collection of highly charring polymers.

The previously described studies demonstrate that the kinetics of thermal decomposition of charring polymers are generally understood well. Methodologies exist that enable material properties to be carefully extracted to populate the input parameter set for comprehensive pyrolysis models to simulate the kinetics and thermodynamics of thermal decomposition. However, these studies employ simplifying assumptions that neglect thermal and mass transport due to the physical size of the tests. Therefore, scaling up the scope of the analysis to include transport processes within the models requires additional experiment measurements to parameterize the associated numerical fire models.

1.2.3: Review of the Effective Thermal Transport within Charring and Intumescent Materials

In addition to defining reaction kinetics and thermodynamics, a comprehensive pyrolysis model requires quantification of thermal transport parameters. Many early studies were conducted in an oxidative environment with relatively poorly controlled boundary conditions. It is widely assumed that the oxidizer in these studies was primarily consumed at the flame sheet of the associated diffusion flame [24,25]; therefore, the effects of oxidation was assumed to be negligible during thermal decomposition. However, the resulting flame which was sustained on the sample surface provided additional complexity in the experimental boundary conditions.

To understand the rate at which heat is transferred through the condensed-phase material, Fourier's law of heat conduction (the product of the material thermal conductivity and temperature gradient along the direction of heat transfer) is often utilized. Thermal conductivity is a measure of the rate of thermal transport through a solid or condensed phase material, as defined by Fourier's Law given by Equation 1.1 [40].

$$q_i'' = -k \frac{\partial T}{\partial x_i} \tag{1.1}$$

where q_i'' is heat flux per unit area, k is thermal conductivity, T is the sample temperature, and x is the Cartesian coordinate in the i-th direction.

Measuring the thermal conductivity of a solid material that does not degrade under external heating is relatively straightforward. The traditional guarded hot plate experiment,

for example, is a common method to evaluate the thermal conductivity of a solid [41]. In the hot plate method, a sample material is placed on both sides of a guarded heater. An additional heated enclosure, maintained at the same temperature as the internal heater, ensures that there are no heat losses on the backside of the test specimen. The temperature of the sample is monitored at several locations to obtain a measure of the temperature gradient. The thermal conductivity is subsequently computed in accordance with Equation 1.1. The hot plate approach has proven to work well for many materials which maintain a constant volume while undergoing heating. However, guarded hot plate experiments are typically not valid for intumescent materials due to the substantial growth in volume when subjected to thermal exposure; thus, alternative approaches must be identified.

As a result of difficulties with the guarded hot plate approach, Anderson et al. [42] developed an alternative procedure to estimate an effective thermal conductivity of intumescent chars. The term effective thermal conductivity, in this study, is used to describe the combination of the material specific thermal conductivity as well as potential negligible contributions from properties such as density, expansion, etc. This new procedure to measure the effective thermal conductivity relies on the temperature of small samples as a function of time. The temperature histories are measured by a Type K thermocouple attached to the center of the back surface of the sample. The samples consisted of an intumescent coating applied to a metal substrate, which was exposed to a radiant heat flux of approximately 115 kW m^{-2} incident to the initial sample surface. The applied heat flux set point is consistent with aviation fuel fires detailed in another study [43]. The associated heat transfer model was based on a simple model that considered the

char to be a porous solid with no convective heat transfer (the pores are sufficiently small). Additionally, it was assumed that the heat absorbed by the char and radiation transfer through the char was negligible. Regardless of the complexity of the physics associated with intumescence, a simple model for conductive heat transfer through a porous char was developed to provide an estimate of the effective thermal conductivity for intumescent coatings applied to a metal substrate.

A similar study estimating the effective thermal conductivity of intumescent coatings was conducted by Bartholmai and Schartel [44]. The method consisted of measuring the sample temperature while conducting cone calorimetry [45] and small-scale furnace [46] experiments. The cone calorimeter is a bench-scale instrument based on a standardized test which is widely used to measure material flammability properties under semi controlled conditions. The cone calorimeter is capable of measuring properties such as time to ignition, critical heat flux for ignition, heat release rate (HRR) through the oxygen consumption principle, mass loss rate (MLR), and heat of combustion of the pyrolyzate gases. Small-scale furnace tests expose a sample to a radiant heat flux from an oil burner while measuring surface temperatures.

The test method employed by Bartholmai and Schartel [44] for assessing the thermal performance of intumescent coatings is outlined by the following steps. First, the intumescent coating was applied in varying thicknesses to steel test plates with Type K thermocouples attached to the surface of the steel plate. The sample holder was then insulated with vermiculite to minimize heat losses from the sides and back. The external heat was applied to the samples via an electric conical heater from the cone calorimeter

(30, 45, 60, and 75 kW m^{-2}) or the oil burner inside the small-scale test furnace following a standard temperature-time curve [47]. The sample holder remained static during the test, resulting in the sample surface receiving a non-uniform heat flux as the surface expanded [48]. The surface temperature was recorded as a function of time from the thermocouples attached to the back center of the steel plates for the test duration of 90 min. Finite difference simulations were subsequently employed to analyze the experimental data. The temperature data served as an input to the finite difference scheme in order to calculate the effective thermal conductivity of the intumescent coating. The computed effective thermal conductivity was assumed to capture the effects of the specific thermal conductivity, heat capacity, density, expansion, and chemical reactions, unanimously.

The residual yields obtained from the cone calorimetry experiments were found to decrease with increasing levels of applied external heating. The residual yields were also found to decrease with decreasing applied thickness of the intumescent coating. It was found that although there were apparent differences between the two test methods, both tools indicated that the applied intumescent coatings greatly reduced the rate of thermal transport to the steel substrate. However, one of the major limitations in this study was that it completely neglected a detailed resolution of chemical processes or mass transport that may occur during pyrolysis. Instead, it strictly calculated a single average effective thermal conductivity for the coating being evaluated. Neglecting detailed analysis of a materials thermal decomposition is arguably the main drawback of any traditional thermal conductivity measurement technique when applied to charring materials. These traditional techniques to measure an effective thermal conductivity are unable to isolate individual

components at elevated temperatures. Additionally, many traditional thermal conductivity measurement techniques require well-defined constant sample shapes to provide adequate thermal contact to the experimental equipment, which is generally unattainable for charring and intumescent materials.

Stoliarov et al. [22] conducted a study that sought to quantitatively understand the pyrolysis of Bisphenol A polycarbonate and poly(vinyl chloride) through experimental and numerical techniques, including the temperature dependence of thermal conductivity. A one-dimensional comprehensive pyrolysis model, ThermaKin [21], was employed to simulate the results of cone calorimetry tests of the aforementioned charring and intumescing polymers. The two primary objectives of this study were to understand the best method to model intumescent char and to determine the model's sensitivity to the uncertainty of various input parameters. Stoliarov et al. inversely analyzed thermogravimetric analysis (TGA), microscale combustion calorimetry (MCC), and cone calorimetry experimental data to determine material properties to serve as modeling input parameters. TGA and MCC are described in detail in section 2.2 of this manuscript.

To account for the growth of the intumescent chars, a sub-model was required. Therefore, a simple approach permitting the chemical reactions to define the expansion was adopted. In this approach, it was assumed that the volatile gases did not contribute to the material's expanded volume. It was observed that the heat flow through the char component was defined by the product of the density and thermal conductivity, which were found to be inversely proportional. To decrease the numerical computational cost, the

density and thermal conductivity were scaled such that the volume of the sample during the simulation remained constant.

The second critical portion of this study by Stoliarov et al. revolved around the sensitivity analysis of the input parameters. According to a previous analysis [49], the peak and average heat release rates are most sensitive to uncertainties in the kinetics of decomposition, heats of decomposition, char yield, and effective heats of combustion of pyrolyzate gases. Stoliarov et al. ruled out uncertainty in the char yield and effective heats of combustion in this study because they were measured very carefully in novel experiments. The Arrhenius reaction rate parameters were varied drastically and were found to produce no significant impact on the final modeling results. This observation of a negligible impact from the reaction rate parameters indicated that significant differences in the parametrization of the kinetics of thermal decomposition does not always translate to significant differences in the simulated heat release rate. The uncertainty in the heats of decomposition, however, were found to have a profound impact on the final simulated heat release rates profiles. Therefore, it was determined that the heats of decomposition must be determined very carefully to produce reliable heat release rate predictions.

Although the one-dimensional model was successfully parameterized to reproduce the cone calorimeter experimental data, the authors noted several limitations to their proposed methodology. The low accuracy of the decomposition thermochemistry can greatly alter the simulated outcome. It was also noted that large discrepancies might be a result of the inability of the one-dimensional model to capture the three-dimensional processes of both the development of the intumescent char layer and the structure of the

flame itself. Therefore, the authors allude to the necessity of a pyrolysis model of higher dimensionality to gain insight into the formation of intumescent char.

Medium density fiberboard (MDF), a relatively newer wood material that is a viable replacement for traditional wood products, has gained significant attention in the fire community. Due to the homogenous nature of MDF, it has been found to be an excellent candidate to provide reliable experimental results for improving pyrolysis models of charring materials. Results from a study conducted by Li et al. [50] demonstrated that the mass loss rate obtained from cone calorimetry displayed two distinct peaks; similar behavior was also observed by Elliott et al. [51]. The valley in between the peaks is believed to be associated with a char layer forming shortly after ignition, which shielded the virgin layer and ultimately reduced the mass loss rate and the burning behavior reached a quasi-steady state region. The second peak was only present when the back of the test specimen was insulated, which was believed to be associated with the thermal transport reaching the back insulation and therefore resulting in an increased thermal wave to the decomposing sample.

Potential limitations of each of these previous studies are related to the testing instrumentation. The testing equipment in these studies are excellent tools to provide qualitative comparisons of a materials fire performance, however, quantitative measurements often incorporate many secondary effects (such as oxidation) resulting from the poorly defined boundary conditions of the experimental configuration. Therefore, it was understood that specialized experimental techniques are required to decouple these secondary effects responsible for misleading results. This critical finding lead to an

understanding that the boundary conditions within the testing equipment must be very well defined throughout the entire experiment.

To control the boundary conditions more carefully, several bench-scale gasification experiments have been developed. A gasification apparatus enables the thermal decomposition of materials within an anaerobic environment, thus eliminating the complexity of surface oxidation and a sustained flame. These instruments include the NIST gasification apparatus [52], fire propagation apparatus (FPA) [53], mass loss calorimeter [54], and controlled atmosphere pyrolysis apparatus (CAPA) [55]. These techniques enable the simultaneous measurement of sample mass loss and sample temperature in an anaerobic environment. Several methods have been proposed to determine a complete set of material properties based on the data obtained from these bench-scale gasification tests.

Chaos et al. [53] employed an advanced optimization scheme (Shuffled Complex Evolution (SCE) approach) to determine the material properties from pyrolysis data collected in the FPA. The SCE approach has the advantage of considerably reducing the iterations necessary to obtaining an optimum and providing more accurate predictions compared to a Genetic Algorithm. The one-dimensional pyrolysis model developed here was based on the principles of Gpyro [20]. The model, coupled with the SCE approach, was employed to estimate the parameters of three practical materials: Poly(methyl methacrylate) (PMMA), single-wall corrugated board, and chlorinated polyvinyl chloride. It should be noted that only MLR data were used as target data. The surface temperature data measured with an infrared pyrometer were not used due to the unknown surface emissivity. The temperature-dependency of properties was not considered. The

combination of the model and optimization scheme predicted the MLR data of the tested materials exposed to several heat fluxes very well. However, it was shown that the obtained model parameters may not be representative of physical and chemical properties and thus the extrapolation to scenarios outside the calibration conditions are unjustifiable [20,56]. This study highlights the necessity to design an approach that can yield physically realistic parameters that describe a material's response to conditions both within and outside the calibration scenario.

Li et al. [55,57] conducted a study to develop pyrolysis models for charring polymers. The study sought to provide improvements to the previous approach presented by Stoliarov et al. [22], however, several limitations were still present. A similar methodology was presented which employed milligram-scale experiments to characterize the decomposition kinetics and thermodynamics. A newly designed gram-scale controlled atmosphere pyrolysis apparatus (CAPA) was utilized to collect mass loss rate and surface temperature data in an anaerobic environment instead of cone calorimetry. Anaerobic conditions were utilized in both milligram- and gram-scale experiments to simulate material degradation under a laminar flame sheet. However, several of the materials experienced significant shape changes due to intumescence, which made it impossible to control the oxygen concentration at the top sample surface. Therefore, the testing apparatus permitted excess oxygen to be present above the top sample surface which eliminated the anaerobic conditions when the sample experienced significant swelling, ultimately resulting in sustained flaming. All experimental results were inversely analyzed using the ThermaKin numerical framework.

Several notable limitations of the CAPA experiments and a one-dimensional modeling framework were revealed when applied to highly intumescent materials. Substantial swelling of the materials during decomposition presented significant uncertainties in the incident heat flux on the top sample surface. It was also found that the intumescent layer was significantly non-one-dimensional, which could not be captured by the one-dimensional modeling framework. Additionally, as the sample surface expanded, the anaerobic conditions were no longer valid which made it impossible to rely on a significant portion of the experimental data. Therefore, this study concluded the need for improved experimental results and a higher-dimensionality pyrolysis model to capture the physics of intumescent thermal decomposition. The authors also noted that it might be required to include some additional solid mechanics and edge effect corrections to extrapolate the modeling results to larger length scales.

Most of the previous studies focus on developing pyrolysis models of pure polymers with effective properties. However, the authors failed to account for the specific impact of the thermal transport within the porous char structure itself. As the demand for more effective and environmentally friendly flame resistant engineered plastics increases [58], it is crucial to extend this methodology to not only account for the pyrolysis of charring and intumescent materials with a higher degree of accuracy, but it is also vital to understand the impacts of the char's physical structure on the heat and mass transfer during thermal degradation.

1.2.4: Review of Char Growth Dynamics and the Specific Thermal Transport in Porous Media

To understand the impacts of the char's physical structure on the thermal transport during pyrolysis, a collection of the cornerstone experimental and numerical studies related to polymeric char formation and intumescence are presented. Char formation is desirable because it has been shown to reduce the flammability of materials. Intumescence, a term referring to growth or increase in volume as a result of heating [59], is also qualitatively understood to reduce the material flammability. Organic intumescent materials consist of the following four critical chemical components: a carbon donor or char former, an acid donor or catalyst, a blowing agent, and a binder [60]. The following studies experimentally and numerically evaluate the methods in which the formation of a char layer reduces the rate of heat and mass transfer during pyrolysis of charring and intumescent materials.

One early description of the heat transfer within an intumescent system is presented by Anderson et al. [61]. It was found that when an external heat source was applied to the intumescent system, it was initially absorbed by the heat capacity of the coating itself. Once the thermal capacity of the system had been reached, the filler components activated which initiated the formation of a hydrated solid. The hydration reaction continued to absorb and dissipate some of the incoming heat flux. A viscoelastic state was then achieved by the molten material, which traped the gases from the blowing agent and ultimately resulted in the intumescent process occurring. Once the proper sequence of reactions took place, the char acted as a thermal barrier because of its low thermal conductivity. The graphitic char layer, upon heating, will often begin to re-radiate a potentially significant amount of energy

back to the surroundings. The gases formed during the intumescent process can also contribute to transporting thermal energy away from the substrate [62].

Staggs expanded a previously developed model [63] to explore the modes of heat and mass transport in a developing char layer [64]. In this study, gas transport through the char was modeled obeying Darcy's law, and the volume was assumed to remain constant. Heat transport was assumed to occur via bulk conduction through the char, convection by the gas flowing through the char, and radiation across large pores at high temperatures; however, conduction was assumed the most prominent. To model conduction heat transfer, an effective thermal conductivity was prescribed. The effective thermal conductivity value was defined based on the two extremes of a composite solid being bounded between two thermal resistors in either parallel or series [65]. However, the actual values for real chars was assumed to lie somewhere in the middle of the upper and lower theoretical bounds. The resulting value could be computed based on a study which used a numerical finite element method to estimate the effective thermal conductivity for three-dimensional voids from a two-dimensional simulation [66].

A critical finding in this study by Staggs [63] is related to the heat transfer at high temperatures. It was found that when the char was at high temperatures, radiation heat transfer across the voids begins to become more dominant than conduction. Kantorovich and Bar-Zig [67] found that radiation across pores must be accounted for when the char temperature is above 1000 K. A similar behavior was also observed by Staggs et al. [68] and Di Blasi [8,69]; at higher temperatures, the effective thermal conductivity is augmented to account for radiation diffusion as a result of high temperatures and high porosities.

In work previously conducted by Stoliarov et al. [22], heat transfer within the intumescent char was assumed to be transported through either conduction or radiation. The resulting heat transfer parameters when only considering conduction were found to be too high to be physical meaningful. Therefore, the radiation sub-model, utilizing the radiation-diffusion approximation [70], was employed for the study. Employing the radiation-diffusion approximation lead to an important analysis that described the char as being a stack of thin, dense, highly conductive, and highly absorptive plates separated by wide, low density, low conductivity, and high transparency gaps. The analysis determined that the thermal insulating potential of a char layer (a quantitative estimate of the char's ability to thermally insulate the virgin material to reduce the rate of pyrolysis) was proportional to the number of pore walls positioned perpendicular to the direction of heat flow, and no other factors. However, experimental data is currently unavailable to support this theoretical analysis.

Staggs [71] employed a purely numerical approach to estimate the thermal conductivity of intumescent chars. The effective thermal conductivity of fully expanded intumescent chars was evaluated with a direct numerical simulation utilizing a finite element method. The effective thermal conductivity was mentioned to be dependent not only on the porosity but also on the shape, spatial distribution, and pore size of the intumescent char. The objective of this study was to estimate the three-dimensional effective thermal conductivity based on a two-dimensional cross sectional image of the actual char. Although several other similar studies [66,72,73] have been performed using finite element methods to estimate the effective thermal conductivity of various porous

solids, Staggs aimed to further that understanding by introducing micro-porous structures into the model. Advanced imaging has shown pore diameters ranging from several millimeters all the way down to several microns, supporting the necessity of including micro-porous structures in the model.

The model was based on physical measurements taken from fully developed char. It was found that the majority of the visible pores have an aspect ratio in the range of 0.75 to 1.25. Visual inspection of the char also determined that the porosity (ratio of the volume of the voids to the total volume) is approximately 30 to 40%. However, further investigation employing helium pycnometry and bulk density measurements revealed that the actual porosity was in excess of 90%, which was consistent with the observed expansion ratios of the char layer. In another study, Staggs et al. [68] found the expansion ratios to be high (on the order of 10 or more) and the resulting chars were therefore highly porous, with low effective thermal conductivities at room temperature. Therefore, it was apparent that a wealth of potentially critical information is not visible to the naked eye.

To accommodate the complexity of the microscopic char structure, a finite element model was developed utilizing a highly segmented black and white char image as a reference. The model, using appropriate boundary conditions, solved the steady temperature equation and employed a steady heat flux for estimating the effective thermal conductivity. An assumption was made that the two-dimensional porosity (ratio of the area of the voids compared to the total area) is directly equal to the three-dimensional porosity. An estimate of the thermal conductivity of the solid char was obtained from the hot disk method, and was found to be 0.45 W m^{-1} K^{-1}. A thermal conductivity sub-model, proposed

by Bruggeman [74], was employed to account for the thermal conductivity of the micro-porous structure.

Although several assumptions were made in the derivation of this model, satisfactory results were obtained and were found to be in agreement with experimental hot disk measurements over a broad range of temperatures (298 to 1193 K). The results also indicated that if the radiative heat transfer across the pores were neglected, the model would grossly underestimate the effective thermal conductivity; therefore, indicating the large effect attributed to radiative transport. The model provided a basis for understanding the heat transfer within porous chars as well as a successful method to compare the thermal insulating potential of fully developed chars.

Once the thermal transport sub-models were developed, it was important to understand the dynamics of char formation. Numerically representing the formation of a char layer in a pyrolysis sub-model, including the dynamics of swelling, is a very complicated task. A mathematical model describing the heat transfer and expansion of the char layer was presented by Staggs et al. [68]. The model used a simple competitive reaction scheme to describe the kinetics of thermal decomposition of the initial gas-forming step of the coating degradation. A char expansion sub-model was employed to effectively trap a fraction of the gas that evolved during the degradation process.

The effective thermal conductivity was described to lie between two bounds as described earlier [67,71]. The effective thermal conductivity was found to depend primarily on the char porosity, pore shape, and to a lesser extent, pore size. It was found that as the expanded char was formed, the visible pores were mostly oblate spheroids with a wide

range of sizes. Nevertheless, Bruggeman's model for randomly distributed spheres [66,67] with randomly distributed radii was employed to model the char layer. It was found that at high temperatures, the thermal conduction was enhanced by radiation across the pores. Therefore, it is possible for an intumescent coating subjected to different thermal histories to produce different char structures which may have different thermal conductivities.

The modeled results were compared to experimental data from furnace tests and mass loss calorimetry (MLC). MLC is a simplified version of the cone calorimeter that enables mass loss histories of samples exposed to an electric radiant heat flux to be measured as a function of time. The mathematical model was found to predict the results of the furnace experiments successfully, however, struggled to predict the expansion process in the MLC experiments. The discrepancy between the experimental and modeled results was attributed to an insufficient representation of the char expansion model. In particular, it was found that the char layer development was dependent upon both the heating regime as well as the local gasification rate and amount of gas locally trapped within the developing char layer. As the gas was produced, the volume of trapped gas (and therefore contributing towards expansion) depends on the viscoelastic properties of the surrounding matrix, the gas pressure, and the porosity of the resulting intumescent char. Therefore, even if a sufficiently complex model were developed, experimental validation would be laborious.

A recent study [75] was conducted on the experimental and numerical temperature developments in sandwich panels consisting of steel sheets and polyisocyanurate (PIR) core. Furnace fire tests were carried out to validate a temperature dependent thermal conductivity model for PIR through numerical heat transfer modeling utilizing a

commercially available finite element model, ABAQUS [76]. It was assumed that heat was transferred through the solid by conduction and through the pores by radiation, conduction, and convection. However, since the pores were sufficiently small, the convection was negligible. A series of expressions from Glicksman et al. [77,78] were adopted to describe the total effective thermal conductivity of the porous foam. It was found that the model captured the experimental data well when the total effective thermal conductivity increased exponentially as a function of temperature. Therefore, the temperature dependence of thermal conductivity in porous media must be taken into consideration in order to accurately predict physical phenomena.

Thermal transport within the porous char is of great interest; however, the transport of gaseous volatiles may contribute to the dynamics of char formation as well. In a previous study, Staggs [63,79] investigated the mass transport in addition to the thermal transport. It was found in this numerical study that the char actually did not offer any resistance to the flow of gases. Therefore, the particular mass transport process prescribed for the gases are not critical in determining the rate of formation of pyrolyzate gases; however, it was found to play an important role in the formation of the char layer. It was determined that the physics of mass transport were the most sensitive to low heat flux situations due to the volatile gases not escaping instantaneously. Therefore, specific research on the bubble translational velocity would prove useful in modeling slow mass loss conditions.

A similar result for mass transport was discovered by Di Blasi [69]. A one-dimensional transient model was developed to investigate thermal decomposition of a system containing a steel substrate coated with an intumescent protective layer.

Independent finite-rate reactions were assigned to each component to estimate the kinetics of thermal decomposition. Mass and heat transfer were assumed to take place across of material that had an evolving volume as the char layer was formed; this was accounted for with a simplified mechanism for bubble dynamics and material swelling. The model was dependent upon two empirical fitting parameters; however, a parametric study showed that the model was only sensitive to the expansion factor. The fraction of gas retained by the degrading sample did not greatly affect the modeling results.

To further evaluate the performance of a char layer, a simple mathematical model of pyrolysis of char-forming polymers was developed [63]. Poly(vinyl chloride) (PVC) is a synthetic polymer that was utilized to provide a basis for the modeling efforts. The following challenges were identified in this study. The kinetics mechanism of PVC char formation is complicated and involves many separate intermediate steps. Additionally, many important model parameters, such as the Arrhenius reaction rate constants, for the char-forming mechanism and the heat transfer properties of the char were not known. Lastly, the problem involved modeling a dynamically evolving char layer, where the thickness of the char layer changed as a function of time. The evolving char layer implied that the physical mechanism by which volatile products move through the char was not a constant process. However, to move forward with the model construction, it was assumed that the char-forming process had already been characterized and that reasonable estimates for the heat transfer properties of the char are known *a priori*.

The model was developed to mimic the testing scenario presented by standard cone calorimetry experiments. A relatively thick, horizontal sample was modeled to degrade

thermally due to exposure to a radiant heat flux on the top surface. The model accounted for radiative and convective heat losses on its top surface as well as the presence of temperature gradients through the thickness of the sample; the sides and bottom were adiabatic. It was assumed that the kinetics of thermal decomposition could be expressed as a series of first-order reactions. The kinetics model was coupled with a heat transfer model that accounted for volume change as the char layer was formed. It is important to note that the volatile gases formed in this model were assumed to escape instantaneously. This model was solved with a solution-adaptive finite difference procedure [80] and implemented the PVC degradation mechanisms developed by Anthony [81].

One of the pivotal findings from this work was related to the effect of the char layer on the transport of volatile gases. The model assumed that there was zero restriction from the char layer on the mass transport, however, this was likely unrealistic. The author suggested that to model this phenomenon more carefully, two extreme situations needed to be understood and coupled into a single sub-model. The first case evaluates a situation when no char is formed which permits the volatile products to escape through the polymer melt by the formation of bubbles. These bubbles grow by diffusion and simultaneously translate through the melt. It was suggested to estimate the bubble translational velocity based on low Reynolds number Navier-Stokes equations. The second case considers the transport of volatile gases through a well-developed char layer which was accomplished by modeling mass transport through a porous medium using Darcy's law [82,83]. However, there was no method available to describe the transition between the two extreme cases to capture a realistic regime, further emphasizing the need for experimental data in anaerobic

conditions to permit a more detailed understanding of the physics of the transport phenomena in evolving char layers.

1.3: Objectives and Research Plan

Most of the previous studies that explored both the heat and mass transfer through porous chars were conducted entirely numerically based on theoretical analyses. Each of these studies were missing detailed experimental data to evaluate the performance of the numerical models. While it is qualitatively known that the presence of a porous char layer is effective in reducing the rate of production and subsequent combustion of volatile gases, the quantitative relationships are lacking. The present study seeks to develop a methodology that investigates the relationship between thermal transport and the physical structure of the intumescent char.

A thorough characterization of the thermal transport inside charring and intumescent polymers during pyrolysis will be conducted using novel experimental and numerical modeling techniques. This research will include the development of experimental tools to provide carefully controlled boundary conditions and highly resolved measurements during the pyrolysis of charring and intumescent polymers. Next, new multi-dimensional thermal transport modeling tools will be incorporated to provide a better approximation of the heat flux incident to the evolving sample surface. Finally, this study will provide a relationship between the thermal transport in the condensed-phase during pyrolysis and the char's physical structure to improve the associated thermal insulating potential of the intumescent char.

The analysis will be conducted on the following materials: poly(vinyl chloride) (PVC), poly(vinyl chloride) with plasticizer (FPVC), Bisphenol A polycarbonate (PC), poly(ether ether ketone) (PEEK), and poly(vinylidene fluoride) (PVDF). These materials provide a representative set of polymers used in a wide range of consumer and construction applications. Each of these materials, on varying levels, are known to produce a carbonaceous condensed-phase residual yield (char) as well as undergo swelling (intumescence) during pyrolysis. Existing and newly designed experimental techniques will be employed to provide quantitative measures of these phenomena. Improved numerical tools will be utilized to inversely analyze all experimental data.

The experimental techniques will employ both milligram- and gram-scale tests. Milligram-scale experiments include Thermogravimetric Analysis (TGA), Differential Scanning Calorimetry (DSC), and Microscale Combustion Calorimetry (MCC). These techniques provide a quantitative measure of the sample mass, heat flow to the sample, and heat release rate of pyrolyzate gases during anaerobic thermal decomposition, as a function of sample temperature. The newly designed Controlled Atmosphere Pyrolysis Apparatus II (CAPA II) enables a comprehensive analysis of pyrolysis of charring and intumescent materials. This apparatus provides well-defined boundary conditions and highly resolved measurements of mass, bottom surface temperature, and sample profile evolution of a material exposed to radiant heat. Partially decomposed samples from the CAPA II experiments will be subjected to further analysis to investigate the physical structure of the developed char layer in order to provide a quantitative relationship with the associated thermal transport properties.

ThermaKin2Ds, an axisymmetric expansion of an existing numerical comprehensive pyrolysis solver (ThermaKin), will be employed to interpret the experimental datasets through a manually iterative inverse analysis process. The numerical solver will be constructed to emulate the conditions of each experimental instrument employed in this study. TGA datasets will be utilized to extract Arrhenius reaction rates and condensed-phase residual char yields for a collection of first order reactions occurring in sequence. It is important to note that this process does not resolve each elementary reaction; instead, it will employ a semi-global reaction scheme to capture the critical trends within the accuracy of experimental data. DSC datasets will be used to determine heat capacities of all condensed-phase components as well as heats of reaction for the associated reactions. MCC data will employed to parameterize the heats of complete combustion for pyrolyzate gases produced during thermal decomposition. Lastly, the CAPA II dataset will be used to inform the characterization of density and thermal conductivity of each condensed-phase component. The fully parameterized comprehensive pyrolysis model will be validated by comparing mean experimental and simulated mass loss rate data for a wide range of heating conditions.

Chapter 2: Experimental Methods

2.1: Materials

The following five representative charring and intumescent polymers were characterized in this work: rigid poly(vinyl chloride) (PVC), flexible poly(vinyl chloride) (FPVC) due to the addition of a plasticizer, Bisphenol A polycarbonate (PC), poly(ether ether ketone) (PEEK), and poly(vinylidene fluoride) (PVDF). The carbonaceous residual char yield from each of these materials, measured by the thermal decomposition of the material in a nitrogen environment up to 1173 K, ranged from 7 to 50 wt. % (see section 4.1). Each of the materials, purchased in large extruded sheets (approximately 6×10^{-3} m in thickness), were further cut for appropriate test samples. The milligram-scale tests required samples to be carefully cut into very small flat pieces approximately 4 – 7 mg in mass. Additional milligram-scale samples were prepared by grinding all rigid materials into powder form; the results were compared to ensure there was no dependence on sample size and shape.

The samples for the gasification tests were carefully cut with a computer numerical controlled (CNC) milling machine to 0.07 m in diameter disks. Samples for the absorption coefficient measurements (described in Section 2.3.1) were a result of further machining 0.07 m diameter disks to a thickness of 1×10^{-3} m in the center (0.02 m diameter) portion of the specimen. All samples were stored in a desiccator for a minimum of 48 h prior to testing. Table 2.1 provides additional details about the materials used in the work. The repeat unit

in the chemical structure of all materials studied in this work is provided in Table 2.2. It is important to note that FPVC contains a significant but unknown amount of organic plasticizers to provide the flexibility of the material; the exact chemical structure of the plasticizers are unknown. Images of representative gasification test samples are provided in Table 2.2.

Table 2.1: Materials studied in this work. The material densities were estimated based on measurements taken at room temperature.

Polymer	**Trade Name**	**Manufacturer**	**Thickness (m)**	**Density (kg m^{-3})**
Poly(vinyl chloride) (PVC)	Vintec I	Vycom Plastics	6.15×10^{-3}	1409
Flexible poly(vinyl chloride) (FPVC)	10 Compound Flexible PVC	TMI Vinyl Solutions	5.45×10^{-3}	1226
Bisphenol A Polycarbonate (PC)	Makrolon GP	Bayer	5.50×10^{-3}	1187
Poly(ether ether ketone) (PEEK)	PEEK 450 G	Victrex plc	6.45×10^{-3}	1297
Poly(vinylidene fluoride) (PVDF)	Flametec Kytec	Vycom Plastics	6.30×10^{-3}	1791

Table 2.2: Repeat unit in chemical structure and images of gasification test samples of all materials studied in this work.

Polymer	Repeat Unit	Gasification test sample
PVC	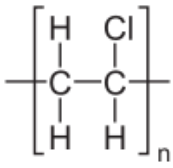	
FPVC	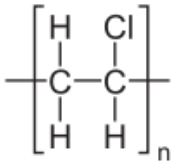	
PC	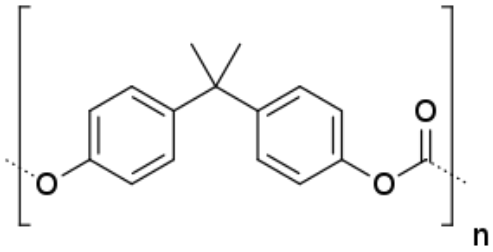	
PEEK	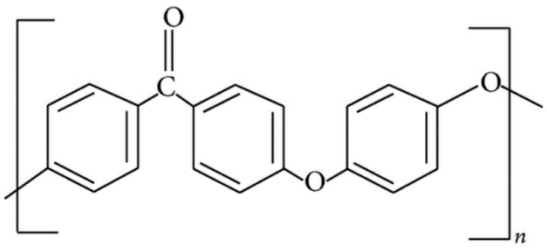	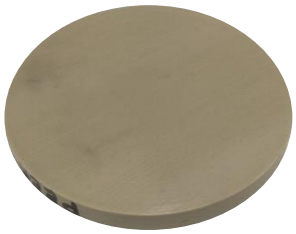
PVDF		

2.2: Milligram-scale Experiments

2.2.1: Thermogravimetric Analysis and Differential Scanning Calorimetry

In this study, a Netzsch Simultaneous Thermal Analyzer (STA) 449 F3 Jupiter [84] was employed to characterize the kinetics and thermodynamics of thermal decomposition. An STA, equipped with a Netzsch TGA-DSC sample carrier, is an instrument that permits microgram-resolution thermogravimetric analysis (TGA) and heat-flux differential scanning calorimetry (DSC) to be conducted simultaneously in the same apparatus. Simultaneous thermal analysis reduces the physical number of tests while also better correlating the temperature dependent behavior of the mass loss and corresponding heat flow. A schematic of the STA is shown in Figure 2.1.

Figure 2.1: Netzsch simultaneous thermal analyzer (STA).

All STA tests followed a carefully prescribed temperature program to define the heating rate of the sample. The temperature program had an initial conditioning period in

which the sample and crucible were held at a constant 303 K for 25 min. This conditioning period enabled all oxygen to be purged from the system which ensured a fully anaerobic environment. Subsequently, a linear heating at a nominal rate of 10 K min^{-1} was followed until the maximum prescribed temperature was reached. The maximum temperature was defined as approximately 100 K higher than any temperature when mass loss was observed. Finally, the test ended with an isothermal period of 10 min, which enabled the sample to achieve an equilibrium state prior to cooling. The furnace and balance were flushed continuously with ultra-high purity nitrogen (99.999 vol.%) to ensure fully anaerobic conditions. The balance purge gas (30 mL min^{-1}) joined the purge gas fed directly into the furnace (20 mL min^{-1}), for a total nitrogen flow rate in the furnace of 50 mL min^{-1}. The heating rate of 10 K min^{-1} was sufficiently slow to decouple the kinetics and thermodynamics of thermal decomposition from energy and mass transport.

All STA tests were conducted in a platinum-rhodium crucible with a lid to ensure a uniform sample temperature and heat flow throughout the test. A small hole in the lid allows any pyrolysis gases produced during the decomposition to escape the crucible freely. All samples were cut very small to achieve a total sample mass ranging from 4 – 7 mg. Thin flat samples were positioned on the bottom of the crucible to ensure adequate thermal contact between the sample and crucible. Previous studies have shown that consistency in the sample positioning improved the thermal contact and repeatability of reliable data [85]. Additional tests were conducted with samples in powder form to ensure that the sample shape and size did not have any adverse impacts on the measurements.

The STA was fully calibrated using a set of seven calibration compounds to ensure the accuracy of the P-type thermocouples and heat flow sensors. The calibration compounds have well-known melting temperatures ranging from 340 to 1080 K and heats of melting. The calibration exercise ensures the accuracy of the temperature and heat flow measurements. The calibration tests were carried out at the same heating rate and gas purge rate to ensure accuracy of the instrument for the conditions in which the majorities of the tests were conducted. The full calibration was completed four times a year to ensure accuracy of the experimental data. Partial calibration checks are completed regularly in the interim to verify the stability of the calibration.

A baseline test was performed with an empty crucible and lid in order to identify and correct the buoyancy effects of the furnace as well as any heat flow sensitivity from the crucible itself. The baseline data was subsequently subtracted from the mass and heat flow measurements of the samples that were undergoing the thermal decomposition. The heat flow baseline was found to be extremely critical for obtaining reliably reproducible DSC data because the heat flow data was very responsive to the surrounding environment. The baseline test and subsequent correction was performed for all STA experiments in this work.

The STA tests were repeated 10 times to accumulate necessary statistics, and the averaged mass and heat flow data is presented for the model development. Additional TGA tests were conducted on each of the sample materials at both 5 and 20 K min^{-1} to serve as validation for the reaction scheme developed with the 10 K min^{-1} dataset. These additional tests at 5 and 20 K min^{-1} were performed in triplicate and averaged results are used for

validation. Validating the resulting reaction model at a range of heating rates ensures that the kinetics parameters can be extrapolated to different thermal exposures.

Additional independent experiments were performed on the residual char yield from the previous tests in an effort to resolve the heat flow histories of the final char component more carefully. The residual char yield from the repeated tests were combined to provide sufficient sample mass for these tests. The residual char was tested using an identical temperature program, which allowed the heat flow to the char sample to be measured at a lower temperature range where the STA is known to have a higher resolution. The results from these tests enabled the characterization of the char heat capacity at a specified temperature range within a reliable region of the data.

2.2.2: Microscale Combustion Calorimetry

The microscale combustion calorimeter (MCC) [86] is a standardized test method used to estimate the heats of complete combustion of pyrolyzate gases produced from thermal decomposition of milligram sized samples. A schematic representation of the MCC is shown in Figure 2.2. The heats of combustion of pyrolyzate gases provides a relationship between the condensed-phase and gas-phase phenomena. The MCC provides a measure of the HRR as a function of the sample temperature. The MCC HRR data can be used in conjunction with STA MLR data (scaled by the heats of combustion) to validate the reaction scheme and provide insight on the overall material's reaction to fire.

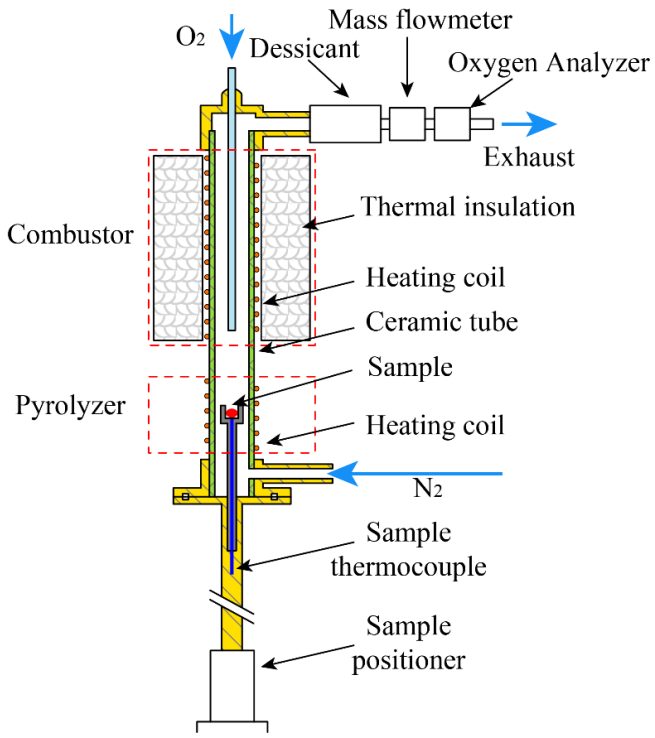

Figure 2.2: Schematic of the microscale combustion calorimeter (MCC).

To enable a direct connection between the MCC and STA data, the MCC tests were conducted at a linear heating rate of 10 K min^{-1}. The sample was heated within the pyrolyzer region of the instrument in a fully anaerobic environment with a continuous nitrogen purge flow rate of 80 mL min^{-1}. The gaseous pyrolyzate were then mixed with excess oxygen, introduced at a flow rate of 20 mL min^{-1}, in the combustor zone. The combustor was heated to a constant temperature of 1173 K, which ensured complete oxidation of the pyrolyzate gases. The total heat released from the combustion process was measured as a function of time and temperature based on oxygen consumption calorimetry principles [45].

All MCC tests were conducted with a prescribed temperature program similar to the STA. The initial stage had a conditioning period where the sample temperature was

permitted to stabilize at 348 K. Subsequently, the sample was exposed to a nominal heating rate of 10 K min^{-1} until the sample temperature was approximately 100 K above when any significant mass loss was detected from TGA experiments. An identical heating rate between the MCC and STA enabled direct comparison between the majorities of the tests.

All MCC experiments were conducted in small ceramic crucibles without lids. The absence of the lids facilitates the pyrolyzate gases to escape the crucible quickly to be carried into the combustor by the nitrogen purge gas. All samples, cut sufficiently small, were carefully placed on the bottom of the crucible. The initial and final sample mass were carefully measured to calculate both the final char yield as well as total mass consumed during the experiments.

The MCC was fully calibrated approximately four times a year. The temperature sensors were calibrated based on the known melting temperatures of a range of pure metals to ensure accurate sample temperature measurements. The oxygen sensor was carefully calibrated using a well-known oxygen/nitrogen mixture to obtain accurate oxygen consumption measurements, which is directly related to the heat release rate of the pyrolyzate. A test was conducted using a polystyrene sample at the beginning of each testing day to verify the calibration of the instrument. All MCC tests were conducted in accordance to the standard operating conditions with the exception of the heating rate. As mentioned before, the heating rate was adjusted to 10 K min^{-1} to enable direct comparison to the STA experimental results. MCC tests were conducted in triplicate for each material due to a high degree of reproducibility. The experimental results were averaged prior to determining the heats of complete combustion through inverse analysis.

2.3: Gram-scale Experiments

2.3.1: Broadband Radiation Absorption

The in-depth broadband radiation absorption coefficient (κ) was quantified based on a methodology introduced by Linteris et al. [87], which was later adopted in several additional studies [55,85,88]. A well-defined radiant heat flux from an electric conical heater was transmitted through the thin samples, positioned 0.07 m below the base of the heater housing, and subsequently measured with a Schmidt-Boelter heat flux transducer (12 mm diameter). The radiation, as depicted in Figure 2.3, was collimated by Kaowool PM insulation board with a cylindrical hole in the center. The hole in the insulation board was comparable in size to the diameter of the heat flux gauge to direct the light waves through the thin ($\approx 1\times10^{-3}$ m) portion of the sample specimen.

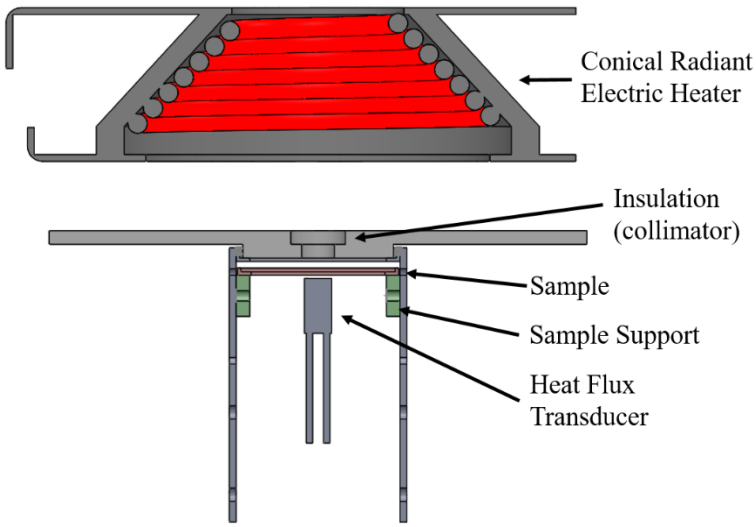

Figure 2.3: Schematic of apparatus to measure the radiative heat flux absorption coefficient.

The heat flux was first measured for 30 s with the sample removed to collect the background information on the heating of the experimental apparatus and the magnitude

of the radiation through the collimator itself. The sample was subsequently placed within the holder and the heat flux signal was measured. The reduced heat flux transmission was averaged for the first 3 s of sample exposure while the surface of the specimen not facing the heater was still near ambient temperature. All measurements were performed at particular heat fluxes (corresponding the specific heater coil temperatures) consistent with the average set point of the gasification experiments discussed in Chapter 5. The measurements were collected when the sample was approximately at ambient temperature. The subsequently derived absorption coefficient was assumed to be independent of the spectral characteristics of the incoming radiation and was used for analysis of the gasification data obtained and lower as well as higher radiant heat fluxes. An estimate of the absorption coefficient was calculated based on Equation 2.1 and Equation 2.2, which were derived from a generalized form of the Beer-Lambert Law.

$$\kappa = \frac{2\ln(\varepsilon) - \ln(\tau_0)}{\rho\delta} \tag{2.1}$$

$$\tau_0 = \frac{I_{x=\delta}}{I_{x=0}} \tag{2.2}$$

where ε is the sample surface emissivity which was taken from literature data. τ_0 represents the transmission coefficient, which was estimated as the fraction of radiation that passed through the sample, as defined by Equation 2.2. ρ is the density of the undecomposed polymer measured at ambient temperature and δ is the thickness of the sample. $I_{x=\delta}$ and $I_{x=0}$ are the radiant fluxes measured by the heat flux transducer through the thickness of the sample and with the sample removed, respectively.

2.3.2: Controlled Atmosphere Pyrolysis Apparatus II

The Controlled Atmosphere Pyrolysis Apparatus II (CAPA II) is a newly designed gasification instrument that enables a comprehensive analysis of pyrolysis of charring and intumescent materials. This gasification apparatus provides well-defined boundary conditions and highly resolved measurements of mass, bottom surface temperature, and sample profile evolution of a disk-shaped 0.07 m diameter material sample exposed to radiant heat. All measurements were collected simultaneously in a nearly anaerobic environment and were recorded as a function of time.

The CAPA II setup is shown in Figure 2.4 and Figure 2.5. It consists of an open-to-the-atmosphere gasification chamber containing the steel sample holder (0.082 m inner diameter). The chamber was constructed from two concentric circular aluminum tubes that each have a thickness of 6.4×10^{-3} m. The chamber walls were cooled by circulating water through copper tubing impressed within channels cut into the walls of the aluminum tubes to maintain well-defined boundary conditions.

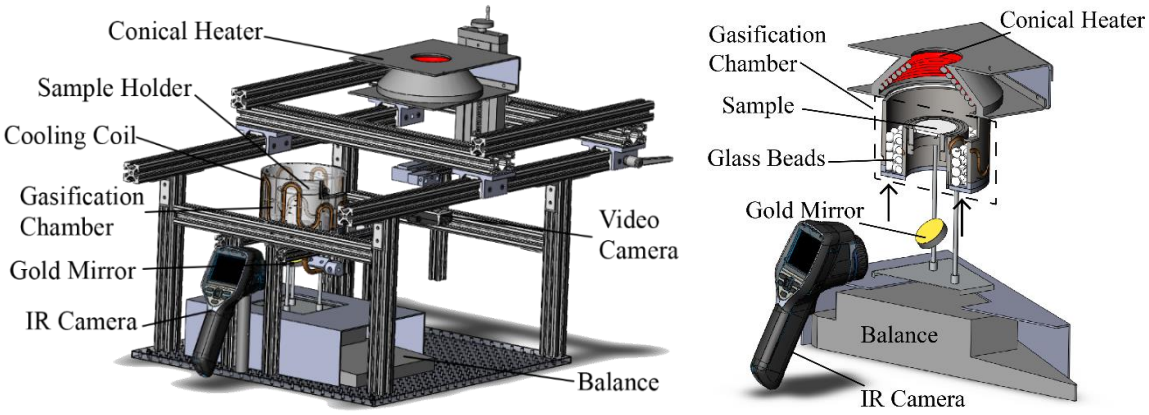

Figure 2.4: Drawing of the controlled atmosphere pyrolysis apparatus II (CAPA II).

A continuous flow of gas, prescribed to be pure nitrogen in this study, was introduced to the apparatus within the channel between the aluminum tubes. The gas was introduced through a layer of glass beads (6.4×10^{-3} m diameter) to ensure a homogenized flow. The top of the outer tube was located 0.03 m above the initial sample surface and 0.01 m below the bottom of the radiant heater housing to minimize entrainment of ambient air. The electric radiant heater, capable of providing up to 100 kW m^{-2} heat flux, was positioned on a moving track to enable its fast placement and removal from above the gasification chamber. The inner wall of the outer aluminum tube was coated with a high emissivity paint to suppress reflections of the heater's radiation.

The material samples of 0.07 m in diameter and approximately 6×10^{-3} m in thickness were used in the current study. Kaowool PM board was used to thermally insulate the samples around the perimeter, as detailed in Figure 2.5. The sample was positioned on top of a piece of 7.6×10^{-4} m thick, diamond-shaped aluminum mesh (covering approximately one third of the sample area) within the sample holder. The aluminum mesh was covered with a thin (2.5×10^{-5} m) copper foil to support the bottom of the samples and prevent entrainment of ambient air. The samples were adhered to the foil with a thin ($\approx 1.5\times10^{-4}$ m) layer of fast curing high temperature epoxy to ensure continuous thermal contact. The sample, thermal insulator, aluminum mesh, and copper foil were all contained within the sample holder. A lip extending from the sample holder blocked the gap between the holder and the inner aluminum tube to minimize ambient air entrainment from beneath the sample.

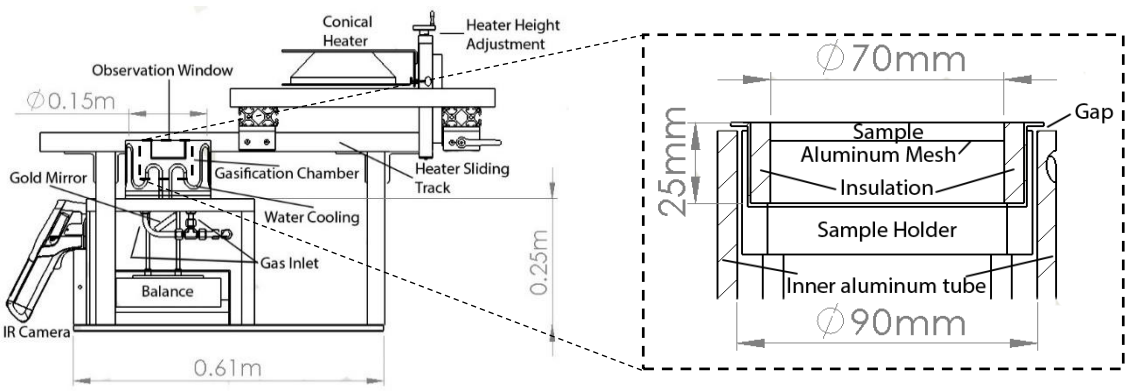

Figure 2.5: Schematic of the CAPA II.

The CAPA II diagnostics included three main components: mass, bottom surface temperature, and sample shape. The instantaneous mass of the sample was recorded using a high precision (1 mg resolution) Sartorius Cubis balance at a frequency of 2 Hz. A FLIR E40 infrared (IR) camera was focused on the thin copper foil holding the sample to measure the bottom surface temperature at a frequency of 7.5 Hz. The foil was coated with a high (0.94) emissivity paint to ensure the accuracy of the spatially-resolved temperature measurements. Due to geometrical constraints, a gold mirror (with an average reflectance of 0.96) was used to direct the view of the IR camera to the bottom of the sample. The emissivity in the IR camera was adjusted to account for the transmission loss in the gold mirror and was validated against thermocouple based temperature measurements. A Logitech C930e high definition camera was focused on the sample through a quartz observation window to monitor the evolution of the sample surface position. Two 1.3×10^{-3} m diameter Type-K thermocouples were used to monitor the inner and outer aluminum wall temperatures during all CAPA II experiments.

Several representative sample profiles were traced manually to sketch a line corresponding to the sample surface shapes. The sketched coordinates were converted to physical dimensions using a calibration that was conducted within a plane of symmetry of the sample holder, parallel to the lens of the video camera. The bottom surface temperature measurements were taken at four radial positions spaced across the entire sample radius. Three points obtained at random azimuthal angles were averaged at each of the four radial positions. The mass loss rate (MLR) was computed using a 5 s time differential and normalized by the initial top surface area of the sample. The data were subsequently grouped into 5 s bins for which mean MLR and mean time values were computed. The temperature and MLR data from repeated tests were grouped together prior to averaging. All uncertainties were computed from the scatter of the experimental data as two standard deviations from the mean.

Each CAPA II experiment was repeated twice to ensure reproducibility and to accumulate necessary statistics. The experiment began when the heater was slid into position above the sample and was terminated when no more mass loss was observed or when the sample fell onto its side (due to pyrolysis induced shape change). The MLR histories computed for the higher heat fluxes were assumed to incorporate the thermal decomposition of the epoxy used in the sample preparation. Therefore, the MLR data were corrected to remove the contribution of the epoxy decomposition. An independent TGA experiment was conducted on the epoxy to determine the onset temperature of thermal decomposition. The onset temperature was defined to occur when 1 wt. % of the epoxy mass was lost. Therefore, it was found that the onset temperature for epoxy thermal

decomposition was 489 K, which lead to a final residual char yield of 12.3 wt. %. The correction for the epoxy decomposition was computed by distributing the mass lost by the epoxy from the time when the bottom sample temperature reached the onset of epoxy thermal decomposition until the termination of the test. The magnitude of this correction was found to have minimal impact on the MLR histories.

2.3.2.1: Gaseous Boundary Conditions

In the current study, the gasification chamber was purged with nitrogen at a constant flow rate of 185 SLPM at 298 K and 101 kPa, which corresponded to the bulk flow speed within the channel between the aluminum tubes of 0.29 m s^{-1}. A spatially resolved and time averaged characterization of the flow in the chamber was performed using an Omega HHF-SD1 hot wire anemometer. This flow characterization was carried out at room temperature (293 K) with the non-energized heater positioned above the gasification chamber. Spatially resolved volumetric oxygen concentration measurements were performed using an E-Instruments E8500 Plus portable emissions analyzer. Unlike in the case of the flow speed measurements, the oxygen concentration mapping was carried out with the heater turned on and set to provide 51.5 kW m^{-2} at the center of the initial sample surface; the cooling was also activated. The oxygen concentration was measured within a cylindrical region occupying the area of the sample and extending vertically 0.075 m (0.035 m into the conical heater). A disk cut from Kaowool PM board was used as a sample surrogate during both the gas flow and oxygen concentration measurements.

With the nitrogen flow turned on and heater turned off, mean vertical gas velocity measurements were performed at a series of vertical distances h_x from the initial sample

surface position; these distances are expressed in a non-dimensional form by normalizing them by the distance to the bottom of the heater housing, H = 0.04 m. The mean vertical gas velocities measured on the axis of the gasification chamber above the sample were found to be 0.25 and 0.35 m s^{-1} at a distance of h_x/H = 0.13 and h_x/H = 0.95, respectively. These velocities decreased to about 0.16 m s^{-1} at the surface of the cylinder corresponding the edge of the sample. The mean horizontal (radial) gas velocity, at h_x/H = 0.25, was approximately 0.19 m s^{-1} near the chamber axis and increased to 0.35 m s^{-1} at the edge of the sample. The average oxygen concentration within the cylindrical region occupying the area of the sample and extending vertically into the heater, which was measured with the heater and cooling turned on, was found to be 0.6 vol.%. The maximum oxygen concentration of 0.9 vol.% was found at the top edge of the outer chamber walls.

2.3.2.2: Radiation Boundary Conditions

To fully characterize the radiant heat exposure to the top sample surface, an axisymmetric heat flux model matching the geometry of the CAPA II gasification chamber was developed. The model was based on the measurements conducted with a Medtherm Schmidt Boelter water-cooled heat flux transducer equipped with a 6×10^{-3} m diameter sensor. The measurements were performed at a series of five vertical distances (h_x/H). At each h_x/H, the heat flux was measured at several horizontal distances r_z from the sample's symmetry axis; these distances were normalized by the maximum initial sample radius, R = 0.035 m. Most of these measurements were performed with the transducer's sensor facing straight upward ($\phi = 0$ in Figure 2.6). For a subset of the measurements, the transducer was positioned at an angle $\phi = \pi/4$ or $\pi/2$, as indicated in Figure 2.6, to capture the impact of

local sample surface orientation. The mass balance and sample holder had to be removed from the apparatus to accommodate these heat flux measurements. The majority of the measurements were performed at a heat flux set point of 51.5 kW m^{-2}, as measured at the point corresponding to the center of the initial sample surface. Several additional measurements were conducted at lower and higher set heat fluxes to ensure that the developed model remains accurate within the full range of possible heat flux settings. The water-cooling and nitrogen flow were turned on during these measurements.

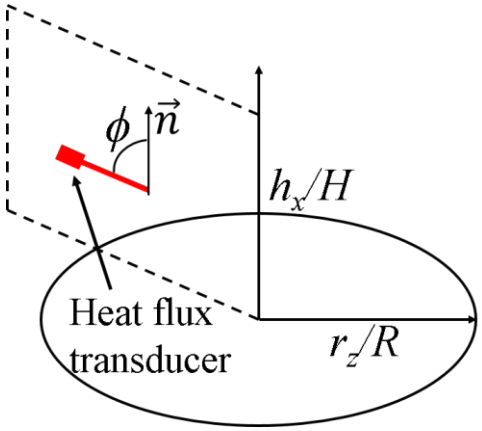

Figure 2.6: Heat flux transducer angular position.

Open circles in Figure 2.7 depict the measured radiation heat fluxes normalized by the center point ($r_z/R = 0$) value at the respective h_x/H. The data were collected over a wide range of azimuthal angles to provide further support for the axisymmetric assumption used in the heat flux model development process. At $h_x/H < 0.5$, the heat flux was found to decrease with an increasing radial position; the inverse was found to be true for $h_x/H > 0.5$.

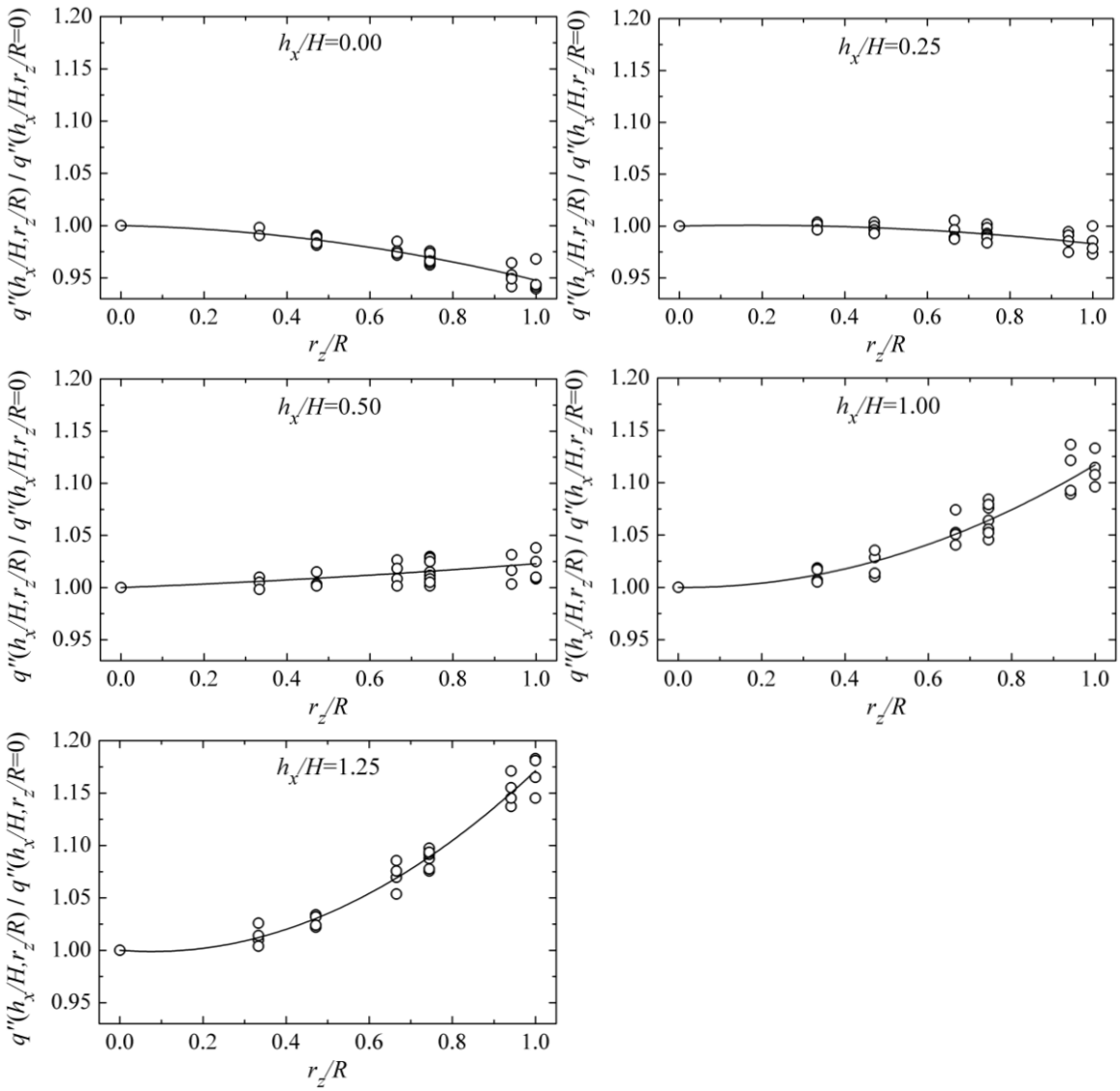

Figure 2.7: Radial dependences of radiant heat flux at a range of vertical distances measured with the transducer's sensor facing upward (ϕ = 0). The open symbols represent individual measurements; the lines are the fit with Equation 2.3.

Open circles in Figure 2.8 show the radiant heat fluxes measured at the axis of symmetry normalized by the heat flux at the center of the initial sample surface, $q''\left(h_x/H=0, r_z/R=0\right)$. The heat flux increased with a decreasing distance to the heater until approximately h_x/H = 0.7. Upon further movement toward/into the heater, the heat flux decreased rapidly. Both the radial and axial trends were consistent with the geometry

of the heating element and its proximity to the volume where these measurements were taken. These trends have been fitted with Equation (2.3):

$$\frac{q''(h_x/H, r_z/R)}{q''(h_x/H=0, r_z/R=0)} = \left(a_2\left(\frac{r_z}{R}\right)^2 + a_1\left(\frac{r_z}{R}\right)+1\right)\left(b_2\left(\frac{h_x}{H}\right)^2 + b_1\left(\frac{h_x}{H}\right)+1\right) \qquad (2.3)$$

In Equation 2.3, a_2 and a_1 coefficients are used to capture the radial trends and are vertical distance dependent quantities. $a_2 = a_{22}(h_x/H)^2 + a_{21}(h_x/H) + a_{20}$ and $a_1 = a_{12}(h_x/H)^2 + a_{11}(h_x/H) + a_{10}$ where a_{22} = 0.126, a_{21} = 0.040, a_{20} = -0.044, a_{12} = -0.088, a_{11} = 0.092 and a_{10} = -0.008. b_2 = -0.393 and b_1 = 0.438 coefficients are used to capture the axial trend. The lines shown in Figure 2.7 and Figure 2.8 demonstrate the accuracy of this model.

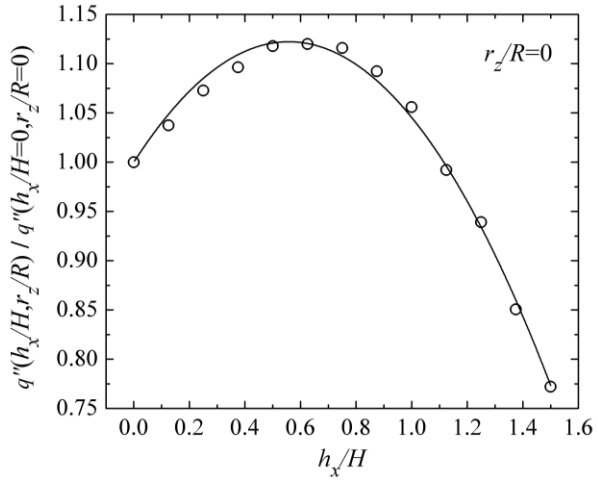

Figure 2.8: Axial dependence of radiant heat flux measured with the transducer's sensor facing upward (ϕ = 0). The circles represent individual measurements; the line is the fit with Equation 2.3.

Equation 2.3 provides an understanding of the heat flux as a function of the sample surface position assuming that the sample surface remained parallel to the initial sample surface. In practice, however, the sample surface experienced many different angles as the intumescent sample underwent pyrolysis. Therefore, it was crucial to provide a correction for the radiation incident to the sample surface when the developing char layer deviated from one-dimensional expansion. The dependence of the radiant flux on the angular orientation is shown in Figure 2.9. Each measurement (depicted as an open symbol) was normalized by the corresponding value at $\phi = 0$. At $\phi = \pi/2$, the data were taken at a range of radial positions (see Figure 2.9(a)). The normalized data indicate an absence of significant dependence on r_z. Therefore, at $\phi = \pi/4$, all measurements (shown in Figure 2.9(b)) were performed at a single radial distance. The dependence of the heat flux on the angle was captured with Equation 2.4:

$$\frac{q''(\phi, h_x/H)}{q''(\phi = 0, h_x/H)} = g_2\phi^2 + g_1\phi + 1 \tag{2.4}$$

where g_2 and g_1 are vertical distance dependent coefficients: $g_2 = g_{22}(h_x/H)^2 + g_{21}(h_x/H) + g_{20}$ and $g_1 = g_{12}(h_x/H)^2 + g_{11}(h_x/H) + g_{10}$. The lines in Figure 2.9 were obtained using g_{22} = -0.191, g_{21} = -0.136, g_{20} = -0.029, g_{12} = 0.482, g_{11} = 0.261, and g_{10} = -0.440.

The product of the parameterized Equation 2.3 and Equation 2.4 provide a capability to compute the incident radiant heat flux distribution for an intumescent material sample from a known set point. Variation of this set point from 30 – 70 kW m^{-2} was examined to

ensure its ability to extrapolate to additional heating conditions. It was found that the mean difference between the model prediction and measured heat fluxes was about 1%, regardless of the set point selection.

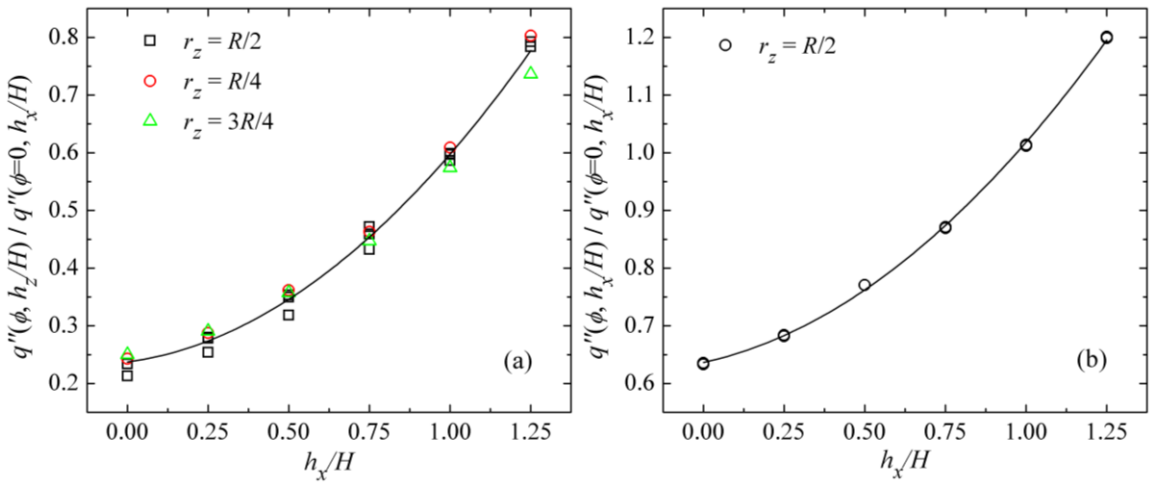

Figure 2.9: Radiant heat fluxes measured at (a) $\phi = \pi/2$ and (b) $\phi = \pi/4$. The symbols represent individual measurements; the lines are the fit with Equation 2.4.

2.3.2.3: Convection Boundary Conditions

Computational fluid dynamics (CFD) calculations have been conducted to analyze convective heat transfer at the sample surfaces. The calculations were performed using the Fire Dynamics Simulator (FDS) version 6.2.0 [89] in the direct numerical simulation mode with the radiation sub-model turned off. An axisymmetric computational domain built to represent the CAPA II gasification chamber is shown in Figure 2.10.

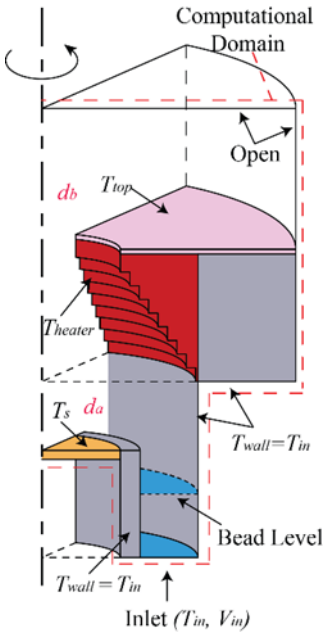

Figure 2.10: CFD model to emulate the CAPA II experimental geometry.

A series of scenarios representative of those encountered in the gasification experiments have been explored in these calculations. In all scenarios, the inlet flow temperature and velocity (T_{in} = 363 K and V_{in} = 0.348 m s^{-1}) and heater surface temperatures (T_{heater} = 999 K and T_{top} = 423 K) were specified to correspond to those measured in the experiments conducted at a 51.5 kW m^{-2} heat flux set point. The sample surface temperature (T_s) and sample shape were varied from scenario to scenario as indicated in Table 2.3 and Figure 2.11. Slope represents the ratio of maximum height versus radius of the top sample surface for scenarios #1-5 and the bottom surface for scenario #6. Nitrogen was defined as the gaseous media in all scenarios with the exception of #6, where air was used instead. Scenario #6 was employed to analyze convective losses from the bottom sample surface. Thus, the choice of gaseous media reflected the fact that, in the CAPA II, the enclosure containing this surface is not purged with nitrogen.

Table 2.3: Summary of input parameters used in the CFD calculations. Slope represents the ratio of maximum height versus radius of the top sample surface for scenarios #1-5 and the bottom surface for scenario #6.

Scenario #	T_s (K)	Slope
1	500	0
2	700	0
3	900	0
4	700	0.5
5	700	1.0
6	600	0

The convective loss heat flux, q_c'' , was calculated as the product of the gas temperature gradient taken along a direction orthogonal to the sample surface (using the grid points nearest to the surface) and the thermal conductivity of the gas at the film temperature. The dots shown in Figure 2.11 depict locations where q_c'' values were computed. To increase computational efficiency, the computational domain was subdivided into two parts, as shown in Figure 2.10. d_a and d_b represent the grid size in the region below and above the bottom of the heater, respectively. A grid convergence study was conducted using scenario #3 (corresponding to the highest sample surface temperature). It was determined that selecting 2.5×10^{-4} and 5×10^{-4} m grid sizes for d_a and d_b, respectively, produces q_c'' values that are within 3% of those computed using a much finer, 1.25×10^{-4} m sized grid.

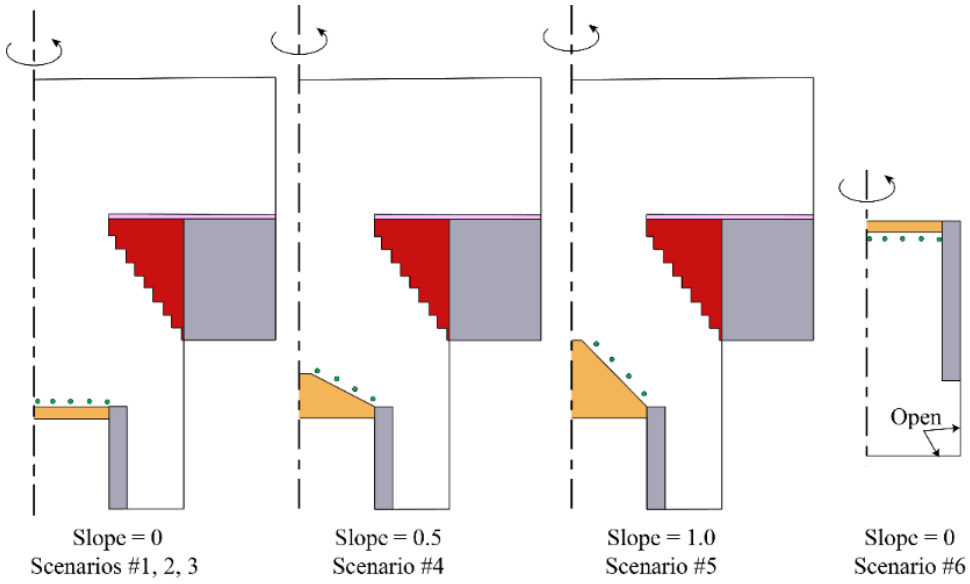

Figure 2.11: Scenarios explored in the CFD calculations. Slope represents the ratio of maximum height versus radius of the sample surface. The dots depict locations where q_c'' values were computed.

The CFD simulations of each scenario were carried out for 18 s. Scenarios #2-5 displayed oscillating flows; thus, the duration of the simulations was selected to reveal the periodic character fully. A set of temperature distribution snapshots taken over one oscillation period for scenario #3 as shown in Figure 2.12. It appeared that near the sample's surface, despite significant forced flow through the gasification chamber, the flow was driven primarily by buoyancy and the observed oscillation was a manifestation of the Rayleigh–Taylor instability.

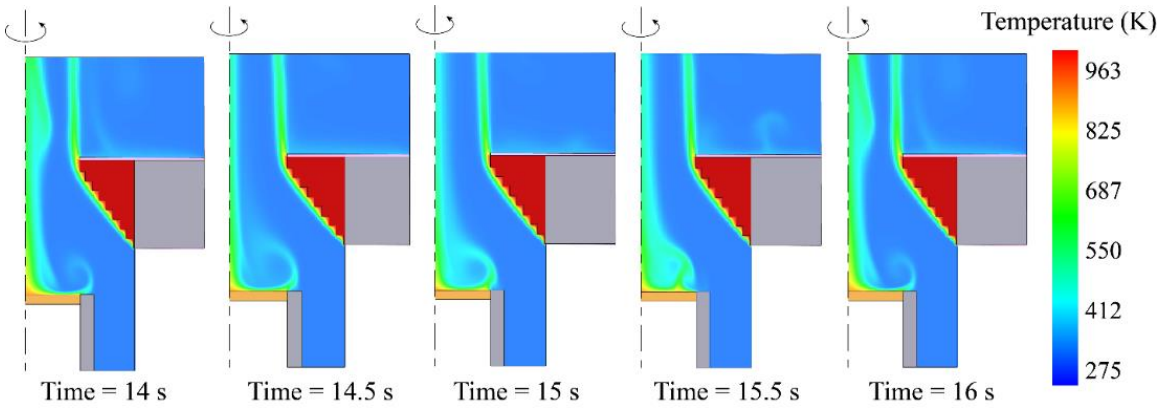

Figure 2.12: Oscillating temperature profile in a single period (14 – 16 s) obtained for scenario #3.

The convective loss heat fluxes computed for the same scenario at two representative radial positions (r_z/R = 0.286 and r_z/R = 0.857) are shown in Figure 2.13. To convert these heat fluxes to convection coefficients, they were first averaged in time over the oscillation period (or over 5 s in the cases of non-oscillating flows). To examine the impact of surface temperature on the convection, the convection coefficients obtained for the scenarios where this temperature was varied (scenarios #1, 2 and 3) were further averaged over the top sample surface area using Equation 2.5:

$$\bar{h}_c = \frac{2}{R^2}\int_0^R h_c r_z dr_z \tag{2.5}$$

Where h_c represented the time averaged and position specific convection coefficient. $\bar{h}_c$ was found to increase from 6.2 to 9.8 W m^{-2} K^{-1} with T_s increasing from 500 – 900 K. This change in $\bar{h}_c$ was deemed to be insufficiently large to justify an increase in the complexity of the convective loss model through the introduction of a surface temperature dependent convection coefficient. The convection coefficients computed at T_s = 700 K for the top

sample surface and T_s = 600 K for the bottom sample surface were postulated to be representative of the corresponding surface temperature ranges.

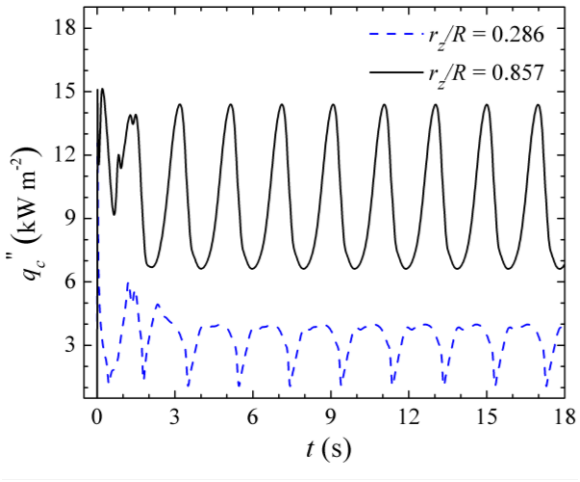

Figure 2.13: Convective loss heat fluxes computed for scenario #3 at a radial position of r_z/R = 0.286 and r_z/R = 0.857.

The time averaged convection coefficients h_c^{top} computed for the scenarios #2, 4, and 5 are plotted with respect to the radial distance in Figure 2.14. As indicated in Table 2.3 and Figure 2.11, these scenarios explored the impact of the shape of the sample on the convective loss from the top surface. The results indicated that the shape of the sample had a minor effect on the convection coefficient, while the impact of radial position was significant. The radial dependence of the convection coefficient was captured with Equation 2.6:

$$h_c^{top} = e_1 \left(r_z / R \right) + e_0 \tag{2.6}$$

where e_1 = 8.45 W m^{-2} K^{-1} and e_0 = 2.97 W m^{-2} K^{-1}.

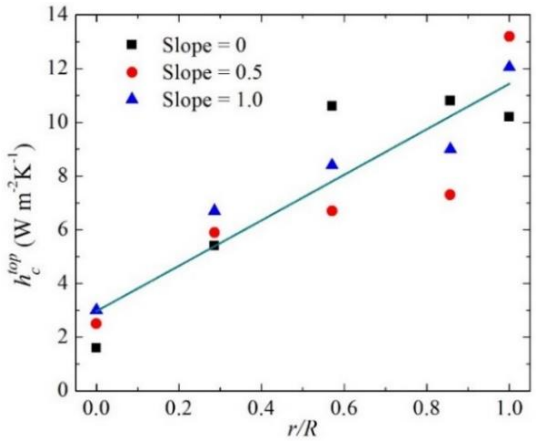

Figure 2.14: Time averaged convective heat transfer coefficients computed for scenarios #2, 4, and 5. The line is the fit of the data with Equation 2.6. Slope represents the ratio of maximum height versus radius of the top sample surface.

In addition to the sample geometries explored in the scenarios above, the impact of a recessed top sample surface (3×10^{-3} m below the edge of the sample holder) was also explored. It was determined that the convective heat transfer in the recessed geometry was well represented by identical parameters. The convection coefficient for the bottom surface (h_c^{bottom}) was found to be weakly dependent on radial distance and its surface area averaged value was determined to be 4 W m^{-2} K^{-1}.

The convection coefficients were calculated as $h_c = q_c'' / \left(T_s - T_{in}\right)$, which provided an expression for q_c'' in terms of the gas or wall temperature that are continuously measured in the experiments. An averaged value of h_c computed for the top surface was validated against an experiment where a copper plate, coated with a 0.94 emissivity paint and attached to Kaowool PM board, was placed into the gasification chamber instead of a material sample. The copper plate was subsequently heated with the radiant heat flux set at 25 kW m^{-2}. The temperature of the plate was measured with three embedded 8×10^{-4} m

diameter Type K thermocouples. The copper plate temperature was subsequently computed using ThermaKin [21] to account for the convective and radiative losses and transient heat transfer through the copper and insulation, in which the thermophysical properties are well known [40,90]. In the experiment, spatial variation in the convective losses could not be resolved. Therefore, the copper plate temperature was modeled using a one-dimensional framework and h_c^{top} averaged over the top surface area of the plate with Equation 2.5 (h_c^{top} = 8.6 W m^{-2} K^{-1} was used in the simulation). As Figure 2.15 indicates, the modeled temperature is in excellent agreement with the results of the experimental measurement.

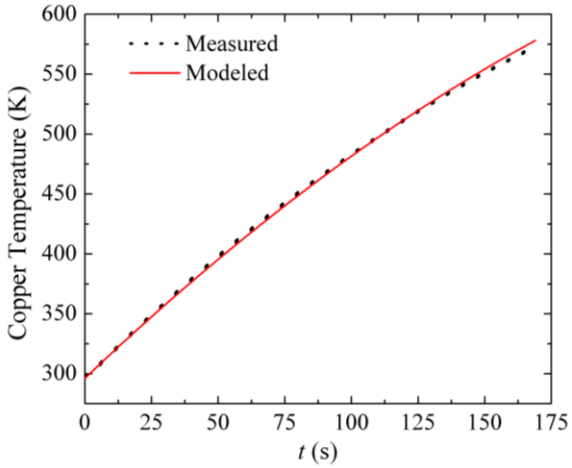

Figure 2.15: Comparison of experimental and modeled temperatures of the copper plate exposed to the incident radiant heat flux set at 25 kW m^{-2}.

To provide a basis for computing the experimental convective heat fluxes for the top sample surface boundary conditions, individual tests were conducted to measure environmental temperature profiles. The heater was set to a range of heat fluxes (30, 40, 60, and 80 kW m^{-2}) to create representative conditions experienced during typical gasification tests; a single test was conducted at each heat flux set point. A disk cut from

Kaowool PM board was used as a sample surrogate during these measurements. With the nitrogen flow turned on, three Type K thermocouples (7.6×10^{-5} m in diameter) were positioned in the nitrogen flow directly above the glass beads to collect the time-resolved environmental temperature histories (T^e) of the top sample surface. The mean heat flux-dependent gas temperature histories for the top sample surface are shown as open symbols in Figure 2.16.

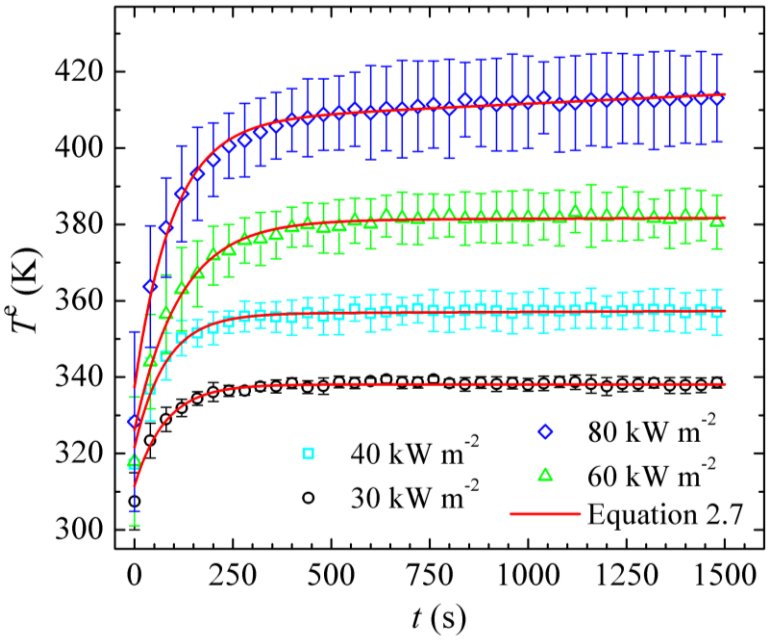

Figure 2.16: Mean environmental temperature histories for a range of heat flux set points measured near the top sample surface. These temperature profiles serve as the basis for computing the convective heat fluxes at the top sample surface. The lines represent the results of Equation 2.7 employing independent fitting parameters for each heat flux.

The mean time-resolved gas temperature histories were subsequently mathematically represented using Equation 2.7.

$$T^e = T_1^e \exp\left(T_2^e t\right) + T_3^e \exp\left(T_4^e t\right) + T_{HFG} \tag{2.7}$$

where all T^e variables with numerical subscripts represent user-specified constants and T_{HFG} is the background environmental temperature. The heat flux-dependent parameters, computed with Equation 2.7 to represent the experimental measurements, are provided in Table 2.4. The solid lines in Figure 2.16 are the resulting environmental temperature profiles employing the fitting parameters provided in Table 2.4.

Table 2.4: Heat flux-dependent fitting parameters for Equation 2.7 describing the time-dependent change in the environmental temperature at the top sample surface.

Nominal heat flux [kW m^{-2}]	T_1^e **[K]**	T_2^e **[K s^{-1}]**	T_3^e **[K]**	T_4^e **[K s^{-1}]**	T_{HFG} **[K]**
30	48.1	3.11×10^{-8}	-26.6	-1.28×10^{-2}	290
40	66.5	9.80×10^{-6}	-35.0	-1.29×10^{-2}	290
60	90.5	1.19×10^{-5}	-54.7	-8.98×10^{-3}	290
80	116.8	4.02×10^{-5}	-69.6	-1.03×10^{-2}	290

In a similar fashion to measuring the top sample surface temperature histories, temperature profiles were measured to provide a basis for the bottom sample surface convective losses. These temperature measurements were collected at a set point heat flux of 30, 40, 60, and 80 kW m^{-2}; measurements at each heat flux were repeated in triplicate. A Type K thermocouple (1×10^{-3} m in diameter) was used to measure the temperature of the inside wall of the inner gasification chamber (T_{inner}). The inner gasification chamber wall temperature profiles were used as representative temperature data for the convective losses from the bottom sample surface. The mean heat flux-dependent temperature profiles for the bottom sample surface are presented as open symbols in Figure 2.17. Post-processing of these bottom surface temperature profiles will be discussed in section 3.4.2.

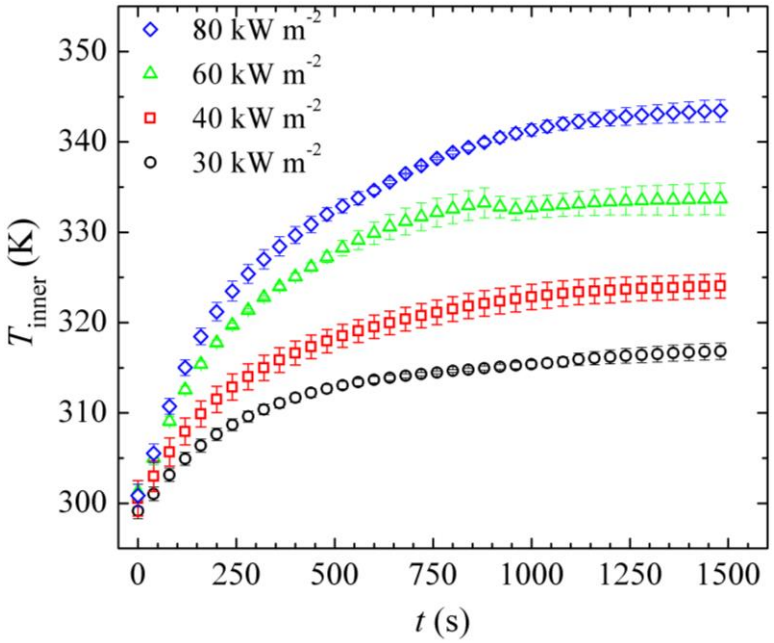

Figure 2.17: Mean experimental inner gasification chamber temperature histories for a range of heat fluxes. These temperature profiles serve as the basis for computing the convective heat fluxes at the bottom sample surface.

2.3.2.4: Char Emissivity

Independent CAPA II experiments were conducted to investigate the surface emissivity of the developed char layer produced during PVC, PC, and PEEK pyrolysis. An undecomposed PVC, PC, and PEEK sample was subjected to 60 kW m^{-2} (set point) until a char layer on the top of the sample was formed, at which point the heater was quickly removed. Once the sample cooled to room temperature, half of the sample top surface was painted with 0.94 emissivity paint while the other half remained unchanged. The sample was subsequently re-subjected to the radiant heat flux for an additional 200 s, after which time the test was terminated. The bottom surface temperatures associated with the painted and unpainted portions of the char layer were compared to estimate the char emissivity.

2.4: Char Structure Examination

To investigate the structure of the developed intumescent char, samples were prepared using separate CAPA II experiments conducted at a high heat flux set point. Subsequent analysis of the char structure provides a measure of the pore size distribution and porosity of the developed intumescent char layer. The pore size distribution provides a histogram of the frequency in which each pore size was observed in the char. The char porosity provides a volumetric fraction of the void space within the total char layer. A relationship between the resulting pore statistics and the associated thermal transport parameters enables a quantitative understanding of the char's thermal insulating potential.

2.4.1: Char Pore Size Distribution

The pores, or void spaces, in the developed char layers were found to include a wide range of sizes. Advanced optical imaging of typical polymeric char samples from a previous study revealed pores ranging from as large as a few millimeters all the way down to several microns in diameter [71]. The pore size distribution provides a relative measure of the number of pores across this wide range of diameters. In this study, char samples were analyzed to obtain an estimate of the pore size distribution in a size range visible to the naked eye (1×10^{-4} m in diameter and larger).

To investigate the PVC, PC, PEEK, and PVDF char structures, samples were prepared using separate CAPA II experiments conducted at 60, 75, 80, and 60 kW m^{-2} (set point), respectively. These experiments were terminated at a time when a fully developed char layer was present on the top portion of the sample with the remaining material below

partially undecomposed, which helped ensure that the sample was not too fragile and could withstand subsequent mechanical treatment. The fully parameterized pyrolysis model, the development of which is discussed in sections 5.2 – 5.6, was employed to compute this termination time and identify the boundary of the top char layer containing fully developed char.

The sample, once cooled to ambient temperature, was carefully cut in half with a band saw to expose its cross sectional profile of the char structure. Subsequently, digital images of this cross section were taken using a Nikon D7100 camera equipped with a Nikon PK-12 14 mm extension tube and Nikon Nikkor 50 mm f/1.8D lens. The images were calibrated with a ruler positioned in the same plane as the cross section to provide a length scale reference. White LED lighting was utilized to improve resolution of the images.

The images were subsequently analyzed using a pore detection algorithm for porous media developed by Rabbani et al. in MATLAB [91]; this script utilized the image processing toolbox in MATLAB version R2015b. The binary (black and white) image with a known scaling resolution was obtained by first converting the color image to grayscale. Next, a specific color gradient threshold was defined to distinguish between pores and solid continuum. A grayscale color gradient threshold value of 0.45 was chosen based on visual comparisons to provide the most accurate representation of the char pore and solid continuum structure. The black regions in the binary image represent the pores (void space) and the white areas represent the solid char.

A pixel-filtering scheme was utilized to distinguish between microscopic pores and camera sensor noise. This pixel-filtering process defined all objects greater than 1×10^{-4} m

in diameter as either a pore or solid continuum. The objects with size below 1×10^{-4} m were considered camera sensor noise. In other words, smaller pores may have been present but were not resolved in the current analysis. A watershed segmentation method [92] was subsequently employed to detect and analyze the relative frequency and average pore sizes within the char. The watershed segmentation method identifies narrowing regions of a pore as the boundary between two individual spherical pores; therefore, this method effectively splits larger non-spherical pores into two or more smaller spherical pores. The pore diameter was computed by transforming the estimated pore area to a perfect circle; this is consistent with the finding from Staggs that the majority of all visible pores had an aspect ratio on the order of unity [71]. All char analysis was performed on a portion the sample cross section identified as being comprised of fully developed char. The char layer from duplicate independent gasification tests were examined to accumulate statistical data.

2.4.2: Char Porosity

The char porosity (Φ) provides a means to quantify the volumetric fraction of the void space within the total char layer, described by Equation 2.8.

$$\Phi = \frac{V_{void}}{V_{total}} \tag{2.8}$$

where V_{void} and V_{total} are the volumes associated with the void and total sample, respectively. In this study, two different methods were employed to investigate the porosity of the rigid PVC, PC, PEEK, and PVDF intumescent char.

The first method to quantify the char porosity was based on the density of graphite; a methodology to evaluate the overall structure of the resulting char. The total volume was computed based on an average sample profile of the fully decomposed char layer. Rigid PVC, PC, PEEK, and PVDF char samples were analyzed at the conclusion of CAPA II experiments conducted at 60, 75, 80, and 60 kW m^{-2} irradiation, respectively, to ensure the sample was fully decomposed. It was assumed that the total volume was comprised of two components: solid continuum and void space. Assuming the molecular structure of the char was similar to graphite [93], the volume of the solid continuum was calculated assuming the char's solid mass was graphitic in nature. Therefore, the volume of the solid continuum portion of the char was computed to enable subsequent calculation of the void volume. The volume of the void was simply the difference between the total volume and the volume of the solid continuum. This method provided a measure of the char porosity based on the density of graphite.

The second method to quantify the rigid PVC, PC, PEEK, and PVDF char porosity was based on image analysis employing the pore detection algorithm described in Section 2.4.1. In this method, the char porosity was computed from a two-dimensional cross-sectional image of the char layer. Similar to a previous study [71], it was assumed that the two-dimensional porosity (the ratio of the area of voids to the total area) computed from the image was identical to the three-dimensional porosity (the ratio of the volume of voids to the total volume) of the developed char. The visual porosity was computed as the average from duplicate, independent tests. This method provided a measure of the intumescent char porosity based on visually detected pores greater than 1×10^{-4} m.

Chapter 3: Numerical Framework – ThermaKin

ThermaKin [21] is a numerical tool that was first developed to compute the transient rate of gaseous fuel production from fundamental physical and chemical properties of components of a one-dimensional (1D) pyrolyzing solid. ThermaKin was later expanded into a Cartesian two-dimensional (2D) pyrolysis solver, ThermaKin2D [94], which incorporated an empirical flame spread sub-model. In the current work, a new version of the solver, ThermaKin2Ds [88], has been developed. This version includes a new module capable of simulating 2D axisymmetric (2Dax) material specimens. This module has been developed to enable accurate simulation of the CAPA II gasification experiments.

3.1: Governing Equations

ThermaKin2Ds is a numerical tool that solves transient mass and energy conservation equations in a two-dimensional axisymmetric framework. The conservation equations account for finite-rate chemical reactions described by Arrhenius reaction rates. The material specimen is represented by a mixture of user-defined components. Every component is characterized by density, heat capacity, thermal conductivity, a gas transfer coefficient, emissivity, and a radiation absorption coefficient. The first four properties in this list are defined by a flexible function of temperature, T, given by Equation 3.1.

$$property = p_0 + p_1 T + p_2 T^n \tag{3.1}$$

where p_0, p_1, p_2, and n are user-specified parameters. Emissivity and absorption coefficients are defined by single (constant) values. All components are divided into three categories: solids, liquids, and gases.

Mass conservation, given by Equation 3.2 in cylindrical coordinates, accounts for each component within the system.

$$\frac{\partial \xi_j}{\partial t} = \sum_{i=1}^{Nr} \theta_i^j r_i - \frac{\partial J_j^x}{\partial x} - \frac{1}{z}\frac{\partial (z J_j^z)}{\partial z} + \frac{\partial}{\partial x}\left(\xi_j \int_0^x \frac{1}{\rho}\frac{\partial \rho}{\partial t} dx \right) \tag{3.2}$$

ξ is the mass concentration of a given component, denoted by subscript j, expressed as mass per unit volume. t is time and Nr is the number of reactions. θ_i^j is a stoichiometric coefficient of the j-th component of the i-th reaction and r (given by Equation 3.4) is the rate of consumption or production from the chemical reaction. J is the mass flux of gases within the solid (calculated by Equation 3.5), ρ is the material density (given by Equation 3.6), and x and z are the axial and radial cylindrical coordinates, respectively. The first term on the right-hand-side of Equation 3.2 accounts for the consumption or production of species. The second and third terms on the right-hand-side of Equation 3.2 accounts for gas transfer in the axial and radial directions and only applies to gaseous components. The last term on the right-hand-side of Equation 3.2 arises due to an application of the Eulerian (stationary) coordinate framework to a medium that contracts or expands in response to density changes. Here it is assumed that the contraction or expansion occurs in one dimension (x), with respect to a stationary plane defined by $x = 0$.

Chemical reactions within ThermaKin2Ds are accounted for by defining chemical equations balanced by stoichiometric coefficients, θ. Each reaction may have 1 – 2

reactants (left-hand-side of the equation) and 0 – 2 products (right-hand-side of the equation), as shown in Equation 3.3.

$$\theta^1 \text{COMP1} + \theta^2 \text{COMP2} \rightarrow \theta^3 \text{COMP3} + \theta^4 \text{COMP4} + h \tag{3.3}$$

The stoichiometric coefficient, θ_i^j, is negative when component *j* is the *i*-th reaction's reactant and positive when it is this reaction's product. *h* is defined as the heat of reaction, and is positive when describing an exothermic reaction. The rate at which the reaction occurs, *r*, is defined in Equation 3.4.

$$r = A\exp\left(-\frac{E}{R_u T}\right)\xi_{\text{COMP1}}\,\xi_{\text{COMP2}} \tag{3.4}$$

where *A* and *E* are the Arrhenius pre-exponential factor and activation energy, respectively, and R_u is the universal molar gas constant. ξ is the concentration of a given component expressed in units of mass per unit volume ($\xi_{\text{COMP1}} = mf_{\text{COMP1}}\rho$), where mf_{COMP1} is the mass fraction of the first component and ρ is the density of the mixture. In the absence of the second reactant, ξ_{COMP2} is set to unity. The rate of consumption/formation of a reactant/product is calculated by multiplying *r* by the corresponding stoichiometric coefficient. The rate of production of heat is calculated as the product of *r* and *h*.

The transfer of gaseous mass is driven by the gradient of volumetric fraction expressed through concentration, as shown in Equation 3.5.

$$J_g^x = -\rho_g \lambda \frac{\partial\left(\xi_g / \rho_g\right)}{\partial x} \tag{3.5}$$

Here, J_g^x is the mass flux of gas g in the x direction; an identical expression is required for mass flux in the z direction. Only gaseous components are assumed to undergo transfer defined by Equation 3.5. λ is the gas transfer coefficient of the material. Note that λ does not depend on the nature of gas that is being transferred (i.e., on a volumetric basis, all gases subjected to the same volumetric fraction gradient are transferred at the same rate); however, may be dependent upon the composition of the solid material through which the gas is being transported. The density of the material (ρ) is defined by Equation 3.6.

$$\rho = \frac{1}{\sum_{s=1}^{N_s} \frac{mf_s}{\rho_s} + \sum_{l=1}^{N_l} \frac{mf_l}{\rho_l} + \gamma \sum_{g=1}^{N_g} \frac{mf_g}{\rho_g}} \tag{3.6}$$

where ρ with a subscript designates component density. Subscripts s, l, and g are used to represent solid, liquid and gaseous components, respectively. The swelling factor γ, which may assume a value between zero and one, describes volumetric change due to the presence of gases. When $\gamma = 0$, the presence of gases has no effect on the volume. When $\gamma = 1$, gases contribute to the volume of material in accordance with their respective densities. γ is calculated by volume-weighted averaging of the swelling factor specified for solids (γ_s) and liquids (γ_l).

The conservation of energy, expressed in cylindrical coordinates, is given in terms of temperature by Equation 3.7. The energy conservation accounts for heat flow due to thermal degradation reactions and phase transitions, defined by the first term on the right-hand-side of Equation 3.7. The second and third terms on the right-hand-side of Equation 3.7 accounts for heat conduction within the condensed phase (Equation 3.8). In-depth

radiation absorption from external sources (Equation 3.9) and radiant heat loss to the surrounding environment (Equation 3.10) is captured by the fourth and fifth terms on the right-hand-side of Equation 3.7. The last two terms on the right-hand-side of Equation 3.7 account for convective heat transfer due to gas transport and energy flow associated with contraction or expansion of the material due to change in density.

$$\sum_{j=1}^{N} \xi_j c_j \frac{\partial T}{\partial t} = \sum_{i=1}^{Nr} h_i r_i - \frac{\partial q_x}{\partial x} - \frac{1}{z}\frac{\partial (z q_z)}{\partial z} - \frac{\partial I_{ex}}{\partial x} + \frac{\partial I_{rr}}{\partial x} - \sum_{g=1}^{Ng} c_g \left(J_g^x \frac{\partial T}{\partial x} + J_g^z \frac{\partial T}{\partial z} \right) + c\rho \frac{\partial T}{\partial x} \int_0^x \frac{1}{\rho}\frac{\partial \rho}{\partial t} dx \tag{3.7}$$

where c is the heat capacity or specific heat of the material. The heat conduction, q, is described by Fourier's law, and is given by Equation 3.8.

$$q_x = -k \frac{\partial T}{\partial x} \tag{3.8}$$

where q_x is the heat flux in the x (axial) direction and k is the thermal conductivity of the material; an identical expression is required for the heat conduction in the radial direction. Thermal radiation from an external source is absorbed inside the material according to a generalized version of the Beer-Lambert law, given by Equation 3.9.

$$\frac{\partial I_{ex}}{\partial x} = -I_{ex} \sum_{i=1}^{N} \kappa_i \xi_i \tag{3.9}$$

where I_{ex} is the radiation flux in the x direction and κ_i is the absorption (or extinction) coefficient of the i-th component. All radiation accounting within the model is assumed to be independent of spectral characteristics. To comply with the second law of

thermodynamics, the material is prescribed to re-radiate energy to the environment according to Equation 3.10.

$$\frac{\partial I_{rr}}{\partial x} = \frac{\sigma T^4 \sum_{i=1}^{N} \varepsilon_i v_i}{I_{ex}^0} \frac{\partial I_{ex}}{\partial x} \tag{3.10}$$

where I_{rr} is the heat flux that is radiated from the in-depth portion of the sample toward and through the material object top boundary (parallel to the *x*-axis) and I_{ex}^0 is the external radiation flux through the boundary (incident flux minus reflected). v is the volumetric fraction of the *i*-th component and σ is the Stefan-Boltzmann constant. ε_i is the surface emissivity of the *i*-th component, which in the current framework equals the complement of reflectivity of the same component. In the case where no external radiation is applied, the I_{ex}^0 term used in Equation 3.10 is set to unity to produce a meaningful calculation of radiative loss.

Equation 3.9 and Equation 3.10 describe radiative exchange between a material object and environment. The radiative transfer inside the object is modeled using the conduction equation (Equation 3.8) combined with the thermal conductivity expressed as the third power of temperature (using Equation 3.1). This approach to model radiative transfer through the conduction equation is referred to as the radiation diffusion approximation; it has been shown to provide accurate results for optically thick medium [70].

3.2: Solution Methodology

To solve the mass and energy conservation equations, a material object is divided into finite volumes (or elements). For 2D axisymmetric objects, the elements are characterized by two sizes: Δx and Δz. These sizes represent discretization with respect to the corresponding axial and radial coordinates. Each element is also characterized by the mass of the components and temperature; these parameters serve as primary object descriptors. The changes in mass and temperature with respect to time are computed using a small time-step, Δt. For the x dimension of any object, the time integration is based on the Crank-Nicolson scheme [96]. A detailed description of this integration procedure can be found in an earlier publication [21]. A simple explicit integration scheme is used for the z direction since it is perpendicular to the primary mass and energy transport.

It should be noted that Δx of individual elements changes with time due to the expansion/contraction of the object. These changes, accumulated over time, may have substantial negative effects on the accuracy of the solution procedure. To minimize these effects, element thicknesses are evaluated after every time-step. If an element has a thickness greater than a preset value of Δx, it is split into two elements. If the element thickness is less than a preset value of Δx, a fraction of the element below is added to bring it to the preset thickness. The temperature and composition of the mixed elements are recalculated to ensure the conservation of energy and species at each time step.

Previously performed simulations [94] indicate that the integration in the x dimension is stable at a wide range of selected values of Δx and Δt; however, the accuracy

of the results gradually decreases with an increasing value of either of these parameters. Therefore, to ensure that a given simulation is converged, a sensitivity of the results to the values of the integration parameters should always be examined. The stability of the solution in the explicit integration dimension (z) is subject to a well-defined condition, given in Equation 3.11.

$$\frac{(\Delta z)^2}{\Delta t} > 2A^* \tag{3.11}$$

where A^* represents either the gas transfer coefficient (λ) or thermal diffusivity ($\alpha = k/\rho c$) of the object, whichever is greater. $\Delta x = 5\times10^{-5}$ m, $\Delta z = 3.5\times10^{-3}$ m and $\Delta t = 0.01$ s represent a good initial guess for a typical pyrolysis problem employing the 2Dax module.

3.3: Verification of the Two-Dimensional Axisymmetric Model

ThermaKin2Ds was employed to investigate a quantitative coupling of the chemical, thermal, and physical processes that take place during condensed phase pyrolysis of charring and intumescent materials. Successful detailed analyses of these processes lead to accurately predicting burning rates for a wide range of materials and fire scenarios. In this work, the ThermaKin2Ds numerical framework has been utilized, through inverse analysis, to fully parameterize all critical processes identified in both the thermally thin (milligram-scale) and thermally thick (gram-scale) experiments described in chapter 2. This ThermaKin modeling framework and methodology has been shown to be successful for non-charring [55,97], charring [39,57], composite [9,85,98], and flame retardant materials [99–101].

To ensure that the 2Dax module was implemented correctly, its performance was compared to relevant analytical solutions by my colleague, Dr. Yan Ding. Four verification cases were examined: heat conduction in the *x* (axial) and *z* (radial) directions as well as mass diffusion in each of these directions. The submodules used within the 2Dax module for the integration of chemical kinetics and solution of the radiation transport were verified previously within the framework of the original ThermaKin [21] and therefore did not require further verification.

3.3.1: Heat Conduction

A cylindrical object was defined using temperature independent properties. The cylinder was initially at a temperature T_i = 300 K and had a height of L = 0.005 m and radius of W = 0.005 m. The origin of the cylindrical coordinates was at the center of the bottom cylinder surface. The top surface boundary ($x = L$) was set to a constant temperature, T_L = 1000 K, while the bottom and side boundaries were defined as adiabatic. The density, heat capacity, thermal conductivity, gas transfer coefficient and emissivity of the cylinder were set at 1000 kg m^{-3}, 2000 J kg^{-1} K^{-1}, 0.2 W m^{-1} K^{-1}, 1×10^{-6} m^2 s^{-1} and 0, respectively.

According to Carslaw and Jaeger [102], the analytical solution for the 1D transient heat conduction in the axial direction is given by:

$$T(x,t) = T_L + \sum_{n=1}^{\infty} B_n \cos(\lambda_n x) \exp(-\lambda_n^2 \alpha t) \tag{3.14}$$

where $\alpha = k/\rho c$ is the thermal diffusivity; and B_n and λ_n are given as $B_n = \frac{2}{L}\int_0^L (T_i - T_L)\cos(\lambda_n x)dx$ and $\lambda_n = \left(n - \frac{1}{2}\right)\frac{\pi}{L}$. The infinite series was evaluated at n = 1000 to make sure that the resulting term did not change. In the ThermaKin2Ds simulation, the element size (Δx) and time step were set at 5×10^{-5} m and 0.01 s, respectively. The convergence of the numerical solution was verified by demonstrating that the results were not sensitive to a factor of four change in the integration parameters. Figure 3.1(a) portrays the comparison of the resulting temperature profiles at different points in time. The two solutions are in a perfect agreement with each other.

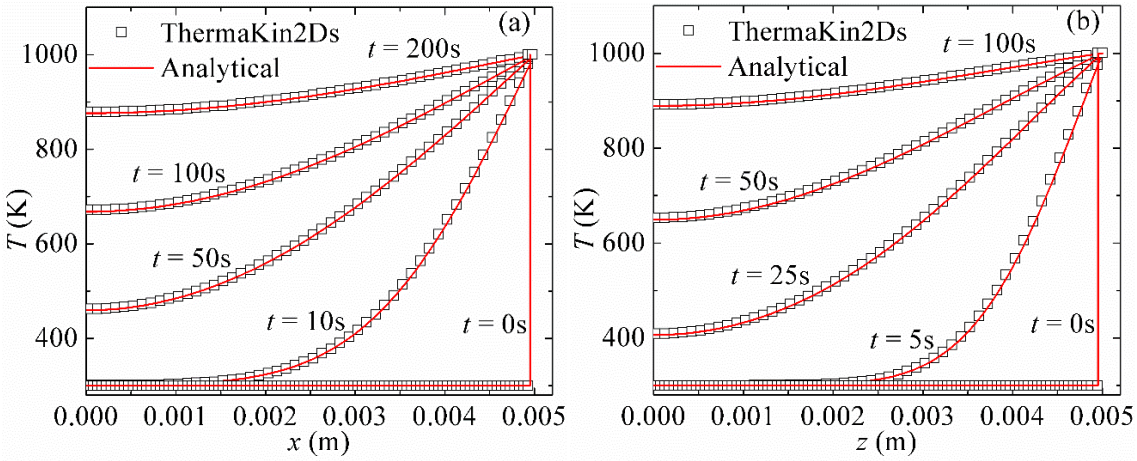

Figure 3.1: A comparison of the temperature profiles arising as a result of transient heat conduction in the (a) axial and (b) radial directions between the ThermaKin2Ds and corresponding analytical solutions [102].

Similarly, the transient heat conduction in the radial direction was examined. The temperature at $z = W$ was set to a constant value, T_W = 1000 K. The top and bottom surface boundaries were defined as adiabatic. The analytical solution for the 1D transient heat conduction in the radial direction is given by [102]:

$$T(z,t) = T_W + \frac{2(T_i - T_W)}{W} \sum_{n=1}^{\infty} \left(\frac{J_0(\lambda_n z)}{\lambda_n J_1(\lambda_n W)} \exp\left(-\alpha \lambda_n^2 t\right) \right) \tag{3.15}$$

where J_0 and J_1 represent Bessel functions. The infinite series was evaluated at n =308 to make sure that the resulting term did was fully converged. A comparison of this solution with the ThermaKin2Ds simulation is shown in Figure 3.1(b). The two results are in complete agreement, which indicates that the heat transport in the radial direction is solved correctly by the 2Dax module.

3.3.2: Mass Diffusion

The transient mass diffusion was examined using the same cylindrical object (identical dimensions and physical properties) as that defined in Section 3.3.1 for heat conduction. The initial gas concentration inside the cylinder was set as 0 kg m^{-3}. For the axial diffusion case, no mass transport was allowed through the side or bottom surface boundary. The gas concentration (C) at the top surface boundary ($x = L$) was set to be a constant value of C_L = 250 kg m^{-3}.

According to Crank [103], the analytical solution for the 1D mass diffusion in the axial direction is given by:

$$C(x,t) = C_L + \sum_{n=1}^{\infty} B_n \cos(\lambda_n x) \exp\left(-\lambda_n^2 \lambda t\right) \tag{3.16}$$

where $B_n = \frac{2}{L} \int_0^L (C_i - C_L) \cos(\lambda_n x) dx$ and $\lambda_n = \left(n - \frac{1}{2}\right) \frac{\pi}{L}$. The infinite series was evaluated using the same approach as discussed in Section 3.3.1. Also, same integration parameters were used in the ThermaKin2Ds simulation. The convergence of the numerical solution

was verified by demonstrating that the results were not sensitive to a factor of four change in the integration parameters. Figure 3.2(a) portrays the comparison of the concentration profiles in the axial direction obtained from the analytical solution and simulation. The results are in perfect agreement with each other, indicating a fully converged solution.

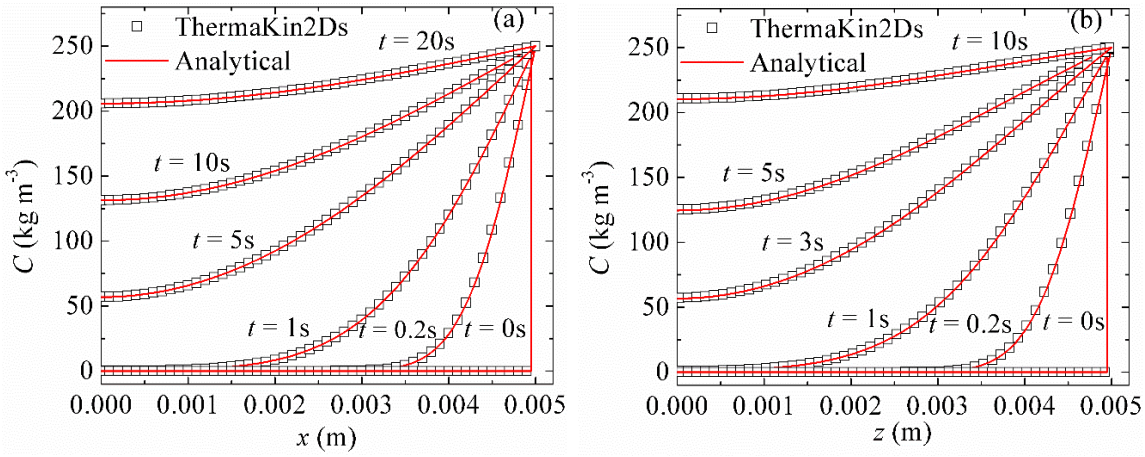

Figure 3.2: A comparison of the concentration profiles arising as a result of transient mass diffusion in the (a) axial and (b) radial directions between the ThermaKin2Ds and corresponding analytical solutions [103].

Similarly, the mass diffusion in the radial direction was examined. The gas concentration at $z = W$ was set as a constant value of $C_W = 250$ kg m^{-3}. No mass transport was allowed through the top or bottom surface boundary. The analytical solution for the 1D mass diffusion in the radial direction is given by [103]:

$$C(z,t) = C_W + \frac{2(C_i - C_W)}{W} \sum_{n=1}^{\infty} \left(\frac{J_0(\lambda_n z)}{\lambda_n J_1(\lambda_n W)} \exp\left(-\lambda \lambda_n^2 t\right) \right) \tag{3.17}$$

A comparison of this solution with the ThermaKin2Ds simulation is shown in Figure 3.2(b). The infinite series was evaluated using the same approach as discussed in Section 3.3.1 for heat conduction. The two results are in complete agreement, indicating that the mass transport is solved correctly by the 2Dax module.

3.4: ThermaKin Modeling Setup and Boundary Conditions

The models constructed in ThermaKin2Ds in this work can be divided into two categories based on the relative scale (or size) of the experimental configuration. The first subset of models was used to simulate the thermally thin behavior of the milligram-scale experiments conducted in the STA to determine the kinetics and thermodynamics of thermal decomposition. The second subset of models was utilized to simulate the thermally thick behavior of the gasification experiments conducted in the CAPA II to parameterize the thermal transport within the pyrolyzing sample and developing char layer. It is important to note that the modeling process is hierarchical in nature and the thermal transport models of the gasification experiments rely on the kinetics and thermodynamics obtained from the previous milligram-scale model development. Throughout the parameterization process, an attempt was made to minimize the number of independent parameters and thus create the simplest model that captures the experimental data with the accuracy comparable with their uncertainty.

3.4.1: Modeling Milligram-Scale Experiments

To model both the TGA and DSC experimental data, ThermaKin2Ds was utilized in the 1D-object mode to capture the thermally thin behavior of the experiments. Under this assumption, the material was prescribed to follow the actual measured heating rate of the STA by defining the convective heat transfer coefficient sufficiently high (1.0×10^{5} W m^{-1} K^{-1}) to ensure the sample followed the temperature profile of the surrounding environment. The model was defined such that the heat was transferred to the sample purely through

convection without any contribution from radiation (emissivity defined as zero). To account for the thermal inertia preventing the STA from reaching the nominal heating rate instantaneously, the actual heating rate was captured by an exponentially decaying sinusoidal function (Equation 3.18).

$$\frac{dT}{dt}(t) = u_1\left\{1-\exp\left(-u_2 t\right)\times\left[\cos\left(u_3 t\right)+u_4\sin\left(u_3 t\right)\right]\right\} \tag{3.18}$$

where the sample temperature is calculated as a function of time, and u_1, u_2, u_3, and u_4 are user prescribed fitting parameters. Figure 3.3 displays an example of the experimental and modeled heating rate from a rigid PVC experiment conducted at a nominal heating rate of 10 K min^{-1} (0.1667 K s^{-1}). To achieve the fit in Figure 3.3, the following parameters for Equation 3.18 were found: u_1 = 0.1667 K s^{-1}, u_2 = 0.0030 s^{-1}, u_3 = 0.0034 s^{-1}, and u_4 = -1.065.

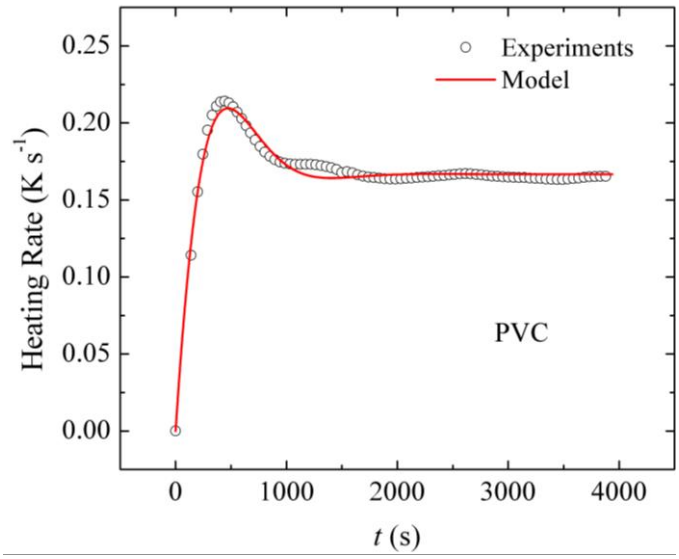

Figure 3.3: STA averaged experimental and fitted (with Equation 3.18) heating rate for PVC at 10 K min^{-1}.

Additional heating rate profiles were fitted for 5 and 20 K min^{-1}, demonstrated in Figure 3.4. The parameters identified for 5 K min^{-1} are u_1 = 0.0834 K s^{-1}, u_2 = 0.0034 s^{-1}, u_3 = 0.0050 s^{-1}, u_4 = -1.029, and 20 K min^{-1} are u_1 = 0.3313 K s^{-1}, u_2 = 0.0022 s^{-1}, u_3 = 0.0055 s^{-1}, and u_4 = -0.6174. It is important to note that for each material (and each heating rate) investigated in this study, the actual heating rate parameters were refitted and used for the model development. Averaged experimental results from 10 repeated tests were used to obtain the fitting parameters of Equation 3.18. For the sake of brevity, the actual heating rate parameters are not shown for each material.

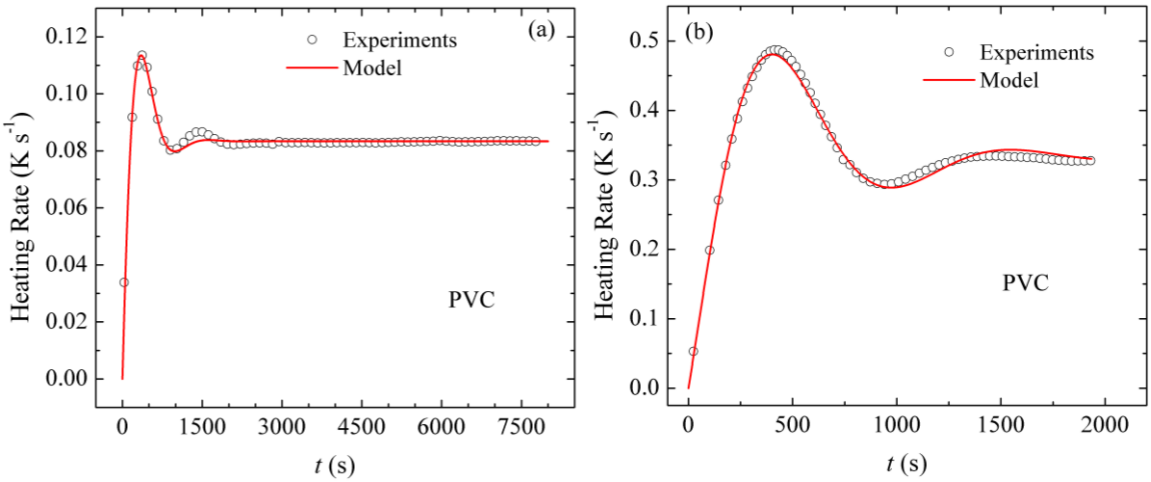

Figure 3.4: STA averaged experimental and fitted (with Equation 3.18) heating rates for PVC at (a) 5 K min^{-1} and (b) 20 K min^{-1}.

The pyrolyzate gases were defined to escape the sample instantaneously. The sample geometry was defined sufficiently small to ensure temperature and concentration gradients did not exist (enforcing the thermally thin assumption). The thermally thin assumption reduces the mass and energy conservation equations (Equation 3.2 and Equation 3.7, respectively) to effectively just the chemical reaction rate term (the first term on the right-

hand-side of each equation). Therefore, all component parameters (density, thermal conductivity, and absorption coefficient) associated with gas transport, heat transfer, and material expansion/contraction did not play a role in the milligram-scale modeling scenarios.

MCC experimental data were subsequently simulated using the previously parameterized model of the kinetics and thermodynamics of thermal decomposition. Equation 3.18 was refitted to capture the unique heating rate histories observed in the MCC tests, which were conducted at 10 K min^{-1}. The individual fitting parameters are not shown for the sake of brevity. Additional details on the MCC modeling methodology are provided in section 4.3.

3.4.2: Modeling Gram-Scale Experiments

To model the gasification experimental data, ThermaKin2Ds was employed in the 2Dax object mode. The 2Dax object can be used to setup 2D axisymmetric pyrolysis or combustion simulations in cylindrical coordinates (1D simulations can also be conducted in the 2Dax object mode by using a single computational element in the radial direction). This 2Dax geometry was developed to emulate conditions in the CAPA II [95], as described in section 2.3.2. Both 1D and 2D versions of the model were utilized in this work; more details are provided in Chapter 5. The resulting models were constructed based on the foundation of the kinetics and thermodynamics model parameterized from the TGA and DSC data sets. Similar to the methodology for the STA inverse analysis procedure, the objective in this procedure was to identify the simplest model that captured the relevant physics within the uncertainty associated with the experimental tools.

The 2Dax object is defined using the cylindrical coordinates x and z, and two boundaries, top and bottom. $x = 0$ corresponds to the position of the bottom boundary, which is orthogonal to the coordinate x. This bottom boundary serves as a reference point for the expansion or contraction of the 2Dax object. $z = 0$ defines the center axis of the object. It should be noted that, either due to the initial geometry specification and/or due to material expansion or contraction during pyrolysis, the top boundary may assume a non-uniform profile (i.e., the object may have thickness that varies with the radial coordinate z). In the 2Dax object boundary definition, the impacts of this non-uniformity on the surface area and heat exposure of the top boundary are taken into account. In this work, the top surface boundary conditions were defined such that the pyrolyzate gases escaped uninhibited from the sample solid at the top boundary.

To emulate the CAPA II experimental conditions at the top surface of the sample, the heat fluxes were defined to account for the effects of the sample surface changes on the radiation and the radial-dependent convective heat transfer coefficients. The external CAPA heat flux module was employed to capture the top surface radiation and convection profiles as described in sections 2.3.2.2 and 2.3.2.3, respectively. The top surface radiation was captured by Equation 2.3 and Equation 2.4 to account for the known radiation incident to the evolving sample surface as a function of sample surface position, including its angular orientation. To account for the temperature of the nitrogen gas surrounding the pyrolyzing sample, which defined the convective losses, Equation 2.7 was employed. It is important to note that a constant background temperature of T_{HFG} = 290 K, which corresponded to the temperature of the heat flux transducer, was used as a baseline for the

temperature fitting process. Equation 2.7 provided a time-resolved history of the evolving nitrogen gas temperature, as shown above in Figure 2.16; the heat flux-dependent fitting parameters are tabulated in Table 2.4. The spatially-resolved top surface convective heat transfer coefficient, shown in Equation 2.6, was employed to compute the top surface convective losses.

The bottom surface radiation and convective boundary conditions were treated differently than the top sample surface since the electric heater was not directly incident to the bottom sample surface. Here, a small radiative and convective heat flux was applied to the bottom sample surface to represent the energy transfer as a result of the evolving bottom sample surface and environmental temperatures. The environmental temperature at the bottom of the sample was assumed to be identical to the temperature of the inner gasification chamber wall; the heat flux-dependent inner gasification chamber temperature profiles are provided in Figure 2.17 in section 2.3.2.3. To simplify the definition of the bottom surface boundary conditions within the ThermaKin2Ds model, a piecewise function was subsequently employed to capture the dominant transient and steady state behavior of the inner gasification chamber wall temperatures; the piecewise function is given by Equation 3.19 and Equation 3.20.

$$T_{wall}(t) = \begin{cases} \beta t & \text{if } t < 800 \text{ s} \\ T_{wall,ss} & \text{if } t \geq 800 \text{ s} \end{cases} \tag{3.19}$$

$$\beta = \frac{\left(T_{wall,ss} - T_{\infty}\right)}{800 \text{ s}} \tag{3.20}$$

where T_{wall} is the instantaneous temperature of the inner gasification chamber wall, $T_{wall,ss}$ is the steady state temperature of the inner gasification chamber wall (measured at

approximately 800 s), and T_∞ is the initial environmental background temperature near the bottom sample surface.

The inner gasification chamber wall temperature consisted of a linear increase beginning at T_∞ until $T_{wall,ss}$ was reached at 800 s (a representative time when the inner gasification chamber wall reached a steady state value). T_∞ = 300 K and the steady state temperature values used in this study for 30, 40, 60, and 80 kW m^{-2} were 316, 323, 334, and 343 K. The convective losses from the bottom sample surface was calculated with a constant convective heat transfer coefficient (4 W m^{-2} K^{-1}) defined in section 2.3.2.3. The small radiation contribution was computed to account for the radiant heat flux from the inner gasification chamber wall to the bottom sample surface. The radiant heat flux from the inner gasification chamber wall to the bottom sample surface was approximated as σT_{wall}^4, where σ is the Stefan-Boltzmann constant and T_{wall} is the time-dependent inner gasification chamber wall temperature given by Equation 3.19.

Chapter 4: Milligram-scale Results and Analysis

A series of milligram-scale experiments were conducted to characterize the kinetics and thermodynamics of thermal decomposition as well as the heats of combustion of the released pyrolyzate gases. TGA data were used to describe the kinetics of thermal decomposition by determining Arrhenius reaction rate parameters and stoichiometric coefficients for each reaction. The DSC dataset was employed to determine the heat capacity and heats of reaction of each condensed-phase component and chemical reaction, respectively. Finally, MCC data were utilized to estimate the associated heats of complete combustion for the volatile gases released during the thermal decomposition process. In each reaction scheme, the model did not resolve individual elementary reactions; instead, it captured global trends of thermal decomposition. A detailed description of the results and analysis of the TGA, DSC, and MCC experiments and subsequent inverse analysis are provided in sections 4.1 – 4.3, respectively.

4.1: TGA: Kinetics of Thermal Decomposition

4.1.1: Development of Kinetics of Thermal Decomposition Models

The averaged TGA experimental data of PVC, FPVC, PC, PEEK, and PVDF are presented as symbols in Figures 4.1 – 4.5. The experimental instantaneous mass, m, and associated mass loss rate normalized by the initial mass, m_0, are shown as a function of temperature. The MLR was obtained by calculating the first numerical derivative of the normalized mass signal. The portrayed data are averaged results from 10 repeated

experiments. The error was calculated as two standard deviations of the mean (some error bars are difficult to discern because they are comparable in size to the data symbols). These TGA datasets were used to determine the kinetics of thermal decomposition. A detailed description of the methodology is provided for the rigid PVC dataset and was applied to the remaining materials following an identical procedure.

The experimental rigid PVC MLR profile contained two prominent peaks (shown in Figure 4.1(b)), the first at 570 K and the second at 740 K, both corresponding to thermal decomposition. The first maximum is known to be primarily associated with the release of hydrogen chloride (HCl). PVC is known to undergo a two-step decomposition process, where the first, low temperature step is dominated by the production of HCl [22,104]. The decomposition produces 19 wt. % of the final condensed-phase residue or char.

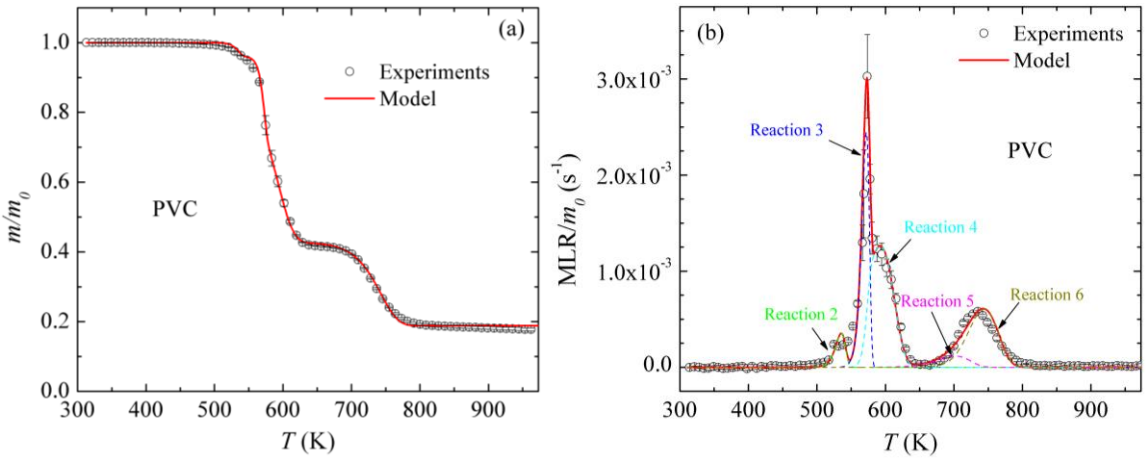

Figure 4.1: Averaged experimental and modeled normalized (a) mass and (b) MLR data obtained for PVC thermal decomposition at a nominal heating rate of 10 K min^{-1}.

Inverse modeling of the TGA data was performed using an approach adopted from several earlier publications [39,97–100,105]; a description of the methodology is provided here. A single first-order Arrhenius reaction was initially employed to model the TGA data.

The stoichiometric coefficients of this reaction were initially set to capture the residual yield observed in the TGA experiments. The Arrhenius activation energy (E) and pre-exponential factor (A) of this reaction were initially estimated using the analytical expressions given in Equation 4.1 and Equation 4.2 [106], which relate these parameters to the temperature and height of the targeted MLR peak.

$$E = \frac{eR_u T_{peak}^2 \left(\frac{MLR_{peak}}{m_0} \right)}{(1-\theta)\frac{dT}{dt}} \tag{4.1}$$

$$A = \frac{MLR_{peak}}{\left(\frac{m(T_{peak}) - m_0\theta}{1-\theta} \right)} \exp\left(\frac{E}{R_u T_{peak}} \right) \tag{4.2}$$

where R_u is the universal gas constant and T_{peak} is the temperature associated with the peak mass loss rate. MLR_{peak} is the magnitude of the peak mass loss rate and m_0 is the initial mass of the condensed phase reactant. θ is the stoichiometric mass coefficient which describes the residual char yield, dT/dt is the nominal STA heating rate, and $m(T_{peak})$ denotes the instantaneous mass corresponding to the temperature at the peak mass loss rate. Subsequently, E and A were refined through a manually iterative process using ThermaKin2Ds until the modeling results were found to be in agreement with the experimental data.

The reaction parameter manipulation was based on the following observations: an increase in the activation energy shifted the MLR curve to a higher temperature and reduced the height of the peak; an increase in the pre-exponential factor shifted the MLR

curve to a lower temperature and increased the height of the peak. The agreement was declared satisfactory when the differences between the average experimental and modeled final mass residues, and temperatures and magnitudes of MLR maxima were found to be within 3%, 5 K, and 8%, respectively. If it was impossible to achieve such agreement, an additional reaction was added to the reaction scheme and its parameters were adjusted iteratively to achieve further improvement. The objective of this study was to derive the simplest reaction scheme possible which had the capability of predicting the experimental data within the predefined fitting criteria.

In the case of rigid PVC, five consecutive mass loss reactions were required to capture the intricacies of the initial rise, multiple maxima, and final decay of the MLR within the accuracy of the instrumentation. These reactions, PVC Reactions 2 to 6, and their Arrhenius parameters are listed in Table 4.1 (Reaction 1 describes a glass transition and did not incur mass loss, therefore, it will be discussed in more detail in section 4.2). It is important to note that the decomposition parameters of all polymers studied in this work are also presented in Table 4.1 and will be discussed later. The component names used in the reaction definitions are self-explanatory. The resulting model predicted mass and MLR (solid lines) is compared with the experimental TGA data in Figure 4.1. The modeled MLR contributions from each reaction are portrayed as dashed lines in Figure 4.1(b). It is important to note that the total modeled MLR (solid line) is the summation of the MLR contribution from each reaction (dashed lines).

Table 4.1: Reaction scheme and kinetic parameters for the thermal decomposition of PVC, FPVC, PC, PEEK, and PVDF. It is important to note that some of the reactions in this table represent phase transitions within the reaction mechanism. Here, a negative value for heats of reaction (*h)* represented endothermic processes.

#	Reaction	A (s^{-1})	E_a (J mol^{-1})	h (J kg^{-1})
1	PVC → PVC_GT	6.0×10^{40}	2.80×10^{5}	0
2	PVC_GT → 0.96 PVC_Res1 + 0.04 PVC_Gas1	1.4×10^{31}	3.36×10^{5}	-3.00×10^{3}
3	PVC_Res1 → 0.78 PVC_Res2 + 0.22 PVC_Gas2	1.4×10^{45}	5.11×10^{5}	-6.20×10^{4}
4	PVC_Res2 → 0.57 PVC_Res3 + 0.43 PVC_Gas3	1.4×10^{9}	1.28×10^{5}	-1.28×10^{5}
5	PVC_Res3 → 0.90 PVC_Res4 + 0.10 PVC_Gas4	3.0×10^{10}	1.70×10^{5}	1.48×10^{5}
6	PVC_Res4 → 0.49 PVC_CHAR + 0.51 PVC_Gas5	3.0×10^{10}	1.80×10^{5}	-6.70×10^{4}
1	FPVC → 0.98 FPVC_Res1 + 0.02 FPVC_Gas1	1.5×10^{32}	3.41×10^{5}	1.8×10^{4}
2	FPVC_Res1 → 0.25 FPVC_Res2 + 0.75 FPVC_Gas2	7.0×10^{11}	1.56×10^{5}	-2.5×10^{5}
3	FPVC_Res2 → 0.75 FPVC_Res3 + 0.25 FPVC_Gas3	$3.0x0^{10}$	1.7×10^{5}	-1.0×10^{4}
4	FPVC_Res3 → 0.35 FPVC_CHAR + 0.65 FPVC_Gas4	3.0×10^{10}	1.8×10^{5}	-3.0×10^{5}
1	PC → PC_GT	6.0×10^{40}	3.4×10^{5}	0
2	PC_GT→ 0.36 PC_Res1 + 0.64 PC_Gas1	6.0×10^{29}	4.83×10^{5}	1.5×10^{4}
3	PC_Res1 → 0.72 PC_CHAR + 0.28 PC_Gas2	3.0×10^{3}	9.2×10^{4}	1.5×10^{4}
1	PEEK → PEEK_M	3.5×10^{33}	4.15×10^{5}	-3.9×10^{4}
2	PEEK_M→ 0.60 PEEK_Res1 + 0.40 PEEK_Gas1	4.3×10^{28}	5.05×10^{5}	2.68×10^{5}
3	PEEK_Res1 → 0.84 PEEK_CHAR + 0.16 PEEK_Gas2	1.4	5.2×10^{4}	1.01×10^{5}
1	PVDF → PVDF_M	7.0×10^{28}	2.6×10^{5}	-5.34×10^{4}
2	PVDF_M→ 0.95 PVDF_Res1 + 0.05 PVDF_Gas1	6.0×10^{30}	4.66×10^{5}	-1.18×10^{5}
3	PVDF_Res1 → 0.26 PVDF_CHAR + 0.74 PVDF_Gas2	2.6×10^{54}	8.2×10^{5}	4.6×10^{4}

The FPVC experimental MLR profile contains two prominent peaks both corresponding to thermal decomposition, as shown in Figure 4.2. This double peak structure was similar to that of rigid PVC, however, the experimental peaks were much more symmetric in the case of FPVC. The first maximum, occurring in the temperature range of approximately 500 – 600 K, is likely associated with both the release of hydrogen chloride (HCl) and the plasticizer additives. The second noticeable experimental peak was observed to take place in the temperature range of approximately 660 – 800 K. The thermal decomposition produced 6.4 wt. % of the final condensed-phase residue.

Inverse analyses of the FPVC data were conducted employing an identical parameterization methodology as described previously for rigid PVC. The fully parameterized FPVC thermal decomposition model was found to require four consecutive mass loss rate reactions to capture the experimental TGA data, as portrayed in Table 4.1. Due to the symmetric experimental peaks, the resulting model for FPVC had fewer necessary reactions than the rigid PVC thermal decomposition model. The results of the fully parameterized kinetics model are shown in Figure 4.2 as the solid lines. The MLR contributions of each reaction are portrayed as the dashed lines in Figure 4.2(b).

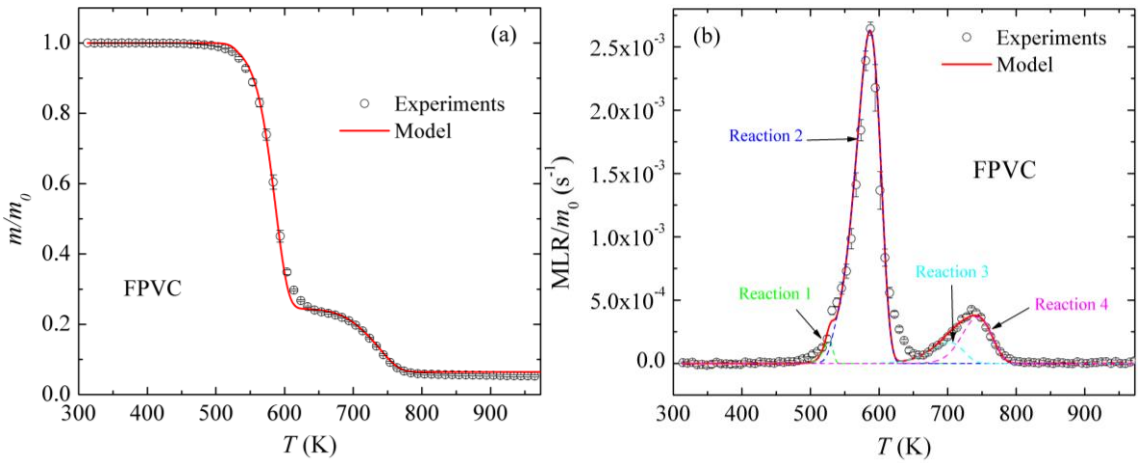

Figure 4.2: Averaged experimental and modeled normalized (a) mass and (b) MLR data obtained for FPVC thermal decomposition at a nominal heating rate of 10 K min^{-1}.

The PC experimental MLR profile contains a single prominent peak, corresponding to thermal decomposition, as shown in Figure 4.3. The entirety of the mass loss was observed to occur in the temperature range of approximately 750 – 900 K, with the maximum mass loss peak occurring at approximately 800 K. The thermal decomposition produced 26 wt. % of the final condensed-phase char. Inverse analysis of the PC data was conducted identically to the rigid PVC dataset in order to fully parameterize a thermal decomposition model. The fully parameterized PC thermal decomposition model was found to require two consecutive mass loss rate reactions to capture the experimental TGA data, as portrayed in Table 4.1. The second consecutive mass loss reaction was required to capture the slow secondary decomposition observed at higher temperatures, as shown in Figure 4.3. Reaction 1 represents a glass transition and did not incur mass loss, therefore, it will be discussed in more detail in section 4.2. The resulting predictions of the fully parameterized kinetics model are shown as solid lines in Figure 4.3.

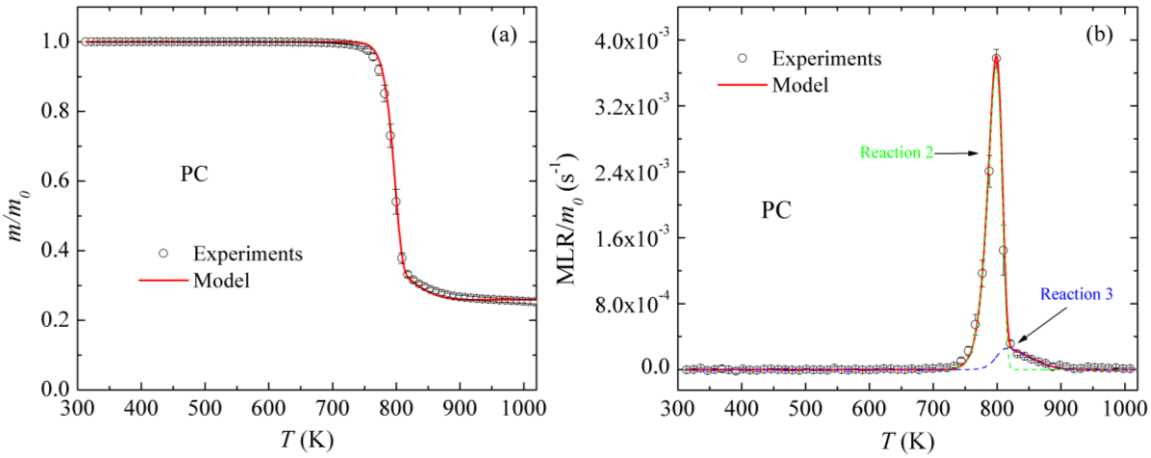

Figure 4.3: Averaged experimental and modeled normalized (a) mass and (b) MLR data obtained for PC thermal decomposition at a nominal heating rate of 10 K min^{-1}.

The PEEK experimental MLR profile contains a single prominent peak (similar to PC), corresponding to thermal decomposition, as shown in Figure 4.4. The entirety of the mass loss was observed to occur over a temperature range of approximately 825 – 900 K, with the maximum mass loss peak occurring at approximately 860 K. The thermal decomposition produced substantial final condensed-phase residue (50 wt. %). Inverse analysis of the PEEK data was conducted identically to the rigid PVC dataset in order to fully parameterize a thermal decomposition model. The fully parameterized PEEK thermal decomposition model was found to require two consecutive mass loss rate reactions to capture the experimental TGA data, as portrayed in Table 4.1. A second consecutive mass loss reaction was required to capture the slow secondary decomposition occurring between 900 – 1100 K, as shown in Figure 4.4. Reaction 1 represents a melting process and did not incur mass loss, therefore, it will be discussed in more detail in section 4.2. The resulting predictions of the fully parameterized kinetics model are shown in Figure 4.4 as the solid lines.

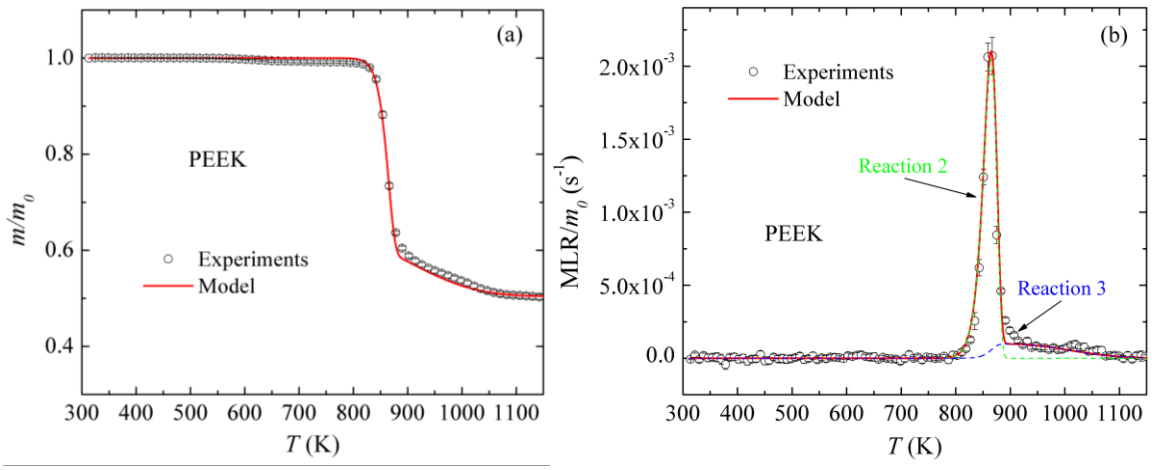

Figure 4.4: Averaged experimental and modeled normalized (a) mass and (b) MLR data obtained for PEEK thermal decomposition at a nominal heating rate of 10 K min^{-1}.

The PVDF experimental MLR profile contains a single peak, similar to both PC and PEEK thermal decomposition, as shown in Figure 4.5. The maximum MLR peak, corresponding with thermal decomposition, was observed to occur over a narrow temperature range of approximately 730 – 780 K. The thermal decomposition produced 25 wt. % of the final condensed-phase residue or char. In the case of PVDF, two consecutive mass loss reactions were required to capture the intricacies of the TGA MLR profile within the accuracy of the instrumentation. The first reaction was required to capture the slow onset of decomposition preceding the dominant mass loss peak, as shown in Figure 4.5. These reactions, PVDF Reactions 2 – 3, and their Arrhenius parameters are listed in Table 4.1 (Reaction 1 represents a melting process and did not incur mass loss, therefore, it will be discussed in more detail in section 4.2). The resulting model predicted mass and MLR (solid lines) is compared with the experimental TGA data in Figure 4.5. The modeled MLR contributions from each reaction are portrayed as dashed lines in Figure 4.5(b).

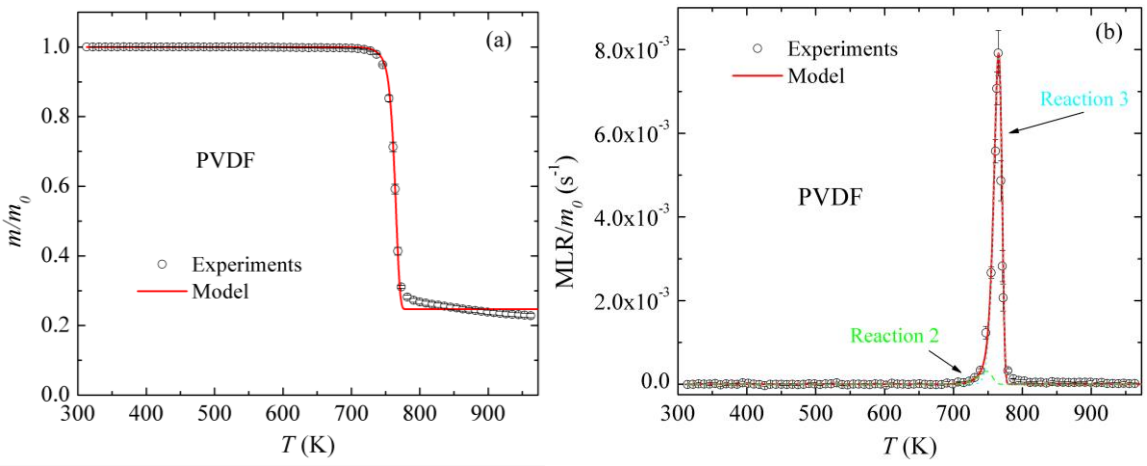

Figure 4.5: Averaged experimental and modeled (a) normalized mass and (b) normalized mass loss rate data obtained for PVDF at a nominal heating rate of 10 K min^{-1}.

4.1.2: Validation of Kinetics of Thermal Decomposition Models

The kinetics models for the thermal decomposition of all materials were validated by comparing simulated and experimental results from additional TGA datasets obtained at nominal heating rates of 5 and 20 K min^{-1}, as shown in Figures 4.6 – 4.10. The kinetics models, parameterized from data collected at a nominal heating rate of 10 K min^{-1}, were utilized to estimate the normalized mass of the extrapolated heating intensities. The resulting model predictions were found to provide excellent agreement with the experimental data for PVC, FPVC, PC, and PEEK, as depicted in Figures 4.6 – 4.9. There are more notable deviations, however, between the experimental and simulated datasets for PVDF at higher temperatures, as displayed in Figure 4.10. These discrepancies are likely associated with the imperfections of the original model constructed at a nominal heating rate of 10 K min^{-1}, where similar differences were observed although to a lesser extent. However, a satisfactory agreement was achieved between the experimental and simulated TGA data for all materials, as shown in Figures 4.6 – 4.10. The reasonable agreement

provided additional confidence that the kinetics models were capable of simulating the thermal decomposition of PVC, FPVC, PC, PEEK, and PVDF for a wide range of heating conditions.

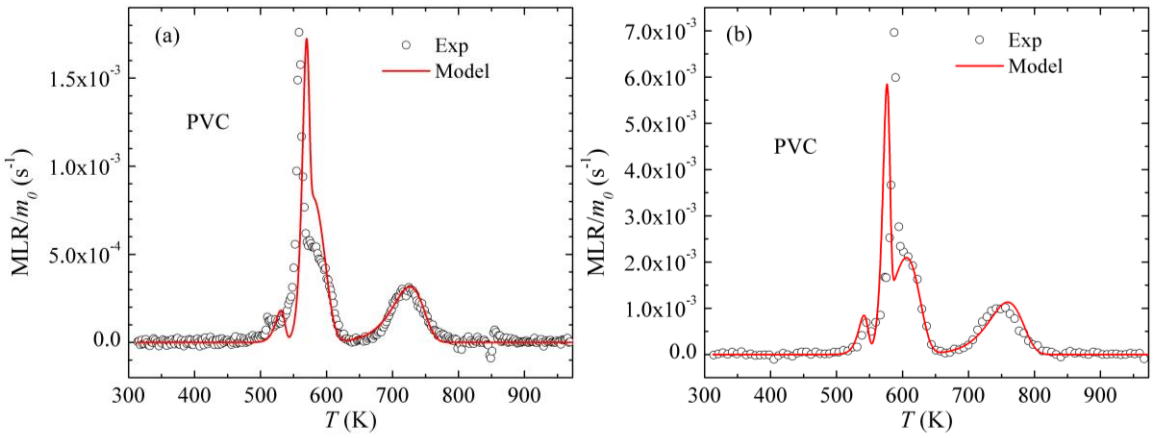

Figure 4.6: Averaged experimental and modeled normalized MLR data for PVC thermal decomposition at nominal heating rates of (a) 5 and (b) 20 K min^{-1}.

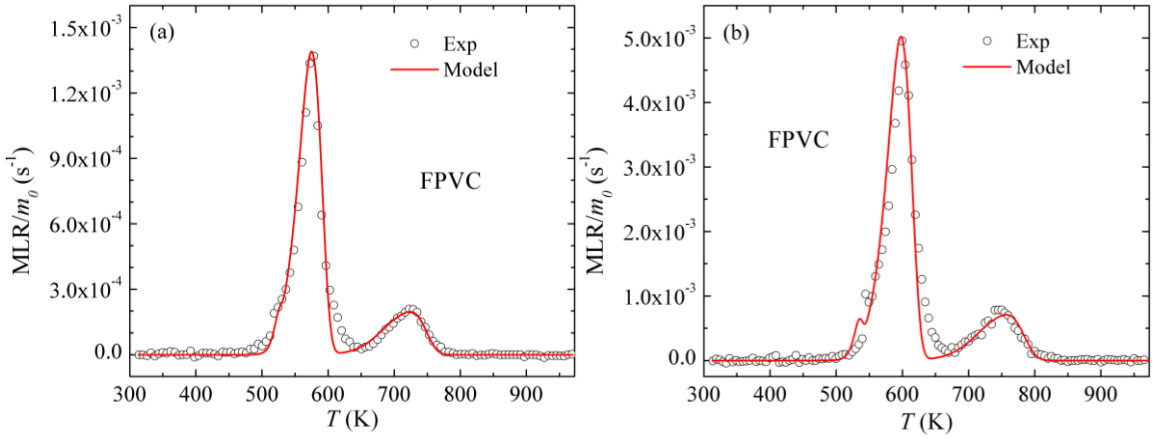

Figure 4.7: Averaged experimental and modeled normalized MLR data for FPVC thermal decomposition at nominal heating rates of (a) 5 and (b) 20 K min^{-1}.

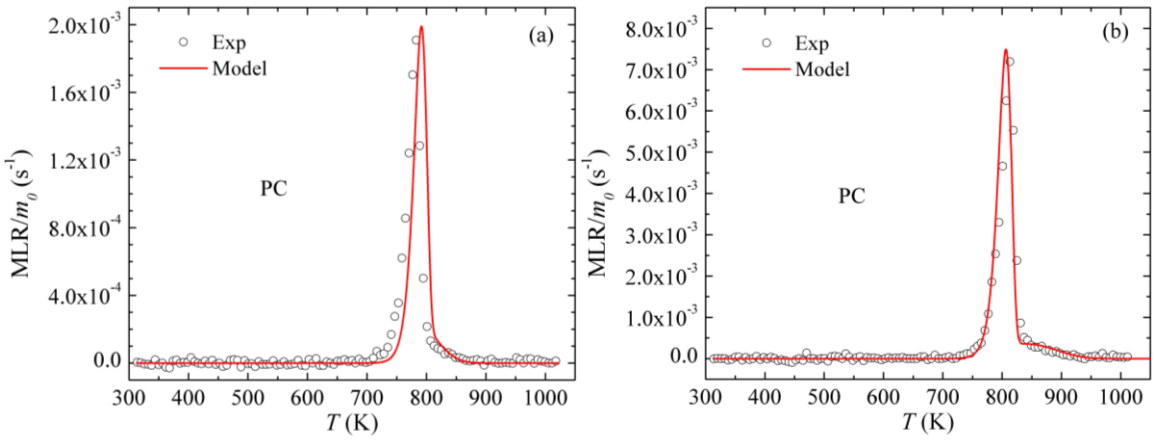

Figure 4.8: Averaged experimental and modeled normalized MLR data for PC thermal decomposition at nominal heating rates of (a) 5 and (b) 20 K min^{-1}.

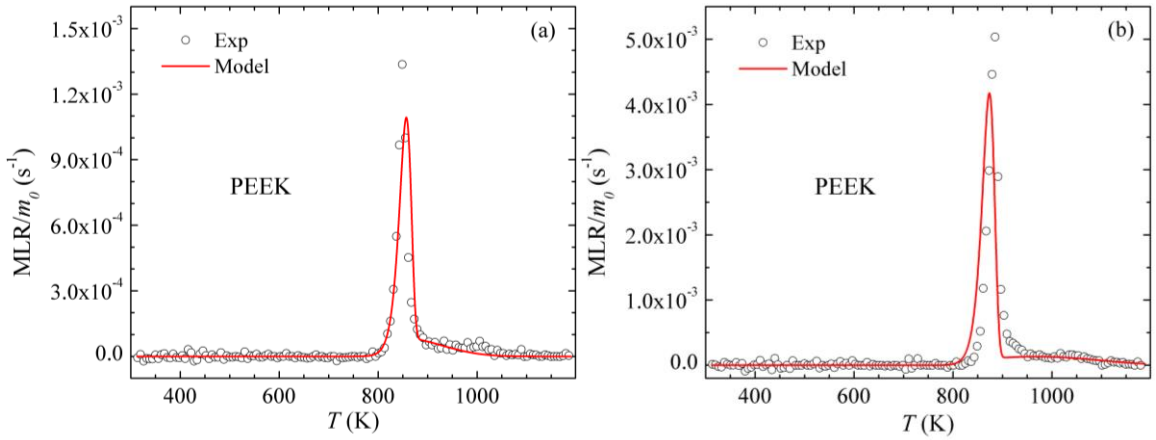

Figure 4.9: Averaged experimental and modeled normalized MLR data for PEEK thermal decomposition at nominal heating rates of (a) 5 and (b) 20 K min^{-1}.

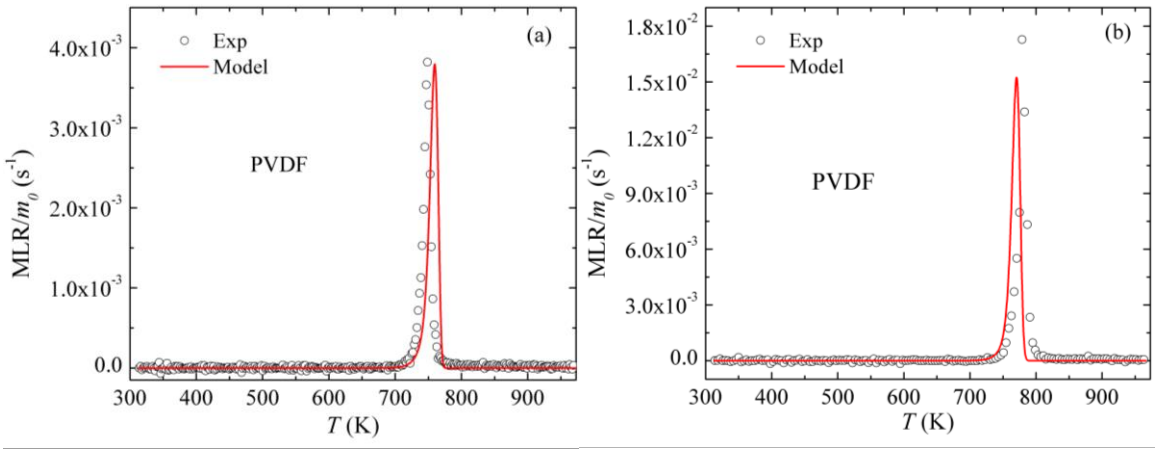

Figure 4.10: Averaged experimental and modeled normalized MLR data for PVDF thermal decomposition at nominal heating rates of (a) 5 and (b) 20 K min^{-1}.

4.2: DSC: Heat Capacity and Thermodynamics of Thermal Decomposition

The average DSC data of PVC, FPVC, PC, PEEK, and PVDF experiments are shown as symbols in Figures 4.11 – 4.15. The heat flow to the sample and integral heat flow, both normalized by the initial mass, are presented as a function of temperature. The integral heat flow to the sample was computed as the summation of all heat flow to/from the thermally decomposing sample. Here, positive values of heat flow indicate endothermic processes. The DSC data are the average of 10 repeated experiments. All error bars were computed from the scatter of the data as two standard deviations of the mean.

Utilizing the fully parameterized kinetics of thermal decomposition model as the basis, inverse analysis of the DSC experimental data was conducted to obtain heat capacities and heats of reaction for each component and reaction, respectively, in the modeling scheme. All DSC experiments, performed in tandem with TGA, were conducted at a nominal heating rate of 10 K min^{-1}. The DSC heat flow data were mathematically represented as shown in Equation 4.3.

$$\frac{\dot{q}}{m_0} = \sum_{j=1}^{N} \frac{V}{m_0} \xi_j c_j \frac{\partial T}{\partial t} + \sum_{i=1}^{N_r} \frac{V}{m_0} r_i h_i \tag{4.3}$$

where $\dot{q}$ is the total heat flow to the sample and m_0 is the initial mass of the reactant. N is the number of components, V is the total sample volume, ξ_j is the concentration of the j-th component, c_j is the specific heat capacity of the j-th component, and $\partial T/\partial t$ is the nominal STA heating rate. N_r is the number of reactants, r_i is the reaction rate of the i-th component, and h_i is the heat of reaction for the i-th component.

The DSC inverse analysis procedure was divided into two main sections: the first section consisted of computing the sensible enthalpy baseline and the second section involved calculating the heat flow associated with reactions and physical transitions. The first term on the right-hand-side of Equation 4.3 represents the sensible enthalpy baseline. In the absence of chemical reactions taking place, the sensible enthalpy baseline was used to approximate the heat flow into the decomposing sample. The second term on the right-hand-side of Equation 4.3 represents the heat absorbed or released (endothermic or exothermic) because of one or more chemical reactions occurring within the decomposing material.

The normalized heat flow curve of PVC decomposition, presented in Figure 4.11, contains several distinct maxima that closely correspond to those observed in the MLR profile. The first local maximum, however, occurred at approximately 350 K, which corresponded to the glass transition temperature of PVC [107]. This glass transition took place prior to any observed mass loss. The next maximum, occurring at 575 K, represented

the first stage of thermal decomposition of the polymer. The last maximum, occurring at approximately 750 K, represented the second stage of thermal decomposition of PVC.

The heat flow data were analyzed by first focusing on the regions not associated with thermal decomposition. The data corresponding to these regions were divided by the DSC experimental instantaneous heating rate and fitted with linear functions representing heat capacities of the corresponding condensed-phase components. The heat flow data between 313 – 350 K and 350 – 500 K were used to determine the heat capacities of PVC and PVC_GT components representing the polymer before and after its glass transition [107]. PVC Reaction 1 (see Table 4.1) was added to the mechanism during the DSC inverse analysis to simulate this glass transition. The heat capacity of PVC_Res1 was assumed identical to PVC_GT. The heat capacity of PVC_CHAR was computed from independent DSC measurements conducted on the final fully decomposed residue, as described in section 2.2.1. It was assumed that the heat capacity of PVC_Res4 was identical to PVC_CHAR since they occur in a very similar temperature range. The heat capacity of the remaining intermediate condensed-phase components (PVC_Res2 and PVC_Res3) were assumed identical and equal to the average heat capacity of PVC_GT and PVC_CHAR. All heat capacity values are listed in Table 4.2.

The sensible heat flow baseline was subsequently calculated as a product of the mass fractions of condensed-phase components (whose temporal evolution was computed by ThermaKin2Ds), corresponding heat capacities, and the instantaneous heating rate. The baseline obtained for PVC is shown as a dashed line in Figure 4.11(a). Subtraction of this baseline from the normalized experimental heat flow and subsequent integration of the

differences yielded the values of the heats of decomposition, *h*. The heats of decomposition were subsequently refined until the simulated heat flow maxima were within 10%, temperatures of the maxima were within 8 K, and the final integral heat flow value was within 5% of the corresponding experimental data. The results of the PVC model, capturing the thermodynamics of thermal decomposition, are shown as solid lines in Figure 4.11. The resulting heats of all decomposition reactions are listed in Table 4.1. It was found that both endothermic and exothermic reactions were required to adequately capture the experimental data; endothermic processes, however, were the most dominant.

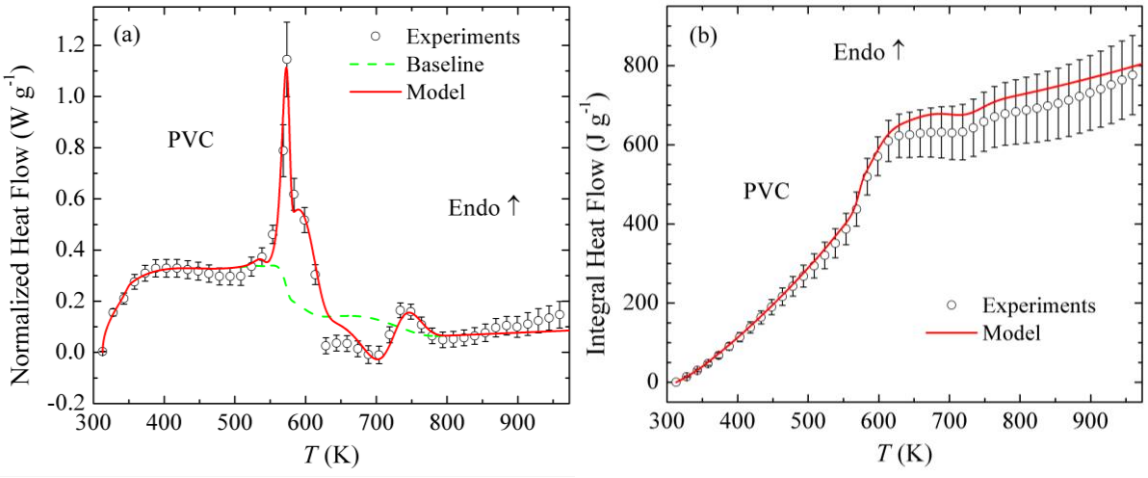

Figure 4.11: Experimental and modeled normalized (a) heat flow and (b) integral heat flow to the PVC sample during thermal decomposition at a heating rate of 10 K min^{-1}.

Table 4.2: Heat capacities of condensed-phase components for PVC, FPVC, PC, PEEK, and PVDF thermal decomposition.

Component	c (J kg^{-1} K^{-1})	Component	c (J kg^{-1} K^{-1})
PVC	-2259 + 10.0T	PVC_Res3	-456 + 3.85T
PVC_GT	-37 + 4.0T	PVC_Res4	-875 + 3.7T
PVC_Res1	-37 + 4.0T	PVC_CHAR	-875 + 3.7T
PVC_Res2	-456 + 3.85T		
FPVC	-221 + 5.1T	FPVC_Res3	1700
FPVC_Res1	739.5 + 2.55T	FPVC_CHAR	1700
FPVC_Res2	739.5 + 2.55T		
PC	-294 + 4.1T	PC_Res1	87 + 1.5 T
PC_GT	675 + 2.4T	PC_CHAR	87 + 1.5T
PEEK	-350 + 4T	PEEK_Res1	632.5 + 2.35T
PEEK_M	1235 + 1.7T	PEEK_CHAR	30 + 3T
PVDF	-673 + 5.8 T	PVDF_Res1	179 + 0.4T
PVDF_M	726.7 + 2.1T	PVDF_CHAR	179 + 0.4T

The normalized heat flow data of FPVC thermal decomposition presented several distinct features in the experimental dataset, as shown in Figure 4.12. The first notable maximum, occurring at approximately 575 K, represented the first stage of thermal decomposition. The second maximum, occurring at approximately 750 K, represented the second distinct step in the thermal decomposition of FPVC. The glass transition, as shown in the rigid PVC data, was not observed for FPVC. Therefore, the FPVC reaction scheme, as shown in Table 4.1, employs four reactions to describe the kinetics and thermodynamics of thermal decomposition.

The heat flow data were analyzed by first focusing on the regions not associated with melting or decomposition using an identical methodology described in detail for rigid PVC. The heat flow data between 313 and 500 K were used to determine the heat capacity of undecomposed FPVC. Due to the small residual char yield (6.4 wt. %) eliminating the feasibility of independent DSC experiments, the heat capacity of FPVC_CHAR was prescribed to be the average heat capacity of chars generated by several representative charring polymers [39]. It was assumed that the heat capacity of FPVC_Res3 was identical to FPVC_CHAR due to the reaction occurring at a similar temperature range. It is believed that the constant heat capacity for the FPVC_Res3 and FPVC_CHAR is responsible for the model slightly under-predicting the heat flow at high temperatures, as shown in Figure 4.12. The heat capacity of the remaining intermediate condensed-phase products (FPVC_Res1 and FPVC_Res2) were assumed identical and equal to the average heat capacity of FPVC and FPVC_ CHAR to reduce the number of independently adjustable parameters. All heat capacity values associated with FPVC thermal decomposition are listed in Table 4.2.

The sensible heat flow baseline was subsequently calculated for FPVC and is shown as a dotted line in Figure 4.12(a). The resulting heats of reaction of FPVC thermal decomposition, estimated through an identical inverse analysis methodology employed for rigid PVC, are shown as solid lines in Figure 4.12. The heats of decomposition, as listed in Table 4.1, are all endothermic processes.

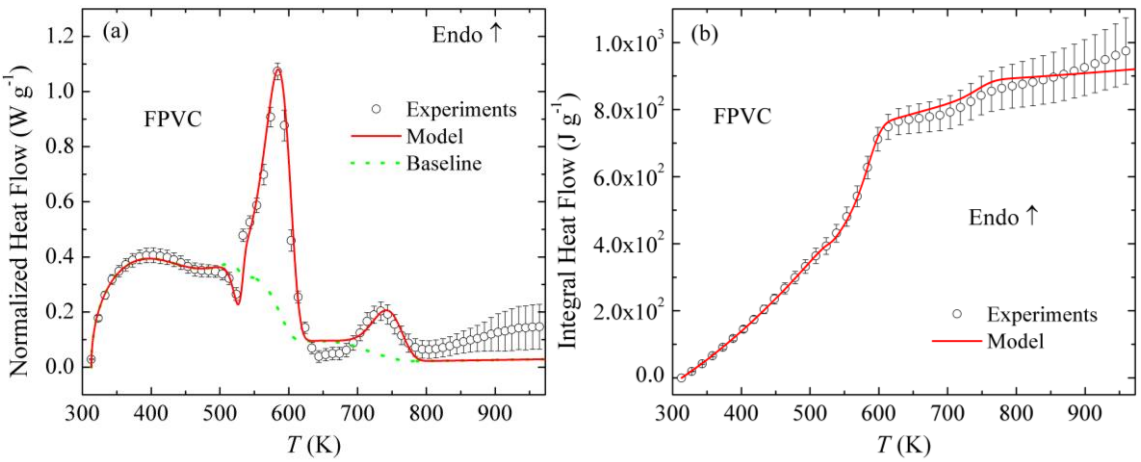

Figure 4.12: Experimental and modeled normalized (a) heat flow and (b) integral heat flow to FPVC during thermal decomposition at a nominal heating rate of 10 K min^{-1}.

The normalized heat flow data of PC decomposition are shown in Figure 4.13 to display several distinct features in the experimental dataset, which closely correspond to the MLR profile. The first notable maximum, occurring at approximately 420 K, is associated with the melting process of PC. The second maximum (750 K), occurring just prior to a sharp decrease in heat flow, represented the first step in the thermal decomposition of PC. A small secondary exothermic reaction was observed to occur consecutively immediately following the primary reaction. The PC reaction scheme, as shown in Table 4.1, employed three reactions to describe the kinetics and thermodynamics of PC thermal decomposition.

The heat flow data were analyzed using the same process described for both rigid PVC and FPVC. The heat flow data below the melting point (420 K) were used to determine the heat capacity of the undecomposed PC. The heat capacity of the component after the glass transition (PC_GT) was estimated prior to any incurred mass loss. Independent DSC experiments were employed to determine the heat capacity of the

PC_CHAR component with data carefully resolved from 400 – 700 K. It was assumed that the heat capacity of the intermediate component, PC_Res1, was identical to PC_CHAR due to the reaction occurring at a similar temperature range. All heat capacity values associated with PC thermal decomposition are provided in Table 4.2.The sensible heat flow baseline was subsequently calculated for PC thermal decomposition and is shown as a dotted line in Figure 4.13(a). The resulting heats of reaction of PC thermal decomposition, estimated through an identical inverse analysis methodology employed for both rigid PVC and FPVC, are provided in Table 4.1. It was found that the PC decomposition reactions consume or produce negligible heat flow, as indicated by the small heats of reaction. The resulting model predicted heat flow and integral heat flow are shown as solid lines in Figure 4.13. The large discrepancies observed in the high temperature region of the dataset was attributed to the reduced sensitivity of the DSC instrumentation. The independent DSC measurements of the PC_CHAR component heat flow provided a means to accurately parameterize the heat capacity of the PC_CHAR component, therefore providing confidence in the accuracy of the model.

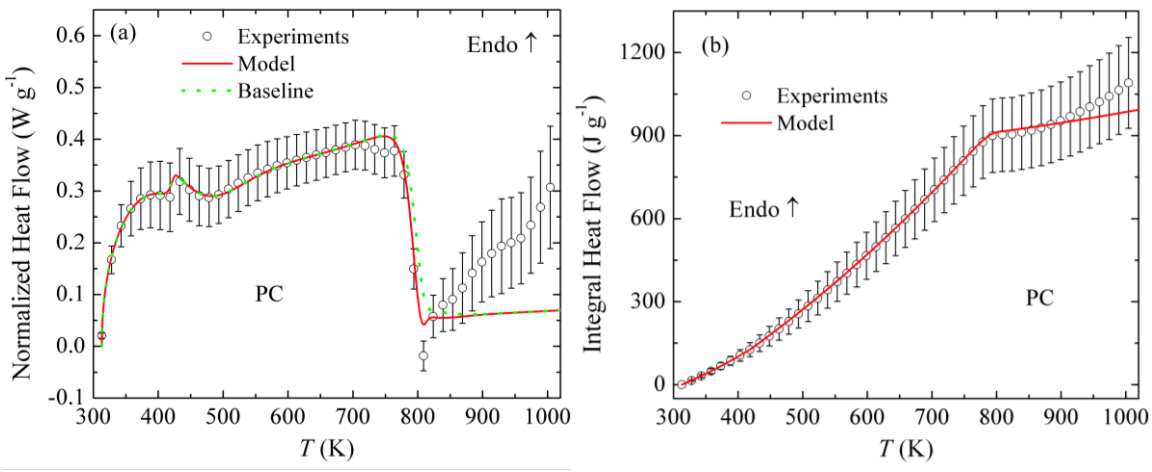

Figure 4.13: Experimental and modeled normalized (a) heat flow and (b) integral heat flow to PC during thermal decomposition at a nominal heating rate of 10 K min^{-1}.

The normalized heat flow data of PEEK thermal decomposition presented several distinct features in the experimental dataset, as shown in Figure 4.14. All experimental maxima were shown to closely correspond to the MLR profile. The first notable maximum, occurring at approximately 610 K, represented the endothermic melting process of PEEK thermal decomposition. A notable exothermic peak was observed at approximately 860 K and was related to mass loss. A small secondary exothermic reaction occurred in the temperature range of 900 – 1100 K, which was also associated with a mass loss reaction. The reaction scheme for PEEK thermal decomposition, as shown in Table 4.1, employed three reactions to describe the kinetics of thermal decomposition as well the endothermic and exothermic heat flow processes. The observed overall exothermicity of PEEK thermal decomposition was attributed to the substantial residual char yield. It was found in a previous study [39] that the relationship between the exothermic decomposition and a high char yield can be explained by the high thermodynamic stability of the resulting carbonaceous char. It was found that when a high char yield was produced, the

thermodynamic stability of the polymer char compensated for an increase in enthalpy associated with the formulation of small molecular mass volatiles.

The PEEK heat flow data were analyzed by first focusing on the regions not associated with thermal decomposition. The heat flow data between 313 – 475 K and 525 – 800 K were used to determine the heat capacities of PEEK and PEEK_M components representing the polymer before and after its melting process. The first reaction in the PEEK thermal decomposition reaction mechanism, shown in Table 4.1, was added during the DSC inverse analysis to simulate this melting process. The heat capacity of PVC_CHAR was computed from independent DSC measurements conducted on the final fully decomposed residue in a temperature range of 500 – 900 K. The intermediate component (PEEK_Res1) was estimated to be an average of the PEEK_M and PEEK_CHAR heat capacities. All PEEK heat capacity values are listed in Table 4.2.

The sensible heat flow baseline was subsequently calculated for PEEK decomposition and is shown as a dotted line in Figure 4.14(a). The resulting heats of reaction of PEEK thermal decomposition, estimated through an identical inverse analysis methodology employed for both PVC and PC, are presented in Table 4.1. The resulting model predicted heat flow and integral heat flow shown as solid lines in Figure 4.14. PEEK was found to be much more thermally stable than other materials investigated in this study due to the substantially higher residual char yield.

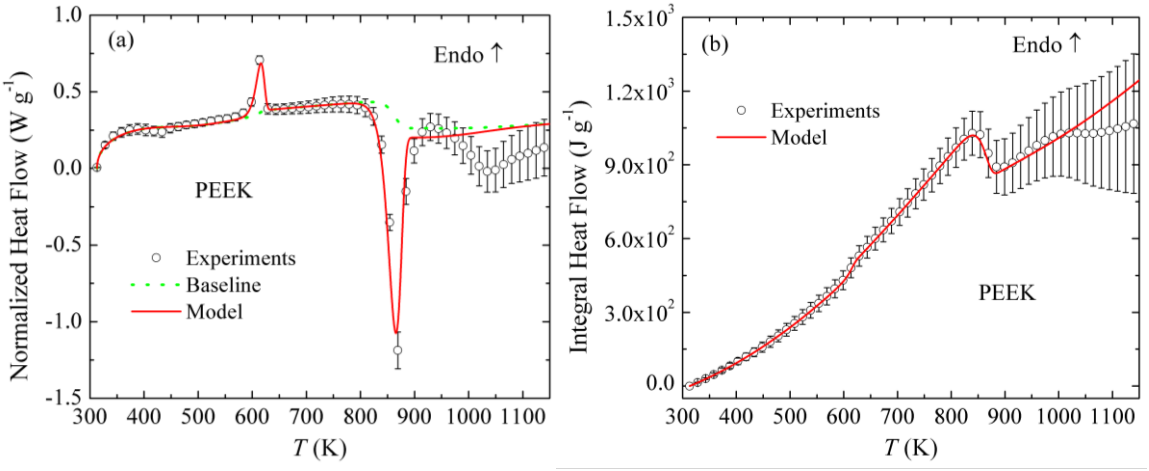

Figure 4.14: Experimental and modeled normalized (a) heat flow and (b) integral heat flow to/from PEEK during thermal decomposition at a heating rate of 10 K min^{-1}.

The normalized heat flow data of PVDF decomposition are shown in Figure 4.15. The first maximum was associated with the melting process of PVDF, which was found to be at approximately 450 K. A second peak in the heat flow profile was observed to occur at approximately 750 K, which was related to an endothermic reaction resulting from mass loss, and was immediately followed by an exothermic reaction. In the case of PVDF, a unique phenomenon was observed where the heat flow drastically transitioned from an endothermic to an exothermic regime. Traditionally, most polymers are predominantly endothermic in nature during thermal decomposition (with the exception of those which produce a substantial char yield, as discussed with PEEK); however, PVDF demonstrated a split between endothermic and exothermic behavior. The PVDF reaction scheme, as shown in Table 4.1, employed three reactions to describe the kinetics as well as the endothermic and exothermic processes associated with PVDF thermal decomposition.

The heat flow data between 313 – 425 K and 475 – 700 K were used to determine the heat capacities of the undecomposed (PVDF) and melt (PVDF_M) components,

representing the polymer before and after its melting temperature; this temperature transition was captured by the introduction of PVDF Reaction 1, as shown in Table 4.1. The heat capacity of PVC_CHAR was computed from independent DSC measurements conducted on the final fully decomposed residue in a temperature range of 460 – 750 K. The heat capacity of PVDF_Res1 was assumed equal to the heat capacity of the final residual component (PVDF_CHAR). All PVDF heat capacity values are listed in Table 4.2. The sensible heat flow baseline was subsequently calculated for PVDF and is shown as a dotted line in Figure 4.15(a). The heat flow predictions of PVDF thermal decomposition are shown in Table 4.1. The resulting simulations are shown to capture both the endothermic and exothermic processes as solid lines in Figure 4.15.

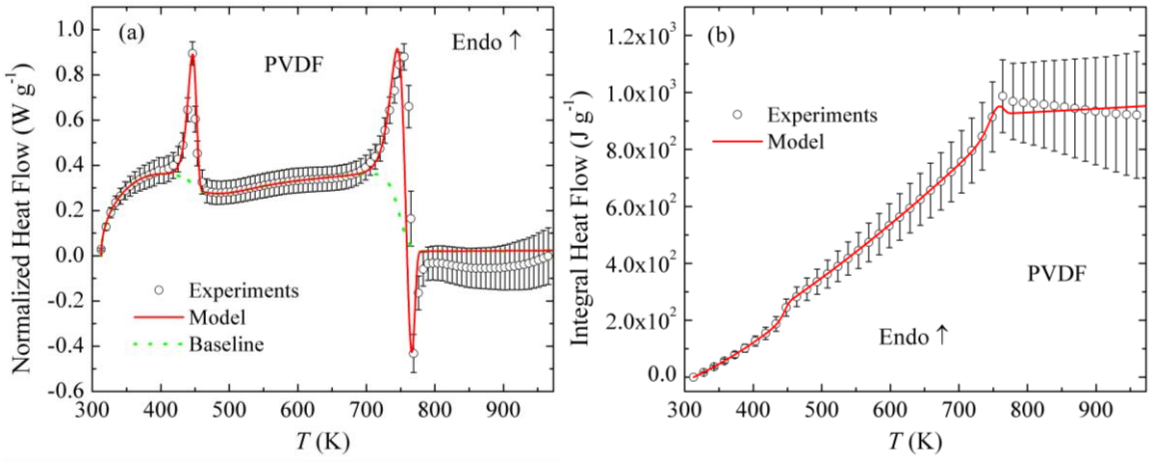

Figure 4.15: Experimental and modeled normalized (a) heat flow and (b) integral heat flow to/from PVDF during thermal decomposition at a heating rate of 10 K min^{-1}.

The heat capacities determined above for all the materials are strictly for condensed phase components. Therefore, it is important to prescribe heat capacities for the gaseous products of thermal decomposition. The heat capacity of all gaseous decomposition products were assumed equal to 2100 J kg^{-1} K^{-1}, which was the mean heat capacities of a

collection of C1 to C8 hydrocarbons at a temperature of 600 K [108]. It was found that varying the heat capacity of gaseous products had negligible impact on the modeling results.

4.3: MCC: Heats of Complete Combustion of Volatile Gases Evolved from Thermal Decomposition

The mean experimental HRR and total heat release (THR) data obtained for PVC, FPVC, PC, PEEK, and PVDF combustion, determined through the oxygen consumption principle in the MCC tests, are presented as a function of sample temperature in Figures 4.16 – 4.20. Both values were normalized by the initial sample mass. The heats of complete combustion, h_{comb}, of gaseous components defined in the reaction mechanism (summarized in Table 4.1) were determined through simulation of the MCC data. MLR profiles were simulated employing heating rate histories specific to the MCC as well as the previously determined reaction mechanism and associated parameters from the STA inverse analysis. HRR is directly related to MLR through the heat of combustion, as shown in Equation 4.4.

$$HRR_{total} = \sum_{i=1}^{N} h_{comb,i} MLR_i \tag{4.4}$$

where HRR_{total} is the total heat release rate. N is the number of gaseous components, $h_{comb,i}$ denotes the heat of complete combustion of the *i*-th gaseous product, and MLR_i is the time-temperature dependent mass loss rate of the *i*-th gaseous product of decomposition.

Initial comparisons between the experimental HRR and modeled MLR profiles, generated using the heating rate history specific to the MCC, revealed some discrepancies.

These inconsistencies were identified through a recognition that any significant heat release should require a concurrent mass loss. These discrepancies were attributed to sample temperature deviations measured by the MCC sensor and were corrected by shifting the experimental curves to a slightly higher temperature, as depicted by dashed lines in Figures 4.16 – 4.20. The magnitude of the temperature shift in the HRR profiles for PC, PEEK, and PVDF (not shown to improve readability of the figures) were 6, 5, and 8.5 K, respectively.

The heats of combustion were first estimated by dividing the shifted experimental HRR data by the rate of production of gaseous components computed by ThermaKin2Ds (consistent with Equation 4.4). A simulated HRR curve was subsequently generated using the estimated h_{comb} values. The values of h_{comb} were further refined until the simulated and experimental HRR and THR data agreed within established MCC criteria. The criteria were defined as differences of less than 8% between the heights of the experimental and modeled HRR maxima, less than 10 K between the temperatures of the maxima, and less than 8% between the final integral HRR values. The determined values for the heats of complete combustion of all materials studied in this work were within a similar range based on a previous extensive study conducted on numerous polymers [109]. The resulting heats of complete combustion are given in Table 4.3. The MCC data simulated using these heats of combustion are shown for PVC, FPVC, PC, PEEK, and PVDF as solid lines in Figures 4.16 – 4.20, respectively. The resulting HRR predictions for all materials were captured well by the models developed through inverse analysis of STA and MCC data.

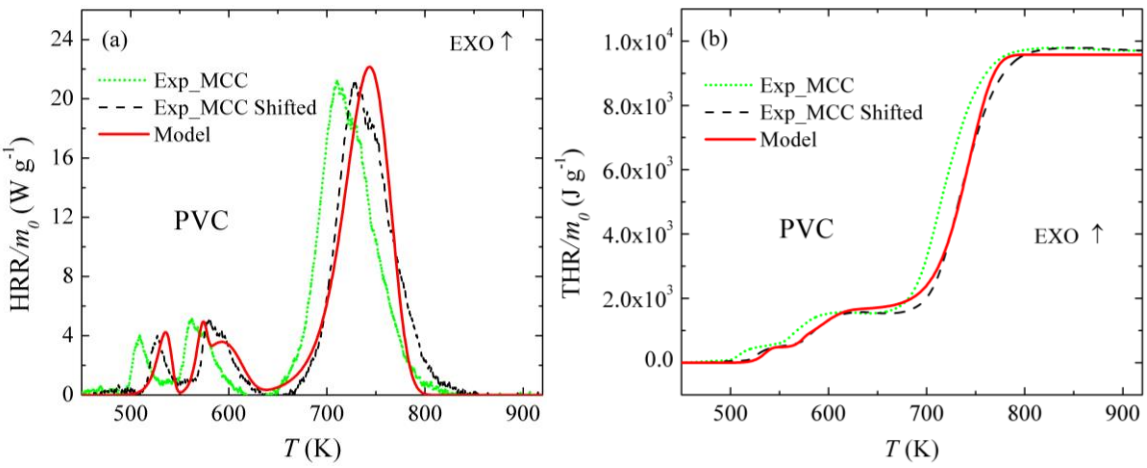

Figure 4.16: Mean experimental and simulated normalized (a) heat release rate and (b) total heat release data from MCC tests of PVC at 10 K min^{-1}.

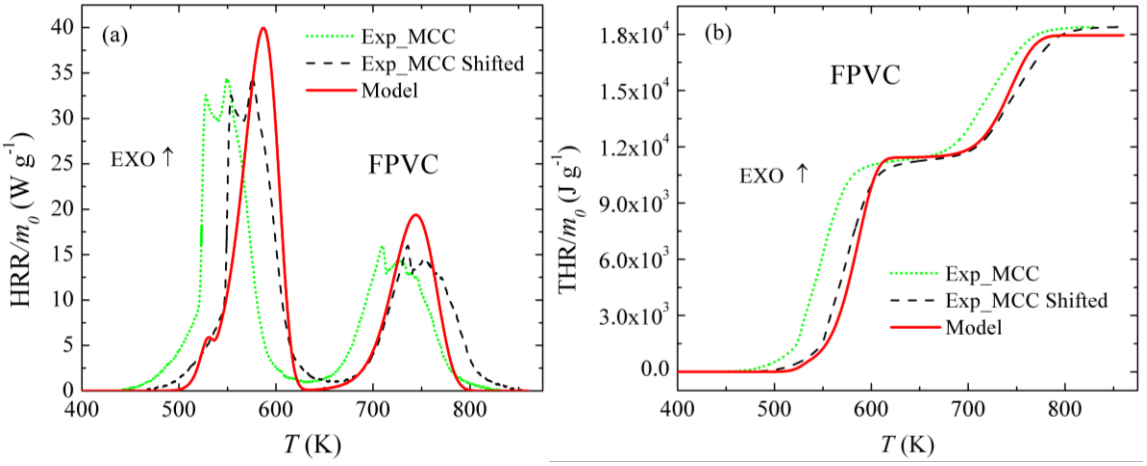

Figure 4.17: Mean experimental and simulated normalized (a) heat release rate and (b) total heat release data from MCC tests of FPVC at 10 K min^{-1}.

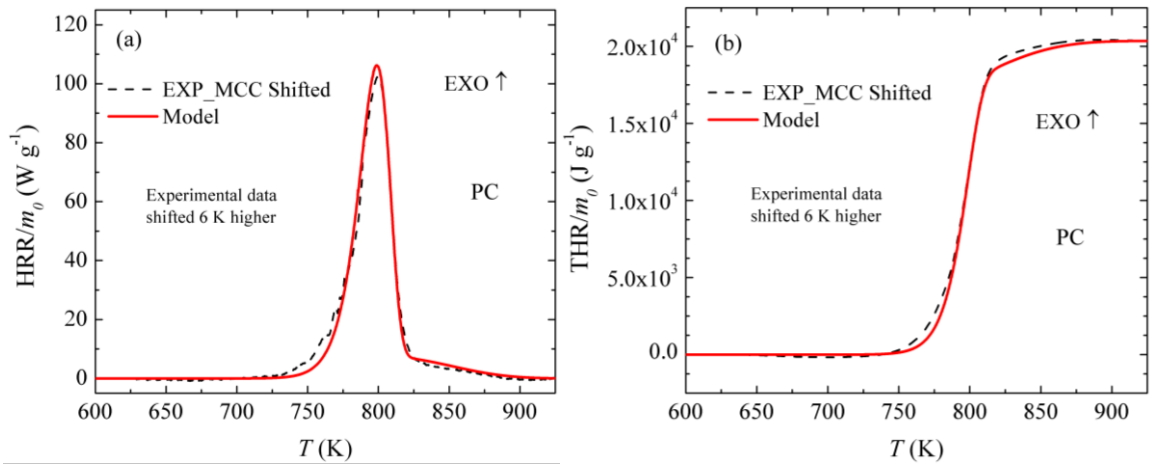

Figure 4.18: Mean experimental (shifted 6 K higher) and simulated normalized (a) heat release rate and (b) total heat release from MCC tests on PC at 10 K min^{-1}.

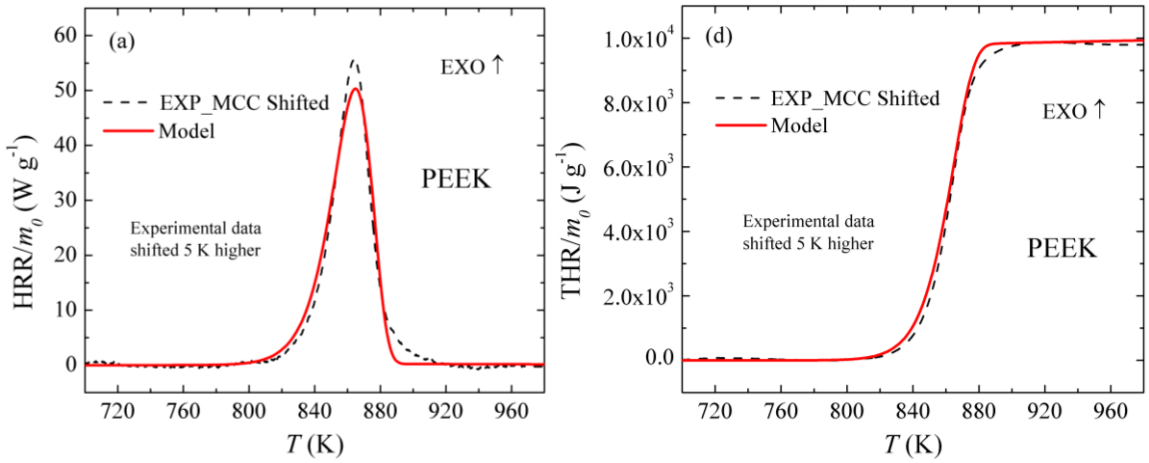

Figure 4.19: Mean experimental (shifted 5 K higher) and simulated normalized (a) heat release rate and (b) total heat release from MCC tests on PEEK at 10 K min^{-1}.

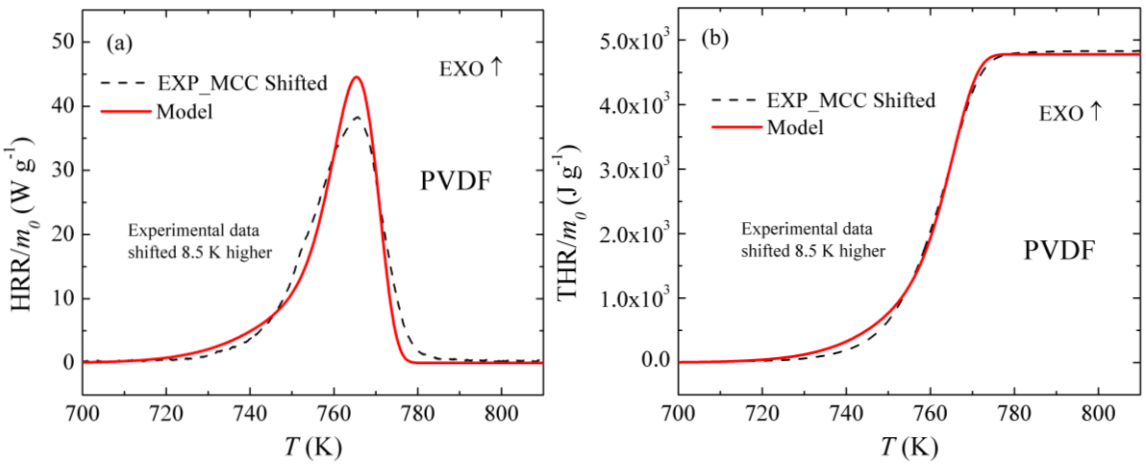

Figure 4.20: Mean experimental (shifted 8.5 K higher) and simulated normalized (a) heat release rate and (b) total heat release from MCC tests on PVDF at 10 K min^{-1}.

Table 4.3: Heats of complete combustion of PVC, FPVC, PC, PEEK, and PVDF gaseous decomposition products (positives values represent exothermic processes).

Component	h_{comb} **(J kg^{-1})**	**Component**	h_{comb} **(J kg^{-1})**
PVC_Gas1	1.20×10^{7}	PVC_Gas4	1.80×10^{7}
PVC_Gas2	1.30×10^{6}	PVC_Gas5	3.65×10^{7}
PVC_Gas3	2.80×10^{6}		
FPVC_Gas1	9.50×10^{6}	FPVC_Gas3	3.65×10^{7}
FPVC_Gas2	1.62×10^{7}	FPVC_Gas4	4.42×10^{7}
PC_Gas1	2.75×10^{7}	PC_Gas2	2.75×10^{7}
PEEK_Gas1	2.45×10^{7}	PEEK_Gas2	2.00×10^{6}
PVDF_Gas1	1.80×10^{7}	PVDF_Gas2	5.52×10^{6}

Chapter 5: Gram-scale Results and Analysis

In-depth radiation absorption measurements and CAPA II gasification experiments were conducted on PVC, FPVC, PC, PEEK, and PVDF gram-sized samples. All radiation absorption measurements were conducted in duplicate at a single heater setting (for each material) in accordance with section 2.3.1. In the gasification experiments, each material was subjected to a minimum of two incident heat fluxes which represented a range of thermal exposure. The lower incident heat flux set point was chosen to capture a relatively slow rate of pyrolysis of each material to obtain fully resolved experimental data while the higher heat flux was chosen to better represent real fire like conditions. All CAPA II experiments were conducted in accordance with the methodology detailed in section 2.3.2.

Building upon the milligram-scale model of the kinetics and thermodynamics of thermal decomposition, ThermaKin2Ds simulations were expanded to emulate the CAPA II experiments by incorporating all relevant boundary conditions (see section 3.4.2) and adequately accounting for thermal transport within the decomposing polymers and developing char. The optical properties (emissivity and absorption coefficients) of the undecomposed material and final residual char are discussed in section 5.1. The density and thermal conductivity of each component were parameterized through a manually iterative inverse analysis procedure utilizing the sample shape profiles and bottom temperature histories, respectively, as fitting targets. The density of all gaseous products were defined not to contribute to the volume of solid samples. Finally, the modeled MLR results were compared to mean experimental MLR data for model validation. A

methodology to construct the simplest model possible (fewest independent parameters) while also capturing the experimental data within the accuracy of the instrumentation was adopted in the model development process.

5.1: Absorption Coefficient Measurements

Analysis of the gram-scale experiments required knowledge of the optical properties (emissivity (ε) and absorption coefficients (κ)) of all the components *a priori*; therefore, a summary is provided. In an effort to simplify the model development and reduce the number of adjustable parameters, the emissivity and absorption coefficient values were grouped (assigned identical values). This grouping process was similar to that used in the heat capacity characterization; however, the specific details will be described for each material in later sections of this chapter. The initial emissivity of all materials were obtained from literature [110], as presented in Table 5.1.

The emissivity of the final residual condensed-phase char was estimated from independent experiments described in Section 2.3.2. The bottom surface temperature of these experiments were analyzed on both the painted and unpainted halves of the char sample. It was found that the temperature profiles were nearly indistinguishable; therefore, it was assumed that the char emissivity was identical to that of the high emissivity paint (0.94). In general, the emissivity of all intermediate species were assigned in relation to either the virgin material or the final char component; a detailed description of the intermediate emissivity values will be discussed for each material in the following sections of this chapter.

The in-depth absorption coefficient (κ) was estimated based on the approach discussed in section 2.3.1 using Equation 2.1 and Equation 2.2. Two samples of each material were carefully machined to a uniform thickness (δ_κ) of approximately 1.0×10^{-3} m, as shown in Table 5.1. The respective fraction of radiation absorbed by the samples, $\tau_{0,}$ is also presented based on Equation 2.2. It is important to note that all absorption coefficient values are normalized by the density of the undecomposed sample at ambient temperature. The upper char layer was observed to appear very optically dark and graphitic in nature. Therefore, the absorption coefficient of char for all materials was defined sufficiently high (100 m^2 kg^{-1}) such that all the radiation was absorbed at the top surface. The in-depth radiation absorption coefficients for the undecomposed component of all material are defined in Table 5.1. The uncertainties in the absorption coefficient measurements were assigned a value of approximately 20% based on the scatter of the experimental data collected in a previous study [55].

Table 5.1: Emissivity, density, and in-depth radiation absorption coefficients for all studied polymers at ambient conditions. δ_κ represents the thickness of the sample utilized for the absorption coefficient measurements.

Material	ε **(-)**	δ_κ **(m)**	τ_0 **(-)**	ρ **(kg m^{-3})**	κ **(m^2 kg^{-1})**
PVC	0.90 [110]	8.76×10^{-4}	96.5	1409	2.6 ± 0.5
FPVC	0.90 [110]	1.23×10^{-3}	83.4	1226	1.1 ± 0.2
PC	0.89 [110]	1.02×10^{-3}	83.3	1187	1.3 ± 0.3
PEEK	0.90 [110]	1.02×10^{-3}	90.8	1297	1.6 ± 0.3
PVDF	0.94 [110]	1.07×10^{-3}	83.7	1791	0.9 ± 0.2

5.2: Inverse Analysis of Rigid Poly(vinyl chloride) Gasification Experiments

This section details the development of the PVC pyrolysis models. Duplicate CAPA II gasification experiments were conducted on PVC samples at a set point heat flux of 40, 60, and 80 kW m^{-2}. The model construction involved analyzing the experimental data with both a 1D pyrolysis model representing the spatially averaged decomposition behavior and a 2D axisymmetric model capable of emulating the observed non-one-dimensional experimental conditions. In both instances, the milligram-scale model for the kinetics and thermodynamics of thermal decomposition remained identical and served as the foundational framework. The prescribed component emissivity and in-depth radiation absorption coefficient values were unchanged between the 1D and 2D models.

The emissivity of the virgin PVC was obtained from literature [110] and found to be 0.90. PVC_GT and PVC_RES1 were assumed to have the same emissivity as PVC since little decomposition had taken place. As discussed earlier, the emissivity value for the fully developed char component (PVC_CHAR) was estimated to be 0.94; PVC_RES4 was prescribed the same emissivity value as PVC_CHAR. The remaining intermediate components, PVC_RES2 and PVC_RES3, were prescribed as the average emissivity of PVC and PVC_CHAR. The emissivity of all PVC condensed-phase components are shown in Table 5.2.

The in-depth radiation absorption coefficients for PVC and PVC_CHAR, as discussed previously, are provided in Table 5.2. PVC_GT and PVC_RES1 were assumed equal and identical to the absorption coefficient of the undecomposed PVC component. The absorption coefficient for PVC_RES2 and PVC_RES3 was assigned to be the average

value of PVC and PVC_CHAR. The in-depth radiation absorption coefficients for all condensed-phase components are defined in Table 5.2.

Table 5.2: Emissivity and absorption coefficients of all condensed phase components of PVC pyrolysis.

Component	ε	κ **(m^2 kg^{-1})**
PVC	0.90	2.6
PVC_GT	0.90	2.6
PVC_Res1	0.90	2.6
PVC_Res2	0.92	51.3
PVC_Res3	0.92	51.3
PVC_Res4	0.94	100
PVC_CHAR	0.94	100

The experimental CAPA II data for PVC pyrolysis at a nominal heat flux of 60 kW m^{-2} are shown in Figures 5.1 and 5.2. Figure 5.1 provides representative sample shape profiles as a function of time. The bottom surface temperature (T_{bottom}) histories of the center and edge of the sample are presented as symbols in Figure 5.2(a). The temperatures at additional radial positions were found to be similar to the center and edge of the sample, therefore, intermediate radial temperature data are not shown to make the figure more readable. The mean experimental MLR data, normalized by the initial top surface area of the sample, are shown in Figure 5.2(b). The 1D and 2D modeling results shown on these figures are discussed in Section 5.2.1 and 5.2.2, respectively.

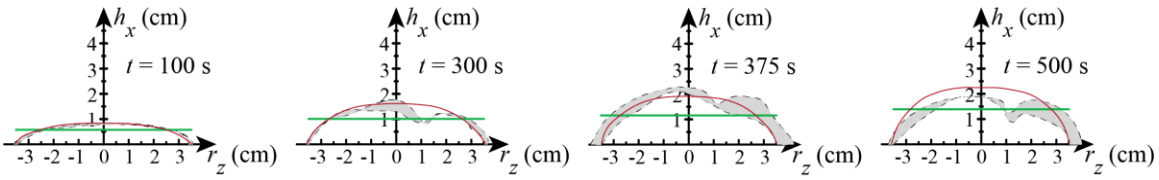

Figure 5.1: The black dashed lines are experimental shape profiles extending above the initial sample top surface from duplicate PVC (6.15×10^{-3} m thick) tests at 60 kW m^{-2}. The gray shaded area indicates the sample profile uncertainty. The straight and curved solid lines represent 1D and 2D model predictions, respectively.

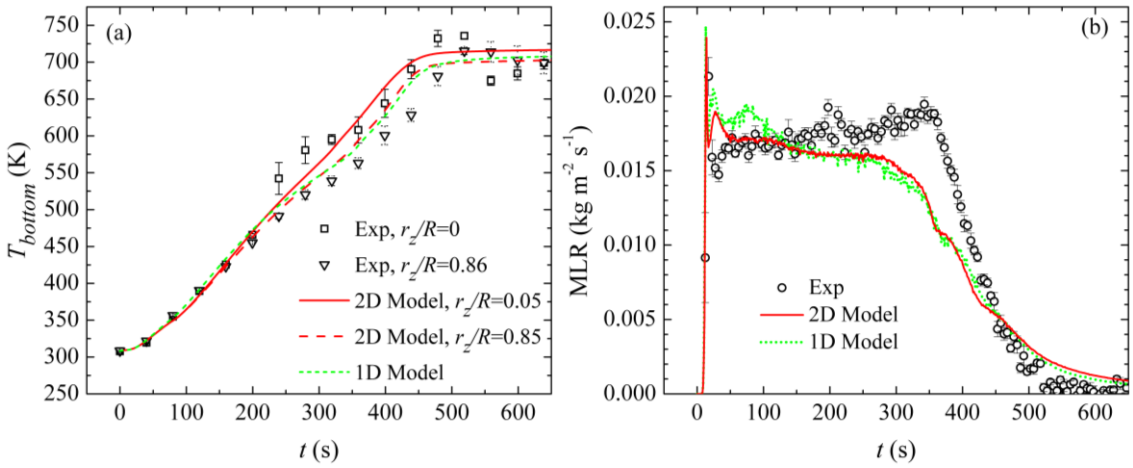

Figure 5.2: Experimental and simulated (a) bottom surface temperature and (b) MLR data from rigid PVC (6.15×10^{-3} m thick) gasification experiments conducted at 60 kW m^{-2}.

Figure 5.1 shows that the sample's swelling process included a simultaneous increase in thickness and reduction in diameter. The diameter reduction was subtle and became apparent only in late stages of pyrolysis. At 60 kW m^{-2}, the increase in thickness was essentially monotonic, except for a small recession in thickness at late stages of pyrolysis. The vertical distance axis for the shape profiles (h_x) begins at the initial position of the top sample surface. The dashed curves represent results of individual experiments. The shaded area between the curves is an indicator of the data's irreproducibility. The bottom surface temperature in Figure 5.2(a) appears to be spatially uniform in the early stages of pyrolysis. In later stages of pyrolysis, the temperature became non-uniform with the edge of the

surface being systematically cooler than the center. The MLR data in Figure 5.2(b) exhibited a subtle sharp peak at the beginning of the experiment, followed by a slow linearly increasing profile prior to the final decay when all mass loss had occurred.

5.2.1: Parameterization of a 1D Average Model of PVC Pyrolysis

The 1D model was parameterized using the parameters derived from milligram-scale experiments and optical properties (discussed in earlier sections) as the foundational framework. The condensed-phase component densities and thermal conductivities were categorized in several groupings and subsequently prescribed identical values to minimize the number of independently adjustable parameters. Therefore, this fully parameterized model was constructed with the fewest independently adjusted parameters while also capturing the essential features of the experimental data.

The sample shape profiles, as shown in Figure 5.1, provided a snapshot of the critical changes in the sample shape as a function of time. The intumescent (swelling) behavior of the PVC pyrolysis was captured numerically in ThermaKin2Ds by prescribing decreasing component densities. In the 1D model, the thickness of the sample expanded uniformly across the entire radius. Therefore, the average sample thickness was employed as a target value for the density parameterization. The densities were initially prescribed to maintain a constant volume throughout the decomposition process. Subsequently, the densities, in their respective groups, were adjusted through a manually iterative procedure such that the predicted sample thickness (solid straight line) captured the critical average shape changes in Figure 5.1. The resulting densities are provided in Table 5.3.

Table 5.3: Densities and thermal conductivities of condensed-phase components for the 1D model of rigid PVC pyrolysis.

Component	ρ **(kg m^{-3})**	k **(W m^{-1} K^{-1})**
PVC	1409	$0.13 + (0.8\times10^{-4})\,T$
PVC_GT	876	$0.13 + (1.6\times10^{-4})\,T$
PVC_Res1	841	$0.13 + (1.6\times10^{-4})\,T$
PVC_Res2	564	$0.13 + (2.4\times10^{-4})\,T$
PVC_Res3	321	$0.13 + (2.4\times10^{-4})\,T$
PVC_Res4	149	$0.13 + (3.2\times10^{-4})\,T + (1.3\times10^{-9})\,T^3$
PVC_CHAR	81	$0.13 + (3.2\times10^{-4})\,T + (1.3\times10^{-9})\,T^3$

The average bottom experimental temperatures were employed as target data for the inverse analysis. The thermal conductivity of each component was first defined as a constant value, to maintain the simplest model possible. However, it was identified that a constant thermal conductivity was unable to capture the temperature history of the sample. Therefore, further complexity was added through the introduction of an additional constant term multiplied by the third power of temperature. The third power of temperature is an approximation that captured the thermal transport within porous media through radiation diffusion [70]; therefore, this term was only introduced to PVC_Res4 and PVC_CHAR because it was only physically meaningful to apply to components that experience a high temperature and porous structure. Even with the introduction of this additional term, unsatisfactory results were obtained. Therefore, a linear temperature dependent term was added to the thermal conductivity values. The resulting bottom surface temperature predictions are shown as the dotted line in Figure 5.2(a). The final thermal conductivities are provided in Table 5.3. The average error between the spatially averaged experimental

and simulated bottom surface temperatures was found to be 1.7%. It is important to note that the density parameterization was dependent upon the thermal transport parameters; therefore, the density and thermal conductivity parameters were iteratively adjusted simultaneously until satisfactory results were obtained.

The MLR data at 60 kW m^{-2}, shown in Figure 5.2(b), were not utilized in the inverse analysis model calibration; therefore, this dataset served as a model validation. The model captured the overall magnitude of the MLR data; however, there were some discrepancies. The most notable discrepancy occurred between 300 and 400 s, where the model did not capture the linearly increasing MLR profile. However, the overall error between the experimental and modeled MLR was found to be 15.1%, which provided validation that the 1D model was capable of capturing the physics of rigid PVC pyrolysis with reasonable accuracy.

5.2.2: Parameterization of a 2D Axisymmetric Model of PVC Pyrolysis

To investigate the importance of the experimentally observed non-uniformity of the sample shape, 2D modeling was carried out. Similar to the 1D model described above, the 60 kW m^{-2} experiments were employed as the target data because these experiments produced fully decomposed char samples when the test was terminated. The 2D model was built upon the same foundation of the milligram-scale-derived parameters and optical properties. The thermal transport parameters were grouped identically to the 1D model described in the previous section.

In the 2D model, the radial dependence of the intumescent (swelling) behavior of the PVC pyrolysis was captured more accurately. To capture the radial trends in the sample shape profiles, the densities were effectively prescribed as a function of radius. To simplify the parameterization, the radial dependence was prescribed as a combination of the center and edge densities. Independent knowledge of the center and edge char expansion dynamics enabled individual parameterization of the respective densities. Two separate initial PVC components, PVC_c (center) and PVC_e (edge), were created with identical properties. The parameters of the resulting decomposition products were also identical between the center and edge components, with the exception of the densities and thermal conductivities. Prescribing different densities and thermal conductivities of the center and edge decomposition products enabled parameterization of the radially dependent sample shape profiles.

To capture the intumescence at the center axis, the densities were prescribed following an identical process to the 1D model characterization; however, the center char thicknesses were employed as the fitting targets instead of the average. While fitting the center densities, the sample radius in the model was reduced from 0.035 to 0.020 m. Reducing the radius ensured that the heat flux to the sample was most representative of the heat flux incident to the center portion of the sample only. The densities were manually adjusted until the center experimental thicknesses, shown in Figure 5.1, were well represented. The densities for the edge components were defined such that the thickness of the sample remained constant to emulate negligible swelling, as experimentally observed in Figure 5.1, which was achieved by multiplying the density of the initial component by

the corresponding stoichiometric mass coefficient of each reaction. The resulting densities of all condensed-phase components for the 2D model of PVC pyrolysis are provided in Table 5.4 denoted by the respective subscript.

Table 5.4: Densities and thermal conductivities of the center (denoted by subscript c) and edge (denoted by subscript e) components for the 2D rigid PVC pyrolysis model.

Component	ρ **(kg m^{-3})**	k **(W m^{-1} K^{-1})**
PVC_c	1409	$0.13 + (0.9\times10^{-4})\,T$
PVC_c_GT	746	$0.13 + (1.8\times10^{-4})\,T$
PVC_c_Res1	716	$0.13 + (1.8\times10^{-4})\,T$
PVC_c_Res2	580	$0.13 + (2.7\times10^{-4})\,T$
PVC_c_Res3	331	$0.13 + (2.7\times10^{-4})\,T$
PVC_c_Res4	116	$0.13 + (3.6\times10^{-4})\,T + (3.2\times10^{-9})\,T^3$
PVC_c_CHAR	57	$0.13 + (3.6\times10^{-4})\,T + (3.2\times10^{-9})\,T^3$
PVC_e	1409	$0.13 + (0.90\times10^{-4})\,T$
PVC_e_GT	1409	$0.069 + (0.95\times10^{-4})\,T$
PVC_e_Res1	1353	$0.069 + (0.95\times10^{-4})\,T$
PVC_e_Res2	1055	$0.072 + (1.5\times10^{-4})\,T$
PVC_e_Res3	602	$0.072 + (1.5\times10^{-4})\,T$
PVC_e_Res4	541	$0.028 + (0.77\times10^{-4})\,T + (0.69\times10^{-9})\,T^3$
PVC_e_CHAR	265	$0.028 + (0.77\times10^{-4})\,T + (0.69\times10^{-9})\,T^3$

To couple the densities between the center and the edge components, a profile describing the mass fraction (mf) of component PVC_c was computed, as shown in Figure 5.3 (r_z used in the $mf_{PVC,c}$ equation is in m). The summation of the PVC_c and PVC_e mass fractions must equal unity. The radially dependent mass fraction of the center components was computed to emulate the PVC sample shape profile at 375 s in Figure 5.1, a

representative profile during the entire duration of the experiments. It was defined such that the center of the sample was comprised entirely of the center component. As the radius increased, the center mass fraction decreased, which, in turn, resulted in the edge mass fraction increasing. The resulting sample shape profiles computed with the 2D axisymmetric model are shown in Figure 5.1 as the solid curved lines. With the exception of slightly over-estimating the sample thickness at 500 s, it was observed that the model captured the overall dynamics of swelling with excellent accuracy.

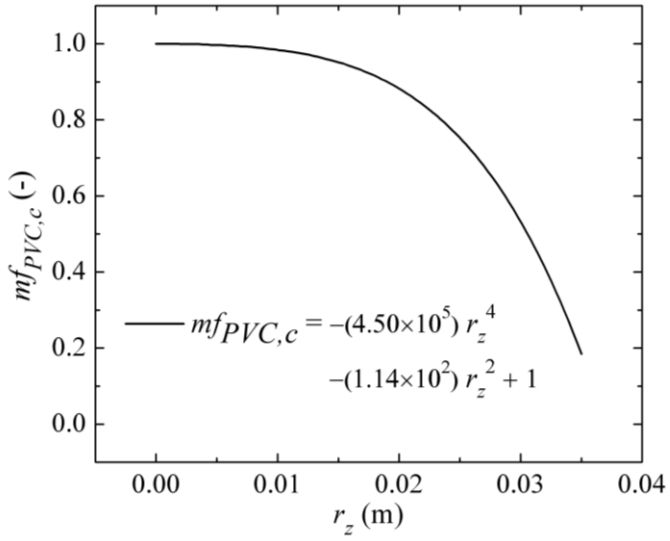

Figure 5.3: Radial mass fraction profile for the PVC_c component used to capture non-uniform swelling of the pyrolyzing sample.

The thermal conductivities of the center components were parameterized following the same methodology discussed for the 1D model. The grouping of the components were identical; however, the values were modified to capture the center experimental temperature profile, shown as square symbols in Figure 5.2(a). The thermal conductivities of the edge components were scaled based on the density ratio between the center (PVC_c) and edge (PVC_e) components. The thermal conductivity was assumed inversely

proportional to the density; therefore, the solid that expanded more upon decomposition was assumed to have proportionally larger thermal conductivity. This scaling was based on a physical argument provided in an earlier publication [22]. Consequently, the edge thermal conductivities were not fitting parameters; instead, they were directly coupled to the center parameters. The resulting temperature predictions at the center and edge of the sample are shown as the solid and dashed lines, respectively, in Figure 5.2(a). An average error between the experimental and simulated bottom surface temperature data was found to be 2.5%. The thermal conductivities of all center and edge components are provided in Table 5.4.

The overall magnitude of the MLR was captured well using the 2D model, shown as the solid line in Figure 5.2(b); however, there were some discrepancies. The most notable discrepancy occurred between 300 and 400 s, where the model under-predicted the experimental data. However, the overall agreement between the experimental and modeled MLR was found to be within 12.6%, which provided validation that the 2D axisymmetric model was capable of capturing the physics of PVC pyrolysis with reasonable accuracy.

Additionally, Figure 5.2 provides a comparison between the 1D and 2D model predictions. The dotted line represents the 1D model and the solid and dashed lines represent the 2D axisymmetric model. The bottom surface temperature, shown in Figure 5.2(a), demonstrates little differences between the two models. The MLR, on the other hand, reveals differences that are more noticeable. The 1D average model over-predicted the experimental data at approximately 75 s, where the 2D model agreed well. At later stages of pyrolysis, both models under-estimated the experimental data, although the 2D

model provided slightly better results. Overall, the MLR validation demonstrated the 2D model yielded a small improvement over the 1D model.

5.2.3: Extrapolation to Additional Heating Conditions

To provide additional validation of the developed rigid PVC pyrolysis models, duplicate CAPA II experiments were conducted at both 80 and 40 kW m^{-2}. These experiments were performed identically to the calibration experiments conducted at a nominal heat flux of 60 kW m^{-2}. The PVC pyrolysis models were employed to extrapolate and predict results outside the calibration conditions. A comparison of the experimental and modeled shape profiles, bottom surface temperatures, and MLR profiles are shown in Figure 5.4 and Figure 5.5.

Figure 5.4 portrays the non-monotonic sample shape profiles of PVC pyrolysis at 80 kW m^{-2}. The sample thickness increased for the first 300 s and then subsequently decreased in thickness until 400 s. These changes in thickness were observed to be reproducible for the early stages and became less reproducible in later stages of pyrolysis. The model slightly over-estimated the char thickness for the first 240 s and then slightly under-predicted the swelling at later stages of pyrolysis. This under-prediction was true for both the 1D and 2D models, although the 2D model was able to capture the sample shape profiles much more accurately.

The experimental bottom surface temperature and MLR histories at an incident heat flux of 80 kW m^{-2} are displayed as symbols in Figure 5.5(a)(b). The modeled temperatures agreed well with the experimental data for the early stages of pyrolysis for both models.

After 200 s, the model predicted temperatures began to over-estimate the experimental temperatures; this was true for both the 1D and 2D version of the models. It was found that the average errors between the experimental and modeled bottom temperature histories for the 1D and 2D models were 10.1% and 10.5%, respectively. The predicted MLR curves from both models captured the overall magnitude of the experimental data very well at 80 kW m^{-2}. However, after 250 s, both models slightly under-estimated the experimental MLR data. In the earlier stages of pyrolysis, the 2D model more closely represented the experimental MLR data. It was found that the average errors between the experimental and modeled MLR histories for the 1D and 2D models were 5.8% and 7.3%, respectively.

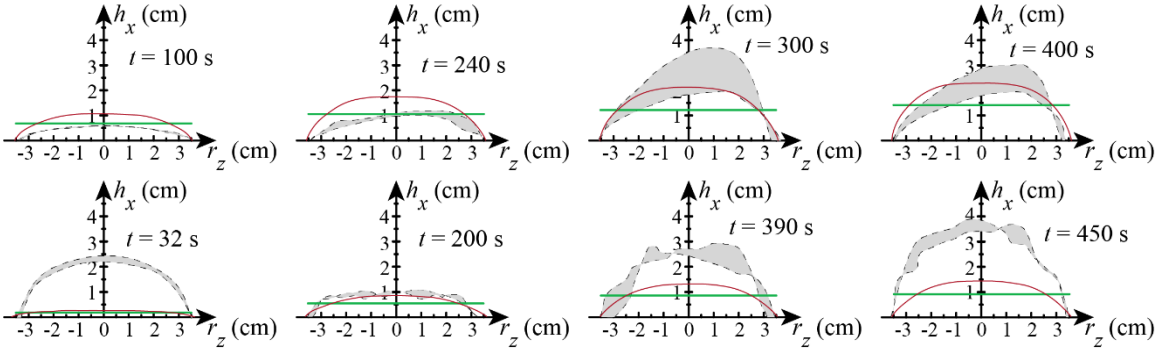

Figure 5.4: Experimental (dashed lines) and modeled (solid lines) sample shape profiles extending above the initial sample top surface for PVC (6.15×10^{-3} m thick) gasification tests conducted at 80 kW m^{-2} (top row) and 40 kW m^{-2} (bottom row).

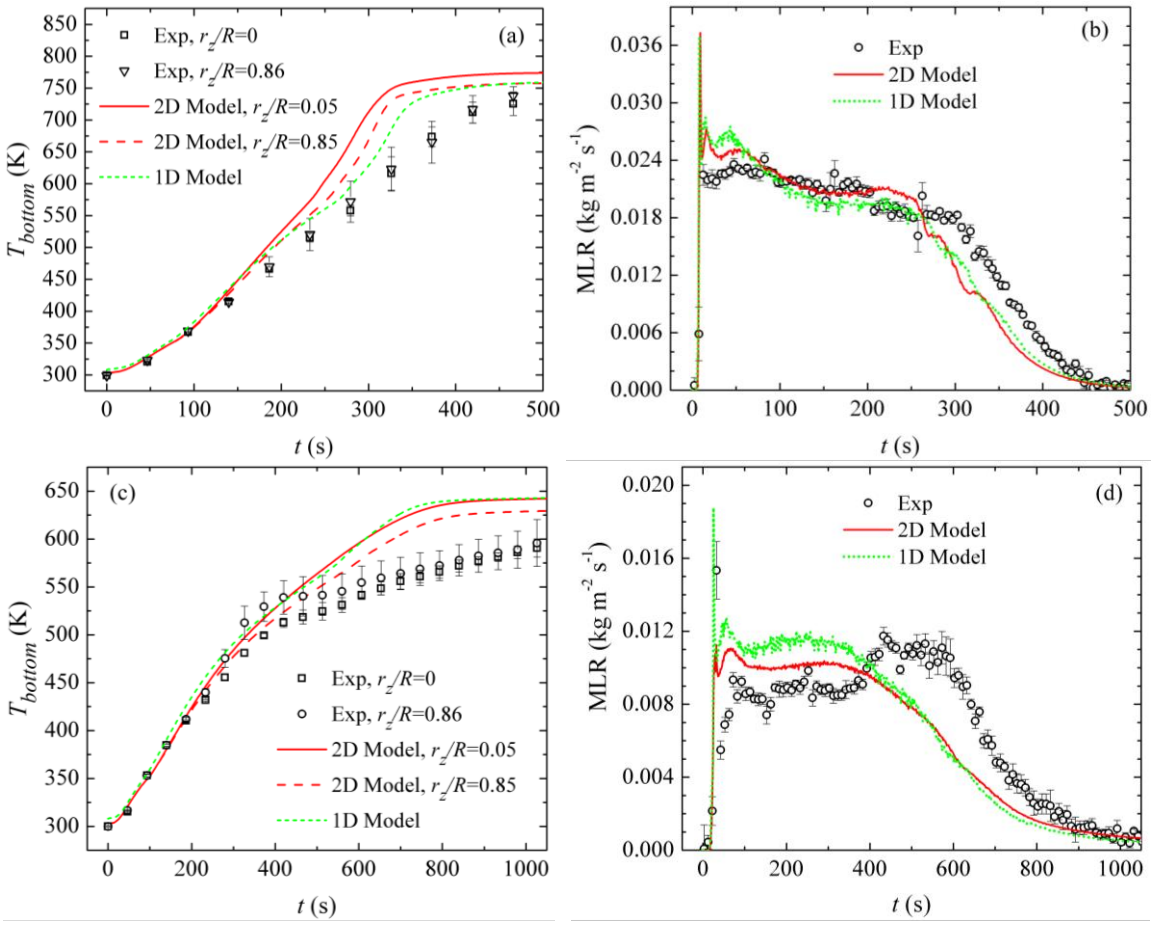

Figure 5.5: Averaged experimental and modeled bottom surface temperatures and MLR data obtained at (a)(b) 80 kW m^{-2} and (c)(d) 40 kW m^{-2} for rigid PVC (6.15×10^{-3} m thick) gasification experiments.

Figure 5.4 also portrayed the non-monotonic sample shape profiles for PVC pyrolysis at 40 kW m^{-2}. The sample thickness quickly increased for the first 32 s and subsequently decreased in thickness until 200 s, after which the sample continued to swell for the remainder of the experiments. This swelling behavior was observed to be reproducible from duplicate experiments. The PVC pyrolysis models (1D and 2D) were unable to capture the bubble formation that occurred at 32 s, however, captured the swelling of the char layer at 200 s. After 200 s, both models consistently under-predicted the char layer thickness.

The experimental bottom surface temperatures and MLR for PVC pyrolysis at 40 kW m^{-2} are displayed as symbols in Figure 5.5(c)(d). The modeled temperature, from both the 1D and 2D simulations, agreed well with the experimental data for the early stages of pyrolysis. After 400 s, the simulated temperature began to over-estimate the experimental temperature; this was true for both the 1D and 2D models. It was found that the average errors between the experimental and simulated bottom surface temperature histories for the first 400 s of the 1D and 2D models were both within 2.1%. The error was only computed for the first 400 s, although it is expected to be significantly greater during later stages of pyrolysis. The predicted MLR curves of both models at 40 kW m^{-2} captured the overall magnitude of the experimental data very well. However, after 400 s, the models were unable to capture the second peak in the experimental MLR data. It was found that the average errors between the experimental and 1D and 2D simulated MLR histories for the first 400 s were 27.0% and 14.7%, respectively.

In the earlier stages of pyrolysis, the 2D model more closely represented the experimental dataset; however, both numerical models struggled to capture the dynamics of the later stages of pyrolysis in the 40 kW m^{-2} experiments. These discrepancies are believed to be associated with the PVC sample experiencing complicated physical movement during pyrolysis. It was observed that the base of the sample moved toward the center causing the sample to shrink significantly in the radial direction, although it was not readily apparent from the profiles in Figure 5.4. The PVC subsequently decoupled from the copper foil, which promoted significant physical changes neglected by the models. This decoupling ultimately resulted in unreliable temperature and MLR data after 400 s.

However, both models demonstrate reasonable accuracy during the early stages of pyrolysis.

5.2.4: Extrapolation to Larger Sample Sizes

It is important to note that different densities and thermal conductivities were required for the 1D and 2D models to capture the experimental data at all heat fluxes. In the 1D model, the densities and thermal conductivities corresponded to averaged values, therefore incorporating edge effects of the small experimental sample sizes. The 2D model attempted to decouple the center and edge physics. Therefore, it is believed that the center component parameters from the 2D model provide the most physically meaningful parameters for extrapolating to larger sample sizes. As the sample size increases, it is believed that the majority of the sample will be similar in thickness to the center of the small-scale sample; therefore, the edge effects will be negligible.

A 1D simulation was conducted to understand the magnitude of the differences between the predicted area-normalized large-scale heat release rate (HRR_{LS}) utilizing the 1D model parameters and those corresponding to the center components of the 2D model. This simple simulation subjected a 6.15×10^{-3} m thick rigid PVC sample (comparable thickness to many decorative and structural building materials made from polymers) to a range (50, 75, and 100 kW m^{-2}) of radiant heat fluxes incident to the top sample surface. This range of heat flux values was representative of lower heat fluxes corresponding to surface heating from small laminar flames [111] up to fully involved room fires [27]. The incident heat flux was constant throughout the entire simulation. The convective losses from the top sample surface were neglected and the bottom sample surface was set as

adiabatic and impenetrable to gas flow. The simulated HRR_{LS} was constructed as the sum of the products of the resulting simulated MLR of individual gaseous decomposition products (see Table 4.1) and the corresponding heats of complete combustion derived from the MCC measurements (see Table 4.3).

Figure 5.6 portrays the simulated HRR_{LS} using the 1D model parameters (labeled as average) and the center component 2D model parameters (labeled as center) for all simulated heat fluxes. It is shown that during early stages of burning, there are minimal differences between these parameter sets. However, at later stages of burning, the HRR_{LS} produced by these two models differ substantially. The peak HRR_{LS} remained nearly constant in magnitude for the center parameter set, while the peak HRR_{LS} is shown to increase in magnitude with increasing heat flux for the average parameter set. In both datasets, the time to peak HRR_{LS} is shown to decrease with increasing heat flux. It is also shown that the HRR_{LS} associated with the center parameters experienced a maximum peak approximately 12 to 27% smaller in magnitude and 30 to 40 s earlier in time than the HRR_{LS} associated with the average parameter set. Therefore, it is shown that there are in fact noticeable differences between the two models, specifically at later stages of burning. These simulated differences justified the necessity of the additional complexity of the 2D axisymmetric model, which accounted for the edge effects during the parameterization of the comprehensive pyrolysis model, to capture an accurate representation of the heat released during a fire event.

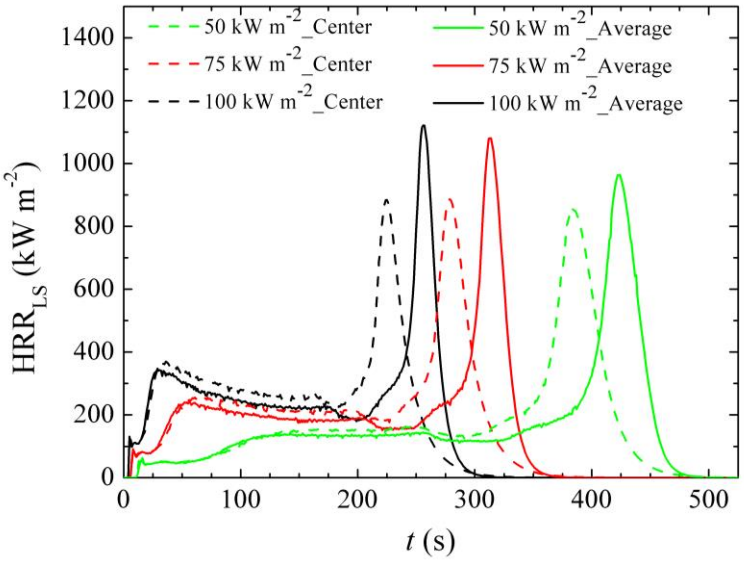

Figure 5.6: Simulated area-normalized heat release rate of large-scale PVC (6.15×10^{-3} m thick) burning, comparing average and center parameters for a range of heat fluxes. The average and center parameters are associated with the 1D and 2D model, respectively.

5.3: Inverse Analysis of Plasticized Poly(vinyl chloride) Gasification Experiments

This section details the development of the model of FPVC pyrolysis. Duplicate CAPA II gasification experiments were conducted on FPVC samples at a set point heat flux of 30 and 60 kW m^{-2}. The sample shape profiles and bottom surface temperatures from CAPA II experiments at 30 kW m^{-2} were employed for the model development. The sample shape profiles and bottom surface temperatures from CAPA II experiments at 60 kW m^{-2}, as well as the MLR from both fluxes, were utilized for model validation purposes. Similar to rigid PVC, the model construction involved analyzing the experimental data with both a 1D pyrolysis model representing the spatially averaged decomposition behavior and a 2D axisymmetric model capable of emulating the observed non-one-dimensional experimental conditions. In both the 1D and 2D model development scenarios, the milligram-scale

model for the kinetics and thermodynamics of thermal decomposition remained identical and served as the foundational framework.

Analysis of the gram-scale tests required knowledge of the emissivity and absorption coefficients *a priori*. The initial emissivity of FPVC (0.90) was assumed to be equal to rigid PVC, which in turn was obtained from literature [110]. The emissivity of FPVC_CHAR (0.94), and thus FPVC_Res3, was estimated based on independent tests described in section 2.3.2.4. The remaining reactants, FPVC_Res1 and FPVC_Res2, were prescribed to have the average emissivity of FPVC and FPVC_CHAR. The absorption coefficient of the undecomposed FPVC, normalized by its density at ambient temperature, was estimated to be 1.1 ± 0.2 m^2 kg^{-1}, based on measurements performed in the current study. The upper char layer was observed to appear very optically dark and graphitic in nature. Therefore, the absorption coefficient of FPVC_CHAR, and thus FPVC_Res3, was defined sufficiently high (100 m^2 kg^{-1}) such that all the radiation was absorbed at the top surface. The absorption coefficient of FPVC_Res1 and FPVC_Res2 were defined to be the average of FPVC and FPVC_CHAR. The emissivity and absorption coefficients of all FPVC condensed-phase components are shown in Table 5.5.

Table 5.5: Emissivity and absorption coefficients of all condensed phase components of FPVC pyrolysis.

Component	ε	κ **(m^2 kg^{-1})**
FPVC	0.90	1.1
FPVC_Res1	0.92	50.6
FPVC_Res2	0.92	50.6
FPVC_Res3	0.94	100
FPVC_CHAR	0.94	100

The experimental CAPA II dataset for FPVC pyrolysis, at a nominal heat flux of 30 kW m^{-2}, are shown in Figure 5.7 and Figure 5.8. Representative shape profiles are provided in Figure 5.7 as a function of time. The bottom surface temperature histories of the center and edge of the sample are presented as symbols in Figure 5.8(a). The mean experimental MLR is shown in Figure 5.8(b). The 1D and 2D modeling results, presented in Figure 5.7 and Figure 5.8, are discussed in sections 5.3.1 and 5.3.2, respectively.

The sample's swelling process included simultaneous increase in thickness and reduction in diameter at later stages of pyrolysis. The increase in thickness was observed to be monotonic in nature. The bottom surface temperature was spatially uniform in the early stages of pyrolysis. In later stages, the temperature becomes non-uniform with the edge of the surface being systematically cooler than the center. The MLR data at 30 kW m^{-2} exhibit a single prominent peak during pyrolysis.

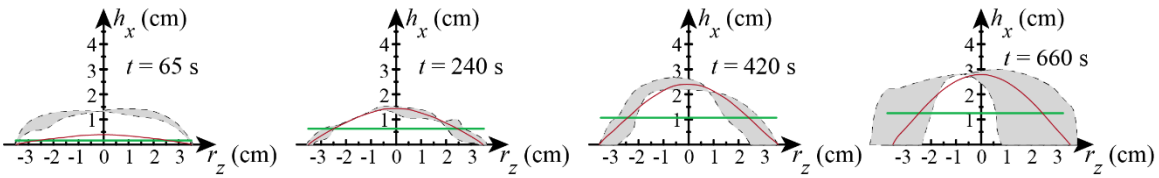

Figure 5.7: The black dashed lines are experimental sample shape profiles extending above the initial sample top surface from duplicate FPVC (5.45×10^{-3} m thick) pyrolysis tests conducted at 30 kW m^{-2}. The shaded area indicates the profiles uncertainty. The straight and curved solid lines represent the 1D and 2D model results, respectively.

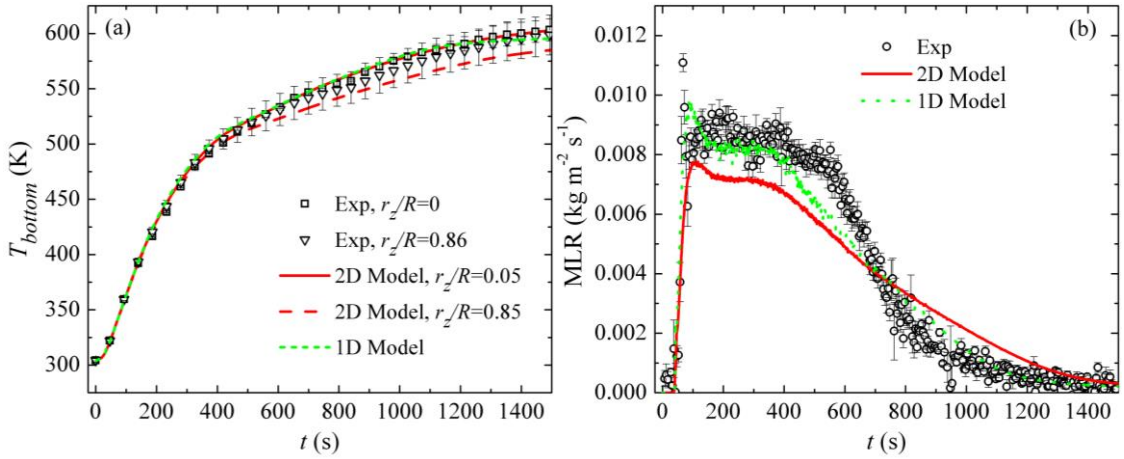

Figure 5.8: Averaged experimental and modeled (a) bottom surface temperatures and (b) MLR data obtained from FPVC (5.45×10^{-3} m thick) pyrolysis tests conducted at 30 kW m^{-2} irradiation.

5.3.1: Parameterization of a 1D Average Model of FPVC Pyrolysis

In the following gram-scale model characterization, the 30 kW m^{-2} shape profile and temperature dataset was employed as fitting targets; therefore, the 60 kW m^{-2} dataset is strictly used as validation for the resulting model. The intumescent behavior of the FPVC pyrolysis was captured numerically in ThermaKin2Ds using an identical approach to that described for rigid PVC. The densities were decreased through a manually iterative procedure such that the fitted sample thickness (solid straight line) captured the critical

shape changes in the 30 kW m^{-2} dataset, shown in Figure 5.7. The densities also factored in reductions in mass associated with the individual reaction steps (listed in Table 4.1). The densities of each component of 1D FPVC pyrolysis are provided in Table 5.6. The density parameterization was dependent upon the thermal transport parameters; therefore, the density and thermal conductivity parameters were iteratively adjusted simultaneously until satisfactory results were obtained.

Table 5.6: Densities and thermal conductivities of condensed-phase components for the 1D model of FPVC pyrolysis.

Component	ρ **(kg** m^{-3}**)**	k **(W** m^{-1} K^{-1}**)**
FPVC	1226	0.12
FPVC_Res1	391	0.41
FPVC_Res2	98	0.41
FPVC_Res3	62	$0.70 + (5.0\times10^{-10})\,T^3$
PVC_CHAR	22	$0.70 + (5.0\times10^{-10})\,T^3$

The average bottom surface temperatures of the 30 kW m^{-2} dataset were employed as target data for the inverse analysis of the thermal transport parameterization of the 1D model. The thermal conductivity of each component was first defined as a constant value, to maintain the simplest model possible. However, it was identified that a constant thermal conductivity was unable to capture the temperature history of the sample. Therefore, a constant term multiplied by the third power of temperature was introduced based on the radiation diffusion approximation [70]; this term was only introduced to FPVC_Res3 and FPVC_CHAR. The resulting fitted bottom surface temperature is shown as the dotted line in Figure 5.10(a). The final thermal conductivities are provided in Table 5.6. The average

error between the experimental and simulated bottom surface temperatures for 30 kW m^{-2} dataset was found to be 0.9%. It is important to note that the density parameterization was dependent upon the thermal transport parameters; therefore, the density and thermal conductivity parameters were iteratively adjusted simultaneously until satisfactory results were obtained.

The 30 kW m^{-2} experimental MLR data, shown in Figure 5.8(b), were not utilized in the inverse analysis model calibration; therefore, comparison between this dataset and the model served strictly as a model validation exercise. The 1D model predicted the 30 kW m^{-2} experimental MLR data with excellent agreement. The overall error between the experimental and modeled MLR was found to be 10.1%. Therefore, the 1D model of FPVC pyrolysis was shown to have the capability of simulating the MLR with reasonable accuracy for data obtained at a set point het flux of 30 kW m^{-2}.

5.3.2: Parameterization of a 2D Axisymmetric Model of FPVC Pyrolysis

2D modeling was subsequently performed to account for variation in the heating conditions along the sample radius and top surface non-uniformity (see Figure 5.7). Similar to the 1D model parameterization, the 30 kW m^{-2} experiments were employed as the target data because these experiments produced the maximum reliable data with minimal radial sample reduction during pyrolysis. The radial dependence of the intumescent behavior of FPVC pyrolysis was captured more accurately by the 2D model employing an identical approach to that defined for rigid PVC. Two separate initial FPVC components, $FPVC_c$ (center) and $FPVC_e$ (edge), were created with identical properties. $FPVC_c$ and $FPVC_e$ were defined to follow an identical decomposition reaction scheme; however, the densities and

thermal conductivities of their products of decomposition were different. Distinguishing between the center and edge enabled parameterization of the radially dependent sample shape profiles.

To capture the intumescence at the center axis, the densities were manually adjusted until the center experimental thicknesses, shown in Figure 5.7, were well represented. The densities for the edge components were defined such that the thickness of the sample remained constant to emulate negligible swelling, as experimentally observed. The resulting densities of all reactants are provided in Table 5.7 denoted by the respective subscript.

Table 5.7: Densities and thermal conductivities of the center (denoted by subscript c) and edge (denoted by subscript e) components for the 2D FPVC pyrolysis model.

Component	ρ **(kg m^{-3})**	k **(W m^{-1} K^{-1})**
$FPVC_c$	1226	0.12
$FPVC_c$_Res1	219	0.62
$FPVC_c$_Res2	55	0.62
$FPVC_c$_Res3	35	$1.1 + (8.0\times10^{-9})\ T^3$
$FPVC_c$_CHAR	12	$1.1 + (8.0\times10^{-9})\ T^3$
$FPVC_e$	1226	0.12
$FPVC_e$_Res1	1202	0.11
$FPVC_e$_Res2	300	0.11
$FPVC_e$_Res3	225	$0.17 + (1.2\times10^{-9})\ T^3$
$FPVC_e$_CHAR	79	$0.17 + (1.2\times10^{-9})\ T^3$

To couple the densities between the center and edge components, a profile describing the mass fraction of the center component ($mf_{FPVC,c}$) was computed; details on this

methodology can be found in section 5.2.2. The center component mass fraction is given as a function of sample radius, r_z (m), in Equation 5.1. The radially dependent mass fraction of the center components was computed to emulate the FPVC sample shape profile at 240 s of the 30 kW m^{-2} dataset. It was observed that the center of the sample was comprised entirely of the center component. As the radius increased, the center mass fraction decreased, which resulted in the edge mass fraction increasing. The resulting sample shape profiles computed with the 2D axisymmetric model are shown in Figure 5.9 as the solid curved lines. With the exception of under-estimating the initial rapid expansion in the 30 kW m^{-2} dataset, it was observed that the model captured the overall dynamics of swelling with excellent accuracy.

$$mf_{\mathrm{FPVC,c}} = 1.24\times10^{5} r_z^{\,4} - 9.52\times10^{2} r_z^{\,2} + 1 \tag{5.1}$$

The thermal conductivities of the center components were parameterized following the same methodology discussed for the 1D model; however, the values were modified to capture the center experimental temperature profile instead of the average. The thermal conductivities of the edge components were scaled based on the density ratio between the center ($FPVC_c$) and edge ($FPVC_e$) components; the scaling used for FPVC was identical to the scaling utilized for rigid PVC. The resulting temperature predictions at the center and edge of the sample are shown as the solid and dashed lines in Figure 5.8(a). An average error between the experimental and simulated results of the 30 kW m^{-2} data was found to be 0.7%. The thermal conductivities of all center and edge components, denoted by their respective subscripts, are shown in Table 5.7.

The MLR data, shown in Figure 5.8(b), were not utilized in the model development. The mean experimental MLR data for the 30 kW m^{-2} data was under estimated during the first 700 s and was subsequently over predicted during later stages of pyrolysis. The overall agreement between the experimental and 2D modeled MLR for the 30 kW m^{-2} datasets were found to have a mean error of 19.0%. Therefore, it is demonstrated that the 2D model provided a reasonable prediction of the experimental MLR profile.

Additionally, Figure 5.8 provides a comparison between the 1D and 2D model predictions. The dotted lines represent the 1D model and the solid and dashed lines represent the 2D model. The bottom temperatures, shown in Figure 5.8(a), demonstrate minimal discrepancies between the two models. The predicted MLR data (Figure 5.8(b)) however, reveals differences that are more noticeable. These differences are likely attributed to the 2D model's ability to capture the radially-dependent evolution of the top sample surface and its associated interactions with the radiation field; the 1D model neglected the radial dependence. The 1D model, although capturing the experimental data more accurately, systematically under predicted the evolution of the top sample surface. As a result, the thermal transport parameters in the 1D model may have partially compensated for the under predicted swelling behavior. The 2D model, on the other hand, under predicted the MLR at 30 kW m^{-2} during the initial stages of pyrolysis due to its inability to capture the rapid sample swelling. Although unable to capture the initial rapid sample swelling, it is believed that the parameter set obtained for the 2D model most accurately represents the physics observed during the pyrolysis experiments.

5.3.3: Extrapolation to Additional Heating Conditions

The experimental CAPA II data for FPVC pyrolysis, at a nominal heat flux of 60 kW m^{-2}, are shown in Figure 5.9 and Figure 5.10. Representative shape profiles are provided in Figure 5.9 as a function of time. The bottom surface temperature histories of the center and edge of the sample are presented as symbols in Figure 5.10(a). The mean experimental MLR is shown in Figure 5.10(b). The modeling results, also presented in Figure 5.9 and Figure 5.10, are predictions from the models developed previously in section 5.3.1 and section 5.3.2.

The sample's swelling process included a simultaneous increase in thickness and reduction in diameter at later stages of pyrolysis, similar to the shape profiles at 30 kW m^{-2}. At all heat fluxes, the increase in thickness was monotonic. The bottom surface temperature profiles were spatially uniform in the early stages of pyrolysis. In later stages, however, the temperature became unreliable due to decoupling of the sample from the copper foil resulting in poor thermal contact; therefore, the temperature data were deemed unreliable and were truncated on Figure 5.10(a). The 60 kW m^{-2} MLR data exhibited multiple peaks during pyrolysis, as shown in Figure 5.10(b).

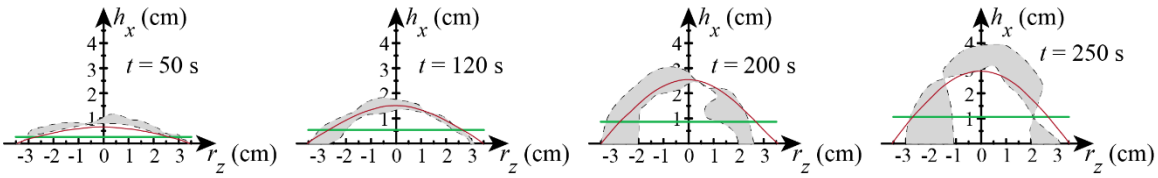

Figure 5.9: The black dashed lines are experimental sample shape profiles extending above the initial top sample surface from duplicate FPVC (5.45×10^{-3} m thick) pyrolysis tests conducted at 60 kW m^{-2}. The shaded area indicates the profiles uncertainty. The straight and curved solid lines represent the 1D and 2D model results, respectively.

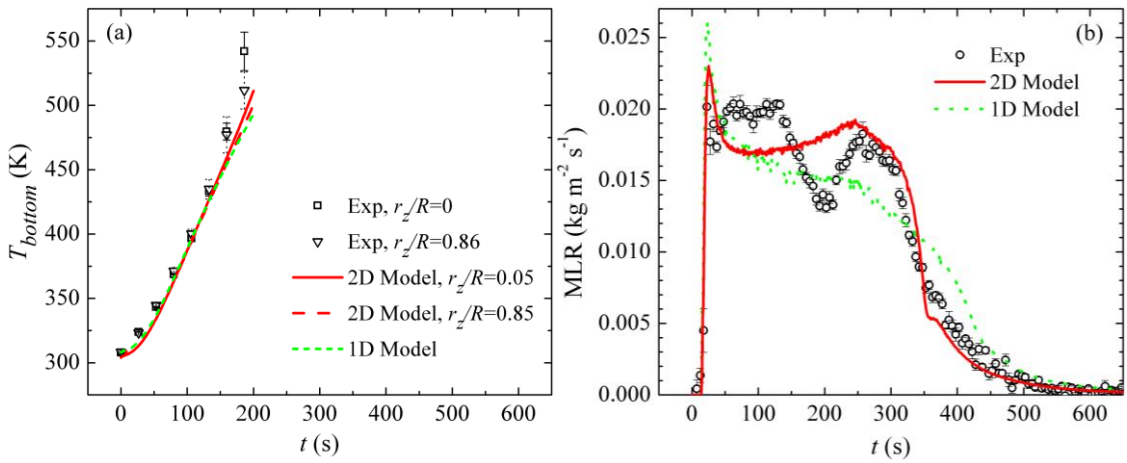

Figure 5.10: Averaged experimental and modeled (a) bottom surface temperatures and (b) MLR data obtained for FPVC (5.45×10^{-3} m thick) pyrolysis tests conducted at 60 kW m^{-2}. The temperature data were truncated during later stages of pyrolysis due to the sample decoupling from the copper foil, resulting in poor thermal contact and ultimately unreliable data.

In the previous gram-scale 1D model characterization, the 30 kW m^{-2} shape profile and temperature dataset was employed as fitting targets; therefore, the 60 kW m^{-2} dataset was strictly used as validation for the resulting model. Figure 5.9 depicts the simulated average char growth dynamics of FPVC pyrolysis with a set point heat flux of 60 kW m^{-2}. The predicted bottom surface temperature histories for the 60 kW m^{-2} data are shown in Figure 10(a). The average error between the experimental and simulated bottom surface temperatures for the 60 kW m^{-2} data was found to be 2.8%. The MLR prediction for the higher flux, shown in Figure 10(b), notably underestimated the experimental MLR data. The overall error between the experimental and modeled MLR for the 60 kW m^{-2} dataset was found to be 13.0%.

The 2D model provided a more accurate description of the boundary conditions which ultimately lead to more accurate predictions of the 60 kW m^{-2} CAPA II experimental

data. The 2D model predicted pyrolyzing sample shape profiles are shown in Figure 5.9 as the solid curved lines. The associated temperature predictions at the center and edge of the sample are shown as the solid and dashed lines in Figure 10(a). An average error between the experimental and simulated 2D results of the 60 kW m^{-2} data was found to be 3.0%. The simulated MLR for the 60 kW m^{-2} tests was found to capture the data very well. The overall agreement between the experimental and 2D modeled MLR for the 60 kW m^{-2} dataset was found to have a mean error of 13.5%.

Additionally, Figure 5.10 provides a comparison between the 1D and 2D version of the pyrolysis models. The dotted lines represent the 1D model and the solid and dashed lines represent the 2D model. The bottom temperatures, shown in Figure 5.10(a), demonstrated minimal discrepancies between the two models. The MLR, however, revealed differences that are more noticeable. These differences are likely attributed to the 1D model's inability to capture the radial dependence of the top sample surface and its associated interactions with the radiation field. The 2D model better captured these surface interactions resulting in improved predictions of the 60 kW m^{-2} MLR during later stages of pyrolysis, however, the overall quality of the predictions between the two models are comparable.

5.3.4: Comparison between Rigid and Plasticized Large-Scale Burning

A simulation of a large burning surface exposed to radiant heat flux, emulating a large-scale fire, was conducted to compare the FPVC and rigid PVC characterized in this work. The simulation enabled a quantitative comparison between the predicted area-normalized large-scale mass loss rate (MLR_{LS}) and HRR_{LS} of FPVC and PVC exposed to

identical conditions. A 6.15×10^{-3} m thick sample was subjected to a constant radiant heat flux of 40 and 70 kW m^{-2} to provide a direct comparison. These simulations were setup identically to that of the rigid PVC large-scale combustion in section 5.2.4. The convective losses from the top sample surface were neglected and the bottom sample surface employed adiabatic boundary conditions. The simulations neglected the potential impact of sample surface oxidation prior to ignition, because the condensed-phase model was parameterized based on anaerobic measurements. Moreover, the additional heat flux provided by a flame that forms on the sample surface upon ignition was also ignored in these simulations. The calculations were terminated when no additional mass loss was observed.

The large surface burning model employed the thermal transport parameters of the center components of the 2D model (see Table 5.7) to factor out the edge effects observed in the CAPA II experiments [88]. The simulated HRR_{LS} was constructed as the product of the simulated MLR_{LS} of individual gaseous decomposition products from the reaction scheme (see Table 4.1) and the corresponding heats of combustion of each independent decomposition product derived from MCC measurements (see Table 4.3). It is especially critical to characterize independent heats of combustion for the decomposition products of materials like rigid PVC, where the heats of combustion of individual products differ substantially.

A comparison between the simulated MLR_{LS} and subsequently computed HRR_{LS} of both FPVC and rigid PVC large-scale burning is portrayed in Figure 5.11. It is shown that there are negligible differences in the MLR_{LS} profiles between the two materials under both 40 and 70 kW m^{-2}. The HRR_{LS}, however, displays substantial differences between FPVC

and rigid PVC at both incident heat fluxes. In the early stages of burning, the HRR_{LS} of rigid PVC is lower than that of the FPVC by a factor of two. However, during the final stages of burning, the HRR_{LS} estimated for rigid PVC has a maximum peak that is a factor of two greater in magnitude than FPVC.

Although rigid PVC produces a greater HRR_{LS} during the final stages of burning in idealistic conditions, this peak is unlikely to contribute significantly to fire growth because it did not occur until very late stages of pyrolysis (requiring high heat flux exposure) and the extensive deformation of the burning material is expected to mitigate its reaction to fire. Therefore, the larger HRR_{LS} of FPVC during the early stages of burning will likely result in a greater flame spread rate during an actual fire event, consequently, making FPVC a greater fire hazard. Unlike rigid PVC which produced a small HRR in the first step of decomposition (see Figure 4.16), FPVC produced a large amount of heat (see Figure 4.17) which is believed to be originated from the organic plasticizers that are added to these materials. As a result, it is imperative that these differences between FPVC and rigid PVC are included in all modeling efforts to capture the material's unique reaction to fire.

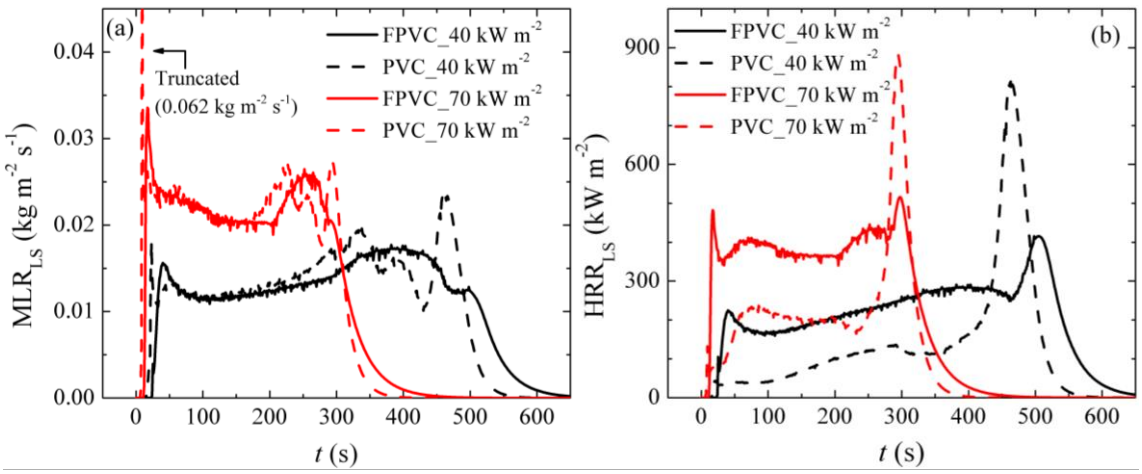

Figure 5.11: Simulated (a) MLR_{LS} and (b) HRR_{LS} of FPVC and rigid PVC, employing the center parameters from the 2D model parameterization, under a nominal heat flux of 40 and 70 kW m^{-2}. The simulated initial sample thicknesses were 6.15×10^{-3} m.

5.4: Inverse Analysis of Bisphenol A Polycarbonate Gasification Experiments

This section details the development of the PC pyrolysis model. Duplicate CAPA II gasification experiments were conducted on PC samples at a nominal heat flux of 50 and 75 kW m^{-2}. The model construction involved analyzing the experimental data with both a 1D pyrolysis model representing the spatially averaged decomposition behavior and a 2D axisymmetric model capable of emulating the observed non-one-dimensional experimental conditions. In both instances, the milligram-scale model for the kinetics and thermodynamics of thermal decomposition remained identical and served as the foundational framework. The prescribed component emissivity and in-depth radiation absorption coefficient were also identical between the 1D and 2D versions of the model.

The emissivity of undecomposed PC was obtained from literature [110] and was found to be 0.89. The emissivity of the fully developed char component (PC_CHAR) was estimated to be 0.94 based on measurements described in section 2.3.2.4. The emissivity

of PC_Res1 was assumed to be identical to PC_CHAR since both condensed-phase products were formed in a similar temperature range. The remaining intermediate component (PC_GT) was prescribed to have an identical emissivity as PC. The in-depth radiation absorption coefficients of undecomposed PC, as provided in Table 5.1, was measured to be 1.3 ± 0.3 m^2 kg^{-1}. The absorption coefficient of the PC_CHAR component, and thus PC_Res1, was assigned very high (100 m^2 kg^{-1}) to ensure all the radiation was absorbed at the top surface of the intumescent char. The absorption coefficient of PC_GT was assigned to be the average value of PC and PC_CHAR, which was required to improve the quality of the subsequent model predictions. The emissivity and absorption coefficients of all PC condensed-phase components are shown in Table 5.8.

Table 5.8: Emissivity and absorption coefficients of all condensed phase components of PC pyrolysis.

Component	ε	κ (m^2 kg^{-1})
PC	0.89	1.3
PC_GT	0.89	50.7
PC_Res1	0.94	100
PC_CHAR	0.94	100

The experimental CAPA II data for PC pyrolysis at a nominal heat flux of 50 kW m^{-2} are shown in Figures 5.12 and 5.13. Figure 5.12 provides representative shape profiles of the developing char layer as a function of time. The bottom surface temperature (T_{bottom}) histories of the center and edge of the sample are presented as open symbols in Figure 5.13(a). The mean experimental MLR is shown in Figure 5.13(b). The 1D and 2D modeling results shown on these figures are discussed in section 5.4.1 and section 5.4.2, respectively.

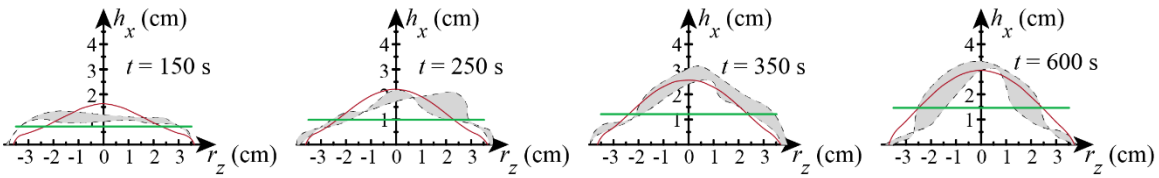

Figure 5.12: The black dashed lines are experimental sample shape profiles extending above the initial top sample surface from duplicate PC (5.50×10^{-3} m thick) gasification tests conducted at 50 kW m^{-2}. The shaded area indicates the profiles uncertainty. The straight and curved solid lines represent the 1D and 2D model results, respectively.

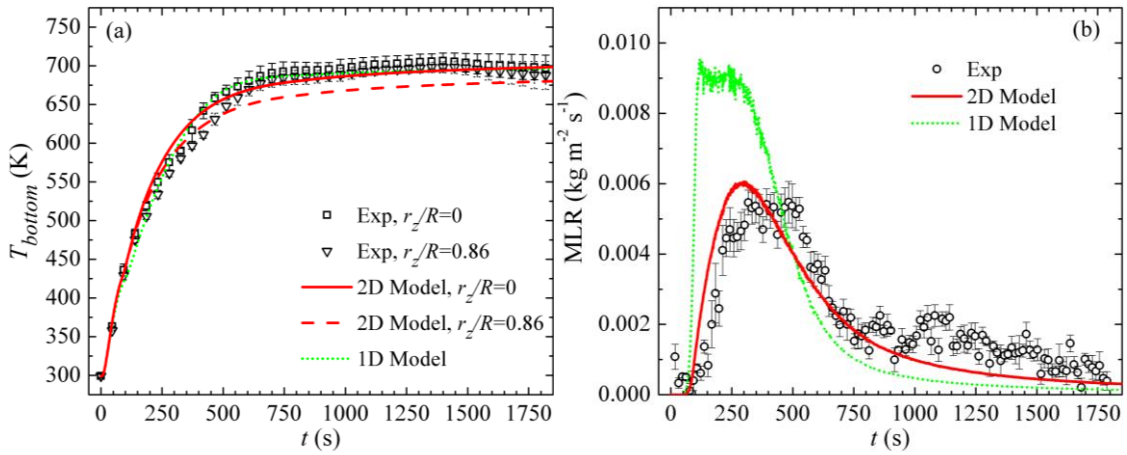

Figure 5.13: Averaged experimental and modeled (a) bottom surface temperatures and (b) MLR data obtained from PC (5.50×10^{-3} m thick) pyrolysis tests conducted at 50 kW m^{-2}.

5.4.1: Parameterization of a 1D Average Model of PC Pyrolysis

The 1D model of PC pyrolysis was parameterized using the parameters derived from milligram-scale experiments and optical properties as the foundational numerical framework. The densities and thermal conductivities of the condensed phase components PC_Res1 and PC_CHAR were grouped and assumed identical. The PC_GT density and thermal conductivity were assigned identical to the undecomposed PC component. Therefore, this fully parameterized PC pyrolysis model was constructed with the fewest

independently adjusted parameters while also capturing the essential features of the experimental data.

The sample shape profiles, as shown in Figure 5.12, provides a snapshot of the critical changes in the sample shape as a function of time. The intumescent (swelling) behavior of the PC pyrolysis was captured numerically in ThermaKin2Ds by prescribing decreasing component densities. Similar to the PVC 1D model development, the average sample thickness was employed as a target value for the density parameterization. The densities were initially prescribed to maintain a constant volume throughout the decomposition process. Subsequently, the densities, in their respective groups, were adjusted through a manually iterative procedure such that the predicted sample thickness (solid straight line) captured the critical average shape changes in Figure 5.12. The resulting densities are provided in Table 5.9.

Table 5.9: Densities and thermal conductivities of condensed-phase components for the 1D model of PC pyrolysis.

Component	ρ **(kg m^{-3})**	k **(W m^{-1} K^{-1})**
PC	1187	0.25
PC_GT	600	0.25
PC_Res1	95	1.9
PC_CHAR	75	1.9

The average bottom temperatures were employed as target data for the inverse analysis using an identical approach to the PVC 1D model development. The thermal conductivity of each condensed phase component was defined as a constant value. The undecomposed PC and PC_GT components were prescribed identical thermal

conductivities under the assumption that the melting process did not greatly impact the material thermal conductivity. In addition, the thermal conductivity of PC_Res1 and PC_CHAR were assumed identical to maintain the simplest model possible. The thermal conductivities were adjusted through a manually iterative inverse analysis procedure and resulting bottom surface temperature predictions are shown as the dotted line in Figure 5.13(a). The final thermal conductivities are provided in Table 5.9. The 1D model of PC pyrolysis was found to predict the experimental bottom surface temperature data with a mean error of 1.0%. It is important to note that the density parameterization was dependent upon the thermal transport parameters; therefore, the density and thermal conductivity parameters were iteratively adjusted simultaneously until satisfactory results were obtained.

The MLR data at 50 kW m^{-2}, shown in Figure 5.13(b), were not utilized in the inverse analysis model calibration; therefore, this dataset served as a model validation. The 1D model over-predicted the magnitude of the experimental MLR peak by 57%. Since the kinetics and thermodynamics of PC thermal decomposition and bottom surface temperatures were captured well by the model, additional analysis was required to determine the result of the discrepancy between the experimental and modeling MLR profiles. It is possible that the 1D model oversimplified the highly non-one-dimensional the experimental boundary conditions and sample shape profiles observed in Figure 5.12. Therefore, 2D modeling was subsequently explored to better resolve the radially-dependent non-one-dimensionality of the PC pyrolysis experimental data to further analyze what physics are responsible for correctly simulating the MLR histories.

5.4.2: Parameterization of a 2D Axisymmetric Model of PC Pyrolysis

2D modeling was subsequently performed to account for variation in the heating conditions along the sample radius and top surface non-uniformity (see Figure 5.12). Similar to the 1D model parameterization, the 50 kW m^{-2} experiments were employed as the target data because these experiments produced reliable fully resolved experimental data. In the 2D model, the radial dependence of the intumescent behavior of PC pyrolysis was captured more accurately than the 1D model in an identical manner to that described for rigid PVC. Two separate initial PC components, PC_c (center) and PC_e (edge), were created with identical properties. PC_c and PC_e were defined to follow an identical decomposition reaction scheme; however, the densities and thermal conductivities of their products of decomposition were different.

To capture the intumescence at the center axis, the densities were manually adjusted until the center experimental thicknesses, shown in Figure 5.12, were well represented. The densities for the edge components were defined such that the thickness of the sample remained constant to emulate negligible swelling, as experimentally observed in Figure 5.12. The resulting densities of all reactants are provided in Table 5.10 denoted by the respective subscript.

Table 5.10: Densities and thermal conductivities of the center (denoted by subscript c) and edge (denoted by subscript e) components for the 2D model of PC pyrolysis.

Component	ρ (kg m^{-3})	k (W m^{-1} K^{-1})
PC_c	1187	0.25
PC_c_M	400	0.45
PC_c_Res1	50	4.7
PC_c_CHAR	42	4.7
PC_e	1187	0.25
PC_e_M	1187	0.15
PC_e_Res1	427	0.55
PC_e_CHAR	308	0.64

To couple the densities between the center and edge components, a profile describing the mass fraction of the center component ($mf_{PC,c}$) was computed; details on this methodology can be found in section 5.2.2 and elsewhere [88]. The center component mass fraction is given as a function of sample radius, r_z (m), in Equation 5.2. The radially dependent mass fraction of the center components was computed to emulate the PC sample shape profile at 350 s of the 50 kW m^{-2} dataset. The resulting sample shape profiles computed with the 2D axisymmetric model are shown in Figure 5.12 as the solid curved lines. It was observed that the model captured the overall dynamics of swelling of PC pyrolysis at 50 kW m^{-2} with excellent accuracy.

$$mf_{\mathrm{PC,c}} = 1.20\times10^{5} r_z^{\,4} - 7.81\times10^{2} r_z^{\,2} + 1 \tag{5.2}$$

The thermal conductivities of the center components were parameterized following a similar methodology discussed for the 1D model; however, the values were modified to

capture the center experimental temperature profile instead of the average. It is important to note that, unlike in the 1D model development, the thermal conductivity of the PC_GT component was required to be a fitting parameter for the 2D model parameterization (see Table 5.10) to achieve adequate modeling results. The thermal conductivities of the edge components were subsequently scaled based on the density ratio between the center (PC_c) and edge (PC_e) components. The thermal conductivity was assumed inversely proportional to the density; therefore, the solid that expanded more upon decomposition was assumed to have proportionally larger thermal conductivity. This scaling was identical to the 2D model development of PVC pyrolysis in section 5.2.2. Consequently, the edge thermal conductivities were not fitting parameters; instead, they were directly coupled to the center parameters. The resulting temperature predictions at the center and edge of the sample are shown as the solid and dashed lines in Figure 5.13(a). The difference between the bottom surface temperatures predicted by the 1D model and the center of the 2D model are indistinguishable. An average error between the experimental and simulated results of the 50 kW m^{-2} data was found to be 2.1%. The thermal conductivities of all center and edge components are shown in Table 5.10.

The MLR data, shown in Figure 5.13(b), were not utilized in the model development. The predicted experimental MLR data for the 50 kW m^{-2} test was simulated very well during all stages of pyrolysis. The 2D model is shown to predict the experimental MLR peak within 5%. Additionally, Figures 5.12 and 5.13 provide a comparison between the 1D and 2D model predictions. The dotted lines in Figure 5.13 represent the 1D model and the solid and dashed lines represent the 2D model. The bottom temperatures, shown in Figure

5.13(a), demonstrate minimal discrepancies between the two models; the edge temperature prediction slightly under-estimates the experimental data. The MLR data (Figure 5.13(b)) however, reveals substantial differences between the 1D and 2D models. These differences are likely attributed to the 2D model's ability to capture the evolution of the top sample surface and its associated interactions with the radiation field more accurately than the 1D model. The 2D model captured the MLR data at 50 kW m^{-2} very well while the 1D model grossly over-estimates the experimental MLR profile.

5.4.3: Extrapolation to Additional Heating Conditions

To provide additional validation of the developed model of PC pyrolysis, duplicate CAPA II experiments were conducted at 75 kW m^{-2}. These experiments were performed identically to the calibration experiments conducted at a nominal heat flux of 50 kW m^{-2}. The PC pyrolysis model was employed to extrapolate and predict experimental results outside the calibration conditions. A comparison of the experimental and modeled shape profiles, bottom surface temperatures, and MLR profiles are shown in Figure 5.14 and Figure 5.15.

Figure 5.14 portrays the non-monotonic sample shape profiles of PVC pyrolysis at 75 kW m^{-2}. The sample thickness increased for the first 180 s and then subsequently slightly decreased in thickness until 300 s. The PC sample swelling was observed to be reproducible for the first 200 s and became slightly less reproducible in later stages of pyrolysis. The PC pyrolysis model captured the experimental sample shape profiles very well for the first 180 s and then over-predicted the swelling during later stages of pyrolysis. This over-prediction

was observed for both the 1D and 2D versions of the model, although the 2D model was able to capture the two-dimensional profiles much more accurately.

The experimental bottom surface temperature and MLR histories at an incident heat flux of 75 kW m^{-2} are displayed as open symbols in Figure 5.15. The simulated temperature profiles captured the experimental data for the early stages of pyrolysis for both models. However, after approximately 175 s, the model predicted temperatures were found to be higher than the experimental temperature profiles; this differences were observed for both the 1D and 2D model predictions. It is believed that the temperature discrepancies are a combination of poor thermal contact between the pyrolyzing sample and the copper foil below, as observed during the experiments, and the degradation of the high emissivity paint, which artificially lowered the experimental temperature measurements at approximately 650 K. Regardless of the potentially unreliable experimental temperatures, it was found that the mean errors between the experimental and simulated bottom temperature profiles for the 1D and 2D models were 4.0% and 6.5%, respectively.

The simulated MLR profiles from both the 1D and 2D models captured the overall magnitude of the experimental data very well at 75 kW m^{-2}. However, the 1D model slightly over-estimated the experimental MLR data for the first 150 s. Therefore, in the earlier stages of pyrolysis, the 2D model more closely represented the experimental MLR data. The error between the experimental and simulated MLR peak for the 1D and 2D models was found to be 10.0% and 2.3%, respectively. It is very evident that in the case of PC pyrolysis, the 2D model provided substantially more accurate predictions of the experimental dataset. The improved predictions are believed to be a direct result of the 2D

model capturing the interactions between the evolving non-one-dimensional top sample surface and the experimental boundary conditions more accurately. Additionally, 2D conduction within the pyrolyzing sample likely contributed to the improved simulated results of the 2D model.

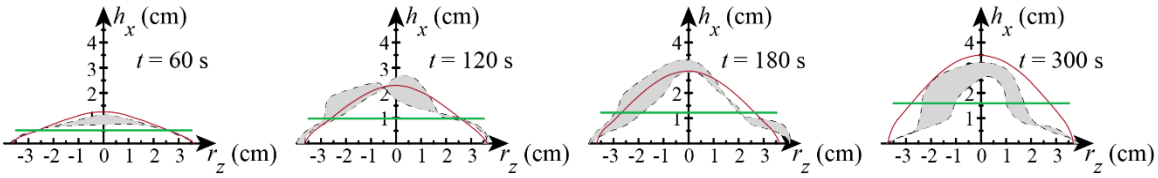

Figure 5.14: The black dashed lines are experimental sample shape profiles extending above the initial top sample surface from duplicate PC (5.50×10^{-3} m thick) gasification tests conducted at 75 kW m^{-2}. The shaded area indicates the profiles uncertainty. The straight and curved solid lines represent the 1D and 2D model results, respectively.

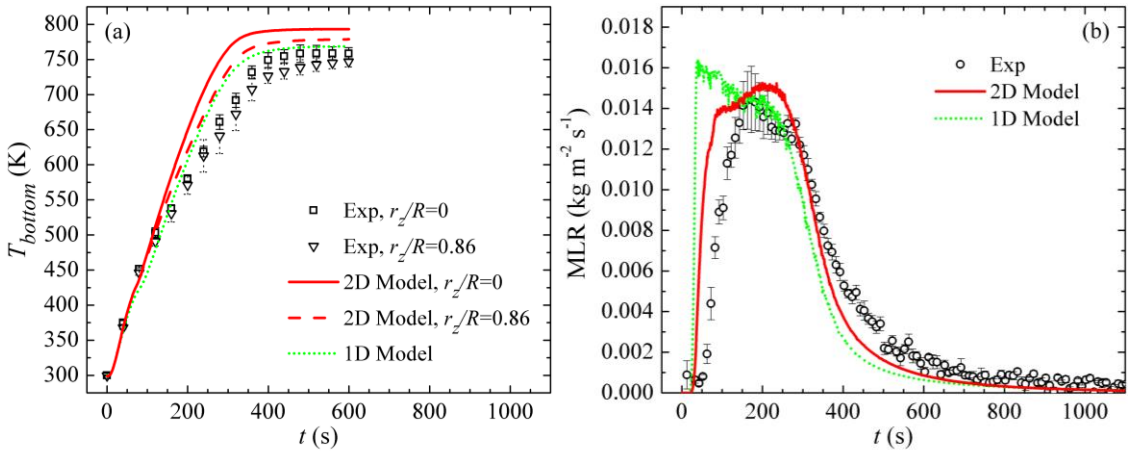

Figure 5.15: Mean experimental and modeled (a) bottom surface temperatures and (b) MLR data obtained for PC (5.50×10^{-3} m thick) pyrolysis conducted at 75 kW m^{-2}. The temperature data were deemed unreliable and truncated at 600 s due to the pyrolyzing sample decoupling from the copper foil below.

5.5: Inverse Analysis of Poly(ether ether ketone) Gasification Experiments

The methodology utilized to fully parameterize a comprehensive model to simulate PEEK pyrolysis is outlined in this section. Duplicate CAPA II gasification experiments were conducted on PEEK samples at a set point heat flux of 60 and 80 kW m^{-2}. In the case of PEEK, the sample shape profiles and bottom surface temperatures from CAPA II experiments at 80 kW m^{-2} were employed for the model development. The higher heat flux was chosen as the calibration dataset because it was the only heat flux tested at which the sample completely decomposed. The sample shape profiles and bottom surface temperatures from CAPA II experiments at 60 kW m^{-2}, as well as the MLR from both fluxes, were utilized for model validation. Similar to the methodology employed for PVC, FPVC, and PC, both 1D and 2D versions of the pyrolysis models were constructed. In both the 1D and 2D model development scenarios, the milligram-scale model for the kinetics and thermodynamics of thermal decomposition remained identical and served as the foundational framework.

Analysis of the CAPA II experimental data requires knowledge of the emissivity and absorption coefficients *a priori*. The emissivity the undecomposed PEEK sample was found to be 0.90, as shown in Table 5.1, and was obtained from literature [110]. The emissivity of PEEK_CHAR (0.94) was estimated based on independent tests described in section 2.3.2 and section 5.1. The emissivity of PEEK_Res1 was assigned to be identical to PEEK_CHAR because it was formed in a similar temperature range. The emissivity of PEEK_M was assigned to be identical to the emissivity of the undecomposed PEEK. The emissivity of all PEEK condensed-phase components are shown in Table 5.11.

The absorption coefficient of the undecomposed PEEK sample, based on measurements outlined in section 5.1, was estimated to be 1.6 ± 0.3 m^2 kg^{-1}. The upper char layer was observed to appear very optically dark and graphitic in nature. Therefore, the absorption coefficient of PEEK_CHAR was defined sufficiently high (100 m^2 kg^{-1}) such that all the radiation was absorbed at the top surface. The absorption coefficient of PEEK_Res1 was prescribed to be the same as PEEK_CHAR. The absorption coefficient of PEEK_M was defined to be the average of PEEK and PEEK_CHAR, which was required to improve the quality of the subsequent model predictions. The absorption coefficients of all PEEK condensed-phase components are shown in Table 5.11.

Table 5.11: Emissivity and absorption coefficients of all condensed phase components of PEEK pyrolysis.

Component	ε	κ **(m^2 kg^{-1})**
PEEK	0.90	1.6
PEEK_M	0.90	50.8
PEEK_Res1	0.94	100
PEEK_CHAR	0.94	100

The experimental CAPA II dataset for PEEK pyrolysis, at a nominal heat flux of 80 kW m^{-2}, are shown in Figure 5.16 and Figure 5.17. Representative sample shape profiles of the developed char layer are provided in Figure 5.16 as a function of time. The bottom surface temperature histories of the center and edge portion of the sample are presented as open symbols in Figure 5.17(a). The mean experimental MLR from PEEK pyrolysis at 80 kW m^{-2} is shown as open symbols in Figure 5.17(b). The 1D and 2D modeling results, also

presented in Figure 5.16 and Figure 5.17 are discussed in detail in sections 5.5.1 and 5.5.2, respectively.

The sample's swelling process was observed to include a monotonic increase in thickness, as shown in Figure 5.16. The sample's swelling was observed to be extremely reproducible during early stages of pyrolysis with slightly more irreproducibility at later stages. The bottom surface temperature was found to be spatially uniform for the entire duration of the pyrolysis experiments, as depicted in Figure 5.17(a). The MLR data at 80 kW m^{-2} exhibit a single peak at approximately 250 s, followed by a slow decay.

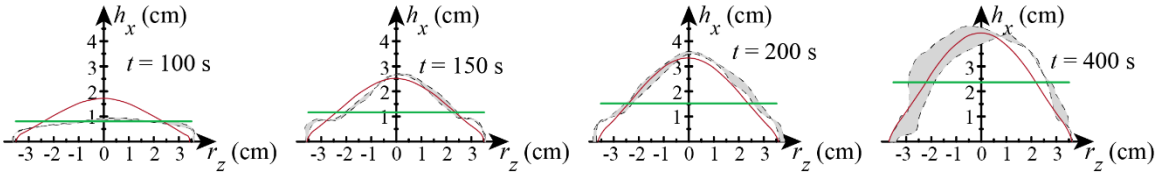

Figure 5.16: The black dashed lines are experimental sample shape profiles extending above the initial top sample surface from duplicate PEEK (6.45×10^{-3} m thick) pyrolysis tests conducted at 80 kW m^{-2}. The shaded area indicates the profiles uncertainty. The straight and curved solid lines represent the 1D and 2D model results, respectively.

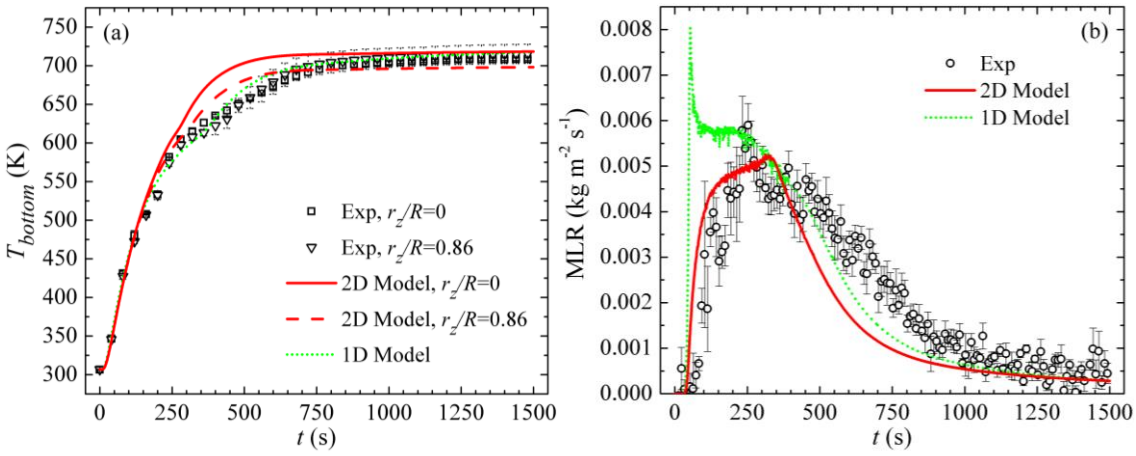

Figure 5.17: Averaged experimental and modeled (a) bottom surface temperatures and (b) MLR data obtained for PEEK (6.45×10^{-3} m thick) pyrolysis conducted at 80 kW m^{-2}.

5.5.1: Parameterization of a 1D Average Model of PEEK Pyrolysis

In the PEEK pyrolysis model parameterization, the 80 kW m^{-2} shape profiles and bottom surface temperature data were employed as fitting targets. Consequently, the shape profiles and temperatures, in addition to the MLR data from both heat fluxes, were reserved strictly for model validation. Employing an identical approach to the 1D model development of PVC, FPVC, and PC, the PEEK 1D model utilized the average sample thickness and bottom surface temperatures as fitting targets for the density and thermal conductivity parameterization, respectively.

The condensed phase component densities were decreased through a manually iterative procedure such that the fitted sample thickness (solid straight line) captured the critical shape changes in the 80 kW m^{-2} dataset, shown in Figure 5.16. In the case of PEEK pyrolysis, the densities of all condensed phase products were first adjusted to maintain a constant sample volume throughout the entire decomposition process. These densities were subsequently decreased uniformly until the final component (PEEK_CHAR) was prescribed to capture the final char thickness. Therefore, the density of PEEK_CHAR was the only independently adjusted parameter during the density parameterization process. The densities of all condensed phase components of the 1D model of PEEK pyrolysis are provided in Table 5.12.

Table 5.12: Densities and thermal conductivities of condensed-phase components for the 1D model of PEEK pyrolysis.

Component	ρ (kg m^{-3})	k (W m^{-1} K^{-1})
PEEK	1297	0.22
PEEK_M	279	0.60
PEEK_Res1	167	$(1.3\times10^{-9})T^3$
PEEK_CHAR	140	$(2.2\times10^{-9})T^3$

The average bottom surface temperature of the 80 kW m^{-2} dataset from PEEK pyrolysis was employed as target data for the inverse analysis of the thermal conductivities of the 1D model. The thermal conductivity of each component was first defined as a constant value to maintain the simplest model possible. However, it was identified that thermal transport within porous media (such as the intumescent char layer) is better represented using the radiation diffusion approximation [70]. Therefore, the thermal conductivity of the products of decomposition from later stages of pyrolysis were assigned a constant term multiplied by the third power of temperature. It has been noted that the radiation diffusion approximation was only physically meaningful to be applied to components that experience a high temperature and porous structure. In the case of developing a 1D model of PEEK pyrolysis, all thermal conductivity values were independently adjustable parameters to obtain an optimal fit of the experimental data. The resulting fitted bottom surface temperature is shown as the dotted line in Figure 5.17(a). The final thermal conductivities of the 1D model of PEEK pyrolysis are provided in Table 5.12. The average error between the experimental and simulated bottom surface temperatures for the 80 kW m^{-2} dataset was found to be 1.3%. It is important to note that

the density parameterization was dependent upon the thermal transport parameters; therefore, the density and thermal conductivity parameters were iteratively adjusted simultaneously until satisfactory results were obtained.

The 80 kW m^{-2} experimental MLR data, shown in Figure 5.17(b), were not utilized in the inverse analysis model calibration; therefore, this dataset served as a validation for the recently development 1D model of PEEK pyrolysis. The 1D model predicted the 80 kW m^{-2} MLR data with reasonable accuracy, however, was shown to over-predict the MLR profile for the first 250 s. After 250 s, the simulation captured the overall MLR peak and decay very well. The overall error between the experimental and modeled MLR was found to be 24.7%. Therefore, it was shown in Figures 5.16 and 5.17 that the 1D model of PEEK pyrolysis was capable of simulating the experimental MLR with marginal accuracy for the 80 kW m^{-2} dataset.

5.5.2: Parameterization of a 2D Axisymmetric Model of PEEK Pyrolysis

2D modeling was subsequently performed to more accurately account for non-uniform heating to the top sample surface due to pyrolysis induced shape changes. Similar to the 1D PEEK model parameterization, the 80 kW m^{-2} experimental data were employed as fitting targets because the sample was fully decomposed at the termination of these tests. In the 2D model, the radial dependence of the intumescent behavior of PEEK pyrolysis was captured identically to the 2D modeling of PVC, FPVC, and PC pyrolysis. Two separate initial PEEK components, $PEEK_c$ (center) and $PEEK_e$ (edge), were created with identical properties. These $PEEK_c$ and $PEEK_e$ components were defined to follow an

identical decomposition reaction scheme; however, the densities and thermal conductivities of their condensed phase components were different.

To capture the swelling at the center axis, the densities were prescribed following an identical process to the 1D model development; however, the center char thicknesses were employed as fitting targets instead of the average. The densities were manually adjusted until the center experimental thicknesses, shown in Figure 5.16, were well represented. The densities for the edge components were defined such that the thickness of the sample remained constant to emulate negligible swelling. The resulting densities of all reactants are provided in Table 5.13 denoted by the respective subscript.

Table 5.13: Densities and thermal conductivities of the center (denoted by subscript c) and edge (denoted by subscript e) components for the 2D model of PEEK pyrolysis.

Component	ρ **(kg m^{-3})**	k **(W m^{-1} K^{-1})**
$PEEK_c$	1297	0.2
$PEEK_c$_M	170	1.1
$PEEK_c$_Res1	102	$2.0 + (1.1\times10^{-9})\ T^3$
$PEEK_c$_CHAR	85	$2.0 + (1.1\times10^{-9})\ T^3$
$PEEK_e$	1297	0.20
$PEEK_e$_M	1297	0.14
$PEEK_e$_Res1	778	$0.26 + (1.4\times10^{-10})\ T^3$
$PEEK_e$_CHAR	654	$0.26 + (1.4\times10^{-10})\ T^3$

To couple the densities between the center and edge components, a profile describing the mass fraction of the center component ($mf_{PEEK,c}$) was computed. The mass fraction of the center component was prescribed as a function of sample radius, r_z (m), in Equation 5.3. The radially dependent mass fraction of the center components was computed to

emulate the PEEK sample shape profile at 150 s of the 80 kW m^{-2} dataset. The resulting sample shape profiles computed with the 2D axisymmetric model are shown in Figure 5.16 as the solid curved lines. With the exception of under-estimating the initial rapid expansion in the 80 kW m^{-2} dataset, it was observed that the model captured the overall dynamics of swelling with excellent accuracy.

$$mf_{\mathrm{PEEK,c}} = 2.96\times10^{5} r_z^{\,4} - 1.09\times10^{3} r_z^{\,2} + 1 \tag{5.3}$$

The thermal conductivities of the center components were parameterized following a similar approach to the 2D model development of rigid PVC. The thermal conductivities of the edge components were scaled based on the density ratio between the center ($PEEK_c$) and edge ($PEEK_e$) components. This scaling applied to the PEEK pyrolysis model was identical to the scaling adopted for rigid PVC pyrolysis 2D modeling described in section 5.2.2. In the case of the 2D model of PEEK pyrolysis, the thermal conductivities of the PEEK_Res1 and PEEK_CHAR components were assigned identical values to reduce the complexity of the model development. The resulting temperature predictions at the center and edge of the sample are shown as the solid and dashed lines, respectively, in Figure 5.17(a). An average error between the experimental and simulated results of the 80 kW m^{-2} data was found to be 3.2%. The thermal conductivities of all center and edge components are shown in Table 5.13.

The MLR data, shown as open symbols in Figure 5.17(b), were not utilized in the model development process; therefore, this datasets was used strictly to provide a validation of the recently developed 2D model of PEEK pyrolysis. The experimental MLR data, with a set point heat flux of 80 kW m^{-2}, were predicted very well with the 2D model

for the first 400 s. After 400 s, the 2D PEEK pyrolysis model began to under-estimate the experimental MLR dataset; however, it is believed that correctly predicting the early stages of pyrolysis and magnitude of the peak MLR is most critical in accurately modeling flame spread and fire growth. The overall agreement between the experimental and 2D modeled MLR profiles for the 80 kW m^{-2} datasets were found to have a mean error of 16.9%.

Figure 5.16 and Figure 5.17 provide a comparison between the 1D and 2D model predictions. Figure 5.16 demonstrates that the 2D model was capable of predicting the radially-dependent sample shape profiles. The dotted lines in Figure 5.17 represent the 1D model and the solid and dashed lines represent the 2D model. The bottom temperatures, shown in Figure 5.17(a), demonstrate minimal discrepancies between the two models. The 2D model is shown to slightly over-predict the experimental temperatures between 300 – 500 s; however, these discrepancies are believed to be associated with the degradation of the high emissivity paint, which artificially lowered the experimental temperature measurements at approximately 650 K. The MLR data displayed in Figure 5.17(b) however, revealed differences that are more noticeable. It is observed that the 2D model captures the early stages of decomposition and peak MLR much more accurately than the 1D model. These differences are likely attributed to the 2D model's ability to capture the evolution of the top sample surface and its associated interactions with the radiation field.

5.5.3: Extrapolation to Additional Heating Conditions

To further validate and demonstrate the extrapolating capabilities of the recently developed 1D and 2D PEEK pyrolysis models, duplicate CAPA II experiments were conducted at 60 kW m^{-2} for comparison. The experimental CAPA II data for PEEK

pyrolysis, at a nominal heat flux of 60 kW m^{-2}, are shown in Figure 5.18 and Figure 5.19. The evolution of the pyrolyzing PEEK sample shape profiles are provided in Figure 5.18 as a function of time. The bottom surface temperature histories of the center and of the sample are presented as open symbols in Figure 5.19(a). The mean experimental MLR data from the PEEK pyrolysis is shown in Figure 5.19(b). The uncertainty in the experimental temperature and MLR profiles were computed from the scatter of the data as two standard deviations of the mean.

The sample's swelling was shown to monotonically increase in sample thickness similar to the intumescent behavior of the 80 kW m^{-2} dataset. The bottom surface temperature was found to be spatially uniform in the early stages of pyrolysis. In later stages of pyrolysis, however, the temperature at the center is systematically cooler than that of the edge. The experimental MLR data at 60 kW m^{-2} exhibit a single peak during pyrolysis, as shown in Figure 5.19(b).

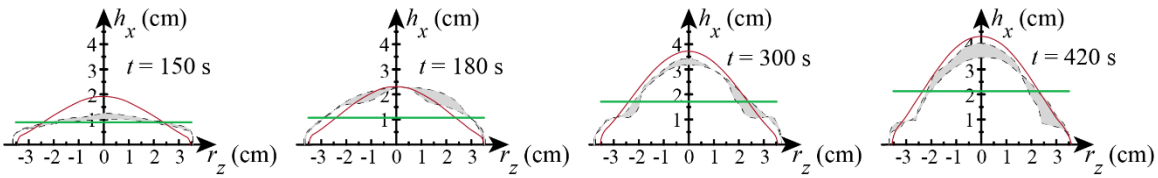

Figure 5.18: The black dashed lines are experimental shape profiles extending above the initial top sample surface from duplicate PEEK (6.45×10^{-3} m thick) gasification tests conducted at 60 kW m^{-2}. The shaded area indicates the profiles uncertainty. The straight and curved solid lines represent the 1D and 2D model results, respectively.

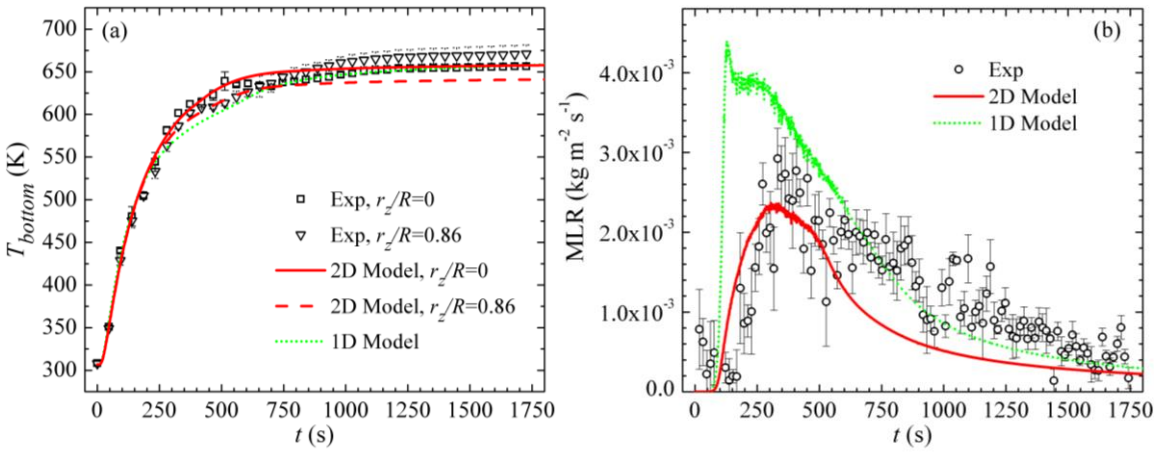

Figure 5.19: Averaged experimental and modeled (a) bottom surface temperatures and (b) MLR data obtained from PEEK (6.45×10^{-3} m thick) pyrolysis conducted at 60 kW m^{-2}.

Since the pyrolysis model development utilized only the 80 kW m^{-2} dataset for model parameterization, the 60 kW m^{-2} dataset served strictly as model validation. Figure 5.18 displays the 1D and 2D model predictions of the char growth experienced during the gasification experiments. Both models were shown to over-estimate the initial thickness at 150 s and then subsequently captured the intumescent behavior during later stages of pyrolysis. The experimental bottom surface temperature profiles, depicted in Figure 5.19(a), were captured very well by both the 1D and 2D versions of the models for the first 1000 s, after which time the models slightly under-predicted the experimental data. The average error between the experimental data and the 1D and 2D models was computed to be 1.4% and 1.8%, respectively. The MLR profiles predicted by the 1D model, shown in Figure 5.19(b), notably over-predicted the experimental data during the early stages of pyrolysis. The 2D model, however, was shown to simulate the early stages of pyrolysis model accurately prior to under-estimating the experimental MLR data. The overall agreement between the experimental and 1D and 2D modeled MLR profiles for the 60 kW m^{-2} datasets were found to have a mean error of 76.8% and 28.1%, respectively.

Figure 5.18 and Figure 5.19 provides a comparison between the 1D and 2D models. Figure 5.18 demonstrates that both models provide reasonable predictions of the experimental data; however, the 2D model captures the non-one-dimensional behavior of the pyrolyzing PEEK sample much more accurately. Because the boundary conditions, in particular the radiation incident to the top sample surface, are captured more accurately, the 2D model is capable of predicting associated bottom surface temperatures and MLR profiles with more detail, as shown in Figure 5.19. Although little discrepancy is observed between the temperature predictions of the two models, the MLR predicted by the 1D and 2D models differ substantially. The significantly over-predicted MLR from the 1D model is believed to be associated with the models inability to replicate the evolving interactions between the sample surface and the surrounding heating conditions. Additionally, 2D conduction within the pyrolyzing sample likely contributed to the improved simulated results of the 2D model. Therefore, as shown in Figure 5.19(b), it is believed that the 2D model provides more accurate predictions of the PEEK pyrolysis behavior.

5.5.4: Comparison between PEEK and PC Large-Scale Burning

Similar to the comparison conducted between rigid and plasticized PVC, idealistic simulations were executed to provide a quantitative comparison between large-scale burning of PEEK and PC. The combustion behavior of PEEK and PC were chosen to be compared due to their chemical similarities. As shown in Table 2.2, the chemical structure of PEEK and PC share similar aromatic groups in the main chain. Additionally, these two materials have similar thermal decomposition reaction mechanisms, however, the residual char yield of PEEK is a factor of two higher than that of PC. Therefore, simulating the

large-scale burning behavior of PEEK and PC enabled a direct comparison of the pyrolysis and combustion properties within idealistic conditions.

The simulations enabled a quantitative comparison between the predicted area-normalized large-scale mass loss rate (MLR_{LS}) and heat release rate (HRR_{LS}) of PEEK and PC exposed to identical conditions. 6.15×10^{-3} m thick samples of PEEK and PC were subjected to a constant radiant heat flux of 40 and 70 kW m^{-2} to provide a direct comparison. These simulations were setup identically to the comparison between the rigid and flexible PVC large-scale combustion in section 5.3.4. The convective losses from the top sample surface were neglected and the bottom sample surface employed adiabatic boundary conditions. The simulations neglected the potential impact of sample surface oxidation prior to ignition, because the condensed-phase model was parameterized based on anaerobic measurements. Moreover, the additional heat flux provided by a flame that forms on the sample surface upon ignition was also ignored in these simulations. The calculations were terminated when no additional mass loss was observed.

The large surface burning model employed the thermal transport parameters of the center components of the 2D models (see Table 5.10 and Table 5.13) to factor out the edge effects observed in the CAPA II experiments. The simulated HRR_{LS} was constructed as the product of the simulated MLR_{LS} of individual gaseous decomposition products from the reaction scheme (see Table 4.1) and the corresponding heats of complete combustion of each independent decomposition product derived from MCC measurements (see Table 4.3). A comparison between the simulated MLR_{LS} and subsequently computed HRR_{LS} of both PEEK and PC large-scale burning is portrayed in Figure 5.20. It is shown that there are

notable differences in the MLR_{LS} profiles between the two materials under both 40 and 70 kW m^{-2}. The differences observed in the MLR_{LS} were directly translated to the HRR_{LS} curves of PEEK and PC large-scale burning at both incident heat fluxes. In all stages of burning, the HRR_{LS} of PC was greater than that of the PEEK by a factor of two; this difference was most notable at the higher heat flux. Additionally, when exposed to identical conditions, the maximum peak HRR_{LS} of PC burning was observed to occur significantly earlier in time than PEEK. Therefore, the larger and faster HRR_{LS} of PC during all stages of burning will likely result in a greater flame spread rate during an actual fire event, consequently, making PC a greater fire hazard than PEEK.

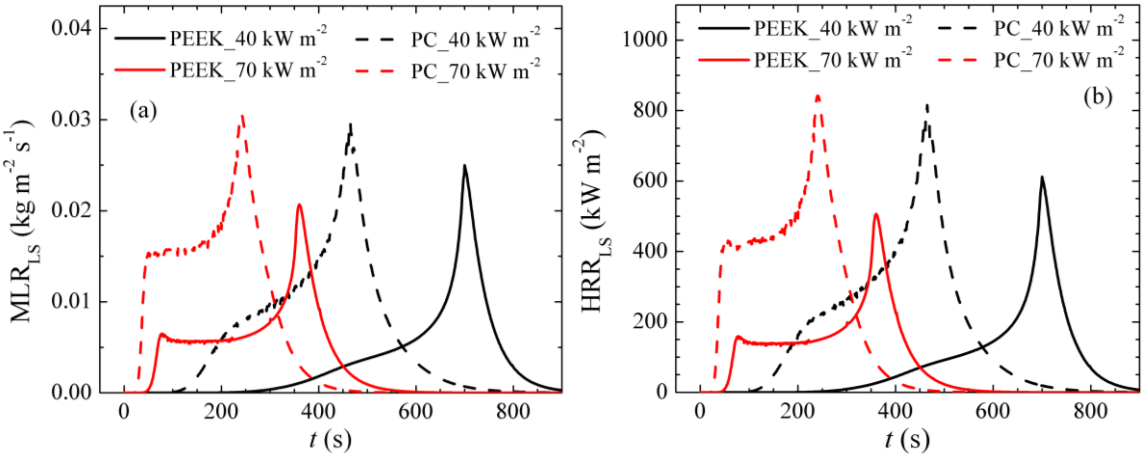

Figure 5.20: Simulated (a) MLR_{LS} and (b) HRR_{LS} of PEEK and PC, employing the center parameters from the respective 2D model parameterization, under a nominal heat flux set point value of 40 and 70 kW m^{-2}. The simulations were conducted with sample thicknesses of 6.15×10^{-3} m to represent typical building materials.

At this point, it is clear that PEEK has a more favorable response to fire, however, a more thorough understanding of which parameters are most responsible for the improved performance of PEEK during large-scale burning simulations is desirable. Considering the gas phase combustion, as demonstrated in section 4.3, the heats of complete combustion of

the volatile gases produced during PEEK thermal decomposition are approximately 12% lower than that of PC. Therefore, the combustibility of the gaseous decomposition products is partially responsible for the observed differences in the HRR_{LS}. However, as shown in Figure 5.20, the MLR_{LS} predictions were drastically different between PEEK and PC; therefore, indicating that the rate of pyrolysis plays a larger role in creating the differences in the simulated HRR_{LS} than the gas-phase combustion.

The most likely factors controlling the rate of pyrolysis include the kinetics of thermal decomposition, the residual char yield, and the thermal insulating potential of the fully developed char. A numerical sensitivity analysis was subsequently conducted to determine which parameters created the most significant impact on the rate of pyrolysis in the simulations of PEEK and PC large-scale burning. The simulations were conducted with a constant applied heat flux of 70 kW m^{-2}. To facilitate a direct comparison, various PC model parameters were systematically prescribed as input parameters within the PEEK large-scale burning model; this was easily attainable due to an identical reaction mechanism between the two materials. The resulting MLR_{LS} from the modified PEEK full-scale burning model (consisting of PC model parameters) was compared to the MLR_{LS} of the original large-scale burning models of both PEEK and PC, as shown in Figure 5.21.

To provide a meaningful comparison during the sensitivity analysis, the simulated MLR_{LS} was divided into two regions: the first region focused on the onset of mass loss (effectively the time to ignition) and the second region included overall average MLR_{LS}. The subsequent analysis identified the Arrhenius reaction rate parameters (A and E) as being responsible for controlling the onset of mass loss. When the Arrhenius reaction rate

parameters of the PC decomposition model were utilized as input parameters in the PEEK full-scale burning model (all other PEEK parameters remained unchanged), the onset of mass loss was shifted to an earlier time which was consistent with the PC MLR_{LS}, as shown in Figure 5.21(a). The stoichiometric coefficients (θ) of the PEEK full-scale burning model were subsequently replaced with those of the PC model in addition to the Arrhenius reaction rate parameters. As shown in Figure 5.21(b), when replacing all the kinetics of thermal decomposition parameters (A, E, and θ), the results of the PEEK model closely represented the large-scale burning behavior of PC. The similarities in the MLR_{LS} of PC and PEEK (simulated with the A, E, and θ parameters of the PC model) indicates that the kinetics of thermal decomposition are largely responsible for the differences between the large-scale burning behavior of PEEK and PC. Therefore, designing charring and intumescent materials with thermally stable kinetics of thermal decomposition will decrease the materials rate of pyrolysis and ultimately improve its reaction to fire.

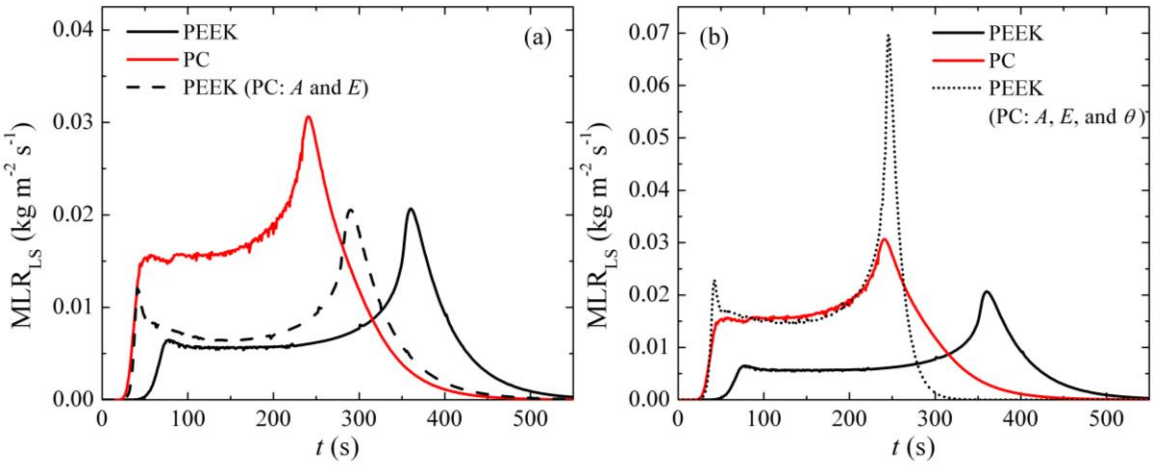

Figure 5.21: Sensitivity analysis of the simulated MLR_{LS} of PEEK and PC large-scale combustion under a nominal heat flux of 70 kW m^{-2} focusing on the (a) onset of mass loss and (b) overall large-scale MLR. The simulations were conducted with sample thicknesses of 6.15×10^{-3} m to represent typical polymeric building materials.

5.6: Inverse Analysis of Poly(vinylidene fluoride) Gasification Experiments

The development of the PVDF pyrolysis model is discussed in this section. Duplicate CAPA II gasification experiments were conducted on VDF samples with a nominal a set point heat flux of both 40 and 60 kW m^{-2}. The experimental dataset was analyzed with a 1D pyrolysis model to represent the spatially averaged decomposition. A 2D model was deemed unnecessary due to the negligible spatially uniform growth in the intumescent char layer observed during the gasification experiments (shown in Figure 5.22). The milligram-scale model for the kinetics and thermodynamics of thermal decomposition, parameterized in Chapter 4, served as the foundational framework of the fully parameterized model of PVDF pyrolysis.

To parameterize the thermal transport parameters, knowledge of the optical properties was required at the onset of the gram-scale model development. The emissivity of the undecomposed PVDF sample was obtained from literature [110] and was found to have a value of 0.94. The emissivity of the final char component (PVDF_CHAR) was also estimated to be 0.94 based on measurements described in section 2.3.2.4. As a result of the initial and final components having an identical emissivity, all intermediate components (PVDF_M and PVDF_Res1) were prescribed an identical value of emissivity to that of the PVDF and PVDF_CHAR components. The emissivity of all PVDF condensed-phase components are shown in Table 5.14.

The in-depth radiation absorption coefficient of the undecomposed PVDF component, as provided in Table 5.1, was found to be 0.9 ± 0.2 m^2 kg^{-1}. Similar to all other materials in this study, the final char component appeared to be very optically dark,

therefore, its absorption coefficient was defined sufficiently high (100 m^2 kg^{-1}) such that all the incoming radiation was absorbed at the top sample surface. The intermediate component, PVDF_Res1, was formed in a similar temperature range to the final char component, therefore, its absorption coefficient was prescribed to be equal to PVDF_CHAR. The absorption coefficient of the PVDF_M component was assigned to be the average value of PVDF and PVDF_CHAR, which was required to improve the quality of the subsequent model predictions. The absorption coefficients of all PVDF condensed-phase components are shown in Table 5.14.

Table 5.14: Emissivity and absorption coefficients of all condensed phase components of the first (Model_v1), second (Model_v2), and third (Model_v3) versions of the PVDF pyrolysis model. Model_v2 and Model_v3 (including PVDF_T1 and PVDF_T2) will be discussed in section 5.6.2 and section 5.6.3, respectively.

Component	**ε (Model_v1)**	**ε (Model_v2)**	**ε (Model_v3)**	**κ (m^2 kg^{-1})**
PVDF	0.94	0.94	0.94	0.9
PVDF_M	0.94	0.70	0.70	50.5
PVDF_Res1	0.94	0.94	0.94	100
PVDF_CHAR	0.94	0.94	0.94	100
PVDF_T1	NA	NA	0.70	100
PVDF_T2	NA	NA	0.94	100

The experimental CAPA II data for the pyrolysis of PVDF at a nominal heat flux of 40 kW m^{-2}, shown in Figures 5.21 and 5.22, provide the model calibration target dataset. Figure 5.22 provides representative shape profiles of the developing char layer as a function of time. The sample thickness was found to increase relatively minimally and was monotonic in nature. Due to the radial uniformity in the char growth, the experimental data

was only analyzed with a 1D pyrolysis model. The bottom surface temperature (T_{bottom}) histories of the center and edge of the sample are presented as symbols in Figure 5.23(a). The temperature profiles were found to be nearly spatially uniform with a tendency for the edge to be minimally cooler than the center. The mean experimental MLR, as shown in Figure 5.23(b), displays two prominent peaks during pyrolysis. The 1D modeling results shown on these figures are discussed in Section 5.6.1.

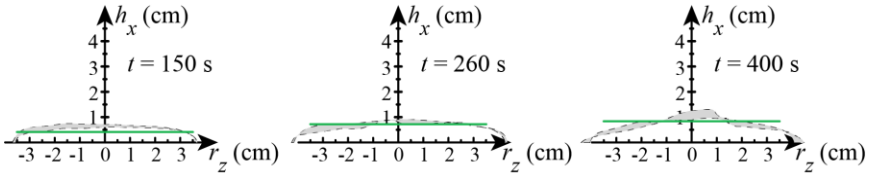

Figure 5.22: The black dashed lines are experimental shape profiles extending above the initial top sample surface from duplicate PVDF (6.30×10^{-3} m thick) gasification tests conducted at 40 kW m^{-2}. The shaded area indicates the profiles uncertainty. The solid lines represent the simulated char thickness from the 1D model of PVDF pyrolysis.

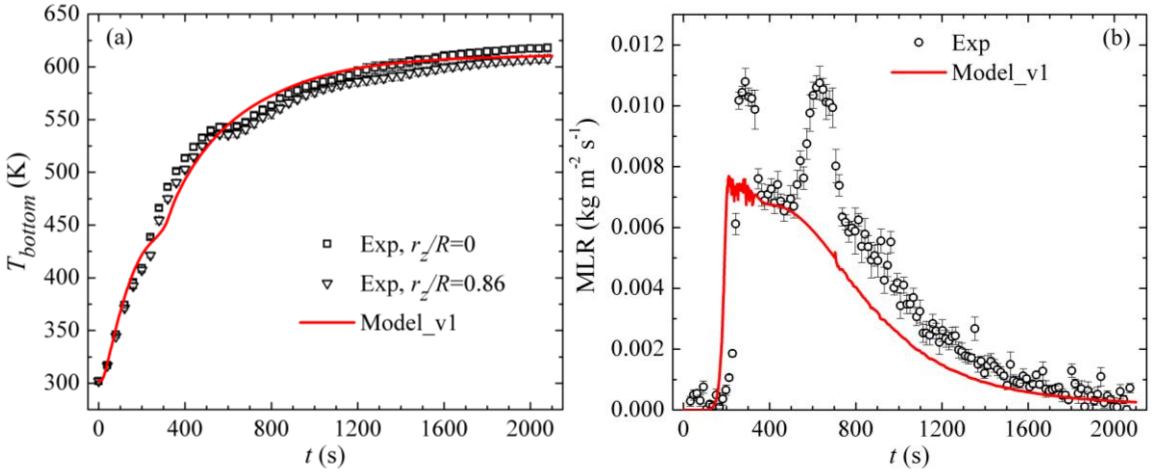

Figure 5.23: Averaged experimental and modeled (a) bottom surface temperatures and (b) MLR data obtained for PVDF (6.30×10^{-3} m thick) gasification tests at a heat flux of 40 kW m^{-2}. The simulated results are obtained from a 1D model of PVDF pyrolysis.

5.6.1: Parameterization of a 1D Model of PVDF Pyrolysis (Version 1)

Employing an identical approach to the model parameterization methodology discussed for all materials studied in this work previously, the first version of the 1D model (Model_v1) of PVDF pyrolysis was developed by expanding upon the previously determined set of parameters derived from milligram-scale experiments as the foundational framework. The condensed-phase component densities and thermal conductivities of the PVDF_Res1 and PVDF_CHAR components were assumed identical and the PVDF_M properties were independent fitting parameters. Therefore, this fully parameterized PVDF pyrolysis model was constructed with the fewest independently adjusted parameters while also capturing the essential characteristics of the experimental dataset.

Figure 5.22 displays representative snapshots of the growth of the sample thickness to demonstrate the evolution of the char layer during pyrolysis. Similar to the 1D model development in previous sections, decreasing component densities were employed to capture the average sample thickness of the developing char layer. The densities were initially prescribed to maintain a constant volume throughout the decomposition process, which was based on the stoichiometric coefficients in the reaction mechanism (see Table 4.1). Subsequently, the densities, in their respective groups, were adjusted manually such that the predicted sample thickness (solid line in Figure 5.22) predicted the average sample thickness. The resulting densities of PVDF pyrolysis are provided in Table 5.15.

Table 5.15: Densities and thermal conductivities of condensed-phase components for the 1D model of PVDF pyrolysis.

Component	ρ **(kg m^{-3})**	k **(W m^{-1} K^{-1})**
PVDF	1791	$0.50 - (6\times10^{-4})\,T$
PVDF _M	770	$0.55 - (4\times10^{-4})\,T$
PVDF _Res1	731	$(1.3\times10^{-9})T^{3}$
PVDF _CHAR	190	$(1.3\times10^{-9})T^{3}$

The mean experimental temperature data from PVDF gasification tests conducted a set point heat flux of 40 kW m^{-2} were designated as fitting targets for the 1D model parameterization. The thermal conductivity of the PVDF and PVDF_M components were first prescribed a constant value. The thermal conductivity of PVDF_Res1 and PVDF_CHAR was initially defined equal and a function of the third power of temperature. The third power of temperature is an approximation to capture the thermal transport within porous media through radiation diffusion [70]; therefore, it was only physically meaningful to apply to components that experience a high temperature and porous structure. The inverse analysis procedure revealed that when prescribing a constant value of thermal conductivity for the PVDF and PVDF_M components, the model was unable to capture the experimental temperature profile during the early stages of pyrolysis. Therefore, a temperature dependent term was deemed necessary and was introduced to the PVDF and PVDF_M components. Figure 5.23(a) displays the resulting bottom surface temperature predictions as a solid line. The final thermal conductivities are provided in Table 5.15. The average error between the experimental and simulated bottom surface temperature profiles for the 40 kW m^{-2} dataset was found to be 2.2%.

Figure 5.23(b) depicts the experimental MLR data from gasification tests conducted at 40 kW m^{-2}. These experimental MLR data were not utilized in the inverse analysis procedure and therefore comparison with the simulated MLR serves as a model validation. The resulting 1D model of PVDF pyrolysis was unable to capture the two prominent peaks observed in the MLR data; however, the model provided a reasonable prediction of the average MLR if the two prominent peaks were neglected. As a result, the overall mean error between the experimental and modeled MLR profiles was found to be 49.3%. Therefore, the first version of the PVDF pyrolysis model (Model_v1) was unable to provide satisfactory predictions of the experimental MLR profile, thus indicating the need for further improvement.

5.6.2: Parameterization of a 1D Model of PVDF Pyrolysis (Version 2)

To further investigate the physics that control the presence of the two prominent MLR peaks in the experimental data shown in Figure 5.23(b), additional numerical studies were conducted. The kinetics and thermodynamics of thermal decomposition, which were determined through inverse analyses of the milligram-scale experimental data, remained unchanged during the subsequent numerical analysis. The milligram-scale parameters were carefully determined and validated based on a robust methodology (detailed in Chapter 4); as a result, there is confidence in the accuracy of the resulting model of the kinetics and thermodynamics of thermal decomposition. Therefore, an effort was made to conduct a parametric study on all optical and thermal transport properties to identify a combination of parameters capable of simulating the presence of the two experimental MLR peaks.

Many different combinations of thermal transport parameters (density and thermal conductivity) were examined in an attempt to capture the experimental data observed in the CAPA II tests. It was found that any substantial changes in these thermal transport parameters had only adverse effects on the prediction of char thickness and bottom surface temperature with negligible improvements to the MLR predictions. Therefore, it was concluded that the thermal transport parameters were not directly responsible for reproducing the dual peaks in the experimental MLR data. As a result, the thermal transport parameters remained unchanged for all future numerical analyses.

A parametric study was subsequently conducted on the optical properties (emissivity and absorption coefficients) prescribed for PVDF pyrolysis. The absorption coefficient, which was measured in this study for the undecomposed sample, was found to have negligible impact on the simulated MLR results; therefore, it was determined that the simulation of the MLR profile was not sensitive to the prescribed absorption coefficients. Lastly, the emissivity value of each condensed phase component was varied to determine its impact on the simulations. It was found that the emissivity of the condensed phase components did in fact have substantial impacts on the MLR predictions.

The parametric study on the emissivity of each condensed phase component revealed that the simulated MLR profile during the early stages of pyrolysis was sensitive to the value of emissivity prescribed for the PVDF_M component. Decreasing the emissivity of the PVDF_M component to a value of 0.70 (see Table 5.14) resulted in the second version of the model of PVDF pyrolysis (Model_v2) accurately predicting the position and magnitude of the first prominent peak in the experimental MLR data, as shown in Figure

5.24. The reduced emissivity of the PVDF_M component decreased the amount of radiant energy being absorbed by the pyrolyzing sample which delayed the onset of mass loss. However, once the reaction mechanism reached the first mass loss step (PVDF_Res1), the sample heating rate was effectively accelerated due to the increased emissivity and ultimately resulted in the sharp increase (second MLR peak) in the simulated MLR profile. The resulting simulations of the Model_v2 are presented as dotted lines in Figure 5.24. It should be noted that the change in emissivity implemented in the Model_v2 had negligible impact on the sample thickness and bottom surface temperature predictions; however, the mean error between the experimental and simulated MLR improved to a value of 27.0%.

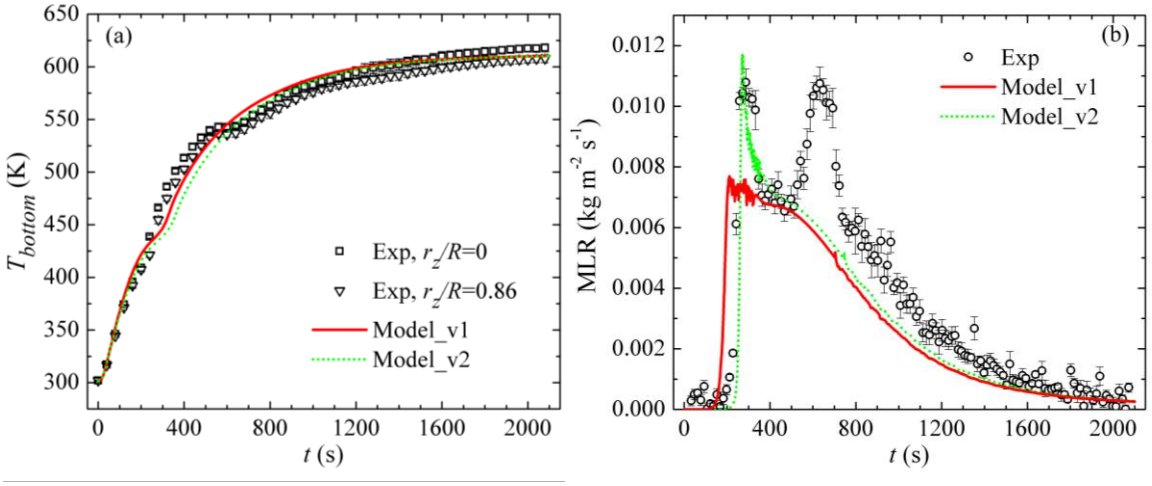

Figure 5.24: Averaged experimental and modeled (a) bottom surface temperatures and (b) MLR data obtained for PVDF (6.30×10^{-3} m thick) pyrolysis experiments conducted at 40 kW m^{-2}. The simulations were conducted with the original (Model_v1) and improved (Model_v2) models of PVDF pyrolysis.

To provide evidence of the sample emissivity impacting the MLR profile, an independent CAPA II experiment was conducted at 40 kW m^{-2} using identical test conditions to the calibration tests. In an effort to provide a constant emissivity during the gasification experiment, the top surface of the sample was painted with a high emissivity

(0.94) paint. It was hypothesized that the paint would provide a stable boundary condition which would prevent the first MLR peak from being observed in the experimental dataset (similar to the MLR predicted by the first version of the PVDF pyrolysis model). As observed in Figure 5.25, the first prominent MLR peak was eliminated in the experimental data when the top surface of the sample was painted. Therefore, it was concluded that the emissivity of the early decomposition product (PVDF_M) was in fact responsible for the presence of the first prominent MLR peak.

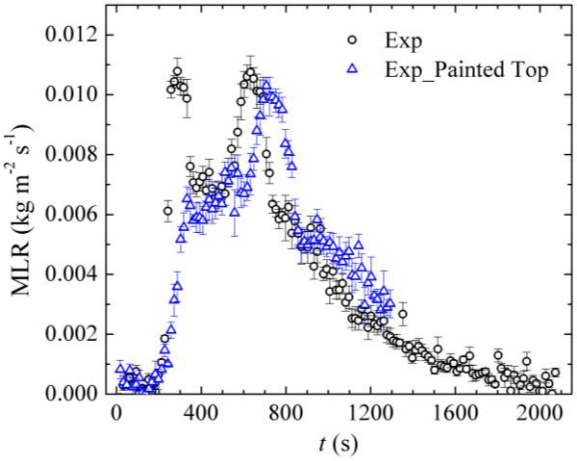

Figure 5.25: Mean experimental MLR data obtained for PVDF (6.30×10^{-3} m thick) pyrolysis tests at 40 kW m^{-2} with both an unpainted and painted top sample surface.

5.6.3: Parameterization of a 1D Model of PVDF Pyrolysis (Version 3)

The second version of the PVDF pyrolysis model (Model_v2), as outlined in section 5.6.2, was found to provide notable improvements to the prediction of the MLR profiles. However, the resulting Model_v2 was unable to capture the second prominent MLR peak, which indicated important physics are yet to be reproduced by the model. As a result of discovering the large impact of emissivity on the MLR during the early stages of pyrolysis, it was believed that the emissivity of the decomposition products formed during later stages

of pyrolysis were responsible for the second MLR peak. Therefore, additional numerical studies were carried out in an attempt to capture the second MLR peak more accurately.

It was determined that the original reaction mechanism of PVDF thermal decomposition (see Table 4.1) did not offer adequate flexibility to accommodate the required change in emissivity values during later stages of pyrolysis. To add the increased modeling flexibility, two temperature transitions were introduced to the modeling scheme. A temperature transition effectively enabled user prescribed changes in component properties to occur instantaneously at a specified component temperature. During each temperature transition, as few or as many component parameters can be adjusted based on user discretion.

In the case of the third version of the PVDF pyrolysis model (Model_v3), two temperature transitions were introduced to the PVDF Model_v2; both transitions were calibrated based on inverse analysis of the experimental MLR data collected at 40 kW m^{-2}. The first temperature transition (PVDF_T1) enabled the surface emissivity of the fully developed PVDF_CHAR component to be instantaneously reduced to 0.70 (an identical value prescribed to the PVDF_M component to capture the first MLR peak) when the temperature of the char component (PVDF_CHAR) reached 805 K. It is important to note that the char component was fully developed when its temperature was approximately 780 K, as shown in Figure 4.5. The emissivity of the PVDF_CHAR component was subsequently defined to undergo a second temperature transition (PVDF_T2) and change back to 0.94 when the component temperature reached 815 K. This first order approximation of the abrupt change in surface emissivity enabled a simplified method to

capture the physics observed in the gasification experiments. The emissivity of all condensed phase components are provided in Table 5.14.

The resulting MLR predicted by the PVDF Model_v3 is shown as dashed lines in Figure 5.26. The mean error between the experimental and modeled MLR was found to be 28.8%. Although the final version of the PVDF pyrolysis model (Model_v3) did not offer any improvement based on the mean error analysis, the model was demonstrated to capture both prominent peaks observed in the experimental MLR data. It is important to note that the two temperature transitions were added to the Model_v2 as the modeling foundation. In other words, the temperature transitions introduced in Model_v3 are only responsible for simulating the presence of the second prominent MLR peak observed during the gasification experiments. Therefore, the PVDF Model_v3 had negligible impacts on the sample shape profiles and bottom surface temperature histories. It is important to note that the validity of modifying the model with temperature transitions could not be verified experimentally because the high emissivity paint only survived the early stages of the gasification experiments.

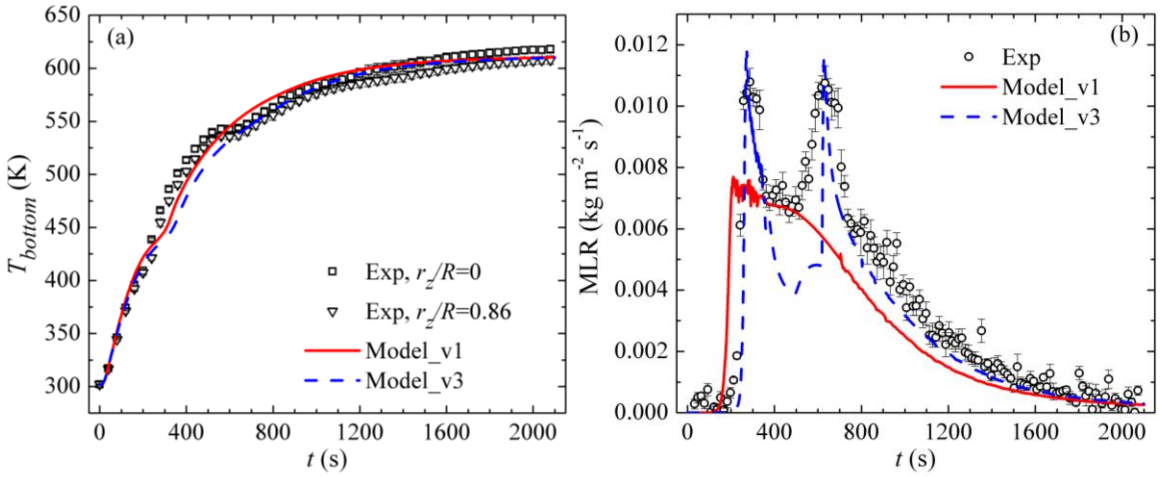

Figure 5.26: Averaged experimental and modeled (a) bottom surface temperatures and (b) MLR data obtained for PVDF (6.30×10^{-3} m thick) pyrolysis experiments conducted at 40 kW m^{-2}. The solid and dashed lines are the results of the original (Model_v1) and final (Model_v3) PVDF pyrolysis model, respectively.

5.6.4: Extrapolation to Additional Heating Conditions

To further validate and demonstrate the extrapolating capabilities of the recently developed 1D model of PVDF pyrolysis (Model_v3), duplicate CAPA II experiments were conducted at alternate heating conditions to provide data for comparison. The experimental CAPA II data for PVDF pyrolysis, at a nominal heat flux of 60 kW m^{-2}, are shown in Figure 5.27 and Figure 5.28. The evolution of the pyrolyzing PVDF sample shape profiles, provided in Figure 5.27, are observed to be one-dimensional with little expansion in char thickness. The bottom surface temperature histories of the center and edge of the sample are presented as open symbols in Figure 5.28(a). The mean experimental MLR data from the PVDF pyrolysis is shown in Figure 5.28(b). Here, the MLR profile displays several notable peaks in the experimental data.

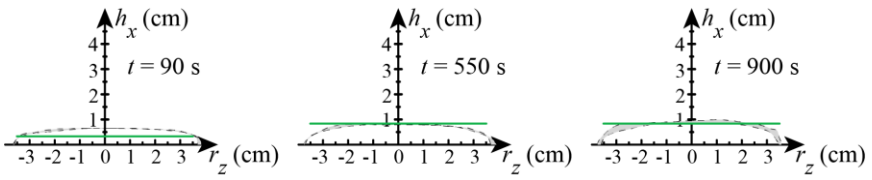

Figure 5.27: The black dashed lines are experimental sample shape profiles extending above the initial top sample surface from duplicate PVDF (6.30×10^{-3} m thick) gasification tests conducted at 60 kW m^{-2}. The shaded area indicates the profiles uncertainty. The solid lines represent the 1D PVDF Model_v3 results.

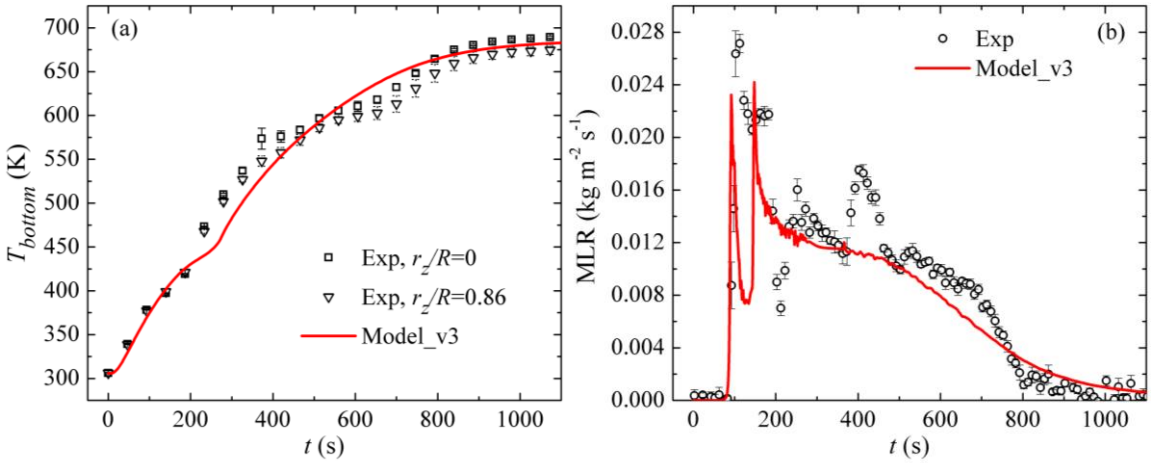

Figure 5.28: Averaged experimental and modeled (a) bottom surface temperatures and (b) MLR data obtained for PVDF (6.30×10^{-3} m thick) pyrolysis at 60 kW m^{-2}. The simulations were conducted using the final model of PVDF pyrolysis (Model_v3).

Since the pyrolysis model development utilized only the 40 kW m^{-2} dataset for model parameterization, the 60 kW m^{-2} dataset serves strictly as model validation. Figure 5.27 displays the PVDF Model_v3 predictions of the char growth experienced during the gasification experiments. The model was shown to reproduce the one-dimensional intumescent behavior observed during the pyrolysis of PVDF. The bottom surface temperature profiles, depicted in Figure 5.28(a), are captured very well by the PVDF Model_v3. The average error between the experimental data and the 1D model was computed to be 1.6%. The MLR profiles predicted by the 1D model, shown in Figure

5.28(b), captures the magnitude of the PVDF pyrolysis; however, the third maximum occurring around 400 s on the experimental curve (which was not present during the low heat flux experiments) was not captured by the model. The mean error between the experimental and 1D modeled MLR profiles for the 60 kW m^{-2} datasets was found to be 26.2%. Therefore, it is demonstrated that the Model_v3 was capable of reproducing the experimental results of PVDF pyrolysis with satisfactory accuracy.

Chapter 6: Char Structure Analysis

6.1: Pore Size Distribution

The rigid PVC, PC, PEEK, and PVDF pore size distributions were computed and analyzed based on the methodology discussed in Section 2.4.1. To investigate the rigid PVC, PC, PEEK, and PVDF char structures, samples were prepared using separate CAPA II experiments conducted at 60, 75, 80, and 60 kW m^{-2} (set point), respectively. The rigid PVC, PC, PEEK, and PVDF ThermaKin2Ds pyrolysis models revealed that at 300, 200, 200, and 600 s, respectively, the top $7\times10^{-3} – 1.2\times10^{-2}$ m of the condensed-phase layer, on average, was comprised of at least 70 wt. % of fully developed char (final char component). The model also indicated that the remaining 30 wt. % of the top layer was comprised of late decomposition products, which suggested that the sample examined was nearly entirely fully developed char. After the heater was removed at the critical times discussed above, the partially decomposed sample remained in the nitrogen purge gas for an additional 300 s to ensure no surface oxidation took place while the sample was cooling. The char profiles were monitored during the cooling process and it was found that no significant shape change took place for any of the materials studied. Once cooled to room temperature, the samples were cut in half and images of the char cross sectional profile were taken and subsequently analyzed.

To utilize the pore detection algorithm (discussed in section 2.4.1), the char images were converted to binary, as shown in Figure 6.1. The pore size distribution analysis

focused on the center portion of the developed char layer (outlined with a solid line in Figure 6.1) to decouple the analysis from edge effects. The outlined region utilized in the char analysis was estimated to capture the location comprised primarily of the fully developed char, as indicated by the pyrolysis model. It is important to note that in the case of PC, the analysis on the developed char was divided into two regions to mimic visual observations.

The first region, represented by the dashed line in Figure 6.1(b), represented the large void observed in the center of the fully developed char layer. This large hollow region, consisting of a single void, occupied over 50% of the total volume of the fully developed char. The image noise observed in the large hollow region of the PC char were reflections from the back wall of the pore and did not represent small pores; therefore, they were removed prior to subsequent image analysis. However, it was observed that the outer shell (the remaining volume of the developed char) was comprised of an intricate pore structure. Therefore, the region outlined by the solid line in Figure 6.1(b) represented the portion of the outer shell analyzed with the pore detection algorithm. The size of the large void was estimated and subsequently added to the pore distribution statistics collected from the outer shell region denoted by the solid line in Figure 6.1(b).

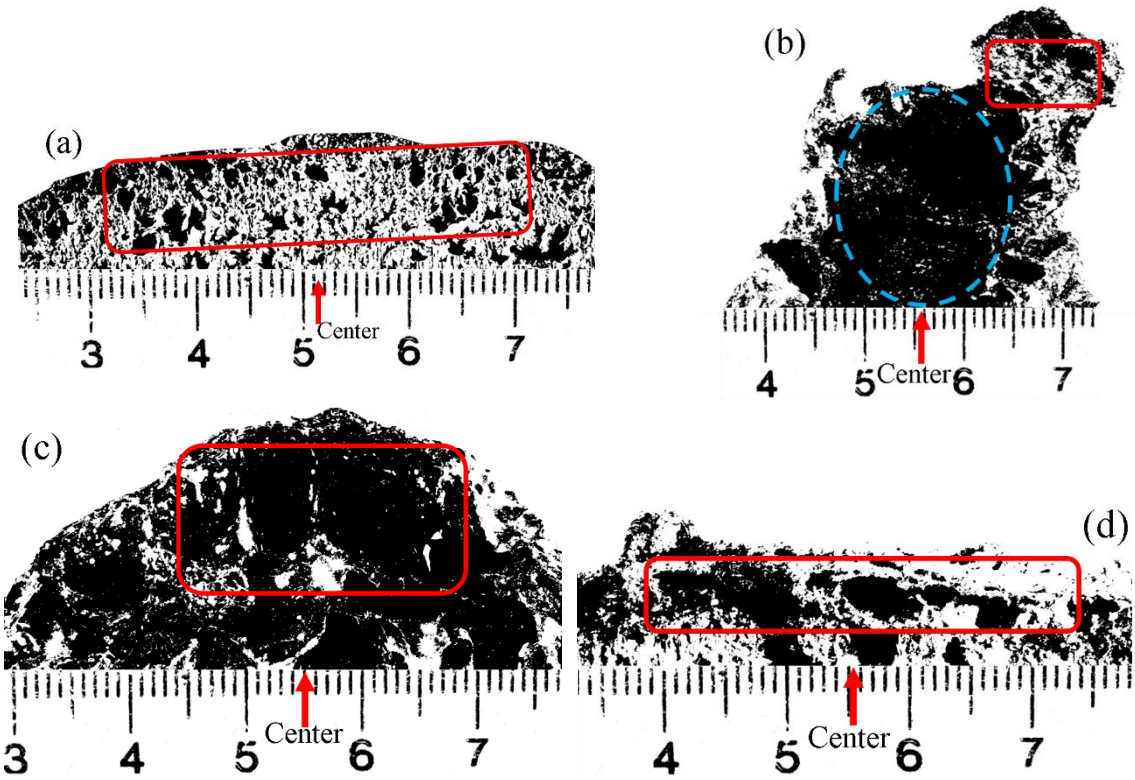

Figure 6.1: Representative black and white processed cross sectional cut of (a) PVC, (b) PC, (c) PEEK, and (d) PVDF char. The black regions in the binary image represent the pores and the white areas represent the solid continuum. The scale is in units of cm. The areas sampled for the char analysis are enclosed by the solid red line. The arrow represents the geometric center of the char sample. The dashed blue line represents a secondary area sampled for the analysis of PC char.

Figure 6.2 portrays a histogram of the number based pore size distribution (ratio of the number of pores of each size and the total number of pores) calculated for the rigid PVC, PC, PEEK, and PVDF intumescent char. It is important to note that these histogram data exclude all pores with a diameter smaller than 1×10^{-4} m, as discussed in section 2.4.1. The data from repeated tests were found to have a relatively high degree of reproducibility, as indicated by the small error bars. The relative number of pores was found to increase exponentially with decreasing pore sizes; this trend was consistent for all materials.

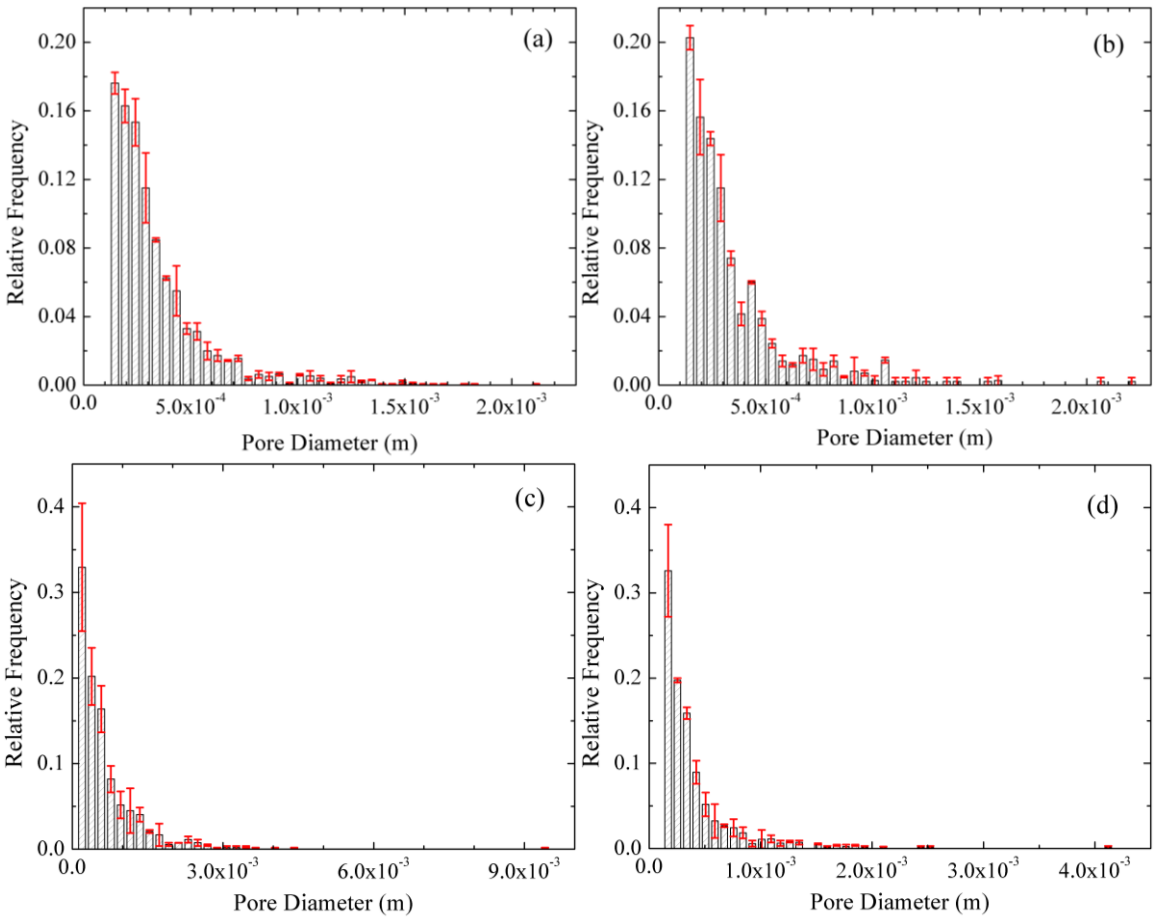

Figure 6.2: Pore size distribution (N_q/N_p) of (a) PVC, (b) PC, (c) PEEK, and (d) PVDF intumescent char. The error bars represent half the difference between duplicate tests. It is important to note the different length scales on the axes.

The mean (d_{mean}) and median (d_{median}) pore diameters were computed from the pore size distributions of each material, as shown in Table 6.1. The volume-weighted mean pore diameters of each material were subsequently computed from the pore size distributions based on Equation 6.1.

$$d_{vol} = \left(\frac{6}{\pi} \sum_{q}^{N_p} \left(\frac{N_q}{N_p} V_q \right) \right)^{1/3} \tag{6.1}$$

where d_{vol} is the volume-weighted mean pore diameter, N_p is the total number of pores evaluated, N_q is the number of pores of the q-th size and V_q is the volume of the q-th pore. The volume-weighted mean pore diameters from repeated tests of each material are presented in Table 6.1. All errors in the char analysis were computed as half of the difference between the duplicate experimental data. Subsequent analysis relating thermal transport properties to each of the pore diameters is presented in section 6.3.

Table 6.1: Mean, median, and volume-weighted mean pore diameters computed for PVC, PC, PEEK, and PVDF fully developed char samples.

Material	d_{mean} **(m)**	d_{median} **(m)**	d_{vol} **(m)**
PVC	$3.44\times10^{-4} \pm 6\times10^{-6}$	$2.72\times10^{-4} \pm 4\times10^{-6}$	$5.09\times10^{-4} \pm 4\times10^{-6}$
PC	$4.6\times10^{-4} \pm 1\times10^{-5}$	$2.67\times10^{-4} \pm 5\times10^{-6}$	$3.6\times10^{-3} \pm 4\times10^{-4}$
PEEK	$6.5\times10^{-4} \pm 7\times10^{-5}$	$4.7\times10^{-4} \pm 9\times10^{-5}$	$1.3\times10^{-3} \pm 2\times10^{-4}$
PVDF	$4.0\times10^{-4} \pm 4\times10^{-5}$	$2.9\times10^{-4} \pm 2\times10^{-5}$	$7\times10^{-4} \pm 1\times10^{-4}$

6.2: Char Porosity

The rigid PVC, PC, PEEK, and PVDF char porosity values were computed with the two independent methods described in Section 2.4.2. The first method was based on the density of graphite ($\Phi_{graphite}$) and the second method utilized image analysis (Φ_{image}). To compute the total volume of the char required for the first method, duplicate images of the sample side view, collected at the conclusion of CAPA II experiments, were analyzed. The rigid PVC, PC, PEEK, and PVDF char samples were obtained from experiments conducted at 60, 75, 80, and 60 kW m^{-2}, respectively. Sample side view images were converted to physical dimensions using the approach described in Section 2.3.2. The sample shape

profiles were subsequently fitted with a symmetric fourth order polynomial, as given by Equation 6.2, to represent the average shape profile of the duplicate tests.

$$h_s = f_4 r_z^{\,4} + f_2 r_z^{\,2} + f_0 \tag{6.2}$$

where h_s (a function of the radius, r_z) is the vertical distance to the instantaneous sample surface from the initial top surface of the sample and f_4, f_2, and f_0 are fitting parameters. The fitted curve was then swept around the vertical axis from the center to the total sample radius (R), as shown in Equation 6.3, to produce an axisymmetric volume representing the total volume (V_{total}) of the fully developed char layer. The total volume accounted for the volume of the initial sample (first term on the right-hand-side of Equation 6.3) and the expanded volume above the initial sample surface (second term on the right-hand-side of Equation 6.3).

$$V_{total} = \pi R^2 \delta_0 + 2\pi \int_0^R r_z h_s dr_z \tag{6.3}$$

where δ_0 is the initial sample thickness, given in Table 2.1. The fully decomposed char samples (calculated at 900, 1000, 1500, and 900 s for rigid PVC, PC, PEEK, and PVDF CAPA II experiments at 60, 75, 80, and 60 kW m^{-2}, respectively) were used to estimate the total char volume. Figure 6.3 provides a representative sample shape profile of the fully developed char from the conclusion of PVC gasification experiments conducted at 60 kW m^{-2}. The dashed lines are experimental data from duplicate tests. The solid line is a fit using Equation 6.2, representing the average sample shape profile. The individual volume of the fully developed char was computed for each material studied in this work. Sample shape profiles of each material are not shown for brevity.

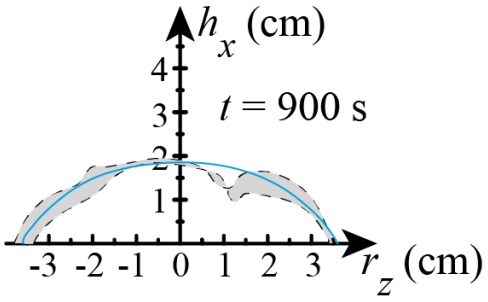

Figure 6.3: Sample shape profile of fully decomposed PVC char obtained at 900 s with a set radiant heat flux of 60 kW m^{-2}.

The volume of the solid continuum portion of the char was assumed graphitic in nature when estimating the porosity based on the density of graphite. Therefore, the volume of the solid continuum was estimated by dividing the sample mass (obtained from CAPA II experimental data) by the density of graphite ($\rho_{graphite}$ = 2210 kg m^{-3} when measured at 300 K [40]). The volume of the void space (V_{void}) was subsequently calculated as the difference between the total char volume and the volume of the solid continuum phase. The char porosity based on the density of graphite was subsequently computed for each material using Equation 6.2 and Equation 6.3. The porosity values based on the density of graphite were found to be very similar and greater than 0.90 for all materials studied in this work. The resulting porosity values based on the density of graphite of rigid PVC, PC, PEEK, and PVDF are shown in Table 6.2. Values of the graphite based porosities were found to be similar to the one reported for an intumescent protective coating (Φ = 0.96) in a previous study conducted by Staggs et al. [68].

A char porosity based on the image analysis was computed using the second method described in Section 2.4.2. The average porosity of the char layer of each material, computed with the pore detection algorithm, is provided in Table 6.2. It is important to

note that the two regions of the PC char, shown in Figure 6.1(b), were both accounted for in computing the image based porosity. The first region (the large single void) was assumed to have a porosity of unity. The porosity of the second region was computed from the image analysis like the other materials. The volume fraction of each respective region was factored into the calculation of the total porosity of the PC intumescent char. It was found that the image based porosity of PVC and PVDF were similar, however the image based porosity of PC and PEEK were significantly higher. In all cases, the porosities based on image analysis were found to be significantly lower than the porosity based on the density of graphite.

To provide a quantitative measure of the difference between the porosity based on the density of graphite and the porosity based on image analysis, an effective density (ρ_{eff}) of the visually observed continuum phase was computed based on Equation 6.4.

$$\frac{\rho_{\text{graphite}}}{\rho_{\text{eff}}} = \frac{1-\Phi_{\text{image}}}{1-\Phi_{\text{graphite}}} \tag{6.4}$$

In all cases, the effective density of the continuum phase, as depicted in Table 6.2, was found to be significantly lower than that of pure graphite. This reduced density of the continuum phase can be explained by a combination of two phenomena. The first factor accounts for the presence of pores that are less than 1×10^{-4} m in diameter, which were not resolved in the char images. Secondly, it is also possible that the carbon molecules in the char layer have a greater molecular spacing than the densely packed structure of graphite. Both factors are likely to have contributed to the reduced density computed for all of the materials studied in this dissertation.

Table 6.2: Char porosity based on the density of graphite ($\Phi_{graphite}$) and based on the image analysis (Φ_{image}) utilizing the pore detection algorithm. The density ratio (computed with Equation 6.4) provides a comparison between the density of graphite and the effective density of the visually observed continuum phase.

Material	$\Phi_{graphite}$	Φ_{image}	$\rho_{graphite}/\rho_{eff}$
PVC	0.96	0.53 ± 0.01	11.8
PC	0.96	0.77 ± 0.02	5.8
PEEK	0.91	0.85 ± 0.04	1.7
PVDF	0.92	0.55 ± 0.02	5.6

6.3: Comparison of the Thermal Insulating Potential of Rigid PVC, PC, PEEK, and PVDF Intumescent Char

One of the primary objectives of this work was to provide a relationship between the thermal transport within the condensed-phase and the associated physical structure of the resulting intumescent char. In other words, understanding which quantities impact the char's thermal insulating potential (its ability to shield the undecomposed material below from thermal exposure) was a principal outcome of this study. To provide a quantitative measure of the char's thermal insulating potential, several quantities representing thermal transport within the fully developed char (thermal conductivity, k, thermal diffusivity, α, and the product of density and thermal conductivity, ρk) were compared as functions of the char structure descriptors computed in section 6.1 and section 6.2 of this manuscript. Each of these thermal transport quantities identified are related to a material's ability to reduce the rate of heat flow through the intumescent char layer.

The char's thermal conductivity was an important parameter to consider because it provides a measure of the char's ability to transport thermal energy through the porous

media. Similarly, the thermal diffusivity, $\alpha = k/\rho c$, provides a measure of the rate of heat transfer across a material from the hot surface to the cold surface. The product of ρ and k, a measure of the char's transparency to heat flow [22], was the third thermal transport quantity of interest within this study. The parameterization of the thermal transport in the 2D pyrolysis models, which took into account the non-uniformity of the char sample shape profiles, was dependent upon the product of ρ and k remaining constant. The resulting 2D pyrolysis models were shown to provide satisfactory predictions of the bottom surface temperatures, therefore indicating that defining the product of ρ and k to remain constant was reasonable. All properties required to compute the pertinent thermal transport quantities were obtained from the center parameter set of the 2D pyrolysis models developed in Chapter 5; the 1D model parameters were utilized for the PVDF char analysis in the absence of a 2D model.

To provide a basis for comparing the thermal insulating potential, the heat capacity and thermal conductivity of all intumescent chars studied in this work are presented in Figure 6.4. The heat capacity, shown in Figure 6.4(a), was found to increase linearly for all chars as a function of temperature. However, the magnitude of the heat capacity was shown to have a very large range in values between the intumescent chars. The large differences in the heat capacities indicate differences in the chemical structure of the intumescent char layer at the molecular level. The thermal conductivity of the char produced from rigid PVC, PEEK, and PVDF pyrolysis, as shown in Figure 6.4(b), was found to increase as a function of temperature; the char produced from PC pyrolysis had a constant thermal conductivity. The thermal conductivity of the char produced from PVC pyrolysis was found to increase

with temperature at a faster rate than that of PEEK and PVDF, therefore, making it difficult to provide a direct comparison with the thermal conductivity of chars produced from the pyrolysis of other materials.

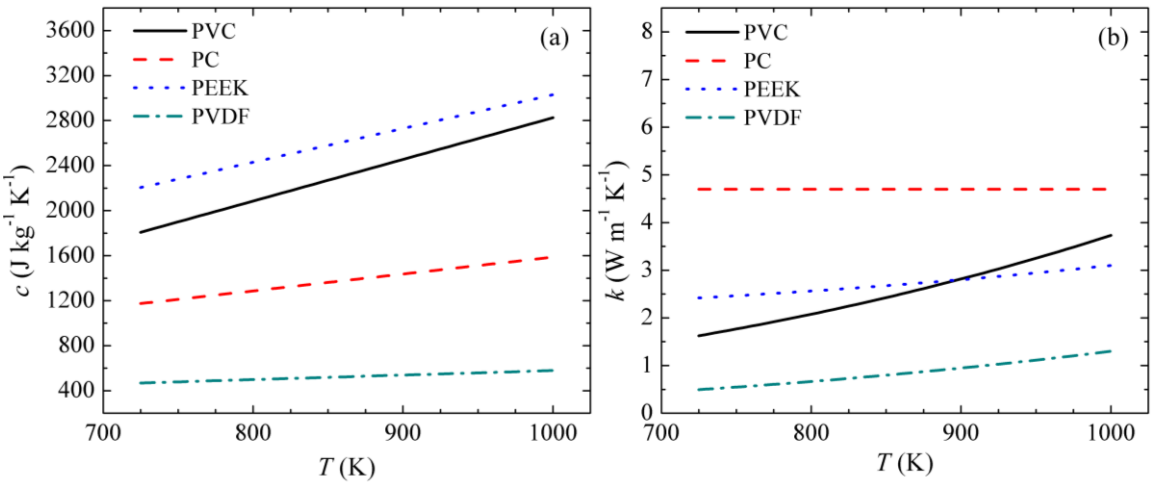

Figure 6.4: Temperature-dependent (a) heat capacity and (b) thermal conductivity of the fully developed intumescent char's studied in this work.

To provide a direct comparison between the heat capacities and thermal conductivities in the subsequent analysis, mean values of all thermal transport quantities were computed for a temperature range of 725 – 1000 K (an identical temperature range portrayed in Figure 6.4). This temperature range is representative of the temperature experienced by the fully developed char during the CAPA II experiments. It is believed that the heat flow within a developing char layer (described by the thermal transport quantities) is directly impacted by the unique physical structure of the intumescent char (pore sizes and porosities). Therefore, the resulting thermal transport quantities of the fully developed char components were plotted as a function of the char's mean, median, and volume-weighted mean pore diameters, as well as its porosity based on both the density of graphite and independent image analysis. In other words, a single thermal transport

quantity was computed for each individual char and plotted with respect to the various descriptors of the physical structure of the intumescent char. The objective of this exercise was to identify all trends that manifest themselves within the resulting data and determine quantifiable relationships, if any, between thermal transport within the condensed phase and the physical structure of the intumescent char.

Figure 6.5 portrays the thermal conductivity (open symbols) of the fully developed char as a function of the char's mean, median, and volume-weighted mean pore diameters, as well as the char's porosity based on both the density of graphite and image analysis. The solid lines represent the best linear fit of the data points; the equations correspond to the linear fit. It is observed in Figure 6.5(a) and Figure 6.5(b) that the thermal conductivity had an extremely weak relationship with the mean (d_{mean}) and median (d_{median}) pore diameters. The thermal conductivity did, however, have a strong dependence on the volume-weighted mean pore diameter (d_{vol}). As shown in Figure 6.5(c), the thermal conductivity linearly increased with an increasing d_{vol}. The linear fit had a coefficient of determination (R^2) of 0.74. Therefore, this relationship is indicative that a small d_{vol} leads to a decreased rate of conduction, which ultimately leads to an improved thermal insulating potential of the char. Lastly, Figure 6.5(d) and Figure 6.5(e) demonstrated that the char's thermal conductivity had a relatively weak dependence on the porosity based on both the density of graphite ($\Phi_{graphite}$) and image analysis (Φ_{image}).

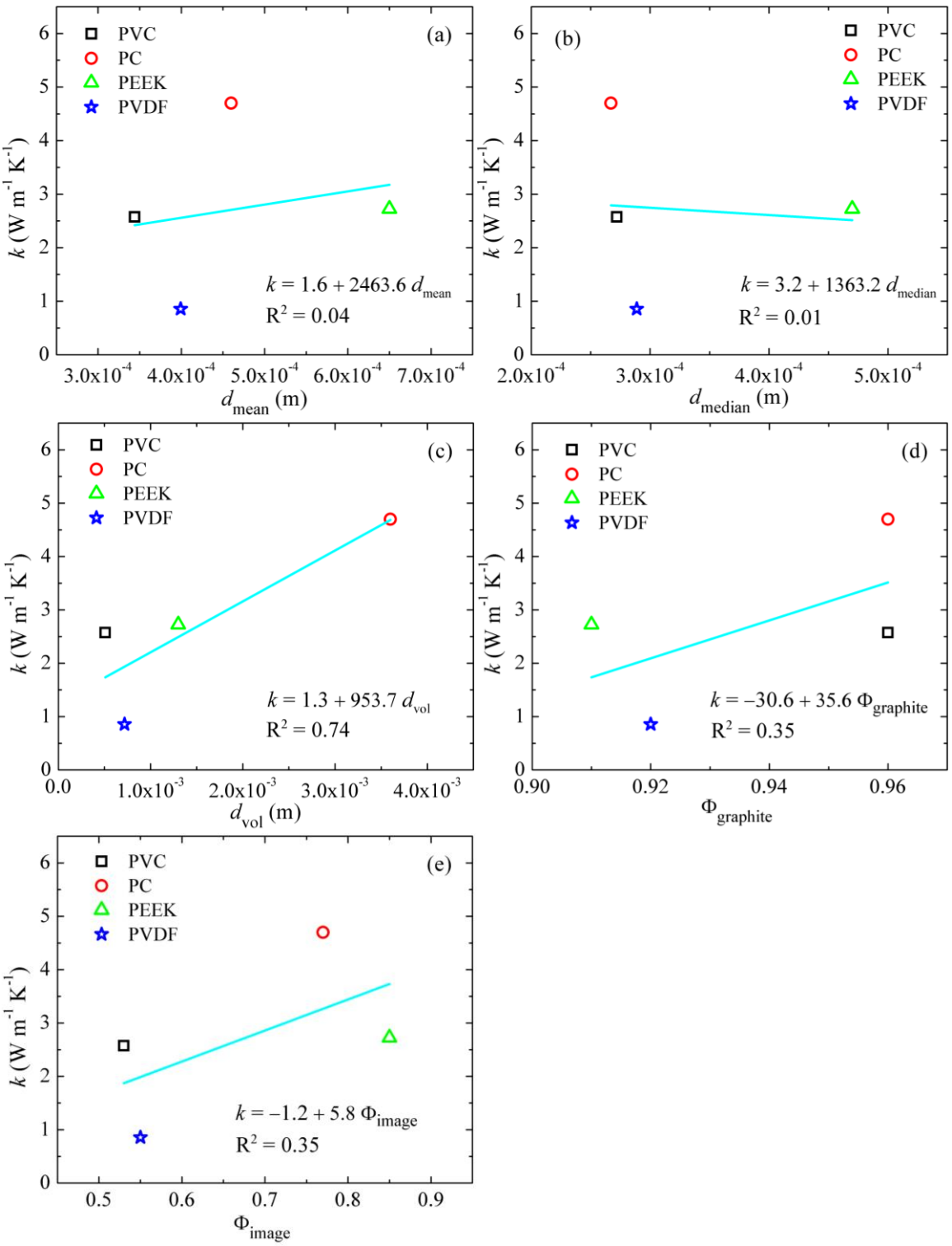

Figure 6.5: Fully developed char thermal conductivity as a function of various quantities describing the physical structure of the intumescent char. The lines represent a linear fit of the data, which are expressed by the equations in these figures.

Figure 6.6 displays the char's thermal diffusivity as a function of its associated mean, median, and volume-weighted mean pore diameters, as well as the char's porosity based on both the density of graphite and image analysis. The char's thermal diffusivity demonstrated negligible correlations with the d_{mean} and d_{median}, as shown in Figure 6.6(a) and Figure 6.6(b). A strong linear relationship ($R^2 = 0.91$) was established between the char's thermal diffusivity and d_{vol}, which is portrayed in Figure 6.6(c). This relationship was found to have a stronger linear correlation than all the thermal conductivity relationships shown in Figure 6.5. However, the observed relationship between the thermal diffusivity and d_{vol} was a consequence of the span in d_{vol} being effectively defined by a single point (PC char); therefore, this relationship was considered somewhat unreliable. The char's thermal diffusivity was found to have minimal correlation with its associated porosity, both based on the density of graphite and image analysis, as shown in Figure 6.6(d) and Figure 6.6(e).

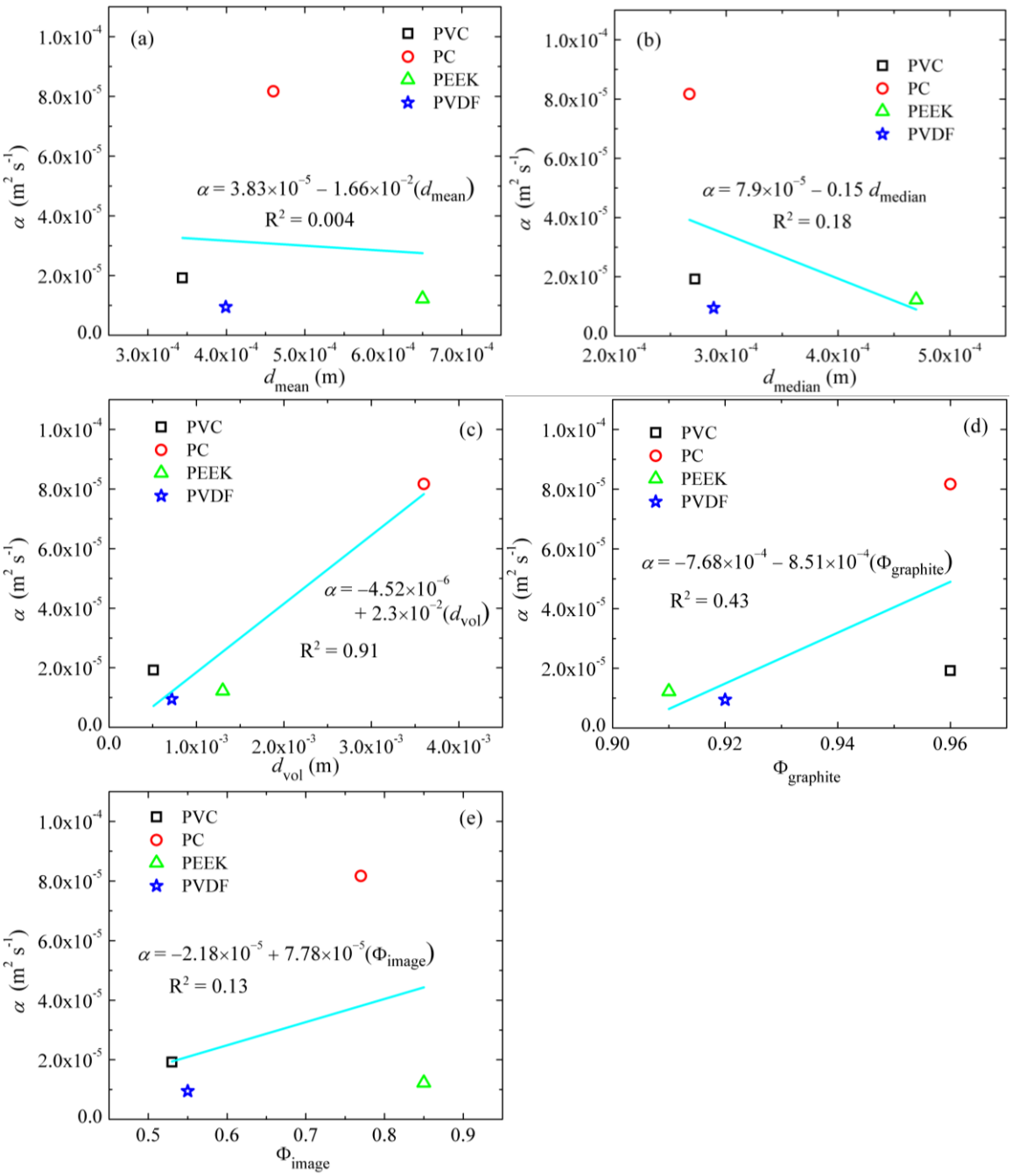

Figure 6.6: Thermal diffusivity of the char as a function of various quantities describing the physical structure of the intumescent char. The lines represent a linear fit of the data, which are expressed by the equations in these figures.

Figure 6.7 portrays the product of ρ and k as a function of the char's mean, median, and volume-weighted mean pore diameters, as well as the char's porosity based on both the density of graphite and image analysis. It was found that the product of ρ and k was strongly related to the d_{mean}, as shown in Figure 6.7(a); a linear relationship was established with an R^2 value of 0.89. The product of ρ and k was found to have a weak relationship with d_{median}, as shown in Figure 6.7(b). It was observed the product of ρ and k had no clear dependence on d_{vol} and $\Phi_{graphite}$, as displayed in Figure 6.7(c) and Figure 6.7(d). However, as depicted in Figure 6.7(e), the product of ρ and k was found to have a nearly perfect linear relationship with Φ_{image}, promoting an R^2 value of 0.98.

The strong linear relationships between the product of ρ and k and both d_{mean} and Φ_{image} can perhaps be explained by a theoretical analysis of the radiative heat transfer through a polymeric char structure outlined by Stoliarov et al. [22]. It was assumed that the char was comprised of a stack of thin, dense, highly conductive, and highly absorptive plates that were separated by wide, low density, low conductivity, and high transparency gaps. A detailed description of the radiative transport, based on the radiation diffusion approximation, defined the product of ρ and k to be a function of the areal density of a single char plate. The analysis concluded that, assuming all char was comprised of the same material, the thermal insulating potential of a char layer was directly proportional to the number of plates within the char layer. In other words, the greater the number of pore walls (perpendicular to the direction of thermal transport) within the fully developed char, the greater the thermal insulating potential. The experimental data displayed in Figure 6.7(a) and Figure 6.7(e) support this theoretical analysis of radiative thermal transport. As the

d_{mean} and Φ_{image} increases, which suggests the number of pore walls per unit thickness will decrease, the char layer will become more transparent to heat flow. In other words, designing charring polymers capable of producing smaller pore sizes, which increases the number of pore walls, results in the development of intumescent chars with an enhanced thermal insulating potential.

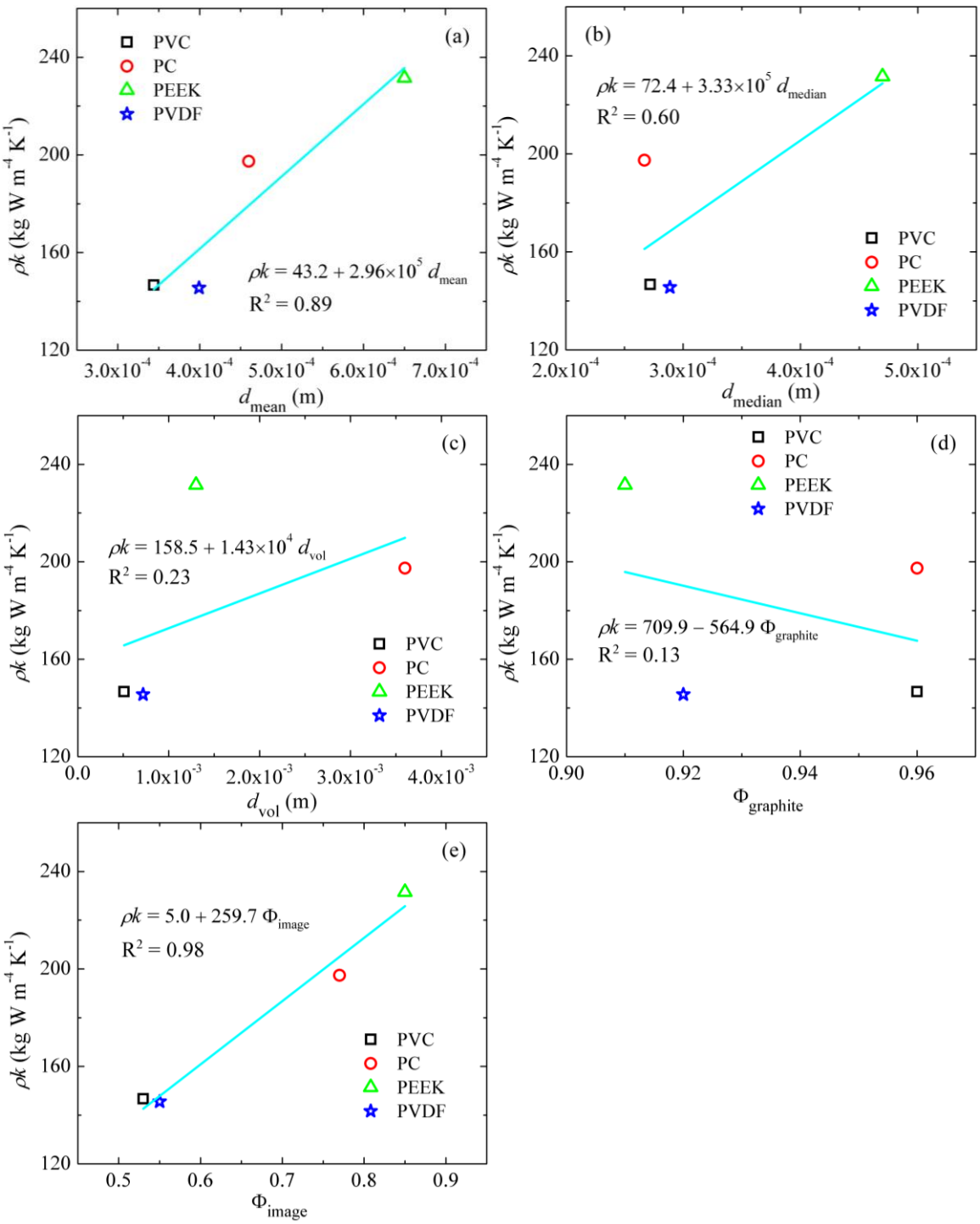

Figure 6.7: The fully developed char's transparency to heat flow as a function of the various quantities describing the physical structure of the intumescent char. The lines represent a linear fit of the data, which are expressed by the equations in these figures.

Chapter 7: Cone Calorimetry Simulations

Cone calorimetry [45] is arguably the most widely used test in the field of fire science due to its ability to measure a material's HRR during combustion. In an attempt to demonstrate the generality of the models of charring materials developed within this study, idealistic 1D cone calorimetry simulations were carried out to emulate this popular testing scenario. These simulations employed highly simplified expressions for the pertinent boundary conditions (the model did not take into account the presence of a flame or the non-uniformity of the radiant heat flux incident to the evolving intumescent sample's surface as a function of both space and time) and the simulations assumed complete combustion of all gaseous products. It is important to note that cone calorimetry experiments were not performed in this work. Instead, literature data [22] for two materials, PVC and PC, were used for comparison. The literature data were collected on materials that were defined as poly(vinyl chloride) and Bisphenol A polycarbonate, although they were produced by a different manufacturer and thus may have had different flammability behavior. Therefore, the results of this comparison should be interpreted with caution.

The simulations employed the center parameters derived from the 2D model of PVC and PC in section 5.2.2 and section 5.4.2, respectively. These simulations subjected a 6.0×10^{-3} m thick rigid PVC sample and 5.4×10^{-3} m thick PC sample to a constant heat flux of 75 kW m^{-2}. The convective losses from the top sample surface were neglected and the bottom sample surface was set as adiabatic and impenetrable to gas flow. The additional heat flux provided by a sustained flame on the sample surface was neglected by the model.

The simulated heat release rate of the cone calorimetry experiments (HRR_{Cone}) was calculated as the sum of the simulated mass flow rate of the individual gaseous decomposition products (see Table 4.1) and their corresponding heats of complete combustion derived from the MCC measurements (see Table 4.3), as given in Equation 4.4.

Figure 7.1 and Figure 7.2 display the experimental mass loss rate from cone calorimetry tests (MLR_{Cone}) and HRR_{Cone} data collected by Stoliarov et al. [22] as open symbols. The experimental data was collected at 1 Hz and is portrayed as the average from five repeated tests. The error was computed from the scatter of the data as two standard deviations of the mean. Prior to averaging, the MLR_{Cone} data was grouped into 5 s bins to reduce the noise associated with the experimental dataset. In the case of PC, the MLR_{Cone} data from two tests was unavailable; therefore, the mean MLR_{Cone} represents the results of three repeated tests. The solid lines displayed in Figure 7.1 and Figure 7.2 represent the simulated results from this work. The total simulated MLR_{cone} is the summation of the mass flow rates of all gaseous decomposition products.

The PVC MLR_{Cone} simulations, as shown in Figure 7.1(a), captured the experimental data very well for the first 300 s of burning. At later stages of burning, the model was shown to decay much quicker than the experimental data. This sharp decay in the simulated results is believed to be a result of the model neglecting the effects of surface oxidation, which are present in the cone calorimetry experiments after the flame is extinguished. The satisfactory agreement between the experimental and simulated MLR_{Cone} results during the first 300 s of burning indicates that the PVC model developed within this work is capable of extrapolating to testing configurations outside of its calibration conditions.

The simulated HRR_{Cone} results of PVC burning, shown in Figure 7.1(b), displayed notable discrepancies when compared to the experimental data. Because the model was capable of predicting the MLR_{Cone} data with satisfactory results, as indicated in Figure 7.1(a), the most plausible explanation of these large discrepancies is due to a reduced combustion efficiency (η_{comb}) observed in the cone calorimetry experiments as a result of gaseous pyrolyzate escaping the sample without combusting [112]. The HRR_{Cone} simulations, on the other hand, utilized the measured heats of complete combustion (see section 4.3) of each gaseous product in the reaction mechanism; therefore, the simulations represented a complete combustion process.

To mimic the two-peak structure observed in the simulated HRR_{Cone} results shown in Figure 7.1(b), a combustion efficiency was constructed for two portions of the data. The combustion efficiency was computed as the ratio between the experimental and simulated HRR_{Cone} profiles. The combustion efficiency of the first portion of the experiments was computed to be 75%. The combustion efficiency was found to be reduced to 54% in the second portions of the experiment. Stoliarov et al. [22] reported the a single combustion efficiency of the PVC experiments as 75%; however, this value did not isolate the reduction in combustion efficiency during later stages of burning. The significant reduction in combustion efficiency indicated a substantial portion of the volatiles produced during the late stages of the cone experiments escaped prior to being combusted. It is likely that the intumescence induced shape change of the PVC sample during burning prevented a continuous flame sheet from being sustained on the top surface of the sample, which ultimately allowed unburned gaseous volatiles to escape freely.

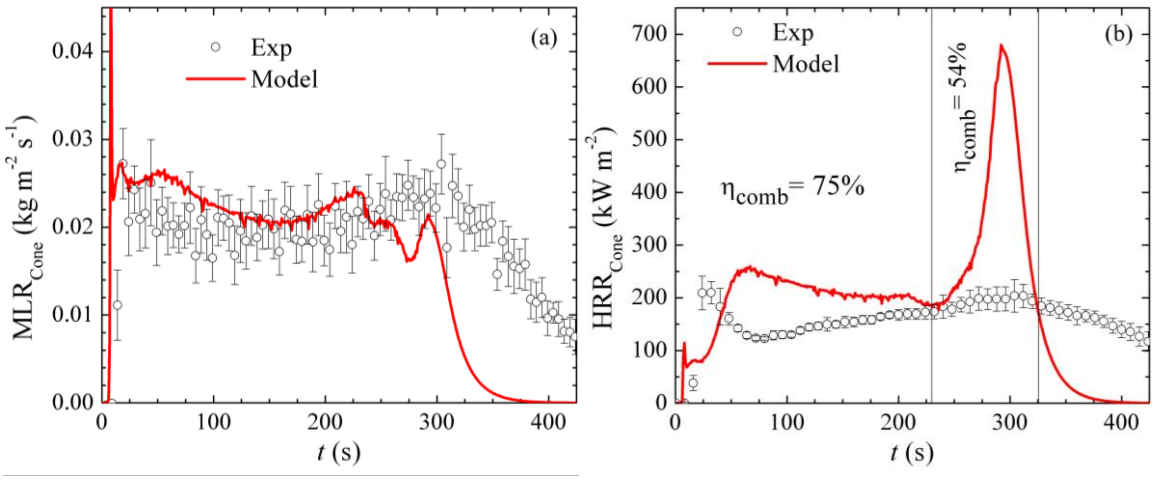

Figure 7.1: Averaged experimental and modeled (a) MLR_{Cone} and (b) HRR_{Cone} data obtained for PVC cone calorimetry experiments at 75 kW m^{-2} irradiation. The experimental data (open symbols) was obtained from tests conducted by Stoliarov et al. [22] and the simulated results (solid lines) were obtained utilizing the center parameters of the 2D model of PVC pyrolysis developed in this work.

The PC MLR_{Cone} simulations, as shown in Figure 7.2(a), captured the experimental data very well for the onset of decomposition and very early stages of burning. At later stages of burning (after 100 s), the experimental data quickly became problematic as the sample physically interacted with the heater as a result of intumescent induced swelling; therefore, the experimental MLR_{Cone} after 100 s was unreliable and could not be used for comparison. However, the satisfactory agreement between the experimental and simulated MLR_{Cone} results during the onset of decomposition and early stages of burning provided satisfactory confidence that the model was capable of capturing the key physics of the PC cone calorimetry experiments.

The simulated HRR_{Cone} results of PC burning, shown in Figure 7.2(b), displayed excellent agreement for the first 150 s of burning and notable discrepancies during later stages of burning. Similar to the argument presented for the PVC results above, these large

discrepancies after 150 s were attributed to the reduced combustion efficiency (η_{comb}) observed in the cone calorimetry experiments. Again, to mimic two-peak structure observed in the simulated HRR_{Cone} results, a combustion efficiency was computed for two regions of the experimental dataset. The combustion efficiency of the first portion of the experiments was found to be 96%, indicating nearly complete combustion in the cone experiments. However, during later stages of burning (after 150 s), a decreased combustion efficiency of 72% was found, which indicated that a relatively significant portion of the volatile pyrolyzates produced during pyrolysis escaped instead of being consumed in the combustion process. Stoliarov et al. [22] computed the overall combustion efficiency of the PC cone calorimetry experiments to be 84%, which was identical to the average combustion efficiency calculated in this study.

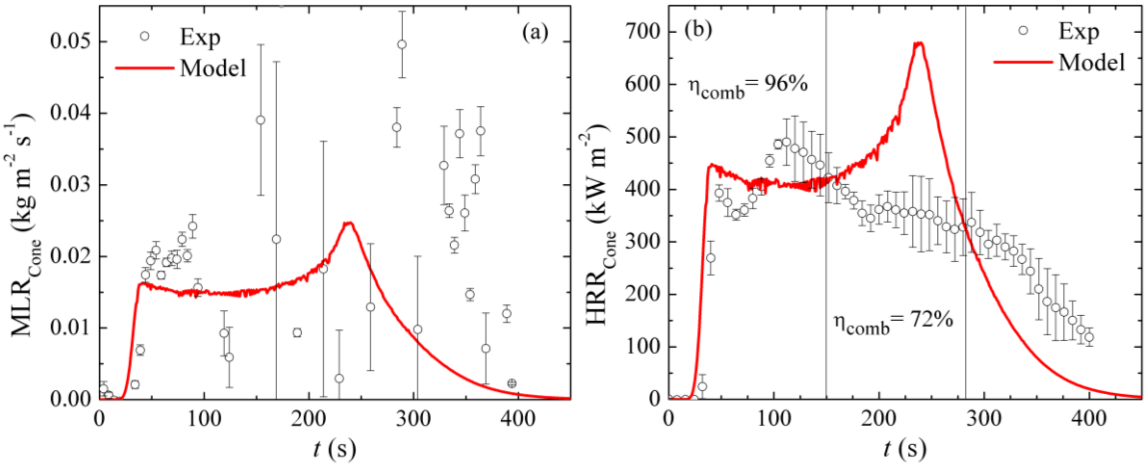

Figure 7.2: Averaged experimental and modeled (a) MLR_{Cone} and (b) HRR_{Cone} data obtained for PC cone calorimetry experiments at 75 kW m^{-2}. The experimental data (open symbols) was obtained from tests conducted by Stoliarov et al. [22] and the simulated results (solid lines) were obtained utilizing the center parameters of the 2D model of PC pyrolysis developed in this work.

Chapter 8: Concluding Remarks

This manuscript presents a systematic methodology to fully parameterize a comprehensive pyrolysis model of charring and intumescent materials. The most essential features of this methodology, which were developed during this doctoral research and serve as primary contributions, are summarized by the following:

- The development of the new gasification apparatus (CAPA II), which enables accurate measurements of mass, unexposed sample surface temperature, and sample shape profiles during the controlled pyrolysis of charring and intumescent polymers. Contributing to the design and assembly of the gasification apparatus as well as a thorough characterization of the boundary conditions were included within this study.
- The development of the new 2D axisymmetric pyrolysis model (implemented within ThermaKin2Ds), which facilitates detailed analyses of the CAPA II experimental data. Careful measurements of the boundary conditions were required to expand the existing ThermaKin model to an axisymmetric framework emulating the CAPA II gasification apparatus.
- The parameterization of comprehensive 1D and 2D pyrolysis models of rigid PVC, FPVC, PC, PEEK, and PVDF (1D only). The resulting pyrolysis models were calibrated utilizing the sample shape profiles and unexposed surface temperature data of a single set point heat flux. The models were subsequently validated against several experimental datasets collected from outside of the model calibration

conditions. To the author's knowledge, these models represent the most detailed pyrolysis models for each material to date.

- The development of new experimental procedures and subsequent analyses to examine the physical structure of the intumescent char using simple, inexpensive equipment. This methodology, developed within this work, enabled quantitative analyses of the physical structure of the intumescent char layer.
- The subsequent char analysis resulted in the derivation of quantitative correlations relating the thermal transport within the developing char layer and the physical structure of the intumescent char.

The complete set of parameters was derived from a foundational framework established from milligram-scale experiments, therefore, a brief overview is provided. TGA and DSC experimental data were employed to parameterize a numerical model capable of predicting the kinetics and thermodynamics of thermal decomposition of rigid PVC, FPVC, PC, PEEK, and PVDF. The reaction mechanism of each material, comprised of a system of sequential first-order reactions, was capable of reproducing the milligram-scale experimental data within the accuracy of the instrumentation. It is important to note that the model did not resolve each elementary reaction; instead, it captured the global mass loss and heat flow trends associated with the thermal decomposition of each polymer. As a result, Arrhenius reaction rates, stoichiometric mass coefficients for each reaction, heat capacities, and heats of reaction were determined for each step in the reaction mechanism.

MCC datasets were utilized to determine the heats of complete combustion of volatile gases produced during each reaction through a manually iterative inverse analysis

procedure. It is important to note that the MCC analysis employed the reaction mechanism developed from the TGA and DSC characterization. A quantitative measure of the heats of complete combustion, coupled with the aforementioned thermal degradation model, enabled a predictive capability of the heat release rate during the combustion of charring and intumescent materials. Individual heats of complete combustion were parameterized for the combustion of the volatile gases produced in each step of the reaction mechanism. Therefore, it is possible to predict the materials contribution to the growth and spread of fire.

The new CAPA II gasification experimental data were used to determine the density and thermal transport parameters of rigid PVC, FPVC, PC, PEEK, and PVDF pyrolysis through inverse analysis employing ThermaKin2Ds. As a result, both 1D and 2D axisymmetric versions of pyrolysis models were fully parameterized to predict the burning rates of all materials studied. In general, the 2D version of the model captured the experimental data more accurately than the 1D version of the model. Due to the radially-uniform and minimal sample swelling observed in the CAPA II tests, only a 1D version of the PVDF pyrolysis model was created. The 2D models were capable of simulating the experimental unexposed surface temperature and MLR histories with a mean error of 2.2% and 16.4%, respectively. The resulting models, to the author's knowledge, provide the most detailed and accurate predictions of the pyrolysis for each of the intumescent and charring polymers investigated in this work.

The aforementioned methodology was employed to analyze a collection of charring and intumescent materials, therefore, a summary of the findings of individual materials is

presented. In the case of rigid PVC specifically, the 2D model demonstrated only minor improvements in simulating the gasification experimental MLR over the 1D model. However, the 2D model did more accurately reproduce the experimental sample shape profiles observed during the gasification tests. It is important to note that different densities and thermal conductivities were required for the 1D and 2D models to capture the experimental data at all heat fluxes. The 1D model employed thermal transport parameters that corresponded to averaged values, which incorporated edge effects of the small experimental sample sizes. The 2D model, on the other hand, attempted to decouple the center and edge physics. Therefore, it is believed that the center component parameters from the 2D model provide the most physically meaningful parameters and thus enables more accurate extrapolation to burning at full-scale.

Idealistic full-scale simulations employing the center parameters were subsequently conducted to provide a comparison between the developed rigid PVC and FPVC pyrolysis models. The comparison yielded similar burning rates but substantially different heat release rates between rigid PVC and FPVC. The combustion of gaseous products originated from the organic plasticizers during the first step of FPVC decomposition is believed to be largely responsible for the significant increase in the heat release rate exhibited by FPVC, with respect to rigid PVC, early in the burning process. Therefore, it is critical to account for the individual heats of complete combustion for each step in the reaction mechanism. It should be noted that the results presented in this manuscript cannot necessarily be generalized to all commercially available FPVC materials as their compositions may differ significantly.

The systematic methodology to parameterize a comprehensive pyrolysis model of intumescent polymers was subsequently applied to PC and PEEK. In the case of both PC and PEEK pyrolysis, the 2D model was shown to display significant improvements over the 1D model counterpart; such improvements were not observed in the case of PVC and FPVC due to the increased radial uniformity of the intumescent char. In the case of PC and PEEK, it quickly became evident that the inability of the 1D model to capture the radial dependence of the sample shape profiles prevented the 1D model from accurately representing the interaction between the sample surfaces and the surrounding radiation exposure. This inability to accurately model the evolution of the sample shape profiles significantly impacted the quality of the material burning rate predictions. Therefore, these modeling results provide a strong justification for introducing the additional complexity of a 2D model for materials that experience significant swelling during pyrolysis.

Idealistic full-scale simulations employing the center parameters of the associated 2D pyrolysis models were subsequently conducted to provide a comparison between the large-scale burning behavior of PC and PEEK. It was shown that there were notable differences in both the MLR_{LS} and HRR_{LS} profiles between the two materials under both 40 and 70 kW m^{-2}. In all stages of burning, the HRR_{LS} of PC was found to be greater than that of the PEEK by a factor of two. Therefore, the larger and faster HRR_{LS} of PC during all stages of burning will likely result in a greater flame spread rate during an actual fire event, consequently, making PC a greater fire hazard than PEEK. Although the unique combustibility of the gaseous decomposition products were likely partially responsible for the observed differences in the HRR_{LS}, further analysis indicated that the kinetics of

thermal decomposition were largely responsible for the differences between the large-scale burning behavior of PC and PEEK. Therefore, designing charring and intumescent materials with thermally stable kinetics of thermal decomposition will decrease the materials rate of pyrolysis and ultimately improve its reaction to fire

Next, the systematic methodology to parameterize a comprehensive pyrolysis model of intumescent polymers was applied to PVDF. In the case of PVDF, only a 1D pyrolysis model was parameterized due to the negligible, radially-uniform sample expansion during the gasification experiments. The resulting model was shown to require several iterations to capture the unique maxima observed in the CAPA II MLR data. It was determined that the emissivity of the top sample surface experienced significant changes throughout the pyrolysis process and was responsible for the multiple maxima observed in the experimental MLR profiles. Therefore, when accounting for the changing emissivity, the resulting 1D model was demonstrated to provide satisfactory results of PVDF pyrolysis.

Finally, the intumescent chars developed as a result of independent CAPA II experiments were analyzed to gain an understanding of the physical structure of the char. Image analysis lead to quantitative measurements of the pore size distributions and porosity of the char produced from the pyrolysis of rigid PVC, PC, PEEK, and PVDF samples. The mean pore diameters and char porosities based on the image analysis for all materials were found to be on the order of 4.6×10^{-4} m and 0.67, respectively. To provide a quantitative measure of the char's thermal insulating potential, several quantities representing the thermal transport within the fully developed char (thermal conductivity, thermal diffusivity, and the product of density and thermal conductivity) were compared as functions of the

char's mean, median, and volume-weighted mean pore diameters as well as the porosities based on the density of graphite and image analysis.

The most notable correlation determined in the char structure analysis was the linearly increasing trend between the product of density and thermal conductivity and the porosity based on image analysis ($\rho k = 5.0 + 259.7\Phi_{image}$); where ρ [kg m^{-3}] is the char density, k [W m^{-1} K^{-1}] is the thermal conductivity of the char, and Φ_{image} is the char porosity based on image analysis. This relationship between the product of density and thermal conductivity (a measure of the char's transparency to heat flow) and the char's porosity based on image analysis (a measure of volumetric fraction of void space within the char layer) indicates that the char is more transparent to heat flow with an increased void space (larger pores). In other words, a char structure with smaller pores (resulting in a larger number of pore walls perpendicular to the direction of heat flow) has a higher thermal insulating potential. Therefore, this critical correlation between the char's transparency to heat flow and volumetric fraction of void space provides a quantitative relationship between the macrostructure of the char and its associated thermal insulating potential.

To further the understanding of an intumescent and charring materials reaction to fire, several topics have been recommended as the focus of future work. The first recommendation involves applying the systematic methodology described in this dissertation to a myriad of additional materials. This dissertation focused on developing the methodology and was shown to provide satisfactory results on a collection of five materials; however, the fire modeling community would benefit from accurate pyrolysis modeling parameters for countless other intumescent and charring polymers. Additionally,

applying this methodology to intumescent coatings and paints could prove to be beneficial to improving their performance during a fire event. Establishing a methodology to measure the surface emissivity of the intermediate reactants could also be beneficial, especially in light of the phenomenon discovered during the PVDF model development. Next, expanding the scope of the methodology to include an aerobic environment during the gasification experiments would enable the parameterization of surface oxidation effects. Surface oxidation effects are most notable prior to a flame sustaining itself on the sample surface, therefore, surface oxidation may play an important role in the prediction of the time to ignition. Collecting well-defined experimental data at a larger scale would provide additional useful validation targets for the models constructed in this work. Lastly, increasing the number of data points (examining the physical structure of the intumescent char of a wide range of additional materials) on the correlation between the product of density and thermal conductivity and the porosity based on image analysis is essential for improving the thermal insulating potential of future intumescent materials.

References

[1] S.M. Halliwell, Polymers in Building and Construction, 2002.

[2] A. Dasari, Z.Z. Yu, G.P. Cai, Y.W. Mai, Recent developments in the fire retardancy of polymeric materials, Prog. Polym. Sci. 38 (2013) 1357–1387. doi:10.1016/j.progpolymsci.2013.06.006.

[3] G.E. Zaikov, S.M. Lomakin, Ecological issue of polymer flame retardancy, J. Appl. Polym. Sci. 86 (2002) 2449–2462. doi:10.1002/app.10946.

[4] S. Bourbigot, S. Duquesne, Fire retardant polymers: recent developments and opportunities, J. Mater. Chem. 17 (2007) 2283. doi:10.1039/b702511d.

[5] F. Laoutid, L. Bonnaud, M. Alexandre, J.-M. Lopez-Cuesta, P. Dubois, New prospects in flame retardant polymer materials: From fundamentals to nanocomposites, Mater. Sci. Eng. R Reports. 63 (2009) 100–125. doi:10.1016/j.mser.2008.09.002.

[6] A.B. Morgan, J.W. Gilman, An overview of flame retardancy of polymeric materials: application, technology, and future directions, Fire Mater. 37 (2013) 259–279. doi:10.1002/fam.2128.

[7] S.Y. Lu, I. Hamerton, Recent developments in the chemistry of halogen-free flame retardant polymers, Prog. Polym. Sci. 27 (2002) 1661–1712. doi:10.1016/S0079-6700(02)00018-7.

[8] C. Di Blasi, Modeling the effects of high radiative heat fluxes on intumescent material decomposition, J. Anal. Appl. Pyrolysis. 71 (2004) 721–737. doi:10.1016/j.jaap.2003.10.003.

[9] M.B. McKinnon, Y. Ding, S.I. Stoliarov, S. Crowley, R.E. Lyon., Pyrolysis model for a carbon fiber/epoxy structural aerospace composite, J. Fire Sci. 35 (2017) 36–61. doi:10.1177/0734904116679422.

[10] H. Fromme, G. Becher, B. Hilger, W. Völkel, Brominated flame retardants - Exposure and risk assessment for the general population, Int. J. Hyg. Environ. Health. 219 (2016) 1–23. doi:10.1016/j.ijheh.2015.08.004.

[11] M. Ezechiáš, S. Covino, T. Cajthaml, Ecotoxicity and biodegradability of new brominated flame retardants: A review, Ecotoxicol. Environ. Saf. 110 (2014) 153–167. doi:10.1016/j.ecoenv.2014.08.030.

[12] L.G. Costa, G. Giordano, S. Tagliaferri, A. Caglieri, A. Mutti, Polybrominated diphenyl ether (PBDE) flame retardants: environmental contamination, human body burden and potential adverse health effects, Acta Biomed. 79 (2008) 172–183.

[13] K. Hoffman, A. Lorenzo, C.M. Butt, S.C. Hammel, B.B. Henderson, S.A. Roman, R.P. Scheri, H.M. Stapleton, J.A. Sosa, Exposure to flame retardant chemicals and occurrence and severity of papillary thyroid cancer: A case-control study, Environ. Int. 107 (2017) 235–242. doi:10.1016/j.envint.2017.06.021.

[14] P.O. Darnerud, Toxic effects of brominated flame retardants in man and in wildlife, Environ. Int. 29 (2003) 841–853. doi:10.1016/S0160-4120(03)00107-7.

[15] T. Kashiwagi, Polymer combustion and flammability-Role of the condensed phase, Symp. Combust. 25 (1994) 1423–1437. doi:10.1016/S0082-0784(06)80786-1.

[16] C. Di Blasi, Modeling and Simulation of Combustion Processes of Charring and Non-Charring Solid Fuels, Energy Combust. 19 (1993) 71–104.

[17] B. Moghtaderi, The state-of-the-art in pyrolysis modelling of lignocellulosic solid fuels, Fire Mater. 30 (2006) 1–34. doi:10.1002/fam.891.

[18] C. Di Blasi, Modeling chemical and physical processes of wood and biomass pyrolysis, Prog. Energy Combust. Sci. 34 (2008) 47–90. doi:10.1016/j.pecs.2006.12.001.

[19] K. Mcgrattan, S. Hostikka, R. Mcdermott, J. Floyd, C. Weinschenk, K. Overholt, Sixth Edition Fire Dynamics Simulator Technical Reference Guide Volume 4: Configuration Management, 4 (2017). doi:10.6028/NIST.SP.1018-4.

[20] C. Lautenberger, C. Fernandez-Pello, Generalized pyrolysis model for combustible solids, Fire Saf. J. 44 (2009) 819–839. doi:10.1016/j.firesaf.2009.03.011.

[21] S.I. Stoliarov, R.E. Lyon, Thermo-Kinetic Model of Burning for Pyrolyzing Materials, in: Fire Saf. Sci. - Proc. 9th Int. Symp., 2008: pp. 1141–1152. doi:10.3801/IAFSS.FSS.9-1141.

[22] S.I. Stoliarov, S. Crowley, R.N. Walters, R.E. Lyon, Prediction of the Burning Rates of Charring Polymers, Combust. Flame. 157 (2010) 2024–2034. doi:10.1016/j.combustflame.2010.03.011.

[23] T.J. Ohlemiller, Smoldering Combustion, Gaithersburg, 1986.

[24] O. Korobeinichev, M. Gonchikzhapov, A. Tereshchenko, I. Gerasimov, A. Shmakov, A. Paletsky, A. Karpov, An Experimental Study of Horizontal Flame Spread Over PMMA Surface in Still Air, Combust. Flame. 188 (2018) 388–398. doi:10.1016/j.combustflame.2017.10.008.

[25] O.P. Korobeinichev, A.I. Karpov, A.A. Bolkisev, A.A. Shaklein, M.B. Gonchikzhapov, A.A. Paletsky, A.G. Tereshchenko, A.G. Shmakov, I.E. Gerasimov, A. Kumar, An Experimental and Numerical Study of Thermal and Chemical Structure of Downward Flame Spread Over PMMA Surface in Still Air, Proc. Combust. Inst. In Press (2018) 1–8. doi:10.1016/j.proci.2018.06.005.

[26] C. Di Blasi, Modeling chemical and physical processes of wood and biomass pyrolysis, Prog. Energy Combust. Sci. 34 (2008) 47–90. doi:10.1016/j.pecs.2006.12.001.

[27] J.G. Quintiere, Fundamentals of Fire Phenomena, John Wiley & Sons, Ltd, Chichester, UK, 2006. doi:10.1002/0470091150.

[28] A.M. Melnick, E.J. Nolan, The Design and Development of a High-Heating-Rate Thermogravimetric Analyzer Suitable for Use With Ablative Plastics, J. Macromol. Sci. Part A - Chem. 3 (1969) 641–648. doi:10.1080/10601326908053833.

[29] Christian Vovelle, Jean-Louis Delfau, Marcelline Reuillon, Jacques Bransier, Najib Laraqui, Experimental and Numerical Study of the Thermal Degradation of PMMA, Combust. Sci. Technol. 53 (1987) 187–201. doi:10.1080/00102208708947026.

[30] T. Ohlemiller, J. Shields, One- and two-sided burning of thermally thin materials, Fire Mater. 17 (1993) 103–110. doi:10.1002/fam.810170302.

[31] W. Parker, R. Filipczak, Modelling the heat release rate of aircraft cabin panels in the cone and OSU calorimeters, Fire Mater. 19 (1995) 55–59. doi:10.1002/fam.810190202.

[32] C. Di Blasi, I.S. Wichman, Effects of solid-phase properties on flames spreading over composite materials, Combust. Flame. 102 (1995) 229–240. doi:10.1016/0010-2180(95)00003-O.

[33] J. Rychly, L. Costa, Modelling of polymer ignition and burning adopted for cone calorimeter measurments: The correlation between the rate of heat release and oxygen index, Fire Mater. 19 (1995) 215–220. doi:10.1002/fam.810190504.

[34] I.S. Wichman, A. Atreya, A simplified model for the pyrolysis of charring materials, Combust. Flame. 68 (1987) 231–247. doi:10.1016/0010-2180(87)90002-2.

[35] R.E. Lyon, Pyrolysis kinetics of char forming polymers, Polym. Degrad. Stab. 61 (1998) 201–210. doi:10.1016/S0141-3910(97)00125-0.

[36] S.D. Watt, J.E.J. Staggs, A.C. McIntosh, J. Brindley, A theoretical explanation of the influence of char formation on the ignition of polymers, Fire Saf. J. 36 (2001) 421–436. doi:10.1016/S0379-7112(01)00008-X.

[37] S.D. Watt, J.E.J. Staggs, A.C. McIntosh, J. Brindley, Comparison of competitive and non-competitive char formation in polymer combustion, Fire Saf. Sci. (2003) 605–616. doi:10.3801/IAFSS.FSS.7-605.

[38] J.E.J. Staggs, A theoretical investigation into modelling thermal degradation of solids incorporating finite-rate kinetics, Combust. Sci. Technol. 123 (1997) 261–285. doi:Doi 10.1080/00102209708935631.

[39] J. Li, S.I. Stoliarov, Measurement of Kinetics and Thermodynamics of the Thermal Degradation for Charring Polymers, Polym. Degrad. Stab. 106 (2014) 2–15. doi:10.1016/j.polymdegradstab.2013.09.022.

[40] T.L. Bergman, A.S. Lavine, F.P. Incropera, D.P. DeWitt, Fundamentals of Heat and Mass Transfer, Seventh, John Wiley & Sons, Hoboken, 2011.

[41] J.P. Holman, Experimental methods for engineers, 1994. doi:10.1016/0894-1777(94)90118-X.

[42] C.E. Anderson, D.E. Ketchum, W.P. Mountain, Thermal Conductivity of Intumescent Chars, (1988) 390–410.

[43] C. Anderson, J. Dziuk, W. Mallow, J. Buckmaster, A Study of Intumescent Reaction Mechanisms, J. Fire Sci. 3 (1985) 161–194.

[44] M. Bartholmai, B. Schartel, Assessing the performance of intumescent coatings using bench-scaled cone calorimeter and finite difference simulations, Fire Mater. 31 (2007) 187–205. doi:10.1002/fam.933.

[45] ASTM International, Standard Test Method for Heat and Visible Smoke Release Rates for Materials and Products Using an Oxygen Consumption Calorimeter, West Conshohocken, 2015. doi:10.1520/E1354-16A.1.8.

[46] NSAI, Test methods for determining the contribution to the fire resistance of structural members — Part 4: Applied passive protection to steel members, 2013.

[47] D. 4102-2, Fire Behaviour of Building Materials and Building Components in Fire - Building Components - Definitions, Requirements and Tests, Berlin, 1981.

[48] B. Schartel, M. Bartholmai, U. Knoll, Some comments on the use of cone calorimeter data, Polym. Degrad. Stab. 88 (2005) 540–547. doi:10.1016/j.polymdegradstab.2004.12.016.

[49] S.I. Stoliarov, N. Safronava, R.E. Lyon, The effect of variation in polymer properties on the rate of burning, Fire Mater. 33 (2009) 257–271. doi:10.1002/fam.1003.

[50] K. Li, D.S.W. Pau, J. Wang, J. Ji, Modelling pyrolysis of charring materials: Determining flame heat flux using bench-scale experiments of medium density fibreboard (MDF), Chem. Eng. Sci. 123 (2015) 39–48. doi:10.1016/j.ces.2014.10.043.

[51] P. Elliot, R. Whiteley, J. Staggs, Steady state analysis of cone calorimeter data, in: Proc. from 4th Fire Mater. Int. Conf., Crystal City, 1995: p. 35.

[52] P.J. Austin, R.R. Buch, T. Kashiwagi, Gasification of Silicone Fluids Under External Thermal Radiation.pdf, (1997). doi:NISTIR 6041.

[53] M. Chaos, M.M. Khan, N. Krishnamoorthy, J.L. de Ris, S.B. Dorofeev, Evaluation of Optimization Schemes and Determination of Solid Fuel Properties for CFD Fire Models using Bench-scale Pyrolysis Tests, Proc. Combust. Inst. 33 (2011) 2599–2606. doi:10.1016/j.proci.2010.07.018.

[54] A. Witkowski, B. Girardin, M. Forsth, F. Hewitt, G. Fontaine, S. Duquesne, S. Bourbigot, T.R. Hull, Development of an anaerobic pyrolysis model for fire retardant cable sheathing materials, Polym. Degrad. Stab. 113 (2015) 208–217. doi:10.1016/j.polymdegradstab.2015.01.006.

[55] J. Li, J. Gong, S.I. Stoliarov, Gasification Experiments for Pyrolysis Model Parameterization and Validation, Int. J. Heat Mass Transf. 77 (2014) 738–744. doi:10.1016/j.ijheatmasstransfer.2014.06.003.

[56] R. Webster, M. Lázaro, D. Alvear, J. Capote, A. Trouvé, Limitations in Current Parameter Estimation Techniques for Pyrolysis Modelling, in: Proc. Sixth Int. Semin. Fire Explos. Hazards, Research Publishing Services, Singapore, 2011: pp. 1008–1019. doi:10.3850/978-981-08-7724-8_15-02.

[57] J. Li, J. Gong, S.I. Stoliarov, Development of Pyrolysis Models for Charring Polymers, Polym. Degrad. Stab. 115 (2015) 138–152. doi:10.1016/j.polymdegradstab.2015.03.003.

[58] A.R. Horrocks, D. Price, Fire Retardant Materials - Knihy Google, n.d.

[59] S. Bourbigot, M. Le Bras, S. Duquesne, M. Rochery, Recent advances for intumescent polymers, Macromol. Mater. Eng. 289 (2004) 499–511. doi:10.1002/mame.200400007.

[60] R.G. Puri, A.S. Khanna, Intumescent coatings: A review on recent progress, J. Coatings Technol. Res. 14 (2017) 1–20. doi:10.1007/s11998-016-9815-3.

[61] C.E. Anderson, D.K. Wauters, A Thermodynamic Heat Transfer Intumescent Systems Model, Int. J. Eng. Sci. 22 (1984) 881–889.

[62] J. Buckmaster, C. Anderson, A. Nachman, A Model for Intumescent Systems, Int. J. Eng. Sci. 24 (1986) 263–276.

[63] J.E.J. Staggs, Simple mathematical models of char-forming polymers, Polym. Int. 49 (2000) 1147–1152. doi:10.1002/1097-0126(200010)49:10<1147::AID-PI481>3.0.CO;2-R.

[64] J.E.J. Staggs, Heat and mass transport in developing chars, Polym. Degrad. Stab. 82 (2003) 297–307. doi:10.1016/S0141-3910(03)00185-X.

[65] J.E.J. Staggs, Estimating the thermal conductivity of chars and porous residues using thermal resistor networks, Fire Saf. J. 37 (2002) 107–119. doi:10.1016/S0379-7112(01)00035-2.

[66] K. Bakker, Using the finite element method to compute the influence of complex porosity and inclusion structures on the thermal and electrical conductivity, Int. J. Heat Mass Transf. 40 (1997) 3503–3511. doi:10.1016/S0017-9310(97)00017-3.

[67] I.I. Kantorovich, E. Bar-Ziv, Heat transfer within highly porous chars: A review, Fuel. 78 (1999) 279–299. doi:10.1016/S0016-2361(97)00258-5.

[68] J.E.J. Staggs, R.J. Crewe, R. Butler, A theoretical and experimental investigation of intumescent behaviour in protective coatings for structural steel, Chem. Eng. Sci. 71 (2012) 239–251. doi:10.1016/j.ces.2011.12.010.

[69] C. Di Blasi, C. Branca, Mathematical model for the nonsteady decomposition of intumescent coatings, AIChE J. 47 (2001) 2359–2370. doi:10.1002/aic.690471020.

[70] R. Siegel, J. Howell, Thermal Radiation Heat Transfer, Fourth, Taylor & Francis, New York, 2002.

[71] J.E.J. Staggs, Thermal conductivity estimates of intumescent chars by direct numerical simulation, Fire Saf. J. 45 (2010) 228–237. doi:10.1016/j.firesaf.2010.03.004.

[72] K. Bakker, H. Kwast, E.H.P. Cordfunke, Determination of a porosity correction factor for the thermal conductivity of irradiated U02 fuel by means of the finite element method, J. Nucl. Mater. 226 (1995) 128–143. doi:10.1016/0022-3115(95)00087-9.

[73] J.K. Carson, S.J. Lovatt, D.J. Tanner, A.C. Cleland, An analysis of the influence of material structure on the effective thermal conductivity of theoretical porous materials using finite element simulations, Int. J. Refrig. 26 (2003) 873–880. doi:10.1016/S0140-7007(03)00094-X.

[74] D.A.G. Bruggeman, Berechnung verschiedener physikalischer Konstanten von heterogenen Substanzen. I. Dielektrizitätskonstanten und Leitfähigkeiten der Mischkörper aus isotropen Substanzen, Ann. Phys. 416 (1935) 636–664. doi:10.1002/andp.19354160705.

[75] Y.C. Wang, A. Foster, Experimental and numerical study of temperature developments in PIR core sandwich panels with joint, Fire Saf. J. 90 (2017) 1–14. doi:10.1016/j.firesaf.2017.03.003.

[76] D. Hibbitt, B. Karlsson, P. Sorensen, ABAQUS Analysis User's Manual, Version 6.12, HKS, Inc., Providence, 2012.

[77] L. Glicksman, M. Schuetz, M. Sinofsky, Radiation heat transfer in foam insulation, 30 (1987) 187–197.

[78] L.R. Glicksman, Heat transfer in foams, in: Low Density Cell. Plast., Springer Netherlands, Dordrecht, 1994: pp. 104–152. doi:10.1007/978-94-011-1256-7_5.

[79] J.E.J. Staggs, A simple model of polymer pyrolysis including transport of volatiles, Fire Saf. J. 34 (2000) 69–80. doi:10.1016/S0379-7112(99)00043-0.

[80] J.E.J. Staggs, Modelling pyrolysis of char-forming polymers, in: Proc. Interflam, Edinburgh, 1999: pp. 167–179.

[81] G.M. Anthony, Kinetic and chemical studies of polymer cross-linking using thermal gravimetry and hyphenated methods. Degradation of polyvinylchloride, Polym. Degrad. Stab. 64 (1999) 353–357. doi:10.1016/S0141-3910(98)00129-3.

[82] G.K. Batchelor, An Introduction to Fluid Dynamics, Cambridge Univerity Press, Cambridge, 1987.

[83] J.E.J. Staggs, Approximate solutions for the pyrolysis of char forming and filled polymers under thermally thick conditions, Fire Mater. 24 (2000) 305–308. doi:10.1002/1099-1018(200011/12)24:6<305::AID-FAM749>3.0.CO;2-B.

[84] NETZSCH, Simultaneous Thermal Analyzer – STA 449 F1 Jupiter®, (2017). https://www.netzsch-thermal-analysis.com/us/products-solutions/simultaneous-thermogravimetry-differential-scanning-calorimetry/sta-449-f1-jupiter/.

[85] M.B. McKinnon, S.I. Stoliarov, Pyrolysis Model Development for a Multilayer Floor Covering, Materials (Basel). 8 (2015) 6117–6153.

[86] ASTM International, D7309-11 Standard Test Method for Determining Flammability Characteristics of Plastics and Other Solid Materials Using Microscale Combustion Calorimetry, West Conshohocken, 2011. doi:10.1520/D7309-11.

[87] G. Linteris, M. Zammarano, B. Wilthan, L. Hanssen, Absorption and Reflection of Infrared Radiation by Polymers in Fire-like Environments, Fire Mater. 36 (2012) 537–553. doi:10.1002/fam.1113.

[88] J.D. Swann, Y. Ding, S.I. Stoliarov, Characterization of Pyrolysis and Combustion of Rigid Poly(Vinyl Chloride) Using Two-Dimensional Modeling, Int. J. Heat Mass Transf. 132 (2019) 347–361. doi:10.1016/j.ijheatmasstransfer.2018.12.011.

[89] K. McGrattan, S. Hostikka, R. McDermott, J. Floyd, C. Weinschenk, K. Overholt, Fire Dynamics Simulator, Technical Reference Guide, Volume 1: Mathematical Model, NIST Spec. Publ. 1018-1. 1 (2013). doi:10.6028/NIST.SP.1018-1.

[90] I.T. Leventon, J. Li, S.I. Stoliarov, A Flame Spread Simulation Based on a Comprehensive Solid Pyrolysis Model Coupled with a Detailed Empirical Flame Structure Representation, Combust. Flame. 162 (2015) 3884–3895. doi:10.1016/j.combustflame.2015.07.025.

[91] A. Rabbani, S. Jamshidi, S. Salehi, An automated simple algorithm for realistic pore network extraction from micro-tomography images, J. Pet. Sci. Eng. 123 (2014) 164–171. doi:10.1016/j.petrol.2014.08.020.

[92] F. Meyer, Topographic distance and watershed lines, Signal Processing. 38 (1994) 113–125. doi:10.1016/0165-1684(94)90060-4.

[93] A. Factor, Char Formation in Aromatic Engineering Polymers, in: G. Nelson (Ed.), Fire Polym. Hazards Identif. Prev., 425th ed., American Chemical Society, Washington DC, 1990: pp. 274–287.

[94] S.I. Stoliarov, I.T. Leventon, R.E. Lyon, Two-Dimensional Model of Burning for Pyrolyzable Solids, Fire Mater. 38 (2014) 391–408. doi:10.1002/fam.2187.

[95] J.D. Swann, Y. Ding, M.B. McKinnon, S.I. Stoliarov, Controlled Atmosphere Pyrolysis Apparatus II (CAPA II): A New Tool for Analysis of Pyrolysis of Charring and Intumescent Polymers, Fire Saf. J. 91 (2017) 130–139. doi:10.1016/j.firesaf.2017.03.038.

[96] W.H. Press, S.A. Teukolsky, W.T. Vetterling, B.P. Flannery, Numerical Recipes in C++: The Art of Scientific Computting, Cambridge Univerity Press, Cambridge, U.K., 1988.

[97] J. Li, S.I. Stoliarov, Measurement of Kinetics and Thermodynamics of the Thermal Degradation for Non-Charring Polymers, Combust. Flame. 160 (2013) 1287–1297. doi:10.1016/j.combustflame.2013.02.012.

[98] M.B. McKinnon, S.I. Stoliarov, A. Witkowski, Development of a Pyrolysis Model for Corrugated Cardboard, Combust. Flame. 160 (2013) 2595–2607. doi:10.1016/j.combustflame.2013.06.001.

[99] Y. Ding, M.B. McKinnon, S.I. Stoliarov, G. Fontaine, S. Bourbigot, Determination of Kinetics and Thermodynamics of Thermal Decomposition for Polymers Containing Reactive Flame Retardants: Application to Poly(lactic acid) Blended with Melamine and Ammonium Polyphosphate, Polym. Degrad. Stab. 129 (2016) 347–362. doi:10.1016/j.polymdegradstab.2016.05.014.

[100] Y. Ding, S. Stoliarov, R. Kraemer, Development of a Semiglobal Reaction Mechanism for the Thermal Decomposition of a Polymer Containing Reactive Flame Retardants: Application to Glass-Fiber-Reinforced Polybutylene Terephthalate Blended with Aluminum Diethyl Phosphinate and Melamine Polypho, Polymers (Basel). 10 (2018) 1137. doi:10.3390/polym10101137.

[101] Y. Ding, S.I. Stoliarov, R.H. Kraemer, Pyrolysis model development for a polymeric material containing multiple flame retardants: Relationship between heat release rate and material composition, Combust. Flame. 202 (2019) 43–57. doi:10.1016/j.combustflame.2019.01.003.

[102] H.S. Carslaw, J.C. Jaeger, Conduction of Heat in Solids, 2nd ed., Oxford University Press, 1959.

[103] J. Crank, The mathematics of diffusion, 2nd ed., Clarendon Press, Oxford, 1975.

[104] H.M. Zhu, X.G. Jiang, J.H. Yan, Y. Chi, K.F. Cen, TG-FTIR Analysis of PVC Thermal Degradation and HCl Removal, J. Anal. Appl. Pyrolysis. 82 (2008) 1–9. doi:10.1016/j.jaap.2007.11.011.

[105] Y. Ding, K. Kwon, S.I. Stoliarov, R.H. Kraemer, Development of a Semi-global Reaction Mechanism for Thermal Decomposition of a Polymer Containing ReactiveFlame Retardant, Proc. Combust. Inst. (2018). doi:10.1016/j.proci.2018.05.073.

[106] R. Lyon, R. Walters, S. Stoliarov, A Thermal Analysis Method for Measuring Polymer Flammability, J. ASTM Int. 3 (2006) 1–18. doi:10.1520/JAI13895.

[107] T. Sterzyński, J. Tomaszewska, J. Andrzejewski, K. Skórczewska, Evaluation of glass transition temperature of PVC/POSS nanocomposites, Compos. Sci. Technol. 117 (2015) 398–403. doi:10.1016/j.compscitech.2015.07.009.

[108] P.J. Linstrom, W.G. Mallard, NIST Chemistry WebBook, NIST Standard Reference Database Number 69, (2018). doi:10.18434/T4D303.

[109] R.N. Walters, S.M. Hackett, R.E. Lyon, Heats of combustion of high temperature polymers, Fire Mater. 24 (2000) 245–252. doi:10.1002/1099-1018(200009/10)24:5<245::AID-FAM744>3.0.CO;2-7.

[110] M. Försth, A. Roos, Absorptivity and its Dependence on Heat Source Temperature and Degree of Thermal Breakdown, Fire Mater. 35 (2011) 285–301. doi:10.1002/fam.1053.

[111] A. Ito, T. Kashiwagi, Characterization of flame spread over PMMA using holographic interferometry sample orientation effects, Combust. Flame. 71 (1988) 189–204. doi:10.1016/0010-2180(88)90007-7.

[112] F. Raffan-Montoya, X. Ding, S.I. Stoliarov, R.H. Kraemer, Measurement of heat release in laminar diffusion flames fueled by controlled pyrolysis of milligram-sized solid samples: Impact of bromine- and phosphorus-based flame retardants, Combust. Flame. 162 (2015) 4660–4670. doi:10.1016/j.combustflame.2015.09.031.